



RF-MEMS based Passive Components and Integration Concepts for Adaptive Millimetre Wave Front-Ends

DISSERTATION

zur Erlangung des akademischen Grades eines

DOKTOR-INGENIEURS
(Dr.-Ing.)

der Fakultät für Ingenieurwissenschaften
und Informatik der Universität Ulm

von

William Gautier
aus Laval

Gutachter: Prof. Dr.-Ing. Wolfgang Menzel
Prof. Dr.-Ing. Hermann Schumacher

Amtierender Dekan: Prof. Dr.-Ing. Klaus Dietmayer

ACKNOWLEDGEMENTS

Among all who have contributed to my post graduate education, my greatest appreciation surely belongs to Dr. Bernhard Schönlinner and Prof. Wolfgang Menzel, who guided me through this thesis. I especially would like to thank Dr. Schönlinner for his excellent mentorship over the three years I worked with him at EADS Innovation Works in Munich. Prof. Menzel was my academical mentor at the University of Ulm. Many thanks are due to him for his advice and thoughtful guidance all along the dissertation. Nevertheless, my acknowledgement would not be complete without mentioning the other members of the Microwave Team at EADS Innovation Works: Ulrich Prechtel, head of the group of research, and Dr. Volker Ziegler. I would like to acknowledge them for their unfailing professionalism, their encouragement, and for their friendship. I also would like to thank my room colleagues, Armin Stehle, Dr. Christian Siegel, Dr. Georgi Georgiev, and Benedikt Schulte, for the friendly ambiance. I really enjoyed working with them all. Finally, I would like to thank all those, who helped me and stood by me through this experience. Each one of them has participated to the good progression of this dissertation. I owe them a frank acknowledgement.

William Gautier

Ulm, Germany

May 2010

Contents

ACKNOWLEDGEMENTS	i
Introduction	1
Motivation	1
Overview	4
1 Experimental Methods and Technologies	7
1.1 Simulation Techniques	7
1.2 RF Measurement Techniques	7
1.2.1 On-Wafer RF Measurement Setup up to 40 GHz	7
1.2.2 Antenna Far Field Measurement in Anechoic Chamber	8
1.3 Control Setup for Electrically Steerable Antennas	10
1.4 Technologies	11
1.4.1 EADS Innovation Works RF-MEMS Technology	11
1.4.2 LTCC Technology	12
1.4.3 EPFL Barium Strontium Titanate Ferro-Electric Varactor Technology	13
1.5 Conclusion	14
2 Fixed and Tunable Cavity Resonator Filters for Millimetre-Wave Front-ends	15
2.1 Introduction	15
2.2 Previous Work on Micro-Machined Filters	17
2.3 Previous Work on Tunable Filters	18
2.4 Theory of Cavity Resonator Band-Pass Filters	20
2.4.1 2-Port Cavity Resonators	20
2.4.2 N-Pole Cavity Resonator Band-Pass Filters	24
2.5 Fixed and Tunable Micro-Machined Cavity Resonator Filters at 20 GHz in Silicon Technology	26
2.5.1 Description of the Targeted Application	26
2.5.2 Fixed-Frequency Filters	29
2.5.3 Frequency-Agile Filter	45
2.6 Fixed and Tunable Substrate-Integrated Cavity Resonator Filters at 15 GHz in LTCC	54
2.6.1 Motivations and Targeted Application for LTCC Filters in Ku-Band	54
2.6.2 Fixed-Frequency Filter	55
2.6.3 Frequency-Agile Filters	61
2.7 Ferro-Electric Varactor based Temperature-Compensated Substrate-Integrated Cavity Resonator	66
2.7.1 Influence of Temperature on the DuPont 943 Ceramic Substrate	67
2.7.2 Previous Work on Temperature-Compensated Resonators and Filters	70
2.7.3 Principle and Design of the Temperature-Compensated Cavity Resonator	71
2.8 Conclusion	74

3	RF-MEMS based Phased Array Antennas for Millimetre-Wave Front-Ends	75
3.1	Introduction	75
3.2	Theory of Fixed-Beam and Phased Array Antennas	77
3.2.1	Various Types of Phased Array Antennas	77
3.2.2	Antenna Basics and Array Factor Theory	78
3.2.3	Theory of Phased Array Antennas	83
3.2.4	Errors in Fixed-Beam and Phased Array Antennas	85
3.2.5	Conclusion	86
3.3	W-Band Antenna Arrays for On-Board Wake Vortex FMCW-Radar	87
3.3.1	Description of the Targeted Application	87
3.3.2	Fixed-Beam Patch Antenna Arrays on Rogers RT/Duroid 5880 Substrate . .	88
3.3.3	Conclusion	100
3.4	Ka-Band Phased Array Antenna for Satellite Communication	100
3.4.1	Description of the Targeted Application	100
3.4.2	Fixed-Beam Aperture Coupled Patch Antenna Array on LTCC	101
3.4.3	Phased Array Antenna	108
3.4.4	Conclusion	122
3.5	X-Band Phased Array Antenna	122
3.5.1	Architecture and Hybrid Integration Concept	122
3.5.2	Fixed-Beam Patch Antenna Array	124
3.5.3	Phased Array Antenna	128
3.5.4	Conclusion	135
3.6	Conclusion	135
4	Future Work	137
	Summary	141
	Appendix A: A 3-bit RF-MEMS Phase Shifter for Ka-Band Electrically Steerable Antennas	143
	Bibliography	147

List of Figures

0.1	Tuning device technologies versus frequency.	3
1.1	Generic setup for far field radiation characteristic measurement.	8
1.2	Photograph of the electric-field probe for W-band waveguide to microstrip line transition.	9
1.3	Control setup for electrically steerable antennas.	10
1.4	Cross-sectional drawing of the EADS Innovation Works RF-MEMS serial switch. . .	11
1.5	Standard LTCC fabrication process.	13
1.6	Cross-sectional drawing of the BST capacitor on LAO substrate.	14
2.1	State of the art of micro- and millimetre-wave resonators.	16
2.2	Rectangular cavity resonator in the Cartesian system of coordinates.	20
2.3	E_y -field component of the fundamental resonant mode in a rectangular cavity resonator. .	21
2.4	Schematic of a 2-port cavity resonator connected by means of impedance inverters. .	23
2.5	Schematic of a n-pole band-pass filter realised with impedance inverters and series-type resonators.	25
2.6	Schematic of a satellite transceiver for communication link (Courtesy of Tesat-Spacecom GmbH & Co. KG).	28
2.7	Cross-section of a KOH-etched micro-machined cavity resonator closed using a top silicon dielectric.	30
2.8	Cross-section (top) and top view (bottom) of the proposed micro-machined filter architecture.	31
2.9	Photograph of a micro-machined filter diced along the A-A cut. The A-A cutting plane is shown in Fig. 2.8.	32
2.10	3D view of the slot coupled microstrip line placed on top of the cavity resonator. . .	32
2.11	3D view of the coupling cavity placed on top of the inter-cavity wall.	32
2.12	1-port external Q-factor versus relative length of the coupling slot.	34
2.13	Normalised inductance $\frac{X}{Z_0}$ versus relative width of the coupling cavity.	36
2.14	Layout of the back-to-back coplanar to microstrip line transition on silicon.	37
2.15	Photograph of the micro-machined filters processed on 8 inch silicon wafer. X-ray picture by courtesy of Philips Semiconductors, now NXP Semiconductors.	38
2.16	Measured return loss and insertion loss of the back-to-back coplanar to microstrip line transition.	39
2.17	Measured response of a weakly coupled 2-port micro-machined cavity resonator. . .	39
2.18	Measured response of the 2-pole fixed-frequency micro-machined filter.	40
2.19	Measured response of the 3-pole fixed-frequency micro-machined filter.	41
2.20	Schematic of the 4-pole linear phase filter.	42
2.21	Architecture of the 4-pole linear phase filter.	43

2.22	Photograph of the 4-pole linear phase filter.	44
2.23	Measured response of the 4-pole linear phase filter.	44
2.24	Measured group delay of the 4-pole linear phase filter.	45
2.25	Schematic of the tunable 2-port cavity resonator.	46
2.26	Calculated response of a 2-port cavity resonator with and without tuning device. . .	47
2.27	Hybrid integration concept of the RF-MEMS tunable stub on the micro-machined cavity resonator silicon substrate.	48
2.28	3D view of the 2-port frequency-agile micro-machined cavity resonator.	49
2.29	Photograph of the 3-pole frequency-agile filter micro-machined in silicon.	50
2.30	Response of the tunable cavity resonator simulated for open/closed RF-MEMS switches.	52
2.31	Measured response of the 3-pole frequency-agile band-pass filter.	52
2.32	Measured response of the 3-pole frequency-agile band-pass filter - wideband plot. . .	53
2.33	3D view of the input/output coupling structure of the substrate-integrated cavity resonator (top plane removed and side-walls idealised).	56
2.34	Value of the 1-port external Q-factor versus via position.	57
2.35	Value of the normalised inductance achieved by the thick inductive iris.	58
2.36	3D view of the 2-pole substrate-integrated filter with the E_y -field component at 15 GHz (top metal plane removed).	59
2.37	Resonance peak of the weakly coupled substrate-integrated cavity resonator.	60
2.38	Measured response of the 2-pole substrate-integrated cavity resonator filter.	61
2.39	Hybrid integration concept of the coplanar RF-MEMS cantilevers on the LTCC substrate.	62
2.40	Photograph of the RF-MEMS frequency-agile filters on LTCC DuPont 943.	63
2.41	Response of the tunable substrate-integrated cavity resonator with one adjustable stub.	64
2.42	Response of the tunable LTCC filter with one adjustable stub per cavity resonator. .	65
2.43	Response of the tunable LTCC filter with one adjustable stub per cavity resonator - wideband plot.	65
2.44	Response of the tunable LTCC filter with two adjustable stubs per cavity resonator.	66
2.45	Layout of the weakly coupled stripline resonator in LTCC DuPont 943 (dimensions in μm).	67
2.46	Variation in % of the resonance frequency of the cavity and stripline resonators against temperature.	68
2.47	Variation in % of the relative permittivity of the DuPont 943 material over temperature.	70
2.48	Hybrid integration concept for the ferro-electric varactor on LTCC.	72
2.49	Photograph of the BST varactor based temperature-compensated cavity resonator in LTCC.	73
2.50	Relative variation of the resonance frequency of the LTCC resonators over temper- ature, with and without BST varactor compensation.	73
3.1	Analog beam forming (left)/digital beam forming (right).	75
3.2	Equally spaced linear array of isotropic point sources.	80
3.3	Rectangular array of isotropic point sources with a regular rectangular grid.	81
3.4	Equally spaced linear array of isotropic sources fed with a linear phase gradient. . .	83
3.5	Specifications of the transmit and receive antennas in the horizontal plane.	88

3.6	Extended Transmission Line Model of a 2-port microstrip antenna.	89
3.7	Equivalent circuit of a resonant serially fed patch antenna array.	90
3.8	Photograph of the serially fed patch antenna sub-array with sixteen patches.	91
3.9	Layout of the 1 to 28 corporate feed network.	92
3.10	Theoretical and simulated excitation coefficients of the 1 to 28 corporate feed network.	93
3.11	Photograph of the fixed-beam transmit antenna.	93
3.12	Theoretical and simulated excitation coefficients of the 3 to 1 power combiner.	94
3.13	Photograph of the receive antenna.	94
3.14	Measured and simulated E-plane far field pattern of the antenna sub-array at 76.5 GHz.	95
3.15	Measured return loss of the serially fed patch antenna sub-array.	96
3.16	Measured and simulated H-plane far field pattern of the transmit antenna at 76.5 GHz.	97
3.17	Measured and simulated H-plane far field pattern of the receive antenna at 76.5 GHz.	97
3.18	Measured return loss of the transmit antenna.	98
3.19	Measured return loss of the receive antenna.	99
3.20	Layout of the foreseen 1 to 28 corporate feed network with branch line couplers and on LTCC.	100
3.21	Cross-section of the Ka-band antenna array on 6-layer LTCC DuPont 943 substrate.	101
3.22	Schematic of the aperture coupled sub-array realised with four patches at the design frequency.	102
3.23	Theoretical and simulated excitation coefficients of the feed network in LTCC DuPont 943.	103
3.24	Transparent drawing of the fixed-beam patch antenna array on LTCC DuPont 943.	104
3.25	Photograph of the Ka-band fixed-beam antenna array on LTCC: front view(left) and back view(right).	104
3.26	H-plane far field pattern of the fixed-beam antenna on DuPont 943 at 35 GHz.	105
3.27	E-plane far field pattern of the fixed-beam antenna on DuPont 943 at 35 GHz.	106
3.28	Return loss of the fixed-beam antenna on LTCC DuPont 943.	106
3.29	Resonance frequency and return loss at 35 GHz of the fixed-beam antenna over temperature.	107
3.30	Drawing of the Ka-band RF-MEMS coplanar shunt switch in Thales-RT technology: top view(top) and A-A cross-sectional view(bottom).	109
3.31	Schematic of the Ka-band RF-MEMS coplanar shunt switch in Thales-RT technology.	110
3.32	Schematic(dashed) and full-wave simulated(solid) S-parameters of the Ka-band RF-MEMS coplanar shunt switch in Thales-RT technology.	110
3.33	Layout of the Ka-band RF-MEMS phase shifter in Thales-RT technology.	111
3.34	Simulated return loss and insertion loss of the Ka-band RF-MEMS phase shifter for the different switching states.	113
3.35	Phase shifts simulated for the eight switching states of the Ka-band RF-MEMS phase shifter.	114
3.36	Simulated mean insertion loss and standard phase deviation of the Ka-band phase shifter.	114
3.37	Hybrid integration concept for the EADS-IW RF-MEMS phase shifters.	116
3.38	3D view of the buried microstrip line to microstrip line transition in LTCC DuPont 943.	116

3.39	Hybrid integration concept for the Thales-RT RF-MEMS phase shifters.	117
3.40	3D view of the buried microstrip line to coplanar line transition in LTCC DuPont 943.117	
3.41	Hybrid integration concept for the Fraunhofer-ISIT RF-MEMS phase shifters.	119
3.42	Photograph of the Ka-band RF-MEMS electrically steerable antenna on LTCC: front view (middle), back view (right), and bond-wire connections (left).	120
3.43	Radiation characteristics measured in the H-plane for the RF-MEMS electrically steerable antenna at 35 GHz.	121
3.44	Measured return loss of the RF-MEMS electrically steerable antenna on LTCC.	121
3.45	Model of the X-band RF-MEMS phased array antenna with two simulated radiation patterns steered in the H-plane.	123
3.46	Architecture of the X-band electrically steerable antenna.	123
3.47	Theoretical and simulated excitation coefficients of the 1-to-4 corporate feed network.125	
3.48	Photograph of the fixed-beam X-band antenna array.	125
3.49	Measured and simulated E-plane far field pattern of the fixed-beam antenna at 9.5 GHz.126	
3.50	Measured and simulated H-plane far field pattern of the fixed-beam antenna at 9.5 GHz.127	
3.51	Measured and simulated return loss of the fixed-beam antenna.	127
3.52	Photograph of the X-band 3-bit RF-MEMS phase shifter.	128
3.53	Phase shifts measured for the eight switching states of the X-band phase shifter.	129
3.54	Insertion loss and return loss measured for the X-band phase shifter.	130
3.55	Standard phase deviation and mean insertion loss of the X-band phase shifter.	130
3.56	Photograph of the X-band phased array antenna demonstrator.	131
3.57	Measured E-plane far field characteristic of the electrically steerable antenna at 9.5 GHz.	132
3.58	Measured H-plane far field characteristics of the electrically steerable antenna at 9.5 GHz.	133
3.59	Measured return loss of the X-band electrically steerable antenna.	133
3.60	Measured and simulated H-plane far field pattern of the X-band electrically steerable antenna.	134
4.1	Example of RF bond-wire-free hybrid integration concept for sawn or hand-broken silicon chips.	137
4.2	Monolithic integration of the RF-MEMS tunable stub on the micro-machined cavity filter.	138
4.3	Importance of RF-MEMS packaging for integration: packaged and sawn silicon chip (left), and chip separated per hand (right).	139
A.1	Photograph of the EADS Innovation Works Ka-band RF-MEMS phase shifter.	143
A.2	Measured return loss and insertion loss of the EADS Innovation Works Ka-band RF-MEMS phase shifter for the eight switching states.	144
A.3	Phase shifts measured for the EADS Innovation Works Ka-band RF-MEMS phase shifter for the eight switching states.	145
A.4	Mean insertion loss and standard phase deviation of the EADS Innovation Works Ka-band RF-MEMS phase shifter.	145

List of Tables

2.1	Electrical specifications of the fixed-frequency micro-machined filters.	27
2.2	Electrical specifications of the frequency-agile micro-machined filter.	29
2.3	Coefficients of the low-pass prototype filters and electrical parameters of the 2- and 3-pole band-pass filters.	33
2.4	Dimensions of the coupling structures of the 2- and 3-pole micro-machined band-pass filters.	37
2.5	Coupling coefficients and electrical parameters of the 4-pole linear phase filter. . . .	43
2.6	Electrical specifications of the fixed-frequency LTCC filter.	54
2.7	Electrical specifications of the frequency-agile LTCC filter.	55
2.8	Coefficients of the low-pass prototype filter and electrical parameters of the 2-pole substrate-integrated band-pass filter.	56
2.9	Dimensions of the coplanar adjustable stubs of the LTCC tunable filters.	63
3.1	Dimensions of the serially fed microstrip antenna array with sixteen patches.	91
3.2	Measured performance of the SPDT and SP4T RF-MEMS switches.	129

Introduction

Motivation

In recent years, successive generations of micro- and millimetre-wave front-ends have come up with constantly increased standards in terms of size, performance, and affordability [1], [2], [3]. Also, due to the emergence of numerous applications in the low radio frequency spectrum, at L- or S-band, many of these applications have been constrained to move progressively towards higher frequencies. A good illustration of this is the migration of applications like satellite communications to the K-band, and even higher up to the W-band for automotive collision avoidance radars. In Europe, this evolution follows the recommendations of the European Radiocommunications Committee (ERC) stipulated in the "European Table Of Frequency Allocations And Utilisations" [4]. Nevertheless, if the move towards higher and previously unused frequency bands is necessary to satisfy both commercial, maritime, and military needs; it presents also technical advantages. For micro- and millimetre-wave systems, higher operating frequencies are synonym of larger bandwidths, reduced sizes, and shorter ranges of operation. The reduction of the operative range of RF front-ends at high frequencies is due to the atmospheric attenuation of microwave signals, which increases with the frequency. This constitutes an advantage or a disadvantage, depending on the application targeted with the system. On one hand, the limited range of a front-end can be favourably used because it prevents interferences between systems. In return, it might also represent a limitation when a target is far away from the sensor or from the communication front-end. Further, in the particular case of sensors, thanks to the higher reflectivity of microwave signals on small scatterers at high frequencies, the echo signal of radars augments with the frequency. This makes possible the detection of geometrically smaller targets in the W-band than in the K-band, for example, which used to be the frequency band of automotive radars. Seduced by these advantages, and especially by the comfortable bandwidths reachable at millimetre-wave frequencies, some communication applications working presently below 4 GHz are now considered for operation at K- or V-band. This is, for example, the case of the indoor point to multi-point domestic wireless local area network (WLAN) working currently at 2.460 GHz, and under development for operation around 60 GHz [5], [6], [7]. For individual users, this migration of the WLAN standard to millimetre-wave frequencies will provide a larger bandwidth of about 1 Gbit/s available for their Internet access, as well as a higher level of security for the data travelling on their personal network: only 10 m of coverage from a base station at 60 GHz.

In order to face this increased interest in the millimetre-wave range, the last decades have seen a lot of work to develop front-ends able to operate up to the W-band, and beyond. These developments occurred principally in two fields complementary for the realisation of RF systems: the design and fabrication of millimetre-wave components, and the integration of these components into front-ends. First, optimised processes and novel design techniques have made possible the advent of reliable MilliMetre-wave Integrated Circuits (MMIC). Many of these circuits such as High and Low-Noise Power Amplifiers (HPA and LNA), switches, and mixers, have been demonstrated with

outstanding properties in terms of power handling, linearity, and Noise Figure (NF) [8], [9]. Today, high-performance active millimetre-wave components are available on two main and complementary platforms: the Silicon Germanium (SiGe) technology, and the Gallium Arsenide (GaAs) technology. The SiGe technology is well suited to low-cost and low-power devices. For this reason, it is widely implemented in commercial applications, where the financial aspect is determining. On the other hand, the GaAs platform is more appropriate for high-power components, which are often expensive and mainly dedicated to the military market. On top of this, novel integration concepts and techniques have been developed for these components. In RF front-ends, the components are integrated either monolithically on a single chip to form a so-called "System on Chip" (SoC), or in a hybrid fashion onto a microwave substrate. Systems assembled in this way with individual chips mounted onto a common mother board are called "System in Package" (SiP). Both SoC and SiP integration techniques have assets and drawbacks depending on the nature of the system. The hybrid integration of front-ends is a compromise solution used to build "heterogeneous microsystems". It enables the use of components which might be fabricated in different technologies. Also, it is especially suitable for large systems which cannot be processed on a single chip. For these systems, hybrid integration allows for substantial cost savings because it uses low-cost microwave substrates such as soft substrates, Liquid Crystal Polymer (LCP) [10], or LTCC (Low-Temperature Co-fired Ceramics), which is presently the most common board technology [11], [12]. Nevertheless, as the operating frequency of front-ends increases, the size of individual components is reduced, and monolithic integration becomes more attractive [13], [14]. At millimetre-wave frequencies, the technique affords both a minimum size and a better reliability of front-ends, as well as lower fabrication costs for large production scales. Also, thanks to the small aperture of antennas at V-band and beyond, SoC front-ends have been demonstrated with antenna arrays directly integrated on the core chip, aside the monolithic active circuitry [15]. However, for the time being, technological challenges still constrict SoC integration to some niche applications operating above at least 60 GHz. Further, it suffers from a limited flexibility for the design of the different components, which all have to be realised in a same and unique technology.

On the other hand, beyond these recurring challenges of performance, size, and cost, reconfigurable front-ends are also becoming a trend. Nowadays, many emerging applications like air traffic control, automotive radars, or smart beam-locked base stations are based on electrically steerable antennas. In these systems, the beam radiated by the antenna is not fixed but steered in different directions of the space. In this way, the antenna is capable of pointing in real-time towards any area or target of interest within its field of view. Also, for other applications, this is the operating frequency, which has to be tuned over time. These reconfigurable front-ends often implement multi-functional and multi-band devices such as frequency-agile filters or tunable matching networks in place of conventional fixed circuitries. In most cases, these reconfigurable components shall be able to switch between different frequency bands that can be, for example, the different channels of a multi-band data link, or diverse bands selected for frequency hopping.

In order to answer this increasing need for reconfigurable front-ends, different kinds of tuning device such as switches and varactors have been developed. On top of conventional PIN-diode and transistor based solutions, three emerging technologies arose to improve on the performance of these tuning devices: the RF-MEMS technology, the ferro-electric thin films, and the Liquid Crystals (LC). Among these, the RF-MEMS technology is most probably the most versatile. It consists of a thin metal membrane, which can be pulled up or down under the action of an electrostatic field. For

usual RF-MEMS devices such as capacitive switches, the position of this membrane determines the value of a capacitance by changing the gap between two electrodes [16], [17]. When the membrane is in the up-state, the distance between the two electrodes of the switch is large, and the value of the capacitance is small. In return, when the switch is in the actuated or down-state, the gap between the two electrodes is reduced, and the capacitance is large. Depending on the configuration of the switch, the capacitance may be in series or in parallel. In this last case, the capacitance is between the signal line and the ground, and the switch is said to be a shunt switch. Further, the variable capacitance can be actuated in different manners: digitally to realise a 2-state varactor [18], or in an analogue way to achieve a continuously variable capacitance [19]. Compared to other technologies, the major limitation of RF-MEMS devices is most probably in their relatively long switching time, typically about 10 μ s. In return, some RF-MEMS technologies have been demonstrated with outstanding power handling capability, up to 6 W and beyond [20]. Opportunities of RF-MEMS have been presented through several successful realisations. To enumerate some of them, these are mostly impedance tuners [21], tunable filters [22], [23], and digital phase shifters [24], [25], all characterised by a relatively low level of insertion loss.

Besides RF-MEMS, ferro-electric thin films constitute a second realistic alternative to standard switch technologies. Basically, they have been implemented to realise the same kind of component as those based on RF-MEMS such as varactor switches [26], [27], and phase shifters [28]. The tuning principle of these components utilises the variation of the dielectric constant of ferro-electric thin films, when the material is exposed to an electrostatic field. Ferro-electric devices have switching times shorter than RF-MEMS, typically about 10 ns, but they suffer from limited Q-factors, especially at high frequencies. This makes them rather lossy and inappropriate at millimetre-wave frequencies, and limits their use to the lower part of the RF spectrum, at best up to the Ku-band (Fig. 0.1).

Finally, well known for their unique properties at optical frequencies, liquid crystals have been also recently investigated for implementation below 100 GHz. Up to now, they have been principally considered for the realisation of phase shifters at millimetre-wave frequencies [29], [30]. They are realised with a transmission line plunged in a bath of liquid crystal, itself enclosed inside a metal or micro-machined body. Liquid crystal components use basically the same principle as ferro-electric devices. They are based on the variation of the dielectric constant of liquid crystal materials in presence of an electrostatic field. Nevertheless, this technology is handicapped by long switching times, typically above 1 ms [31], and it is sometimes cumbersome to integrate because it requires

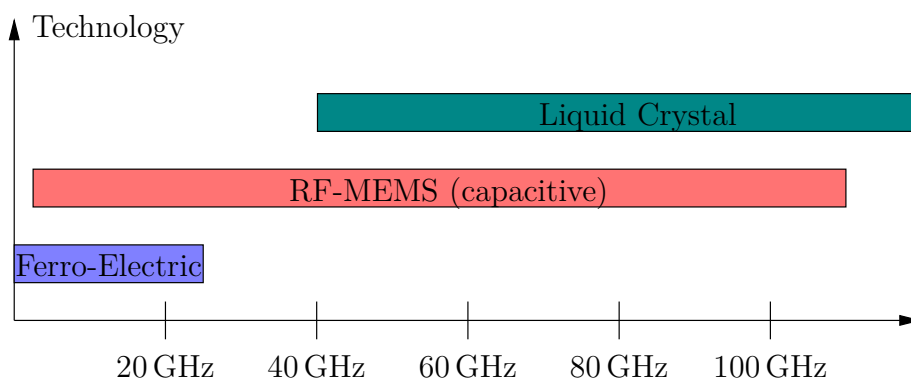


Fig. 0.1: Tuning device technologies versus frequency.

a receptacle to contain the liquid crystal. Despite this, it offers excellent performance in terms of insertion loss at very high frequencies above the K-band [32].

However, the practical implementation of these emerging technologies is still limited by issues related to their lack of maturity. Although they work well and have shown outstanding performance compared to what can be achieved with usual solutions, their practical implementation still relies on the development of reliable packaging solutions and low-cost integration techniques. These challenges, as well as the design, the realisation, and the measurement of fixed and tunable components for millimetre-wave front-ends, are the main lines of the present work. All these questions with their related issues constitute the essence of this thesis and are developed in the various sections and chapters of this manuscript.

Overview

This thesis is dedicated to RF-MEMS based passive components for fixed and adaptive millimetre-wave front-ends. It is focused on the design and realisation of different components forming what is generally known as the "passive front-end" of RF transmit/receive systems. This includes the antennas, the phase shifters, and the filters, but excludes all the active circuitry, such as the power amplifiers and mixers. Further, beyond the pure design of individual components, a large part of the work is concerned about the way the various circuits can be integrated and assembled at component level, but also at system level. Aside a first chapter providing an overview of the experimental tools and techniques employed in this work, two kinds of components are principally addressed in the two main chapters of the manuscript: the fixed and frequency-agile band-pass filters, and the electrically steerable antennas.

Chapter 2 is devoted to the development of fixed and frequency-agile band-pass filters. The chapter starts with an account of the work previously accomplished in the field of silicon micro-machined filters and that of band-pass tunable filters. Further, it describes the theoretical background of RF band-pass filters, and it provides the reader with the concepts and methods necessary to design them. In the fifth section, silicon micro-machined band-pass filters designed for operation at 20 GHz are demonstrated. The filters are horizontally integrated cavity resonator filters based on the pioneering work presented by Papapolymerou et al. in [33]. They are designed with two silicon wafers containing respectively, the coupling structures, and the cavity resonators. Nevertheless, for these filters, a novel architecture is proposed, which makes possible the fabrication of the filters with a single micro-machining process. The filters are manufactured using exclusively the KOH-wet etching of silicon for both, the cavity resonators, and the inter-resonator couplings. Also, since the geometry of the coupling structures realised in this way is different from the inductive irises commonly designed in waveguide filters, the usual formulas presented in [34] cannot be re-used. For this reason, in the section an effort has been made to explicit the method and equations used for the design of the demonstrated filters. In a later section, the chapter proposes a revisited implementation of the tuning technique presented originally in [35]. Beyond a presentation of the concept, the section demonstrates a 3-pole frequency-agile band-pass filter based on this technique and designed with RF-MEMS capacitive switches. Finally, in that same section, the hybrid integration concept of the RF-MEMS chips onto the silicon substrate of the micro-machined filters is described. The second part of the chapter presents Ku-band fixed and tunable band-pass filters on ceramics. These filters, demonstrated in section 2.6, are cavity resonator filters made out of LTCC

DuPont 943 substrate. They are realised according to the Substrate-Integrated Waveguide (SIW) technique and the cavity resonators are filled with LTCC material [36]. In this section, the design of a fixed-frequency 2-pole filter is described and is validated by good measurement results. Later, this fixed filter is used as starting point for the design of frequency-agile filters. These tunable filters on ceramics are based on a tuning technique similar to that introduced firstly for the silicon micro-machined filters. In this section however, it is adapted to fit the particular configuration of substrate-integrated cavity resonator filters, and different RF-MEMS structures are used. Two frequency-agile band-pass filters are realised according to this technique and measurements are presented for both filters. The chapter ends with an investigation into the temperature dependence of a substrate-integrated cavity resonator made out of LTCC. The last section presents the variation of the properties of the DuPont 943 material against temperature, and it describes the experiment from which the results have been gained. Also, in order to compensate for the frequency shift observed when the temperature increases, an actuation-free compensating structure has been developed. The compensation concept and the way it has been practically implemented are in this last section as well. Finally, the compensation technique based on Temperature-dependent (T-dependent) ferro-electric varactors is assessed by satisfactory measurement results, which conclude this second chapter.

Chapter 3 addresses the design and the realisation of phased array antennas. The chapter describes three antennas, where two are made electrically steerable by means of RF-MEMS phase shifters. For these antennas, the RF-MEMS phase shifters are processed on silicon and they are integrated in a hybrid fashion between the feed network and the antenna array. In the third section of the chapter, a first antenna array designed for airborne wake-vortex detection front-end is described. The antenna is designed for operation at W-band, and it is manufactured on low-loss Teflon-based Rogers RT/Duroid 5880 substrate. The section presents the design of the antenna array implemented with serially fed patch antenna sub-arrays, and an equivalent circuit is given for a 2-port microstrip antenna [37]. Further, the design and the realisation of the fixed-beam antenna are validated by measurement results in good agreement with full-wave simulations. Due to the relatively high operating frequency of the antenna, a brief discussion also addresses the influence of the fabrication tolerances on the RF performance of the antenna. In a later integration step, this antenna is intended to be equipped with the W-band RF-MEMS phase shifters presented in [38]. Later, in another section of that same chapter, a Ka-band electrically steerable antenna on LTCC is demonstrated. The antenna is a four by four microstrip antenna array fabricated on 6-layer LTCC DuPont 943 substrate. It is designed according to the aperture coupling technique with a microstrip feed network processed in a buried layer of the ceramic dielectric [39]. The complete design of the fixed-beam antenna is described and good measurement results are presented. Also, integration concepts are presented for the mounting of the RF-MEMS phase shifters onto the ceramic substrate of the antenna. Finally, the fixed-beam antenna presented at the beginning of the section is equipped with 3-bit RF-MEMS phase shifters to form an antenna electrically steerable in the H-plane. The fully integrated phased antenna and the related measurement results are part of the section as well. The end of the chapter reports the design, the realisation, and the measurement of an X-band electrically steerable antenna. Like the first antenna presented in the chapter, the X-band antenna is realised with serially fed antenna sub-arrays, and it is processed on Rogers RT/Duroid 5880 substrate. The last section presents the design of the different elements of the phased antenna: antenna array, feed network, phase shifters, and DC-control board, and

it describes the practical integration of these components into a stand-alone X-band RF-MEMS antenna demonstrator. For this electrically steerable antenna, all simulation and measurement results are also provided.

Further, since this work, like any other, constitutes only a part of longer developments and studies, the opportunity is taken in the fourth and last chapter to propose some future research ideas related, but not limited, to the components presented in this work.

Finally, the thesis concludes with a summary of the work presented through the four chapters of the manuscript. In this way, in the very last section of the document, the main achievements and some key numbers are recalled to the reader to give a concise but precise review of the work done. All along the writing of this manuscript, a special attention has been paid to keep the different chapters and sections as independent and self-consistent as possible. It has been written with the ambition that the various design techniques, tuning concepts, and integration methods will be used to develop devices other than those explicitly presented in this work. A good example of this effort can be found in the second chapter on band-pass filters. There, the coupling structures of the filters are always presented with their equations in order to allow for the design of couplings different from those of the demonstrated filters. All this has been done with the hope that interested readers will have the possibility to implement the proposed structures in other components such as diplexers, oscillators, or as transitions in RF distribution networks.

1 Experimental Methods and Technologies

1.1 Simulation Techniques

Various simulators have been used to design and optimise the different components presented in this work. Among all these, the workhorse which has been used to simulate a large majority of the structures, antennas, switches, and filters, was the electromagnetic simulation software EMPIRE. The simulator was installed on a conventional desktop computer, and it has been used in its 5.12 XCcel version and beyond [40]. EMPIRE is a Finite Difference Time Domain (FDTD) 3-dimensional electromagnetic field solver commercialised by IMST GmbH. It allows for full-wave simulations of structures, which can be excited through various kinds of ports, such as microstrip, waveguide, or coplanar. Full-wave simulations are a major tool for the design and analysis of microwave networks. They take radiation phenomena and coupling effects into account, and they allow for the calculation of complete 3-dimensional structures. In the available versions of the software however, only 3-dimensional rectangular grids were possible to discretise the structures. This unique discretisation option has been found to be somewhat cumbersome for the simulation of structures non aligned on the mesh cells, which have to be approximated by stepwise contours. The second software implemented during this work was the 2.5-dimensional simulation software Microwave Office. This tool, commercialised by Applied Wave Research [41], has been especially suitable for the simulation of planar structures such as microstrip antennas and planar feed networks. Aside this electromagnetic software, the schematic simulator tool of Microwave Office has also been utilised. This last tool has been mostly implemented to aid the realisation and the verification of equivalent circuits. Beyond these commercial simulators, several engineering C/C++ programs have also been written and employed. In this group, a software has been used to calculate the excitation coefficients of antenna arrays [42]. The software computes the amplitudes and phases with which a given antenna array shall be fed such that its array factor is the best approximation in the Tchebycheff sense of a goal array factor function (not physically achievable) [43], [44]. It is based on an iterative method known as the "Remez" algorithm, and allows for the realisation of array factors with given beamwidths, prescribed nulls, and minimum uniform side lobe levels [45].

1.2 RF Measurement Techniques

1.2.1 On-Wafer RF Measurement Setup up to 40 GHz

Apart from the far field pattern of antennas, all circuits demonstrated in this work have been measured at EADS Innovation Works in Ottobrunn. They have been characterised using a probe station equipped with IZI coplanar measurement probes, both commercialised by Sues MicroTech AG. Depending on the Device Under Test (DUT), two sorts of probes have been used. On one hand, 150 μ m-pitch Ground Signal Ground (GSG) probes have been utilised for the measurement of components processed on silicon, i.e. the micro-machined filters and RF-MEMS circuits. On the

other hand, 250 μm -pitch GSG probes from that same family have been used to connect the test set to the circuits, filters and antennas, made out of ceramics [46]. The measurement probes were connected to a network analyser Agilent E8363B PNA by means of coaxial cables mounted with K-connectors. This ensemble, network analyser, test set cables, measurement probes, and probe station, used to form a setup capable of measuring S-parameters up to 40 GHz on-wafer or using coaxial interfaces.

In order to measure S-parameters independently of the characteristics of the test set, the influence of the interconnects and of the setup itself had to be de-embedded. As it is usual, this has been done with a calibration of the measurement setup prior to the measurement of the DUT. For the components presented in the following sections, two calibration methods have been used: the TRL (Thru-Reflect-Line) and the SOLT (Short-Open-Load-Thru) calibration techniques. TRL calibration has been used each time a part of the on-wafer structure had to be calibrated out of the measurement. This occurred typically when the DUT was connected to the probes by means of coplanar-to-microstrip transitions implemented only for measurement purposes. In this case, in order to characterise the device without the influence of these transitions, TRL standards were processed on the wafer aside the structures to characterise. Otherwise, the setup was calibrated directly at the probe tips using SOLT calibration. The substrate used to perform SOLT calibrations was a CS-5 calibration substrate manufactured by GGB Industries [47].

1.2.2 Antenna Far Field Measurement in Anechoic Chamber

Three different facilities have been used to measure the radiation characteristics of the antennas demonstrated in the third chapter. The location where the various measurements have been performed was chosen depending on the availability of each one of the test ranges, and on their equipments suitable or not for the considered frequency range. Basically, all antenna far field test ranges are based on the same architecture built around an anechoic chamber (Fig. 1.1).

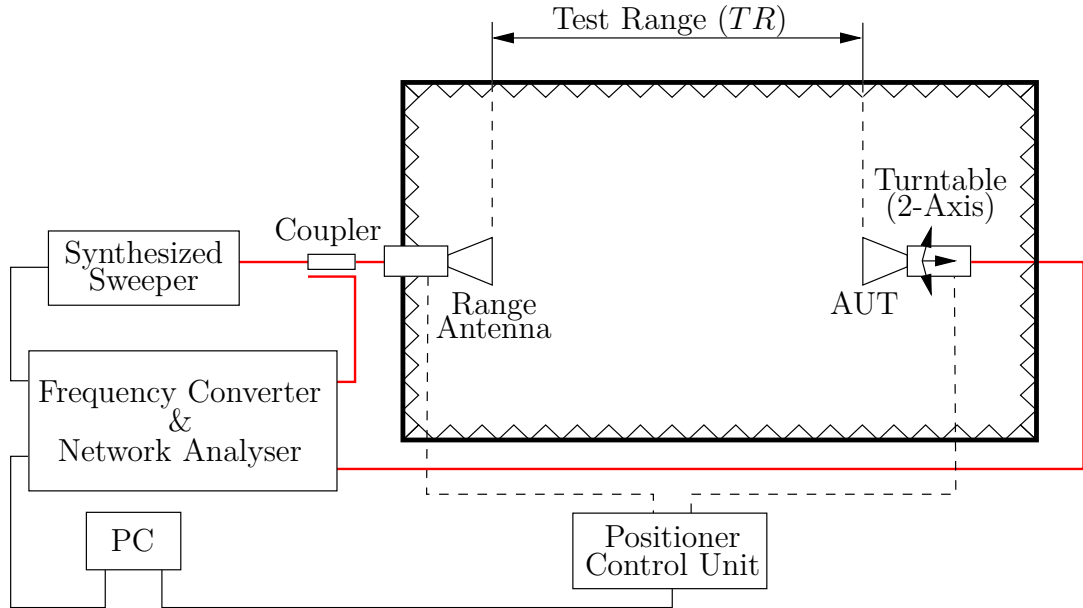


Fig. 1.1: Generic setup for far field radiation characteristic measurement.

In this chamber, in order to measure the far field radiation characteristic of an antenna in good conditions, a minimal distance has to be respected between the Antenna Under Test (AUT) and the Range Antenna (RA). This distance called Test Range (TR) is chosen such that the electromagnetic wave radiated by the range antenna is seen as a plane-wave, or quasi plane-wave, by the AUT. In this case, the test range is said to satisfy the far field conditions. The Far Field Range (FFR) is defined by

$$FFR = \frac{2D^2}{\lambda}, \quad (1.2.1)$$

where λ is the free-space wavelength at the frequency at which the pattern is measured, and D is the diameter of the largest AUT measurable in the chamber.

The three antennas demonstrated in the following have been designed in various frequency bands, namely the X-band, the Ka-band, and the W-band. For this reason, they have been measured in anechoic chambers very different in terms of size and equipment, but also regarding the technique used to connect them. The X-band antenna presented in section 3.5 has been measured at EADS Astrium in Ottobrunn. It was connected to the measurement setup using a flanged microstrip-to-SMA adapter. The adapter was soldered to a microstrip line on the antenna substrate on one side, and connected to the coaxial cable of the test set on the other side. This transition alone has been measured with a return loss better than 20 dB up to 15 GHz, and was thus suitable for measurements in X-band. The radiation characteristic of the Ka-band antenna processed on LTCC and demonstrated in section 3.4 has been measured at the University of Ulm. For these measurements, the RF-interface was implemented with a mini-SMP connector. The connector was soldered on a footprint printed on the ceramic substrate of the antenna to form a coplanar to mini-SMP transition. Also, the mini-SMP interface was connected to the coaxial cable of the test set through a mini-SMP to K-connector adapter designed for operation up to 35 GHz. Finally, the W-band antenna designed for wake vortex detection front-end has been measured at 76.5 GHz at Astyx GmbH in Ottobrunn. For this measurement, due to the relatively high attenuation of the signal at W-band, it was impossible to connect the antenna to conventional test set cables. To overcome this, the antenna has been connected to a W-band rectangular waveguide by means of an electric-field probe [48]. The probe realised on ceramics was placed onto the test fixture of the antenna using conductive epoxy, and it was connected using Au RF bond-wires. A photograph of the W-band transition is shown in Fig. 1.2.

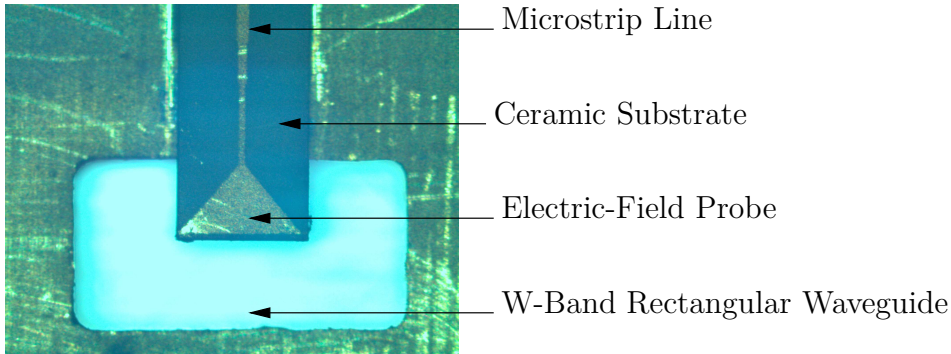


Fig. 1.2: Photograph of the electric-field probe for W-band waveguide to microstrip line transition.

1.3 Control Setup for Electrically Steerable Antennas

Two electrically steerable antennas are demonstrated and have been measured during this work. These antennas are based on digital RF-MEMS phase shifters integrated between the antenna array and the feed network. In order to steer the beam radiated by an antenna, various switches in the phase shifters have to be actuated with the appropriate actuation voltage. For the EADS RF-MEMS technology mostly used in this work, they are actuated with a symmetrical rectangular signal of 50% of duty cycle, with no offset, 10 Hz, and with an amplitude of $V_{cc} = \pm 20V \dots \pm 30V$. This actuation signal is preferred over a constant DC-voltage to prevent an accumulation of electric charges in the dielectric, which would lead to a sticking of the MEMS structures. Also, in order to steer the beam in a specific targeted direction, this actuation voltage has to be applied to certain switches, whilst the others have to be left un-actuated. In finalised and completely integrated systems, this task is executed by a beam forming unit. This module calculates the switches to actuate for the aimed pointing direction, and validates their actuation by applying the pull-in signal. Nevertheless, at antenna level and even before it is further integrated, the antenna has to be measured and an experimental control setup has to be implemented. This setup was based on an electromechanical switch matrix. The utilised switch matrix was an USB ERB-24 matrix commercialised by Measurement Computing [49]. It is formed by a bench of twenty four electromechanical relays, having all one separate input and two outputs, normally open and normally closed. In the proposed setup, all inputs of these relays are connected to a pattern generator delivering the above mentioned actuation signal. On the other hand, the outputs of the relays are connected to a DC-control board implemented below the antenna. The DC-control lines in the control board are also connected to the electrodes of the switches via bond-wires and high resistivity lines designed on the phase shifters chips (Fig. 1.3). In order to actuate only the necessary switches, the twenty four relays of the switch matrix are controlled by a LabView software running on a laptop computer. This control software is mainly a Look Up Table (LUT), which contains a list of the switches to actuate for each scan angle of the antenna beam. Contrary to the rest of the setup, which does not depend on the antenna to control, the LUT implemented in the software is specific for each antenna.

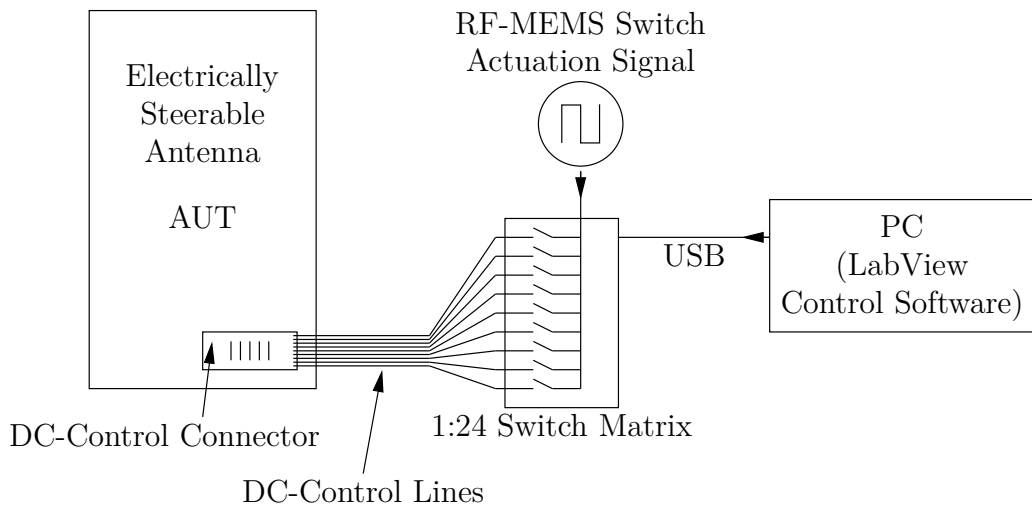


Fig. 1.3: Control setup for electrically steerable antennas.

1.4 Technologies

1.4.1 EADS Innovation Works RF-MEMS Technology

RF-MEMS technology was widely implemented through the work presented in this manuscript. The technology has been used to realise several components such as phase shifters, varactor switches, and adjustable stubs with very low loss. Among the presented RF-MEMS circuits, a large majority has been manufactured at EADS Innovation Works in Ottobrunn. These RF-MEMS devices have been processed according to a unique low-cost and low-complexity technique described in several publications [50], [51], [52], [53]. Typical RF-MEMS components are serial capacitive switches. They are designed in microstrip topology, and they are fabricated on high resistivity silicon substrate. The switch itself is formed by a free-standing cantilever made out of aluminium alloy. The alloy is deposited by evaporation in such a way that the resulting metal layer has an intrinsic stress. This stress enables the free-standing tip of the cantilever to bend $40\text{ }\mu\text{m}$ upwards above the substrate, and by approximately the same amount above the fixed metal structures (Fig. 1.4).

This gap ensures a satisfactory isolation of about -20 dB between the input and output of the switch, when it is left open. The switch is actuated by an electrostatic field generated by a voltage of approximately 25 V (See above). The actuation voltage is applied between the free-standing cantilever and the ground plane of the microstrip line processed on the back side of the silicon dielectric. Under the effect of the electrostatic force, the cantilever is bent downwards at the same level as the fixed metal structures. In the down state, the tip of the cantilever is separated from the fixed microstrip line by only $2\text{ }\mu\text{m}$, and the two parts of the switch couple capacitively. The accuracy necessary to process this interstice of $2\text{ }\mu\text{m}$ is made possible by implementing a lift-off process to pattern the metal structures. Further, in order to prevent a DC-short circuit between the top and bottom electrodes of the switch, i.e. between the free-standing cantilever and the ground plane, a 120 nm -thick silicon dioxide (SiO_2) layer is thermally grown on top of the silicon substrate. This layer of isolating silicon dioxide is grown before the metal structures are processed on the wafer in order to isolate the top metal structures from the silicon material. Also, in order to increase the capacitance between the two parts of the switch, an implantation zone is realised under

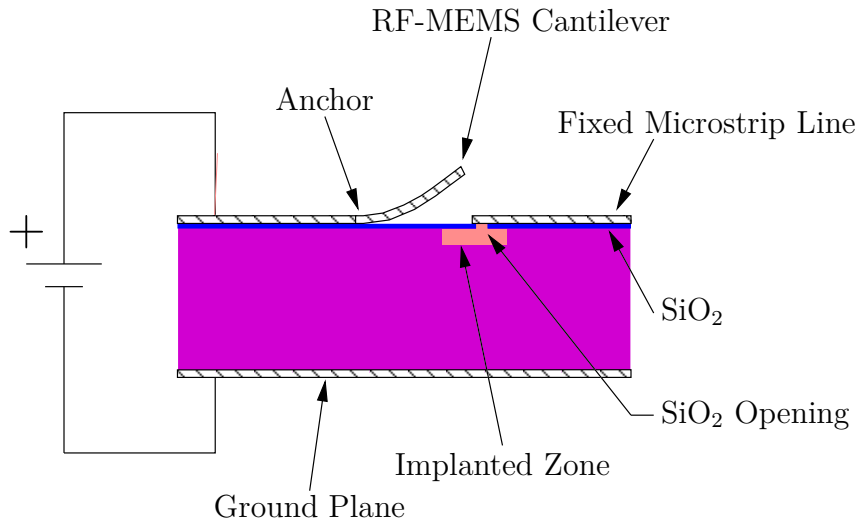


Fig. 1.4: Cross-sectional drawing of the EADS Innovation Works RF-MEMS serial switch.

the discontinuity between the fixed and movable lines. This implantation zone is implemented by doping a small area on the top side of the silicon substrate (Fig. 1.4). It is achieved by implantation of phosphor ions into the silicon substrate, in order to increase locally its conductivity. Finally, the doped zone is connected to the fixed microstrip line through an opening patterned in the silicon dioxide layer, as close as possible from the aperture between the two lines. The switchable cantilever realised in this way forms a serial microstrip switch capable of connecting two lines by changing the series capacitance between them. The typical $C_{\text{on}}/C_{\text{off}}$ capacitance ratio of serial microstrip switches designed and processed in this technology is about 70.

The EADS RF-MEMS technology has been demonstrated in various applications such as tunable filters [54], phase shifters [24], switchable antennas [55], high isolation switches [17], and Single Pole Multi Throw switches (SPMT) [56]. Thanks to the capacitive nature of the switches, it is appropriate for a wide range of applications operating in very different frequency bands, from approximately 2 GHz up to the W-band and beyond [57], [58], [38]. Switches processed in this technology have been also demonstrated with outstanding RF performance, especially in terms of insertion loss. In [59] and [60], a coplanar serial switch is demonstrated with 0.75 dB of insertion loss up to 80 GHz, and in [56], a microstrip SP3T switch is measured with an insertion loss better than 0.5 dB at Ka-band. Further, the technology has been found to have interesting power handling capabilities: the hot switching of a serial switch at Ku-band has been demonstrated up to 6 W, limited by the measurement setup [20]. Finally, in [61], a switching time of 10 μs is reported for the switches processed in this technology.

1.4.2 LTCC Technology

LTCC, or Low Temperature Co-fired Ceramics, is a technology that enables the realisation of multilayer modules. Nevertheless, the technological process to manufacture these modules is very different from those of standard multilayer components, such as laminate based multilayer interconnects. Contrary to other multilayer fabrication techniques, the manufacturing of LTCC works individually on the different layers of a same module. The VIAs (Vertical Interconnect Access) are punched and filled separately in each one of the ceramic layers at an early stage of the process. Following this, the metal structures are patterned on the different layers of the module. Up to this fabrication stage, the ceramic layers are still separated and they are in a so-called "green" state. The processed layers are brought together and aligned only at a late stage of the fabrication, just before a lamination step preceding the final firing of the whole module. The standard LTCC process is illustrated in the flow-chart given in Fig. 1.5.

In the last decades, LTCC technology has been extensively used to reduce the size of RF modules operating up to the L-band. In this low microwave range, numerous highly integrated consumer-oriented and military applications have highlighted the opportunities offered by that technology [62], [63]. Up to recently however, technological challenges have limited the use of LTCC to applications operating mostly below 2 GHz. This is only in the late 90s that LTCC materials have been optimised for higher frequencies, and that the fabrication techniques used to pattern the structures have been demonstrated with improved accuracy [64]. Thanks to this, the field of application of LTCC moved progressively towards the millimetre-wave range. Today, the technology is considered as one of the most promising technologies in the Ku-, K-, and Ka-bands, and even in the W-band [65]. This advent of LTCC at high frequencies, principally up to 40 GHz, offers opportunities in terms of miniaturisation and integration of millimetre-wave front-ends. It makes possible the realisation

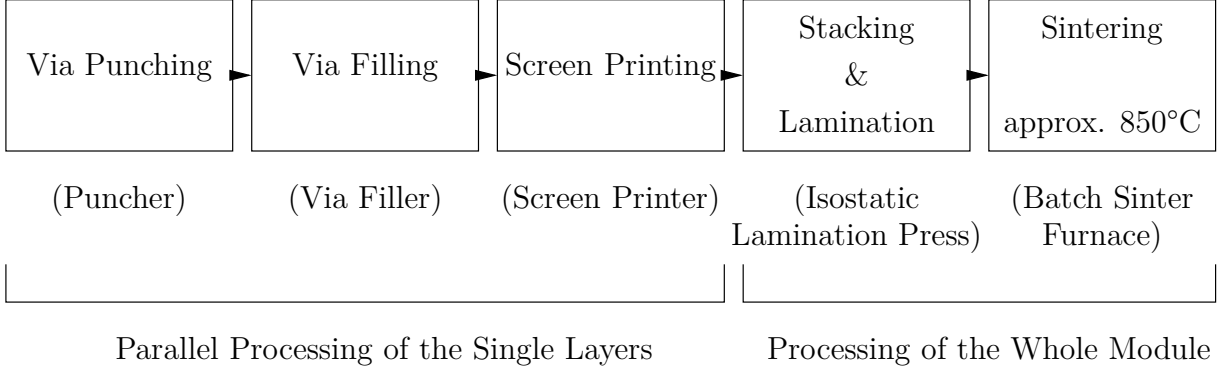


Fig. 1.5: Standard LTCC fabrication process.

of 3D integrated millimetre-wave Multi-Chip Modules (MCM), in which the different components are packaged and integrated with high density. These fully integrated ceramic modules are more compact than hybrid integrated sub-systems made out of low-loss soft substrates. Also, they are more reliable, exhibit better performance, and are more cost-effective for large production scales. Nevertheless, not all ceramic substrates are suitable for millimetre-wave applications, and only few of the commercially available LTCC materials have performance comparable to low-loss organic substrates [66], [67], [68]. Due to its excellent high frequency performance, the DuPont 943 tape system with Au paste ($\epsilon_r=7.4$, $\tan\delta=0.0015$, $\sigma=4.09e7$ S/m) has been chosen for the fabrication of the structures presented in this work. Further, in order to keep the thickness of the proposed structures at an acceptable level, a setup with six 110 μm -thick LTCC layers has been used for both the antennas and the filters. The structures demonstrated in this thesis have been manufactured by Micro Systems Engineering GmbH and Via Electronic GmbH, which are both Germany based LTCC foundries. Their design rules for LTCC structures are given in [69] and [70], respectively.

1.4.3 EPFL Barium Strontium Titanate Ferro-Electric Varactor Technology

In section 2.7, the influence of temperature on the resonance frequency of a cavity resonator is investigated. There also, the measurement of the structure over temperature exhibits a down-shift of the resonance frequency as the temperature increases, and a ferro-electric varactor based compensation technique is presented. The ferro-electric varactors used to demonstrate the technique were provided by the EPFL Swiss Federal Institute of Technology. They have been developed within the frame of the European funded project "RETINA" (FP6-2003-AERO1:#516121). The components are fabricated on 200 μm -thick LaAlO_3 (LAO) substrate with epitaxially grown Barium Strontium Titanate thin film ($\text{Ba}_x\text{Sr}_y\text{TiO}_3$ or BST). On the chip, the capacitor is formed by two electrodes patterned on top of the ferro-electric film (Fig. 1.6). These two electrodes are separated by a thin slot building a capacitive region between them. Also, since the area under the interstice is covered with high permittivity BST film, the series capacitance between the electrodes depends strongly on the dielectric constant of the ferro-electric material.

In the frame of the demonstrated technique, it is for their temperature-dependent behaviour, that ferro-electric varactors have been implemented. The dielectric constant of BST materials decreases when the temperature increases. This property makes possible the realisation of temperature-controlled capacitances, especially suitable for actuation-free temperature compensation.

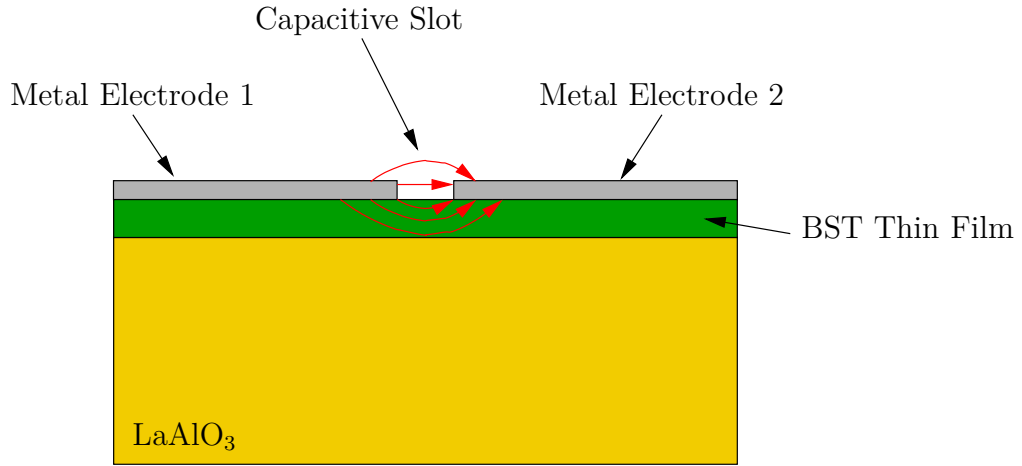


Fig. 1.6: Cross-sectional drawing of the BST capacitor on LAO substrate.

Two sorts of ferro-electric varactors have been provided by the EPFL. A first set of varactors was manufactured on BST 70-30 film, and a second lot was processed on BST 55-45 film. Among these two families, the varactors fabricated with BST 55-45 material are more sensitive to temperature variations and offer potentially larger temperature compensation. Nevertheless, this higher response is at the price of higher insertion loss, and BST 70-30 varactors have been found to be more convenient for the considered task. BST 70-30 varactors have a capacitance of 290 fF at 30°C and 120 fF at 120°C.

1.5 Conclusion

The techniques, tools, and technologies described in this first chapter constitute the toolbox of the work presented in this thesis. Often or more sporadically, all these have been implemented to support the design, to characterise, to control, or to realise the different components demonstrated in the two main chapters. Each time it has been found to be necessary, the following sections and paragraphs of the thesis will refer to the art described in this chapter.

2 Fixed and Tunable Cavity Resonator Filters for Millimetre-Wave Front-ends

2.1 Introduction

Microwave band-pass filters are key components of many micro- and millimetre-wave front-ends. In these systems, they isolate the finite spectrum of relevant signals out of a broadband noised signal. Also, despite the long effort put into their development over the last 50 years, filters remain in many cases a bottleneck in the design of RF components. Today, the need for compact, easily integrable, and low-loss filters still drives the research towards more efficient and low-cost filters [71]. In the special case of band-pass filters, the technology used to realise the resonators has to be chosen with particular attention. This choice depends on the operating frequency of the application, the space available to integrate the filter, the technology of the other components of the front-end, and finally, on the loss budget allowed for the filter. The insertion loss of a band-pass filter depends to a large extent on the insertion loss of a single resonator, which of course has to be as low as possible. The quantity used to assess the performance of a single resonator is the so-called unloaded quality factor or Q-factor. The higher the unloaded Q-factor, the lower is the power lost by dissipation in the resonator.

The panoply of resonators available to realise band-pass filters is constantly increasing in order to meet the always higher requirements of modern RF front-ends. On one hand, the filters based on waveguide cavity resonators are bulky and cumbersome to integrate, but they have very good performance in terms of insertion loss. On the other hand, the filters implementing end-coupled transmission line resonators are easy to integrate but they are limited in terms of Q-factor. "In between", there is a number of other solutions. Some of them like Surface Acoustic Wave resonators (SAW) or Bulk Acoustic Wave resonators (BAW) have been proposed to realise low-loss filters, but are limited to the centimetre-wave range, principally below the S-band [72], [73]. Dielectric resonators overcome the frequency limitation of SAW and BAW resonators. They allow for the realisation of efficient filters up to 40 GHz, but they are cumbersome to integrate on a planar mother board. The performance of some common types of resonators are compared versus frequency in Fig. 2.1, where the most popular resonator technologies are represented in blue.

In this 2nd chapter dedicated to band-pass filters, two resonator technologies presented in the recent literature are discussed and implemented. These, represented in red in the graph of Fig. 2.1, are micro-machined cavity resonators and Substrate-Integrated Cavity (SIC) resonators. These two technologies have been chosen because they are expected to cover application fields that were up to recently without reliable solution, and where however, most of the emerging millimetre-wave applications are currently being developed. First, micro-machined cavity resonators are expected to fill the gap existing between high performance but bulky waveguide resonators, and easy to integrate but lossy transmission line resonators. The resonators based on that technology are expected to provide planar and easily integrable filters suitable for applications operating between

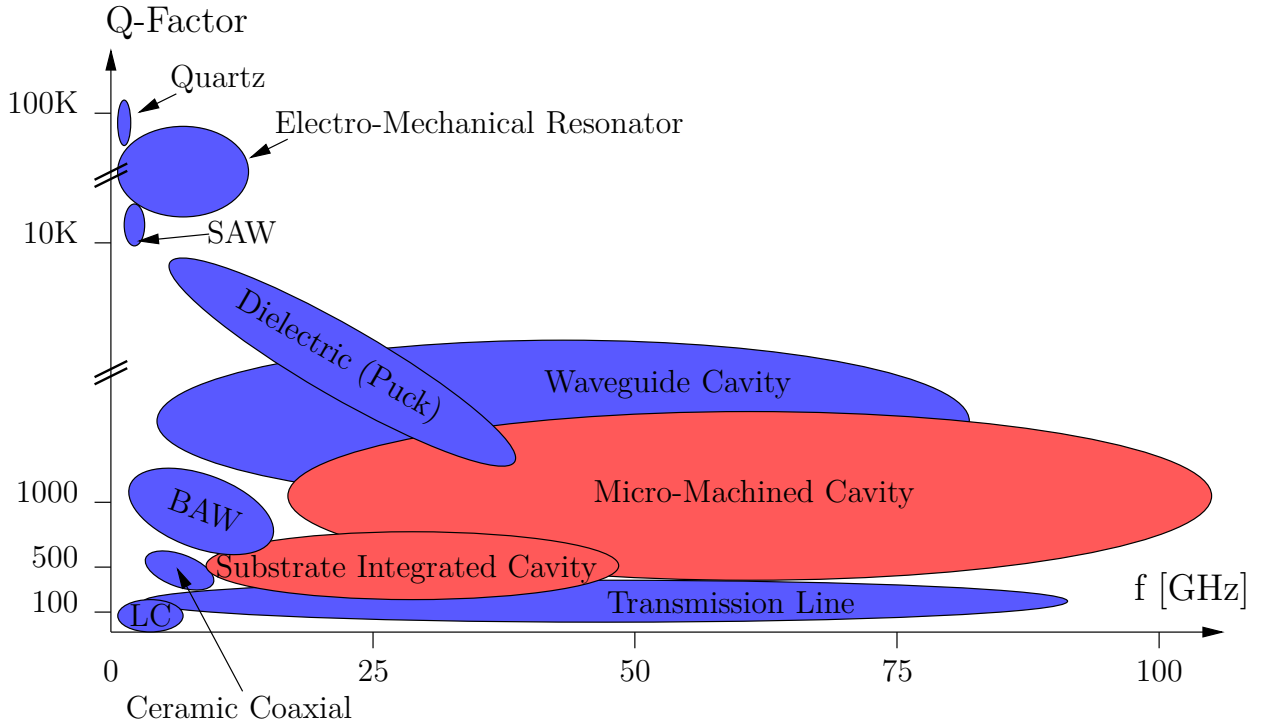


Fig. 2.1: State of the art of micro- and millimetre-wave resonators.

the K- and the W-band, and for which a Q-factor between approximately 500 and 2500 is targeted. Further, substrate-integrated cavity resonators are adapted to applications driven also by other motivations than uniquely filter insertion loss. They are expected to be particularly appropriate for front-ends in which the space is limited, and for which the insertion loss of the filter has to be fair with a Q-factor of about 500.

Motivation and Drivers for Frequency-Agile Band-Pass Filters

Besides the higher integration density and improved performance expected for the next generation of RF components, the trend is now also to evolve towards adaptive systems. More and more, RF front-ends have to be capable of handling multi-functional data-link or sensing tasks, which occur more often in different frequency bands. A good illustration of this is the recent development of systems designed for both Line Of Sight (LOS) and Beyond Line Of Sight (BLOS) communication link with VHF-UHF software-defined radio transceivers [74]. Also, this need for more reconfigurability is driven by the advent of frequency-hopping communications in electronic warfare or for spectrum management [75], [76]. At filter level, this frequency steering can be implemented mainly using two different approaches: with a switchable bank of filters, or using frequency-agile filters. The filter-bank approach, which is the most common and straight-forward solution, is also the bulkiest and the most expensive one. It requires the use and integration of several filters dedicated to the different channels, and two or more switches to address the appropriate filter. In this case, the filters are fixed in frequency and a filter in the bank is used only when the front-end operates at the corresponding frequency. Also, when a filter is addressed, the other filters are left unused. The adaptive filter approach is a more sophisticated solution achieving the same task with only

one filter steerable over frequency. The centre frequency of the filter is made steerable in real time by means of tuning devices acting on the resonators of the filter. Hence, even if tunable filters are generally larger than the fixed-frequency filters from which they are derived, this alternative is more compact than banks of filters. Also, it provides a major gain in terms of activity of the components because the unique filter is always working, whatever the operating frequency is.

In this chapter, fixed and frequency-agile filters are demonstrated. The filters are realised in one of the previously mentioned technologies, micro-machined in silicon or processed in LTCC. The frequency-agile filters are made steerable over frequency by means of RF-MEMS devices, and they are based on the fixed-frequency filters presented in the first place. On top of this, the last section of the chapter addresses the issue of the temperature-dependence of ceramic based filters. Also, it presents a technique aiming at reducing the influence of the temperature on the response of a single 2-port resonator. Further, in order to provide a background to the presented designs, the first sections of the chapter present some pioneering studies and give some benchmarks published in the field. Finally, the theory of cavity resonator band-pass filters is presented. It gives the basics of the designs developed later in the manuscript and aims at a better understanding of the described design procedures.

2.2 Previous Work on Micro-Machined Filters

The use of micro-machining of silicon in the fabrication of millimetre-wave components was first considered in the early 90s. At that time, the technique was favourably introduced to improve on the manufacturing costs of millimetre-wave waveguides, complex and time-consuming to fabricate using standard machining techniques. Already in 1993, McGrath et al. [77] demonstrated a micro-machined rectangular waveguide operating at W-band. The waveguide is processed using wet chemical etching of $\langle 110 \rangle$ silicon, and it is covered with $3\mu\text{m}$ of Au. The structure exhibits 0.04 dB of insertion loss per wavelength, comparable to the performance of standard rectangular waveguides machined out of metal. Three years later, major contributions of the University of Michigan broadened the application field of these fabrication techniques. Looking into the way micro-machining techniques could reduce the loss and dispersion of planar resonators, they proposed, in 1996, a first topology based on membrane-supported transmission lines [78], [79], [80]. In the demonstrated realisations, the stripline or microstrip line resonator is suspended on a $1.4\mu\text{m}$ -thick $\text{SiO}_2/\text{Si}_3\text{N}_4/\text{SiO}_2$ dielectric membrane processed on silicon. The papers reported excellent performance for the suspended micro-machined resonators with unloaded Q-factors measured between 350 and 500, in the K-, V-, and W-bands. These values are approximately ten times larger than those of conventional planar resonators on Gallium Arsenide (GaAs) or silicon, and two times larger than microstrip line resonators on Teflon-based microwave substrate. Further, complete 3- and 5-pole filters based on that principle have been demonstrated with little insertion loss: 1.4 dB for the 3-pole filter and 2.2 dB for the 5-pole filter. In [80], a 7-pole planar suspended inter-digital band-pass filter for operation at 20 GHz and with a relative bandwidth of 15% is found to have only 0.79 dB of in-band insertion loss. In [81], that same concept is compared to a cavity resonator etched out of silicon and metallised. The micro-machined cavity resonator is operated either in the fundamental TE_{101} -mode at 24 GHz, or in the TE_{201} -mode at 38 GHz. At these frequencies, the cavity resonator is measured with an unloaded Q-factor of 1117 and 1163, respectively. In [33], a micro-machined cavity resonator operating at X-band and realised in a similar way ex-

hibits an unloaded Q-factor of 506. In both cases, the good values measured for the unloaded Q-factor of the metallised micro-machined cavity resonators are very close to the theoretical values of standard metallic cavities. Further, micro-machined cavity resonators have been implemented to realise complete band-pass filters. These filters demonstrated by Harle et al. are either vertically integrated, i.e. the micro-machined cavity resonators are processed in different silicon substrates stacked on top of each other, or integrated horizontally. In [82], a 3-pole vertically integrated filter at X-band is demonstrated with 2 dB of in-band insertion loss for a relative bandwidth of 3.7%. The filter is realised with three micro-machined cavity resonators processed by wet etching of three 500 μm -thick silicon substrates. These substrates containing the cavity resonators are mounted together with 100 μm -thick silicon substrates including the coupling slots between the resonators. From the same author, a 2-pole filter and a 4-pole linear phase filter with good performance have been also demonstrated [83]. In these realisations, the cavity resonators are processed by Deep Reactive Ion Etching (DRIE), and they are patterned side by side such that there exist common inter-cavity walls between them. Also, the resonators are coupled by inductive irises processed in the inter-cavity walls using the same DRIE isotropic etching of silicon. The unloaded Q-factor of a weakly coupled 2-port cavity resonator is reported at 1422, and a 2-pole band-pass filter at K-band is found to have 1.6 dB of insertion loss for a relative bandwidth of 2.2%. More recently in [84], a filter based on an inter-digital structure grounded using via holes micro-machined in silicon has been demonstrated. It is reported with 1.9 dB of in-band insertion loss for an 8-pole Tchebycheff band-pass filter with 20% of bandwidth.

Apart from the diverse configurations of micro-machined filter presented in the recent literature, some topologies and techniques have been patented. In [85], the etching of elongated rhombic shaped (with no more than two sides of equal length) cavities out of $\langle 110 \rangle$ silicon is protected, and some microstrip and coplanar coupling techniques are presented. Another patent, [86], deals more specifically with the realisation of evanescent transitions for the coupling of two micro-machined cavity resonators. It introduces a novel coupling concept based on a so-called coupling cavity processed out of silicon. This silicon dielectric is placed on top of the cavity resonators and closes them on their top open side. Finally, beyond the scope of band-pass and band-stop filters, [87] describes a micro-machined cavity resonator mounted in reflection (1-port). The structure presented in the patent aims at reducing the phase noise in voltage controlled oscillators, which is also directly related to the unloaded Q-factor of the resonator.

2.3 Previous Work on Tunable Filters

Considering the large variety of filter topologies and the numerous tuning techniques presented in the literature of the last decades, a compilation of the state of the art of tunable filters arises as a laboured task, which can hardly be exhaustive [88]. Also, a more realistic ambition of this paragraph is to provide the reader with an overview of the most common and successful tunable filter techniques demonstrated recently. In spite of the diverse techniques presented to make filters adaptive in frequency, all aim at a same clear goal. On top of the specifications known for fixed-frequency filters like a limited in-band insertion loss, a defined bandwidth, and a sharp roll-off, the response of tunable filters has to be steered over frequency. There exist basically three kinds of tunable filters: the mechanically tunable filters, the magnetically tunable filters, and the electrically tunable filters.

Mechanically tunable filters are cumbersome to integrate, have long switching times, and they are heavy-weighted because of the presence of mechanical actuators. For these reasons, they are generally inappropriate for implementation into modern multi-band communication systems, and especially on-board of mobile systems.

Intensively developed from the late 50s [89] and still investigated in the recent literature [90], magnetically tunable filters are based on ferri-magnetic materials like Yttrium Iron Garnet (YIG) or barium ferrites. They offer usually good performance in terms of tunability (multi-octave) and insertion loss [88], [91]. However, these filters are often handicapped by long switching times and are, in most cases, not capable of handling high power signals [88]. Further, they are inconvenient to implement practically because they require a magnetic field to polarise the ferrite material used to tune the resonators.

For these reasons and because they are technically more accessible to manufacture, electrically tunable filters are now considered as the most promising solution towards frequency-agile filters. Here again, the techniques available to realise tunable filters are rather diverse depending on the targeted application and on the tuning range expected for the filter. Three tuning elements are principally used in the fabrication of tunable filters. These are namely: the diode varactor, the ferro-electric varactor, and the RF-MEMS devices used either as varactor or as a switch. In [92], a varactor diode is used to tune a micro-machined suspended inter-digital filter. The demonstrated filter shows an excellent tunability of about 70% in the X-band, which is however at the price of 5 dB of in-band insertion loss. Another example of varactor diode based tunable filter is presented in [93]. The filter is realised in multilayer ceramic technology. It has a satisfactory tuning range of 13% at 800 MHz with, nevertheless, an insertion loss of 2 dB, rather important considering the low operating frequency. This exemplifies the advantages and limits of diode based tunable filters. Diode varactors offer a good tunability - the value of the tunable capacitance varies commonly within a ratio of 10:1 - but have a series resistance of about $1\ \Omega$, which increases the overall insertion loss of the filter. The insertion loss is also a known limitation of ferro-electric varactor based filters. Especially at high frequencies above 15 or 20 GHz, BST (Barium Strontium Titanate) varactors have modest Q-factors generally below 70-80. This limits the Q-factor of the resonators and increases the overall insertion loss of the filter [94], [95]. Nevertheless, for applications operating below the K-band, BST varactors exhibit fair properties: Q-factors of about 200 and approximately 2:1 of on/off capacitance ratio; and good performance has been demonstrated using this technology [96], [97]. To overcome the high insertion loss of diode and ferro-electric varactors at high frequencies, high-Q (350-450) RF-MEMS devices have been implemented in tunable filters [98], [99]. In some realisations, RF-MEMS were used as tunable capacitances to load the resonators of filters [100]. Among the proposed topologies, a structure known as Distributed MEMS Transmission Line (DMTL) demonstrated good performance. It consists of coplanar transmission lines loaded periodically with movable capacitive RF-MEMS bridges [101], [102]. In [103], a 3-pole coplanar filter operating in the K-band is realised on glass substrate according to a similar principle. The filter exhibits a satisfactory tunability of 7%, and an insertion loss below 4 dB. Also, it shows an almost constant shape and bandwidth for the pass-band response. This last remains constant and within $7.5 \pm 0.1\%$ over the entire tuning range. Based on a completely different principle, Siegel et al. [54] presented another promising technique to tune the resonant length of microstrip resonators. There, the tuning succeeds by actuating fixed-free cantilever beams flat onto the silicon substrate. This actuation of RF-MEMS cantilevers changes the effective dielectric constant of the microstrip lines at the open ends of the

resonators, without influencing the coupling between them. In this way, a 2-pole microstrip filter with 17.6% of tunability and 1.7 dB of in-band insertion loss was demonstrated.

Nevertheless, if the recent literature has proposed a large number of solutions for the tuning of planar transmission line resonators, the tuning of other kinds of resonators like high-Q cavity resonators has been only poorly investigated. A technique proposed in [35] describes a cavity resonator coupled to an RF-MEMS varactor. Nevertheless, the experimental results presented in the paper are not good. The performance is limited by the use of an inappropriate substrate for the fabrication of the tunable resonator, as well as by an excessive length of the interconnections between the cavity and the varactor. This is however, to the best of the author's knowledge, the only contribution associating a low-loss RF-MEMS device to a high-Q cavity resonator, which could represent a real opportunity to reduce insertion loss in frequency-agile filters.

2.4 Theory of Cavity Resonator Band-Pass Filters

2.4.1 2-Port Cavity Resonators

A cavity resonator is a volume of arbitrary shape enclosed in electrical boundaries, and in which one assumes the presence of electromagnetic energy. Depending on the electrical dimensions of the cavity and for certain frequencies of the electromagnetic field, the superposition of the waves bouncing back and forth inside the cavity creates constructive interferences. Also, at each one of these frequencies, the constructive interferences build a so-called standing-wave regime inside the cavity, and the distribution of the electromagnetic field is called resonant mode. The frequencies allowing for the realisation of resonant modes are called resonance frequencies of the cavity. The resonant modes susceptible to exist in a cavity resonator are classified between TE and TM modes. The assignment of a given mode to one or the other depends on the "Transverse Electric" or "Transverse Magnetic" nature of the electric and magnetic fields, perpendicular or not to the direction chosen as direction of propagation. Further, if two resonant modes have the same resonance frequency, they are called degenerate modes. For a given cavity shape and dimensions, the resonant mode having the lowest resonance frequency is called fundamental mode of the cavity resonator.

In the special case of rectangular cavity resonators, one assumes a cavity in the Cartesian system of coordinates as depicted in Fig. 2.2.

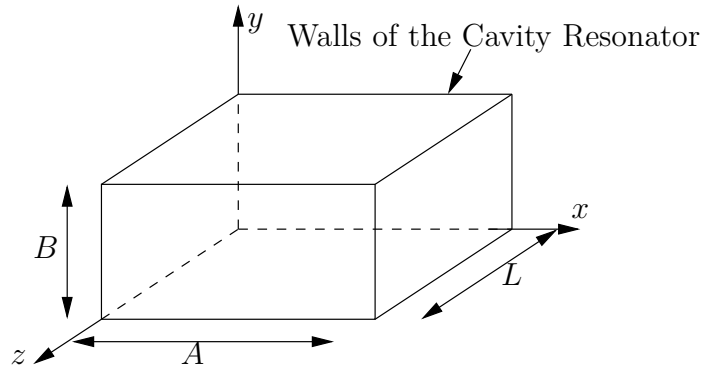


Fig. 2.2: Rectangular cavity resonator in the Cartesian system of coordinates.

The dimensions of the rectangular cavity resonator are denoted by A , B , and L along the X-, Y-, and Z-axes, respectively. Also, it is assumed that the dimensions A , B , and L are such that $B < A$ and $B < L$, and that the Z-axis is taken as the direction of propagation. In rectangular cavity resonators, the modes are numbered with three indexes m , n , and p : TE_{mnp} and TM_{mnp} . The indexes correspond to the number of half-wavelengths that the mode exhibits in the cavity along its X-, Y-, and Z-axes, respectively. Also, the fundamental mode being the mode with the lowest resonance frequency, it is the mode having the smallest possible values for the triplet (m,n,p) . For a rectangular cavity resonator, it is shown in [104] that the smallest possible values of (m,n,p) is with "0" for the index corresponding to the smallest dimension of the cavity, and "1" for the two remaining indexes. Hence, for the cavity in Fig. 2.2, this is verified for $(m,n,p)=(1,0,1)$. Finally, since the Z-axis is chosen as direction of propagation, the fundamental mode of the cavity resonator is the TE_{101} mode. The resonance frequency of that mode is given by

$$F_{0,TE_{101}} = \frac{c}{2\pi\sqrt{\mu_r\epsilon_r}} \cdot \sqrt{\left(\frac{\pi}{A}\right)^2 + \left(\frac{\pi}{L}\right)^2}, \quad (2.4.1)$$

where c is the speed of light, μ_r is the relative permeability of the medium filling the cavity, and ϵ_r , its relative permittivity. The distribution of the electric field at that fundamental resonance frequency is shown in Fig. 2.3.

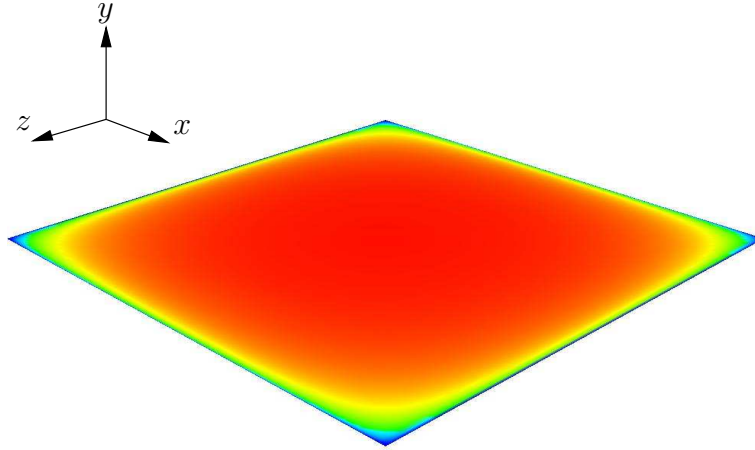


Fig. 2.3: E_y -field component of the fundamental resonant mode in a rectangular cavity resonator.

At the fundamental resonance frequency, the electromagnetic energy is completely stored in the TE_{101} mode. Also, at that frequency for two ports inductively coupled and placed on both sides of the cavity along the Z-axis, the cavity resonator shows a series-type resonance. Hence, such an ideal rectangular cavity resonator can be modelled by an ideal LC lumped element series resonator [34]. This series resonator has a reactance $X(\omega)$, which cancels itself at $F_{0,TE_{101}}$. The reactance slope parameter x giving the slope of the reactance $X(\omega)$ around the resonance frequency is given by

$$x = \frac{\omega_0}{2} \frac{dX(\omega)}{d\omega} \bigg|_{\omega=\omega_0}. \quad (2.4.2)$$

The reactance slope parameter x depends on the dimensions of the cavity resonator. It is a measure of the quantity of electromagnetic energy that a resonator is able to store. However, physical cavity resonators cannot store electromagnetic energy without dissipating some of it. Thus, a more realistic model for a rectangular cavity resonator is a lossy RLC series circuit. The performance or "quality" of a resonator is measured by the ratio called unloaded Q-factor noted Q_u . It is given by

$$Q_u = \omega \cdot \frac{\text{energy stored inside the resonator}}{\text{average power dissipated inside the resonator}}. \quad (2.4.3)$$

For a series-type resonator having a reactance slope parameter x and a resistance R , the unloaded Q-factor is calculated by

$$Q_u = \frac{x}{R}. \quad (2.4.4)$$

There are two phenomena, which may lead to a dissipation of power in physical cavity resonators: the loss due to the finite conductivity of the metal used for the walls of the cavity, and the one caused by the loss in the medium filling the cavity. The limitation of the unloaded Q-factor due to the dielectric loss is independent of the shape of the cavity. It is calculated by

$$Q_{u,d} = \frac{1}{\tan \delta}, \quad (2.4.5)$$

where $\tan \delta$ is the loss tangent of the dielectric filling the cavity resonator. The dielectric loss can be minimised by choosing low-loss dielectrics to fill the cavity, or even cancelled if the cavity resonator is filled with air or vacuum. This is however at the price of a larger cavity size for a same given resonance frequency. On the other hand, the ohmic loss depends on the shape and dimensions of the cavity resonator. For a rectangular cavity resonator with the dimensions given in Fig. 2.2, the value of the normalised unloaded Q-factor due to the conductor loss is calculated by

$$Q_{u,c} \frac{\delta}{\lambda} = \frac{ABL}{2} \cdot \frac{(p^2 + r^2)^{\frac{3}{2}}}{p^2 L (A + 2B) + r^2 A (L + 2B)}. \quad (2.4.6)$$

In this formula, $p = \frac{1}{A}$, $r = \frac{1}{L}$, and the coefficient $\frac{\delta}{\lambda}$ depends on the conductivity of the walls of the cavity. This coefficient is tabulated in [34] for some common metals. From (2.4.6), the unloaded Q-factor of a cavity resonator increases when the ratio "T = volume enclosed inside the cavity/overall surface of the cavity walls" increases. This can be understood by the fact that a larger enclosed volume means a larger amount of energy stored inside the cavity, whilst a larger surface of the cavity walls leads to higher ohmic loss. T and thus $Q_{u,c}$ increase as the smallest dimension of the cavity (here B) augments. Also, for a cavity depth B fixed, the Q-factor reaches its maximum when the base of the cavity is square $A = L$. The unloaded Q-factor of a physical cavity resonator Q_u is calculated from $Q_{u,d}$ and $Q_{u,c}$ using

$$\frac{1}{Q_u} = \frac{1}{Q_{u,d}} + \frac{1}{Q_{u,c}}. \quad (2.4.7)$$

In real systems like oscillators and filters, the cavity resonator is linked to other components, with which it has to interact. There are two ways of connecting a cavity resonator, either in reflection or in transmission. A cavity resonator is said to be mounted in reflection when it has only one interface, otherwise it is connected in transmission. The way a cavity resonator is mounted into the whole system depends on the application, and on the function to achieve with the cavity. Reflection-mounted cavities are the elementary components of oscillators and band-stop filters, whilst transmission-mounted cavities are implemented in band-pass filters. This last is thus the configuration of interest here. The schematic of a cavity resonator mounted in transmission with exactly two ports is shown in Fig. 2.4. The cavity resonator is coupled to two transmission lines by means of two impedance inverters K_{01} and K_{12} . They represent the impedance transformation realised by the coupling structures between the cavity resonator and the networks connected to each one of its two ports.

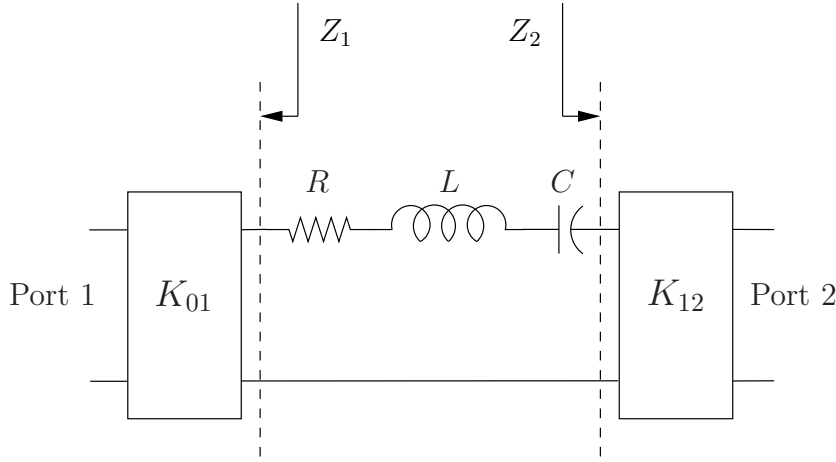


Fig. 2.4: Schematic of a 2-port cavity resonator connected by means of impedance inverters.

Due to the presence of input and output couplings, a 2-port cavity resonator is loaded by two impedances Z_1 and Z_2 . The value of these impedances depends on the environment of the resonator, usually $50\ \Omega$, and on the value of the impedance inverters. For weakly coupled cavity resonators, i.e. when the coupling coefficients are small, the values of Z_1 and Z_2 are modest ($\Re Z_1 + \Re Z_2 \ll R$). In this case, the resonance of the cavity is not affected to a large extent because only a small part of the energy contained in the resonator is exchanged through the ports. In return, for strongly coupled cavity resonators, the impedances seen by the cavity resonator are large ($R < \Re Z_1, \Re Z_2 < 50$), and an important part of the energy stored in the resonator is transmitted to, or received from external networks. The way a resonator is coupled, weakly or strongly, is assessed by calculating a so-called external Q-factor Q_e . Assuming that Z_1 and Z_2 are purely real and equal to R_1 and R_2 , respectively, the 2-port external Q-factor of a cavity resonator is defined by (2.4.8). Also, for design purposes, it is convenient to define a 1-port external Q-factor at each one of the two ports of the cavity [34]. The 1-port external Q-factors $Q_{e,1}$ and $Q_{e,2}$ defined at the ports 1 and 2, respectively, are calculated by (2.4.9). The 2-port external Q-factor Q_e is related to $Q_{e,1}$ and $Q_{e,2}$ using (2.4.10). Finally, the loaded Q-factor Q_l is calculated from the external and unloaded Q-factors using (2.4.11).

$$Q_e = \frac{x}{R_1 + R_2} \quad (2.4.8)$$

$$Q_{e,1/2} = \frac{x}{R_{1/2}} \quad (2.4.9)$$

$$\frac{1}{Q_e} = \frac{1}{Q_{e,1}} + \frac{1}{Q_{e,2}} \quad (2.4.10)$$

$$\frac{1}{Q_l} = \frac{1}{Q_u} + \frac{1}{Q_e} \quad (2.4.11)$$

Cavity resonators can be characterised experimentally. For 2-port cavity resonators, the resonance frequency and Q-factors can be gained from the measured or simulated response $|S_{21}|$ of the cavity resonator [105]. The loaded Q-factor is computed directly from the resonance frequency F_0 , and from the left and right cutoff frequencies of the transmit response (2.4.12). The unloaded Q-factor is calculated afterward from the first determined loaded Q-factor, and from the insertion loss $|S_{21}|$ at $f = F_0$, in dB, and at the resonance peak (2.4.13). Finally, the 2-port external Q-factor is computed from the loaded and unloaded Q-factors using (2.4.11). For cavity resonators mounted symmetrically, the 1-port external Q-factors are equal, and they are directly the double of the 2-port external Q-factor.

$$Q_l = \frac{F_0}{F_{2,-3\text{dB}} - F_{1,-3\text{dB}}} \quad (2.4.12)$$

$$Q_u = \frac{Q_l}{1 - 10^{\frac{|S_{21}|_{f=F_0}}{20}}} \quad (2.4.13)$$

(2.4.12) and (2.4.13) are theoretically valid for any values of the various Q-factors. However, for an accurate determination of the unloaded Q-factor, it is preferable to have a weakly coupled cavity resonator. This has to be observed because, for strongly coupled resonators, the value of the denominator $1 - 10^{\frac{|S_{21}|_{f=F_0}}{20}}$ becomes small and highly sensitive to measurement inaccuracies.

2.4.2 N-Pole Cavity Resonator Band-Pass Filters

The synthesis of band-pass filters consists in determining the parameters of a microwave network, such that it achieves a response meeting a set of specifications. These specifications stipulate typically the centre frequency of the pass-band F_0 , the bandwidth of the response ΔF , the maximum level of in-band insertion loss IL , rejection levels at certain frequencies, and sometimes, the maximum variation of the group delay allowed in the pass-band ΔGD . Also, the parameters to calculate from these specifications are the number and the resonance frequency of the resonators and the coupling coefficients between them.

A usual method used to synthesise band-pass filters is based on the transformation of a low-pass prototype filter into a band-pass filter [34]. The method consists in two steps. In a first time, it determines the values of the elements of a low-pass prototype filter. The values of these lumped elements are determined from the type of filter response to achieve, Butterworth, Tchebycheff, or Bessel for example, from the targeted specifications, and from the number of resonators in the filter. In a second step, the coefficients of the low-pass prototype filter are changed by two operations

called the denormalisation of impedance and the low-pass to band-pass transposition. The denormalisation of impedance modifies the coefficients in order to match the filter to the input/output impedances with which it has to be connected, typically $50\ \Omega$. The low-pass to band-pass transposition replaces the capacitances and inductances of the low-pass network by parallel- and series-type resonators, respectively. This last step aims at changing the normalised low-pass response into a band-pass response centred at the targeted frequency.

In most cases however, the practical realisation of filters with parallel and series resonators is cumbersome, and one often prefers to design filters with only one kind of resonator. For this reason, the band-pass filter is modified to include only series-type resonators having reactances $X_j(\omega)$. The series resonators are separated by impedance inverters $K_{j,j+1}$. A schematic of the modified generic n-pole band-pass filter is given in Fig. 2.5.

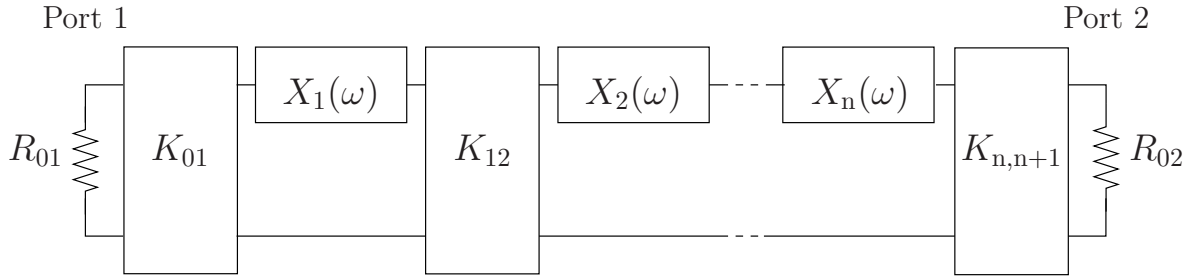


Fig. 2.5: Schematic of a n-pole band-pass filter realised with impedance inverters and series-type resonators.

For shunt inductance coupled cavity resonator filters, the values of the impedance inverters can be calculated directly from the values of the external Q-factors and coupling coefficients. These formulas are of particular interest for determining experimentally the couplings between the resonators and in input/output of the filter. From [34], they are given by

$$\frac{K_{01}}{Z_0} = \sqrt{\frac{\pi}{2} \frac{w_\lambda}{w Q_{e,1}}}, \quad (2.4.14)$$

$$\left. \frac{K_{j,j+1}}{Z_0} \right|_{j=1,\dots,n-1} = \frac{\pi w_\lambda}{2 w k_{j,j+1}}, \quad (2.4.15)$$

$$\frac{K_{n,n+1}}{Z_0} = \sqrt{\frac{\pi}{2} \frac{w_\lambda}{w Q_{e,2}}}, \quad (2.4.16)$$

where w and w_λ are the fractional bandwidth and the guide-wavelength fractional bandwidth, respectively. These two expressions of the bandwidth are defined by

$$w = \frac{\omega_2 - \omega_1}{\omega_0}, \quad (2.4.17)$$

$$w_\lambda = \left[\frac{\lambda_{g1} - \lambda_{g2}}{\lambda_{g0}} \right] \approx \left(\frac{\lambda_{g0}}{\lambda_0} \right)^2 \left(\frac{\omega_2 - \omega_1}{\omega_0} \right). \quad (2.4.18)$$

Further, the shunt reactance $X_{j,j+1}$ coupling the resonators j and $j + 1$ is calculated from the impedance inverter $K_{j,j+1}$ using

$$\frac{X_{j,j+1}}{Z_0} = \frac{\frac{K_{j,j+1}}{Z_0}}{1 - \left(\frac{K_{j,j+1}}{Z_0}\right)^2}. \quad (2.4.19)$$

This expression computes the value of the shunt reactance $X_{j,j+1}$ that the inductance connected between the corresponding resonators has to exhibit at the centre frequency. This formula, together with (2.4.14), (2.4.15), and (2.4.16) are the design equations of shunt inductance coupled cavity resonator filters.

2.5 Fixed and Tunable Micro-Machined Cavity Resonator Filters at 20 GHz in Silicon Technology

2.5.1 Description of the Targeted Application

Band-pass filters belong to large components of data link millimetre-wave equipments. This is especially true for spaceborne applications like satellite transceivers. In these applications, very low-loss filters are mandatory and waveguide cavity resonator filters have been implemented up to now because of their excellent RF performance. However, these filters directly machined out of metal present quite a few disadvantages for on-board use. Their bulkiness and heaviness are bottlenecks, which limit the integration density of the entire system, and they represent a severe cost factor for the transportation into orbit of the complete payload. Also, waveguide filters are more often connected by means of coaxial connectors, which make them cumbersome to integrate onto Printed Circuit Boards (PCB). On the economic point of view, waveguide filters are expensive to manufacture. They require high-precision machining as well as fine tuning made by hand, and the costs are not dramatically decreased for large production scales. In order to overcome these limitations of waveguide filters, one is interested in replacing them by more compact micro-machined filters. Micro-machined filters are easier to integrate than their waveguide counter-parts, and they are expected to have satisfactory performance in terms of insertion loss. The micro-machined filters presented in the following sections are made out of silicon dielectric. They can be easily integrated in a hybrid fashion onto a front-end fabricated in LTCC or in soft Teflon substrate, or even monolithically if the front-end is manufactured in silicon. Furthermore, the interfaces of micro-machined filters are planar transmission lines (microstrip or coplanar), and they can be easily connected using flip-chip or bond-wires. Finally, micro-machined filters are manufactured using well-established and robust silicon micro-machining techniques. These techniques allow for tight and repeatable fabrication tolerances, and they have the advantage of being cost effective for large production scales.

The micro-machined filters demonstrated below constitute the first development step of filters intended for integration in satellite transceivers. The performance expected for these filters in terms of insertion loss and power handling makes them suitable for the middle stage of transceivers. This means after the Low-Noise Amplifiers (LNA) but before the final power amplification stage. In this segment of the transceiver, two major applications can be envisaged. Before the frequency

conversion, micro-machined filters could be implemented as post-LNA filters operating in the up-link frequency band (about 30 GHz). There, they could filter out spurious frequencies generated by the non-linearity of the LNA. However, the number of filters necessary for this task is limited and therefore, the gain in size and weight achieved by replacing the existing filters is expected to be limited. Another possible use of micro-machined filters is after the frequency conversion. Here, silicon filters could replace advantageously the present filters required to separate the down-converted signal (approximately 20 GHz) into different channels. Also, due to the likely size and weight reduction that could be gained by a higher integration density and a smaller size of the numerous filters necessary at this stage, this is the application, which has been chosen to demonstrate the potential of the proposed filters. A schematic of a satellite transceiver indicating the foreseen location of the micro-machined filters is shown in Fig. 2.6.

The specifications of the micro-machined filters presented below are those of channel partitioning filters implemented in recent satellite transceivers. They aim at the filtering of 500 MHz-wide channels centred at various frequencies around 20 GHz. For the channel centred at 19.95 GHz, these specifications are listed in Table 2.1.

Parameter	Value
Centre Frequency F_0	19.95 GHz
0.3 dB Bandwidth ΔF	500 MHz
Insertion Loss IL	<1.5 dB
In-Band Return Loss	20 dB
Max. ΔGD in 40 MHz (19.7 to 20.2 GHz)	<0.7 ns
Out-of-Band Rejection:	
19.6 GHz	>20 dB
0 to 19 GHz	>40 dB
21 to 32 GHz	>40 dB

Table 2.1: Electrical specifications of the fixed-frequency micro-machined filters.

In this set of specifications, the out-of-band rejection specified at 19.6 GHz aims at filtering the second harmonic of the local oscillator at 9.8 GHz. Further, a maximum variation of the group delay in the pass-band is required to avoid an excessive distortion of the signal passing through the filter.

Beyond the replacement of waveguide filters through more compact micro-machined filters, a further size and weight reduction of satellite transceivers could be reached if frequency-agile filters were used. Also, for tunable filters capable of switching between two contiguous channels, the number of partitioning filters in the transceiver could be reduced by half. This would logically reduce the costs of transceivers, which would be dramatically smaller, lighter, and easier to transport than existing systems. Further, it is evident that the size and weight reduction would be even more impressive, if the tunable filters were capable of switching between more than two channels: three or even four frequency bands for example. From this, the specifications of a 3-state tunable filter have been derived from the specifications known for the fixed-frequency filter. It has been decided

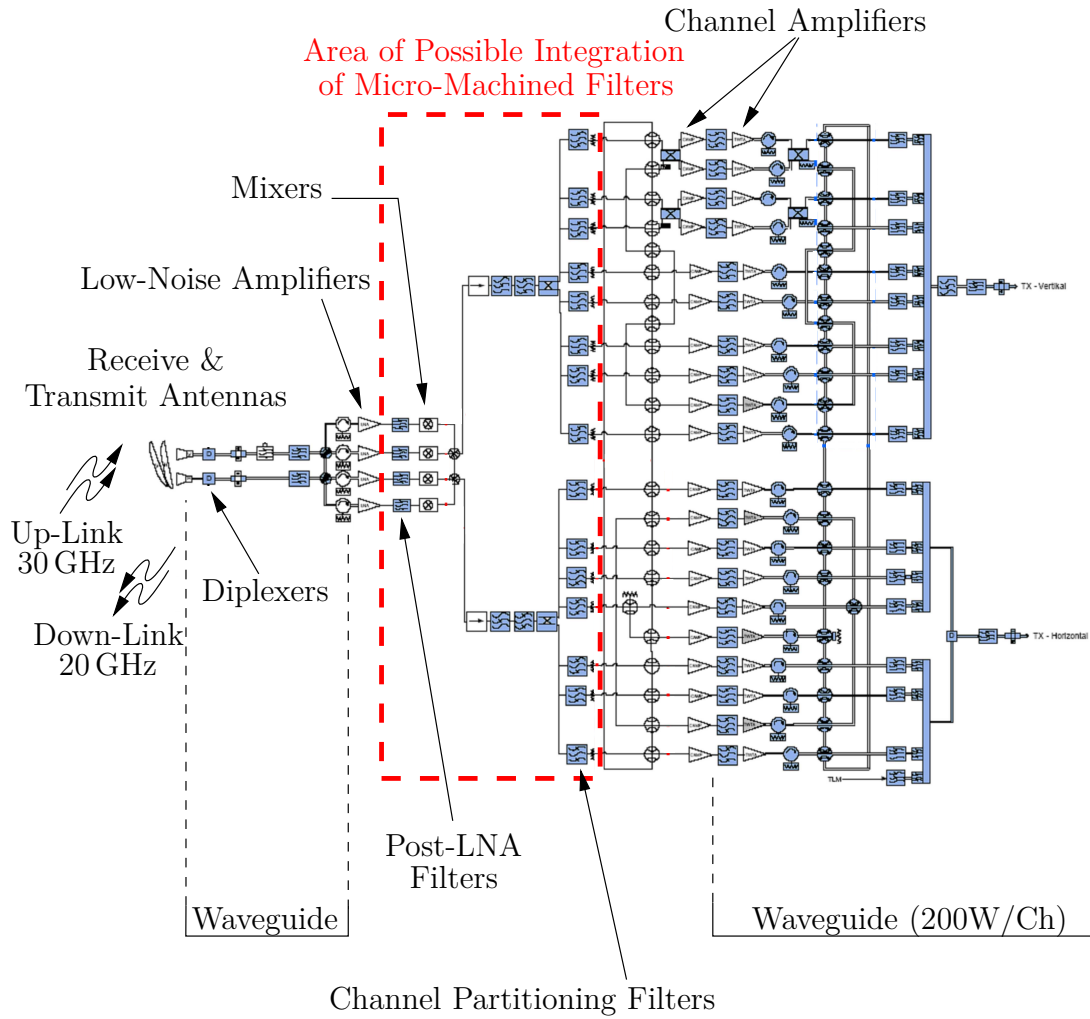


Fig. 2.6: Schematic of a satellite transceiver for communication link (Courtesy of Tesat-Spacecom GmbH & Co. KG).

that the frequency-agile filter should be capable of switching between three neighbouring data-link channels centred at 19.45 GHz, 19.95 GHz, and 20.45 GHz, respectively. The specifications of the tunable filter are summarised in Table 2.2.

Parameter	Value State 1	Value State 2	Value State 3
Centre Frequency F_0	19.45 GHz	19.95 GHz	20.45 GHz
0.3 dB Bandwidth ΔF	500 MHz	500 MHz	500 MHz
Insertion Loss IL	<1.5 dB	<1.5 dB	<1.5 dB
In-Band Return Loss	20 dB	20 dB	20 dB
Out-of-Band Rejection:			
19.6 GHz	–	>20 dB	–
0 to 19 GHz	–	>40 dB	–
21 to 32 GHz	–	>40 dB	–
19.1 GHz	>20 dB	–	–
0 to 18.5 GHz	>40 dB	–	–
20.5 to 31.5 GHz	>40 dB	–	–
20.1 GHz	–	–	>20 dB
0 to 19.5 GHz	–	–	>40 dB
21.5 to 32.5 GHz	–	–	>40 dB

Table 2.2: Electrical specifications of the frequency-agile micro-machined filter.

2.5.2 Fixed-Frequency Filters

Technology and Architecture of Silicon Micro-Machined Filters

The development of silicon micro-machined filters aims at the realisation of filters showing performance comparable to conventional waveguide cavity resonator filters. However, depending on the technique used to fabricate the structures out of silicon, it may not be possible to reproduce the geometry of waveguide filters.

This is especially true for the heated potassium hydroxide (KOH) wet-etching process of silicon chosen for the fabrication of the micro-machined filters presented here. KOH-etching of silicon is an anisotropic etching process, which removes silicon with respect to the $\langle 111 \rangle$ plane of the crystal. This main crystal axis forms an angle of 54.74° with the $\langle 100 \rangle$ plane of the silicon crystal, on which the top and bottom of silicon wafers are aligned. Hence, the cavities etched out of silicon using this technique have slanted side-walls with respect to the top and bottom of the silicon wafer, and thus with respect to the top and bottom of the cavities (Fig. 2.7). Another geometrical constraint imposed by the KOH-wet-etching process concerns the coupling sections between the resonators and in input/output of the filters. In waveguide filters, inductive couplings are mainly achieved using thin inductive irises, which are not technically feasible using wet-etching of silicon. For this reason, the evanescent coupling structures have to be designed differently in regard to what can be realised using KOH-etching.

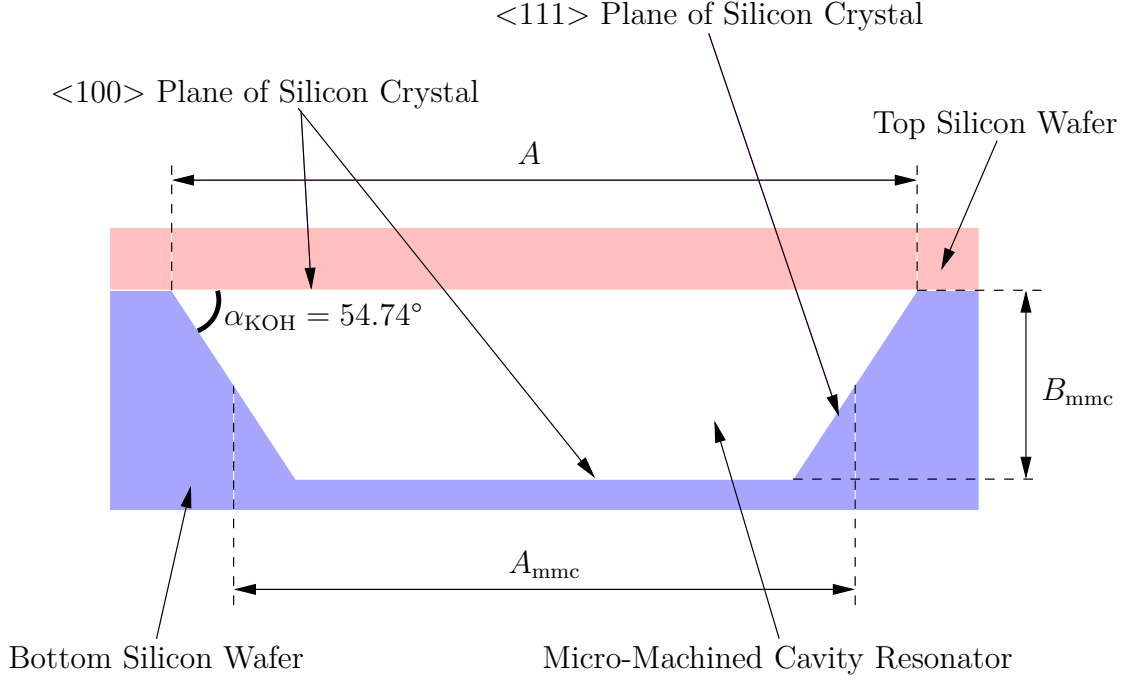


Fig. 2.7: Cross-section of a KOH-etched micro-machined cavity resonator closed using a top silicon dielectric.

According to the proposed architecture depicted in Fig. 2.8 and 2.9, the filters are realised using two silicon substrates bonded together. The cavity resonators are etched out of the bottom silicon substrate, and they are closed on their top side by a top silicon dielectric. The input/output and inter-resonator coupling structures are processed in the top silicon substrate. The input/output feeding lines are microstrip lines realised on the top silicon dielectric. They are coupled to the first and last cavity resonators of the filter using metal-free areas called "coupling slots" (Fig. 2.10). These coupling slots are patterned on the back side of the top silicon substrate according to the aperture coupling principle presented in [33]. Also, as for waveguide filters the resonators of the micro-machined filters are connected by means of evanescent coupling sections. Nevertheless, in the present case they are implemented with so-called "coupling cavities" (Fig. 2.11). The coupling cavities are etched out of the back side of the top silicon dielectric, above the inter-cavity wall. Also, in order to minimise the number of different technological processes for the fabrication of the filters, the coupling cavities are processed using the same KOH-wet-etching process as for the cavity resonators. The architecture allows for an horizontal integration of the cavity resonators, and it avoids the need for stacking of several wafers as when the cavity resonators are vertically integrated [82]. Further, it constitutes a low-complexity and low-cost alternative to isotropic etching techniques such as DRIE (Deep Reactive-Ion Etching), which could enable the fabrication of irises but at the price of a more complex and costly technology.

The top silicon dielectric is made out of 300 μm -thick high resistivity Float Zone silicon (FZ-silicon). In this top silicon dielectric, the coupling cavities are etched with a depth of 200 μm . The bottom silicon wafer is made out of low-cost silicon and it is 1300 μm -thick. This thickness enables the realisation of 1000 μm -deep cavity resonators. Both, the cavity resonators and the coupling cavities, are completely metallised by sputtering (Fig. 2.9), except for the input/output coupling slots.

The metallisation is made with 3 μm of Au, which is more than 5 times the skin depth in Au at the

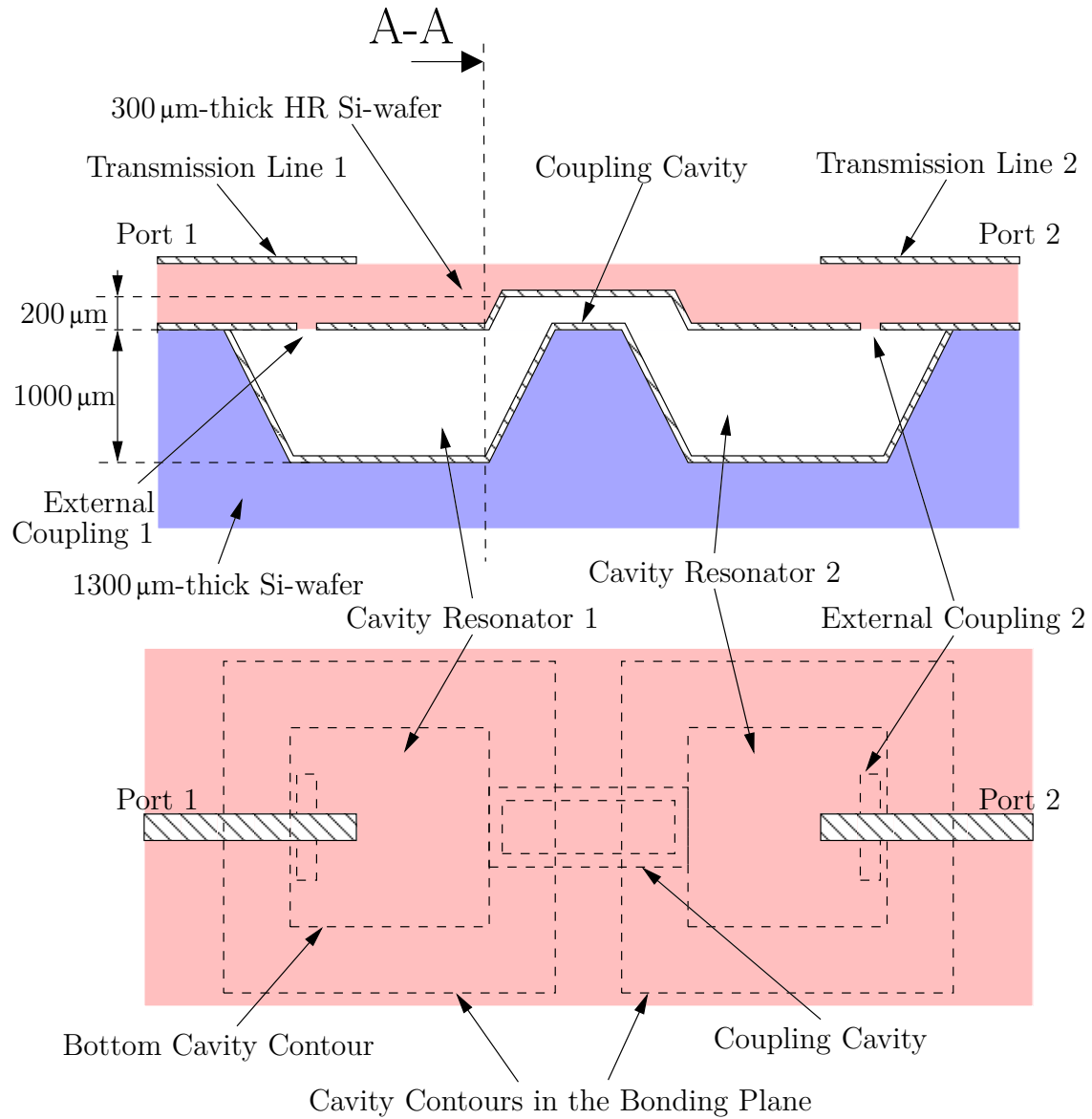


Fig. 2.8: Cross-section (top) and top view (bottom) of the proposed micro-machined filter architecture.

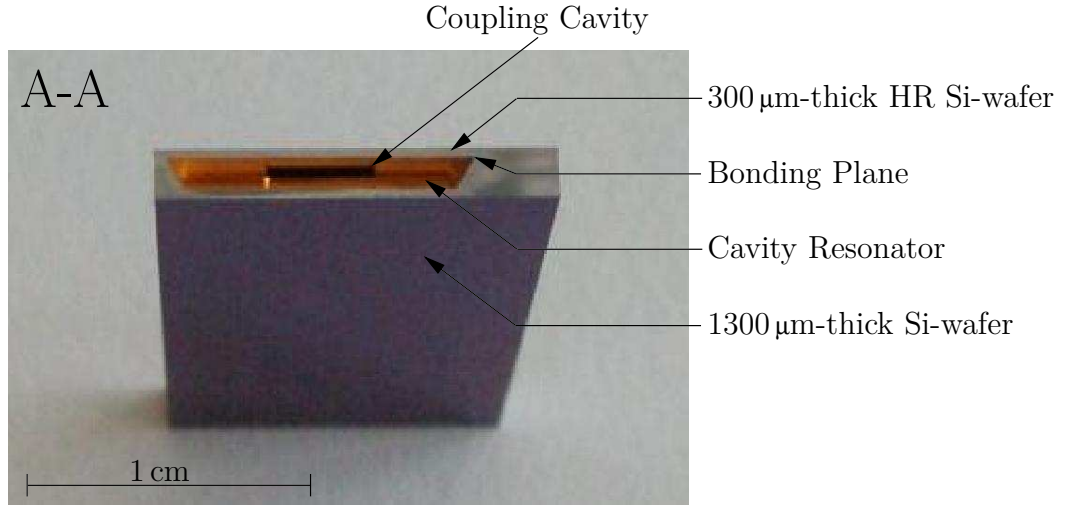


Fig. 2.9: Photograph of a micro-machined filter diced along the A-A cut. The A-A cutting plane is shown in Fig. 2.8.

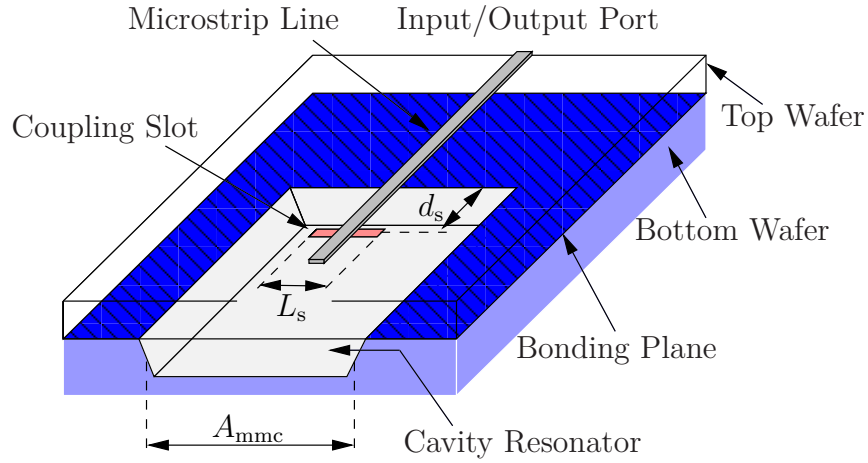


Fig. 2.10: 3D view of the slot coupled microstrip line placed on top of the cavity resonator.

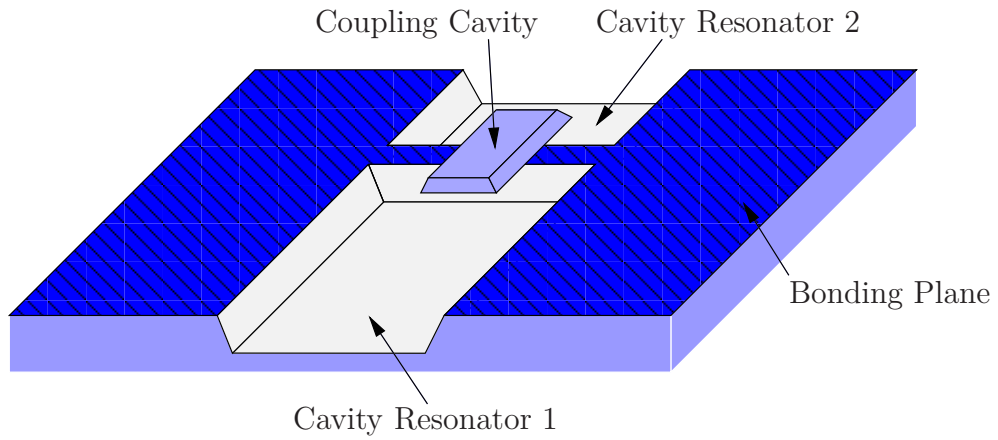


Fig. 2.11: 3D view of the coupling cavity placed on top of the inter-cavity wall.

design frequency of 19.95 GHz. The input/output microstrip lines are processed by lithography, and are 3 μm -thick. The two silicon substrates are assembled either using wafer-to-wafer or die-to-wafer bonding. They are mounted together by Au-Au thermo-compression using an AML AWB04 wafer bonder at a temperature of 300°C. The wafers are aligned using infrared transmission alignment, and they are contacted at 150°C under a vacuum better than $5 \cdot 10^{-5}$ mbar. The time necessary to wet-etch the cavities out of silicon is approximately 20 hours for the 1000 μm -deep cavity resonators, and 50 minutes for the 200 μm -deep coupling cavities.

For convenience, in what follows the lateral dimensions of micro-machined cavities are described using an effective length and width. These effective dimensions are defined by the arithmetical mean of the size of the cavity. From this, the effective width of a micro-machined cavity is given by

$$A_{\text{mmc}} = A - \frac{B_{\text{mmc}}}{\tan(\alpha_{\text{KOH}})}, \quad (2.5.1)$$

where B_{mmc} is the cavity depth, A is the width of the cavity resonator in the bonding plane, and α_{KOH} is the angle between the top plane of the cavity and its side-walls (Fig. 2.7). The effective length of the cavity resonator L_{mmc} is defined in the same way such that A_{mmc} , B_{mmc} , and L_{mmc} are the effective dimensions of the micro-machined cavity along the X-, Y-, and Z-axes, respectively.

Design of the Fixed-Frequency Filters

In a first development step, two fixed-frequency filters with two and three poles have been realised. The filters were designed using the low-pass to band-pass transformation. They are (quasi) Tchebycheff filters with an in-band ripple of 0.3 dB and a bandwidth of 500 MHz (Table 2.1). The coefficients of the low-pass prototype filters as well as the electrical parameters of the band-pass filters are summarised in Table 2.3.

	2-Pole Filter	3-Pole Filter
Low-Pass Proto. Filter		
$(g_0; g_1; g_2; g_3(; g_4))$	(1; 1.18046; 0.69572; 1.69674)	(1; 1.37126; 1.13785; 1.37126; 1)
Band-Pass Filter		
$Q_{e,1}$	47.22	54.85
$Q_{e,2}$	(made symmetric) 47.22	54.85
$\frac{X_{1,2}}{Z_0}$	0.087502	0.063255
$\frac{X_{2,3}}{Z_0}$	–	0.063255

Table 2.3: Coefficients of the low-pass prototype filters and electrical parameters of the 2- and 3-pole band-pass filters.

The electrical parameters of the band-pass filters have been calculated from the coefficients of the low-pass prototype filters using (2.4.14), (2.4.15), (2.4.16), and (2.4.19). Also, in order to realise micro-machined filters with little insertion loss, a Q-factor of $Q_u = 1000$ is required for the cavity resonators. For an air-filled cavity covered with Au ($\sigma_{\text{Au}} = 41 \cdot 10^6$ mhos/m), this is achieved with a 626 μm -deep ideal square cavity (2.4.6). Nevertheless, micro-machined cavities are different from

ideal cavities. They have slanted side-walls that increase the surface of the metallisation, and they have a bond at the junction between the two silicon dielectrics. For these reasons and in order to compensate for the losses which these features might add, a depth of $1000\mu\text{m}$ has been chosen for the cavity resonators.

In order to assess the influence of that particular geometry of KOH-etched cavities, a 2-port cavity resonator has been characterised using full-wave simulations. According to these, the resonance frequency of a micro-machined cavity resonator is 0.17% below the resonance frequency of an "equivalent" rectangular cavity having the same dimensions A_{mmc} , B_{mmc} , and L_{mmc} .

For practical filter design, the input/output coupling structures have to be dimensioned such that they achieve the required coupling coefficients at the two ports of the filter. To do this, the 2-port cavity resonator has been simulated for two kinds of coupling slots, rectangular and H-shaped, and for various lengths of these slots. The external Q-factor $Q_{e,1/2}$ has been calculated from the simulated responses and for each configuration of the coupling structures. The calculations were performed using successively (2.4.12), (2.4.13), (2.4.11), and (2.4.10). The values of the 1-port external Q-factor versus the normalised length of the coupling slot $\frac{L_s}{A_{\text{mmc}}}$ are plotted in Fig. 2.12.

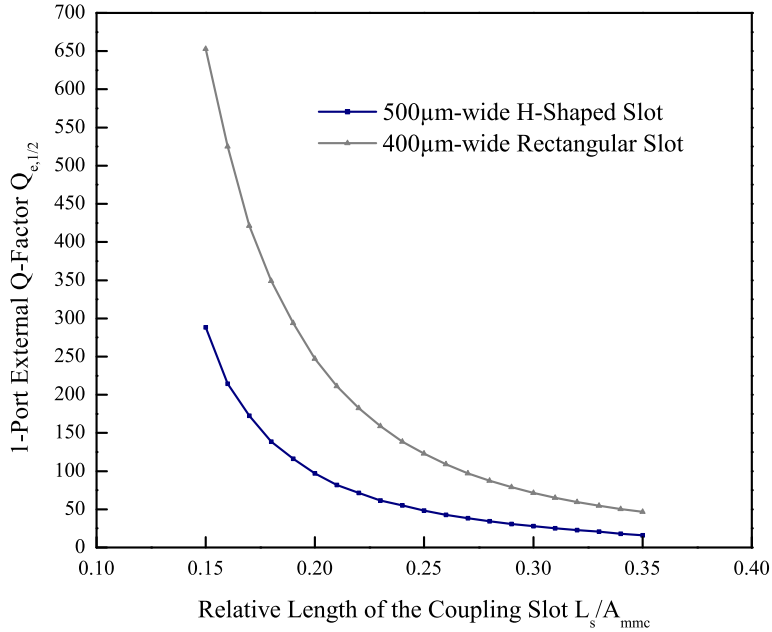


Fig. 2.12: 1-port external Q-factor versus relative length of the coupling slot.

In order to be able to calculate the length of a coupling slot so that it achieves an aimed Q-factor, the points calculated from the simulations have been interpolated with 4th order polynomials. The relative length of the coupling slot $\frac{L_s}{A_{\text{mmc}}}$ allowing for the achievement of a targeted 1-port external Q-factor $Q_{e,1/2}$ is given by (2.5.2) for a 400μm-wide rectangular slot, and by (2.5.3) for a 500μm-wide H-shaped coupling slot.

$$\begin{aligned} \frac{L_s}{A_{mmc}} = & 0.51781231 - 0.48998473 \cdot 10^{-2} \cdot (Q_{e,1/2}) + 0.31903006 \cdot 10^{-4} \cdot (Q_{e,1/2})^2 \\ & - 0.88933617 \cdot 10^{-7} \cdot (Q_{e,1/2})^3 + 0.76959418 \cdot 10^{-10} \cdot (Q_{e,1/2})^4 \end{aligned} \quad (2.5.2)$$

$$\begin{aligned} \frac{L_s}{A_{mmc}} = & 0.45474213 - 0.81567310 \cdot 10^{-2} \cdot (Q_{e,1/2}) + 0.11137177 \cdot 10^{-3} \cdot (Q_{e,1/2})^2 \\ & - 0.69203132 \cdot 10^{-6} \cdot (Q_{e,1/2})^3 - 0.13573153 \cdot 10^{-8} \cdot (Q_{e,1/2})^4 \end{aligned} \quad (2.5.3)$$

These formulas and the graph in Fig. 2.12 are the rules for the design of slot-coupled cavities and filters. They indicate the dimension that a coupling slot shall have to achieve a given 1-port external Q-factor for the cavity resonator and thus, a given coupling coefficient in input/output of the filter. The formulas and the graph in Fig. 2.12 are only valid for coupling slots placed on the axis of symmetry of the cavity resonator and for a $\lambda/4$ -long open-circuited microstrip line stub. Also, the rectangular and the H-shaped coupling slot have been simulated for two different distances d_s between the centre of the slot and the adjacent side-wall of the cavity (Fig. 2.10). This distance is $2454 \mu\text{m}$ for the rectangular slot and $1358 \mu\text{m}$ for the H-shaped slot.

The strategy used to design the coupling structures between the micro-machined resonators is based on a similar principle. The evanescent coupling section formed by the coupling cavity has been characterised alone using full-wave simulations. Here, the simulated structure includes and is limited to the coupling cavity, a small length of the two cavity resonators, and the wall separating these two cavity resonators (Fig. 2.11). Also, in order to compute the S-parameters of the coupling structure the two sections of cavity resonator are terminated by two waveguide ports. The structure has been simulated for various dimensions of the micro-machined coupling cavity, and for each one of the simulated responses the coupling inductance has been calculated. The normalised coupling inductance $\frac{X}{Z_0}$ is calculated from the simulated S_{21} -parameter using

$$\frac{X_{j,j+1}}{Z_0} = \frac{|S_{21}|}{2\sqrt{1 - |S_{21}|^2}}. \quad (2.5.4)$$

The depth of the coupling cavity is fixed at $200 \mu\text{m}$ limited by the thickness of the top silicon dielectric. Therefore, the coupling between two resonators can be adjusted principally by varying the width of the coupling cavity between them. The length of the cavity has been found to have only a limited influence on the RF behaviour of the structure. For these reasons, the simulations have been performed for various widths of the coupling cavity, but with a cavity depth fixed at $200 \mu\text{m}$ and a length fixed at $L_{cc}=2000 \mu\text{m}$. Further, a thickness of $T_{icw}=100 \mu\text{m}$ has been chosen for the wall between the two resonators. This thickness is given in the bonding plane. The values of $\frac{X}{Z_0}$ are plotted against the relative width of the coupling cavity $\frac{W_{cc}}{A_{mmc}}$ in Fig. 2.13.

Also, in the same way as for the design of the input/output couplings, the values calculated for the coupling inductance have been interpolated with a 4th order polynomial. This polynomial calculates the relative width of the coupling cavity $\frac{W_{cc}}{A_{mmc}}$, such that it achieves an aimed coupling inductance $\frac{X}{Z_0}$.

This polynomial is given by

$$\begin{aligned} \frac{W_{cc}}{A_{mmc}} = & 0.14530567 + 7.82100111 \cdot \left(\frac{X}{Z_0}\right) - 106.48527295 \cdot \left(\frac{X}{Z_0}\right)^2 \\ & + 741.60230038 \cdot \left(\frac{X}{Z_0}\right)^3 - 1785.57893576 \cdot \left(\frac{X}{Z_0}\right)^4. \end{aligned} \quad (2.5.5)$$

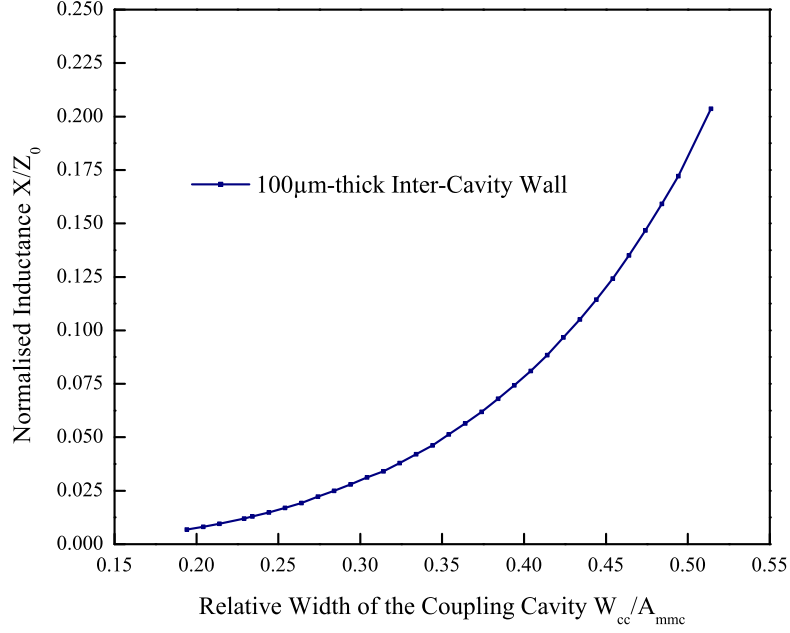


Fig. 2.13: Normalised inductance $\frac{X}{Z_0}$ versus relative width of the coupling cavity.

The polynomials (2.5.2), (2.5.3), and (2.5.5) are the design equations of micro-machined filters realised according to the architecture presented in Fig. 2.8. They calculate the physical size of the coupling structures, coupling slots and coupling cavities, necessary to achieve the coupling coefficients required for the filter.

Finally, the filters designed with the proposed method have been calculated using 3D electromagnetic simulations. The dimensions of the coupling structures of both, the 2- and 3-pole filters are summarised in Table 2.4.

Beyond the filter design, a coplanar to microstrip line transition was processed in input and output of the filters. The transition was implemented to aid the integration of the filters, which cannot be directly connected with microstrip line interfaces because of the buried ground plane. The structure is realised using radial stubs that achieve a via-less transition working around the filter response [106]. Like straight stubs, they connect virtually the ground planes of the coplanar line to that of the microstrip line. Nevertheless, they provide a larger capacitance against the ground plane of the microstrip line, which benefits the bandwidth of the transition. The coplanar line used as interface is 300µm-long, and it has lateral dimensions (line to ground and ground to ground

	2-Pole Filter	3-Pole Filter
Input/Output Couplings		
Coupling Slot	Rectangular	H-shaped
$\frac{L_s}{A_{mmc}}$	0.29	0.33
W_s	400 μm	500 μm
$l_{ms \text{ stub}}$	1398 μm	1376 μm
d_s	2454 μm	1358 μm
Inter-Resonator Coupling(s)		
$\frac{W_{cc}}{A_{mmc}}$	0.37	0.46
L_{cc}	2141.8 μm	2000 μm
H_{cc}	200 μm	200 μm
T_{icw}	68 μm	100 μm

Table 2.4: Dimensions of the coupling structures of the 2- and 3-pole micro-machined band-pass filters.

spacings) compatible with 150 μm -pitch coplanar measurement probes. Thanks to this coplanar interface, the filters can be connected in different ways depending on the configuration of the mother board. If the filter is placed in a cavity manufactured in the receiving board, it can be connected by means of bond-wires. In return, if the silicon chip is intended to be flip-chipped onto a PCB, the coplanar lines on the board and the ones on the chip can be connected using stud bumps. A layout of the transition is depicted in Fig. 2.14. The structure is fully metallised on the back side of the dielectric. Nevertheless, for better visibility, the metal ground plane is not shown in the picture.

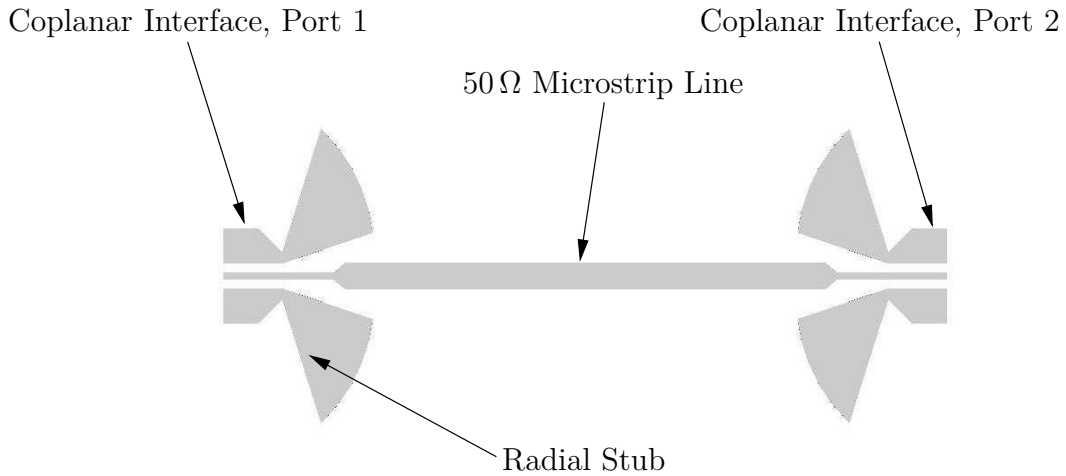


Fig. 2.14: Layout of the back-to-back coplanar to microstrip line transition on silicon.

Characterisation and Measurements

The structures have been processed by Philips Research in the MiPlaza facilities in Eindhoven. They have been designed and manufactured in two different runs. The wafers of the first batch

contained only single 2-port cavity resonators and 2-pole band-pass filters. On top of these, the second run included also 3-pole band-pass filters and a 4-pole linear phase filter, which is the topic of a later section. A photograph of the wafer processed during the second process run and containing all structures discussed here is depicted in Fig. 2.15.

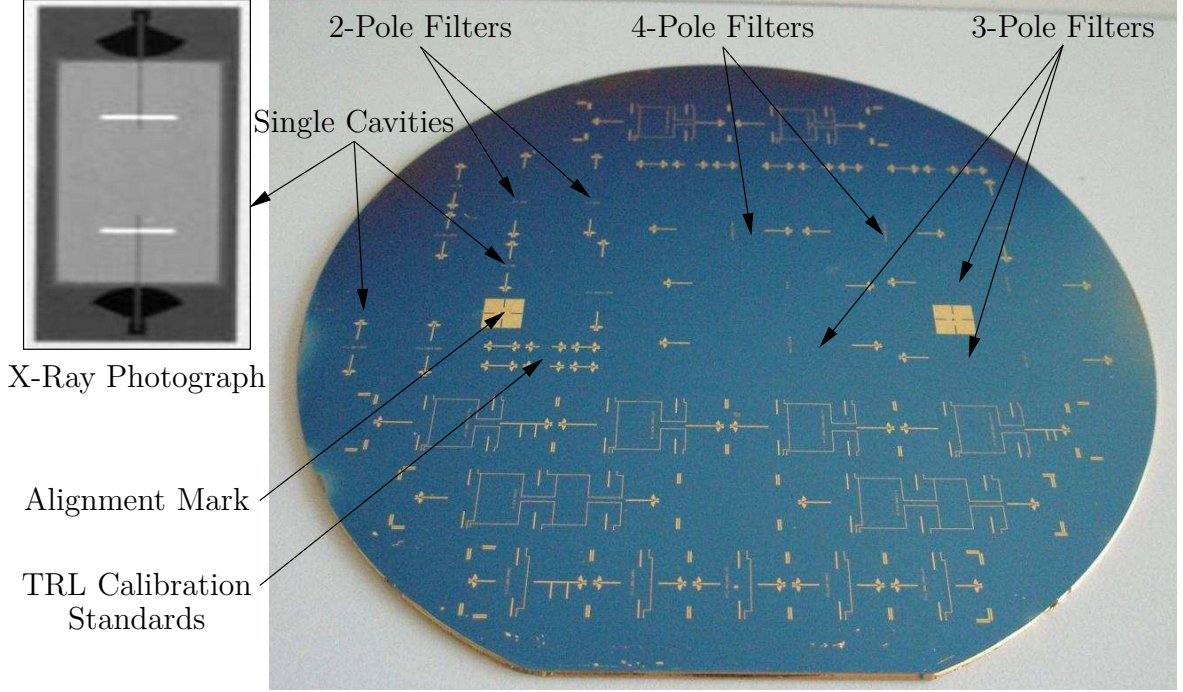


Fig. 2.15: Photograph of the micro-machined filters processed on 8 inch silicon wafer. X-ray picture by courtesy of Philips Semiconductors, now NXP Semiconductors.

The filters have been characterised at EADS Innovation Works in Ottobrunn. They have been measured on-wafer using 150 μm -pitch coplanar measurement probes connected to a vector network analyser. Firstly, the via-less coplanar to microstrip line transition has been measured. The structure is the previously presented back-to-back transition depicted in Fig. 2.14. The insertion loss and return loss of the structure measured using SOLT calibration are plotted in Fig. 2.16. The transition exhibits a satisfactory broadband behaviour from 8.75 GHz up to 24.75 GHz (95.5%). Over this frequency range, the return loss of the back-to-back transition is better than 13 dB and its insertion loss is below 2 dB.

In order to measure accurately the unloaded Q-factor and the resonance frequency of a KOH-etched cavity resonator, a weakly coupled 2-port cavity resonator has been fabricated. The effective dimensions of the fabricated cavity are $A_{\text{mmc}}=10600 \mu\text{m}$, $B_{\text{mmc}}=1000 \mu\text{m}$, and $L_{\text{mmc}}=10600 \mu\text{m}$. The transmit response measured for this cavity is plotted in Fig. 2.17.

The measured resonance frequency is 19.879 GHz. It is 0.66% below the theoretical resonance frequency $F_{0,TE_{101}}=20.012 \text{ GHz}$ of an "equivalent" waveguide cavity having the same dimensions. Also, from the simulation presented previously it is 0.5% below the resonance frequency of 19.978 GHz, which would be expected for a perfectly manufactured KOH-etched cavity resonator. This down shift of the resonance frequency is attributed to an under-etching of the side-walls of the cavity. In this case, the 0.5% frequency drift is justified by a 26.6 μm under-etching of the cavity walls on all four sides of the resonator. The insertion loss measured for the micro-machined cavity res-

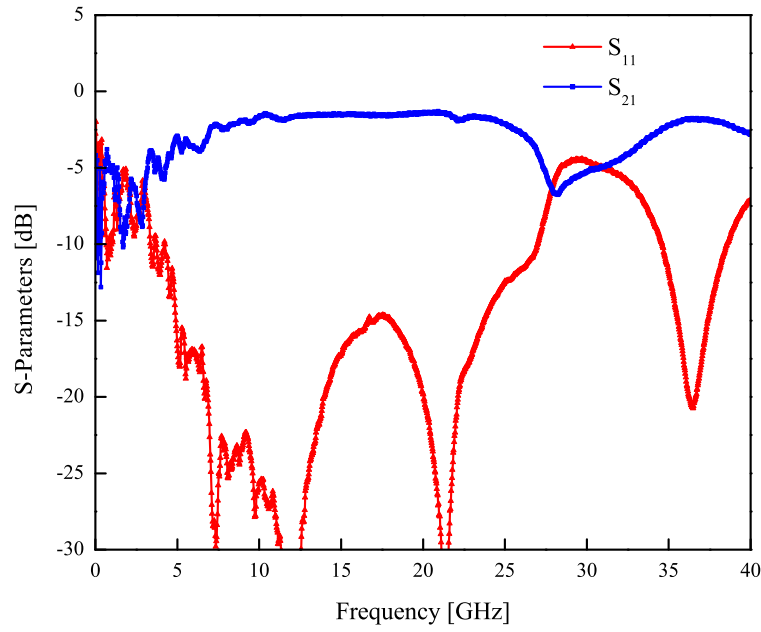


Fig. 2.16: Measured return loss and insertion loss of the back-to-back coplanar to microstrip line transition.

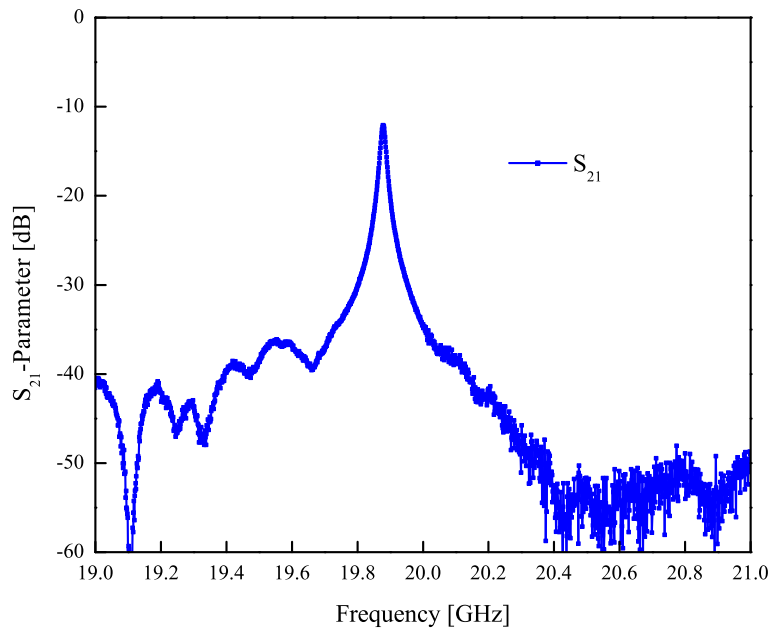


Fig. 2.17: Measured response of a weakly coupled 2-port micro-machined cavity resonator.

onator is 12.1 dB and the 3 dB bandwidth around the resonance peak is 18.7 MHz. The unloaded Q-factor calculated from these values and using (2.4.12) and (2.4.13) is $Q_u=1410$. It is better than the targeted unloaded Q-factor of $Q_u=1000$. This value is very close to the theoretical unloaded Q-factor of an "equivalent" waveguide cavity: $Q_u=1515$ for an air-filled and Au-covered waveguide cavity resonator. This good value obtained for the unloaded Q-factor is a good indicator for the technology. It shows especially the good conductivity of the Au-metallisation sputtered on the walls of the cavity, and it underlines the good quality of the bonding process of the two silicon substrates.

The 2- and 3-pole filters have been measured in the same way as the single 2-port cavity resonator. They were measured using TRL calibration to de-embed the input/output coplanar to microstrip line transitions. The response measured for the 2-pole filter is plotted in Fig. 2.18 and that of the 3-pole filter is shown in Fig. 2.19.

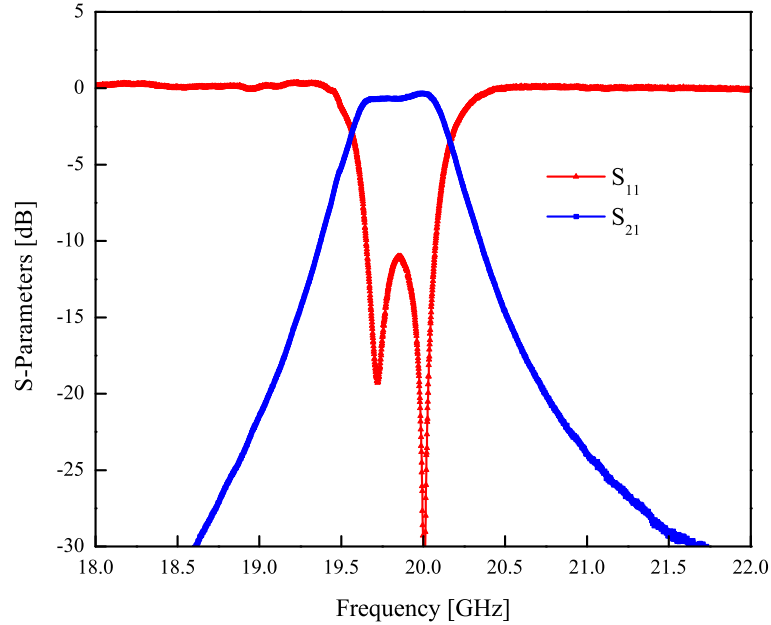


Fig. 2.18: Measured response of the 2-pole fixed-frequency micro-machined filter.

The response of the 2-pole filter is centred at 19.860 GHz. It is 90 MHz (0.4%) below the centre frequency of $F_0=19.95$ GHz specified in Table 2.1 for that filter. This shift corresponds approximately to the one observed for the single cavity resonator, and it is caused by a comparable under-etching of the structures. Further, the ripple of the response in the pass-band is 0.41 dB and the bandwidth measured at that same level is 0.401 GHz (2.02%). It is almost 100 MHz below the value required for the filter. This slight inaccuracy is attributed to a drift of the coupling coefficients away from their targeted values. It is most probably due to the fabrication tolerances of the coupling structures, i.e. under-etching of the coupling slots and coupling cavity, but also eventually to a small misalignment of the two silicon dielectrics. Finally, the in-band insertion loss and return loss are 0.31 dB and 11 dB, respectively. From (2.5.6) [34], this insertion loss measured for the filter corresponds

to an unloaded Q factor of about $Q_{BP}=1000$ for the two micro-machined cavity resonators. It is approximately 400 below the unloaded Q-factor measured for the weakly coupled cavity resonator. This difference is explained mainly by the larger loss dissipated through the wider coupling slots implemented in the 2-pole filter.

$$Q_u = Q_{BP} = \frac{8.686 C_n \omega'_1}{w \cdot IL} \quad (2.5.6)$$

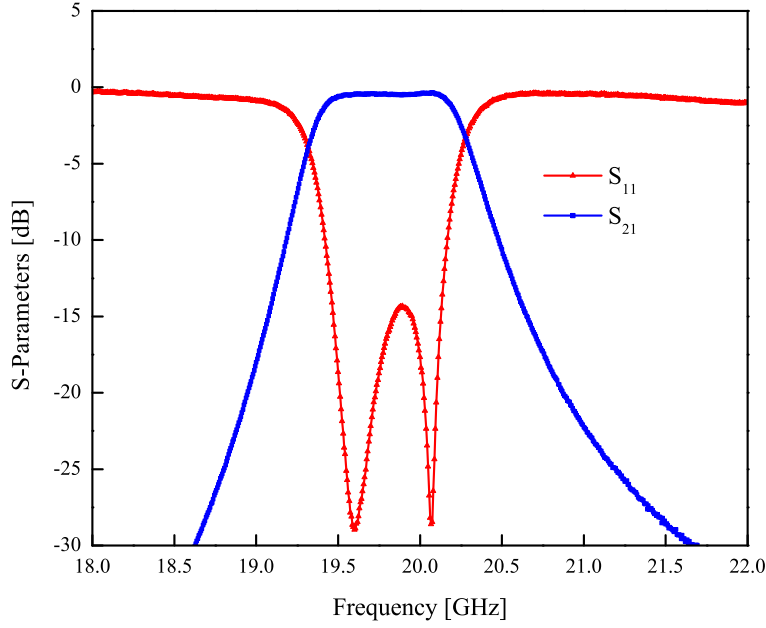


Fig. 2.19: Measured response of the 3-pole fixed-frequency micro-machined filter.

The 3-pole micro-machined filter was measured with a response centred at 19.86 GHz. The pass-band response exhibits a limited in-band ripple, below the 0.3 dB level specified for the filter. At that level, the filter has a bandwidth of 650 MHz (0.3%), which is 150 MHz wider than the 500 MHz given in Table 2.1. The return loss of the filter in the pass-band is better than 14.5 dB.

4-Pole Linear Phase Filter

Standard filters like Tchebycheff filters have transfer functions with non-linear phase in the pass-band. Since the group delay is the first derivative of the phase with respect to frequency, these filters have a non-uniform group delay. For these filters, the signal packets of a broadband signal reach the output of the filter at different times, and the signal is distorted. This situation can be overcome by implementing linear phase filters having by definition a flat group delay. In linear phase filters, all components of the input signal are transmitted to the output of the filter at the same time, and the signal travelling through the filter is not distorted.

Linear phase filters are realised by designing couplings between resonators, which are not electrically adjacent. These additional couplings called cross-couplings enable multiple paths for the signal travelling through the filter. Also, for a suitable amplitude and phase of the cross-couplings, destructive interferences appear between the signals of the various paths, and transmission zeros show up in the transfer function. If these transmission zeros arise at real finite frequencies, the filter response exhibits an infinite attenuation at these frequencies and the filter is said to be elliptic. In return, if the additional transmission zeros are created at imaginary frequencies, the transfer response of the filter shows an improved linearity of the phase in the pass-band. The type of filter response, elliptic or linear phase, depends on the phase of the cross-couplings. In [107], it is shown that a linear phase filter can be realised when both the direct and cross-couplings have the same sign. Thus, it is possible to design linear phase filters with cavity resonators coupled with direct and cross-couplings all realised with inductive coupling cavities.

In the following, a 4-pole linear phase filter with one cross-coupling between the first and the fourth resonator is demonstrated. A schematic of the filter is given in Fig. 2.20.

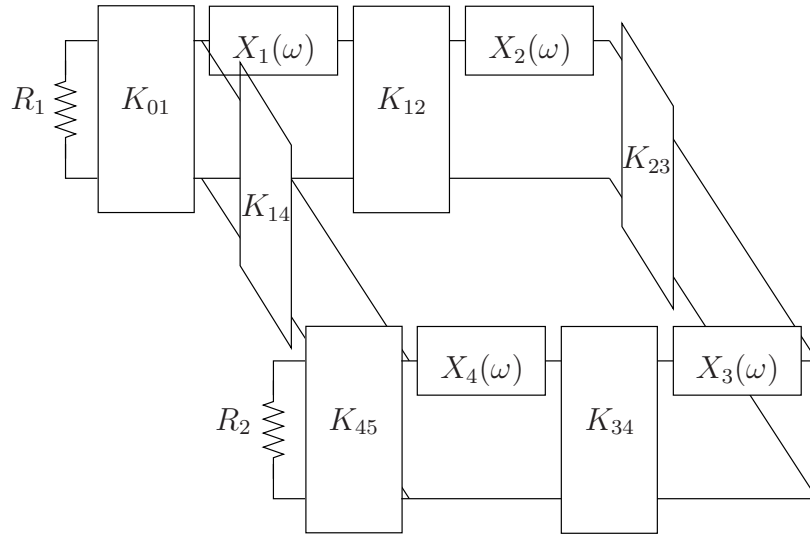


Fig. 2.20: Schematic of the 4-pole linear phase filter.

The filter is designed with four resonators coupled with three direct couplings K_{12} , K_{23} , and K_{34} , and one cross-coupling K_{14} . As previously mentioned, both the direct and cross-couplings have the same phase and are inductive. The filter is realised in the same architecture as the one presented in Fig. 2.8 for the 2- and 3-pole micro-machined filters. In the present case however, the filter is realised with four KOH-etched cavity resonators arranged in a square (Fig. 2.21). The direct couplings as well as the cross-coupling are implemented using KOH-etched coupling cavities.

The coefficients of the filter have been provided by Tesat-Spacecom GmbH, and they have been determined according to the method proposed in [108]. These coefficients as well as the electrical parameters of the filter are summarised in Table 2.5.

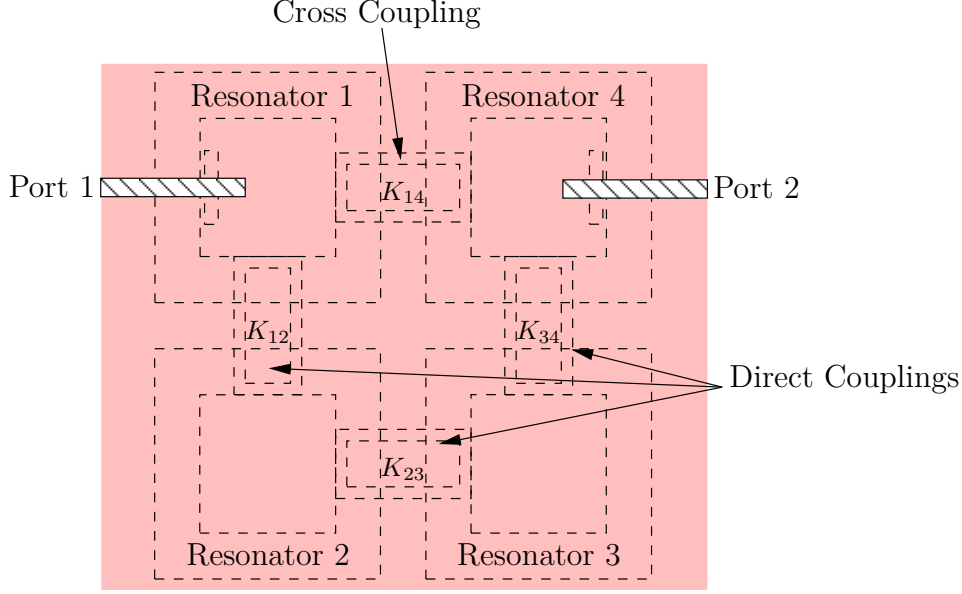


Fig. 2.21: Architecture of the 4-pole linear phase filter.

Coupling Coefficients		Electrical Parameters	
Parameter	Value	Parameter	Value
k_{01}	0.0315	$Q_{e,1}$	30.18
k_{12}	0.0281	$\frac{X_{1,2}}{Z_0}$	0.1037
k_{23}	0.0187	$\frac{X_{2,3}}{Z_0}$	0.0682
k_{34}	0.0281	$\frac{X_{3,4}}{Z_0}$	0.1037
k_{45}	0.0315	$Q_{e,2}$	30.18
k_{14}	0.0057	$\frac{X_{1,4}}{Z_0}$	0.0208

Table 2.5: Coupling coefficients and electrical parameters of the 4-pole linear phase filter.

The electrical parameters of the linear phase filter have been determined in the same way as those of the 2- and 3-pole micro-machined filters. The inductances $\frac{X_{i,j}}{Z_0}$ are calculated using (2.4.15) and (2.4.19), and the external Q-factors $Q_{e,1}$ and $Q_{e,2}$ are calculated from (2.4.14) and (2.4.16), respectively. Also, the coupling structures are similar to the ones implemented in the previously presented micro-machined filters, and especially the 3-pole filter. The coupling slots in input/output of the filter are H-shaped and they are $W_s=500\mu\text{m}$ -wide. They are placed at a distance $d_s=1358\mu\text{m}$, given in the bonding plane, from their respective adjacent side-wall. The coupling cavities are $H_{cc}=200\mu\text{m}$ -deep, $L_{cc}=2000\mu\text{m}$ -long, and all inter-cavity walls are $T_{icw}=100\mu\text{m}$ -thick. A photograph of the realised filter is shown in Fig. 2.22. The response measured for the filter is plotted in Fig. 2.23, and the corresponding group delay is depicted in Fig. 2.24.

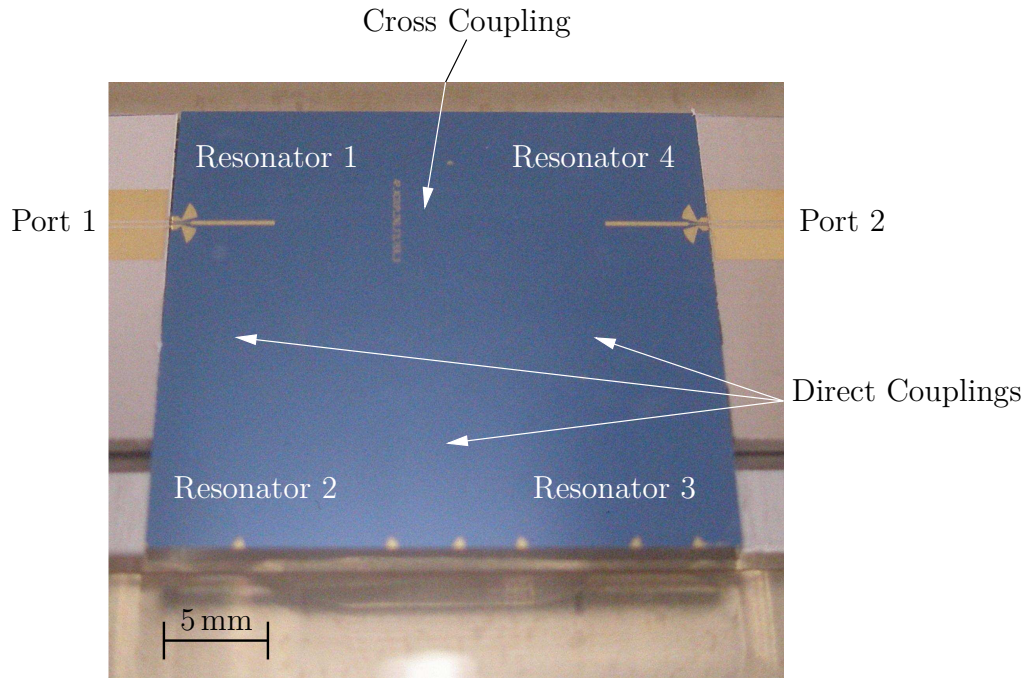


Fig. 2.22: Photograph of the 4-pole linear phase filter.

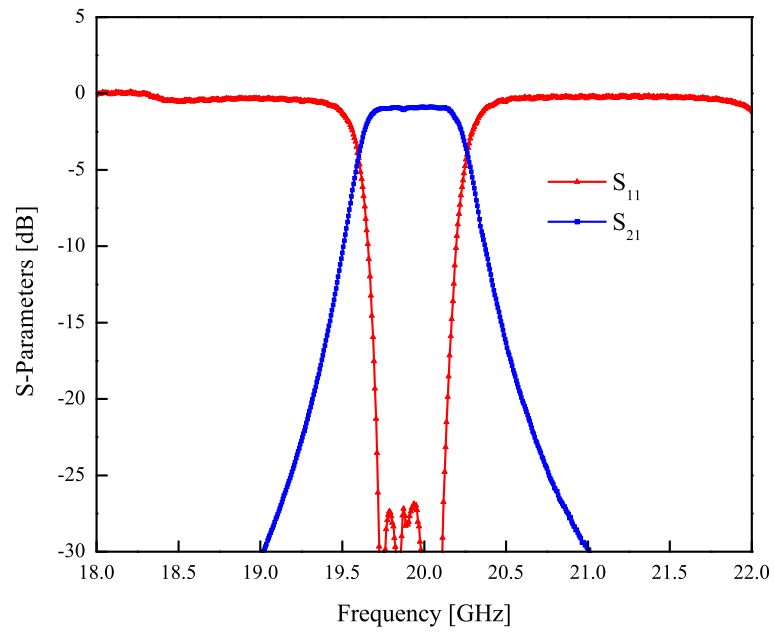


Fig. 2.23: Measured response of the 4-pole linear phase filter.

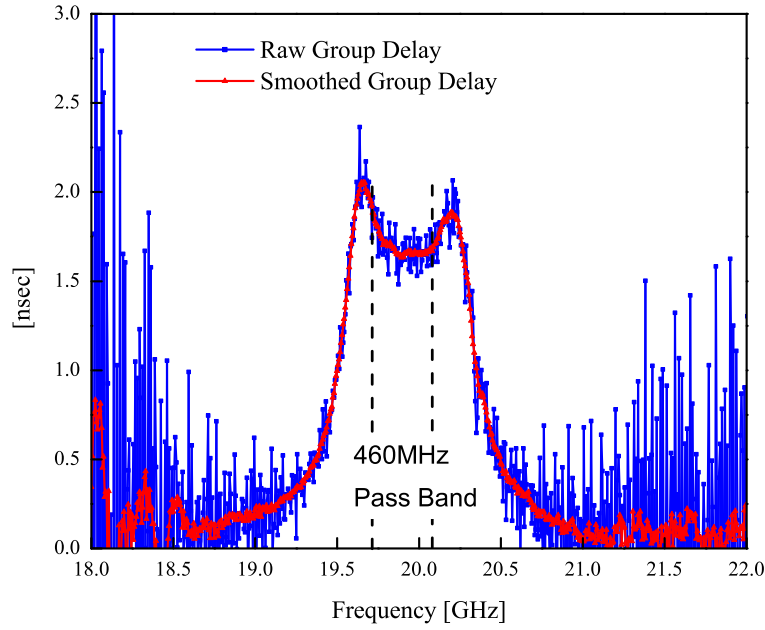


Fig. 2.24: Measured group delay of the 4-pole linear phase filter.

The response measured for the 4-pole filter is centred at 19.93 GHz, which is extremely close to the targeted centre frequency of 19.95 GHz (Table 2.1). The ripple measured in the pass-band is negligible and it is by far below the 0.3 dB of variation allowed for the in-band response. The bandwidth measured at that level is 460 MHz (2.3%). The response exhibits a very low in-band insertion loss of 0.9 dB. This insertion loss for the 4-pole filter corresponds to an outstanding unloaded Q-factor of 1133 for the micro-machined resonators. The overall variation of the group delay in the pass-band is 0.49 ns (0.32 ns for the smoothed group delay). This value measured for the filter is better than the maximum 0.7 ns of group delay variation required for the filter. Also, it is sensibly below the variation of the group delay that would be obtained with a 4-pole Tchebycheff filter having similar performance, generally above 1 ns.

2.5.3 Frequency-Agile Filter

Theory and Principle of the Tuning Technique

The frequency-agile filter is based on the 3-pole fixed-frequency band-pass filter. The filter is made steerable over frequency by means of adjustable lines coupled to each cavity resonator of the filter [35]. The adjustable lines are microstrip lines open-circuited at both ends. They are designed on top of the filter, at the same level as the input/output transmission lines. They are inductively coupled to the cavity resonators through coupling slots patterned in their ground plane, in the same way as for the input/output couplings presented in Fig. 2.10. On one side of the slot, the electrical length of the microstrip lines is adjustable by means of RF-MEMS switches. On the other side of the slot, their length is fixed and about one quarter of wavelength. Also, depending on the electrical length of the adjustable stub, the reactance coupled to the cavity resonator can be capacitive or

inductive, and it may take different values changing the resonance frequency of the resonator. The variable impedance Z_{var} created by the stub is in parallel with the series RLC -resonance of the original cavity resonator. The schematic of a tunable 2-port cavity resonator with one adjustable stub is shown in Fig. 2.25.

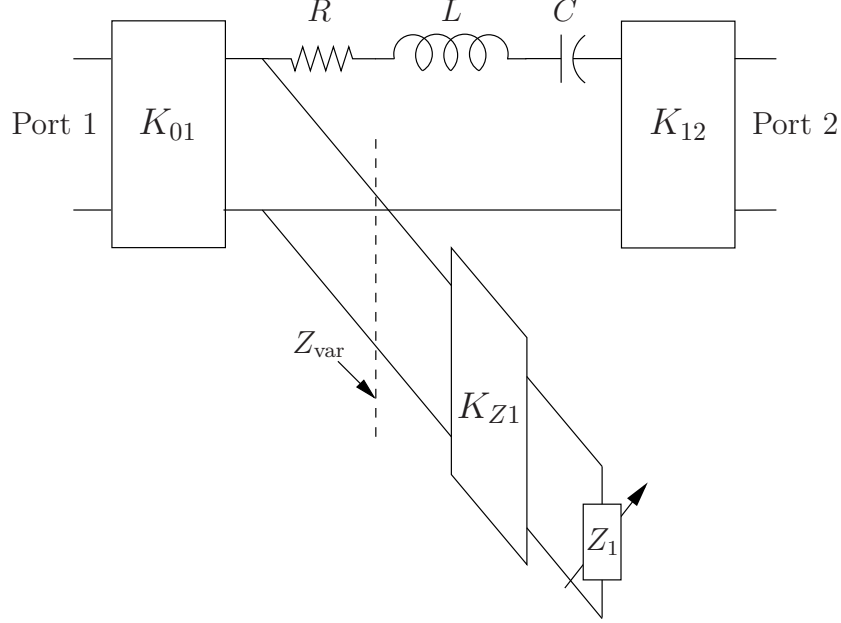


Fig. 2.25: Schematic of the tunable 2-port cavity resonator.

The tunable impedance Z_{var} loading the cavity resonator is the impedance provided by the adjustable stub Z_1 after it is transformed by the coupling structure. With K_{Z1} the impedance inverter corresponding to the coupling structure described above, Z_{var} is given by

$$Z_{\text{var}} = jX_{\text{var}} = j \frac{\tan(\beta l)}{Z_{0,\text{as}}(K_{Z1})^2}, \quad (2.5.7)$$

where β and $Z_{0,\text{as}}$ are the propagation constant and the characteristic impedance of the adjustable stub, respectively. Also, l is the physical length of the adjustable stub between the centre of the coupling slot and its open-circuited end. This length l is exclusively on the adjustable side of the stub and it is changed by actuating the RF-MEMS switch. According to Fig. 2.25, the S_{21} -parameter of a tunable 2-port cavity resonator is given by

$$S_{21} = \frac{-2}{(R + jL\omega + \frac{1}{jC\omega})(\frac{1}{Z_{\text{var}}} + \frac{Z_0}{K^2}) + \frac{K^2}{Z_{\text{var}}Z_0} + 2}, \quad (2.5.8)$$

in which Z_0 is the normalisation impedance (50Ω), and $K = K_{01} = K_{12}$ is the value of the input/output impedance inverters. The S_{21} -parameter calculated using (2.5.8) is plotted in Fig. 2.26 for a fixed and a tunable cavity resonator.

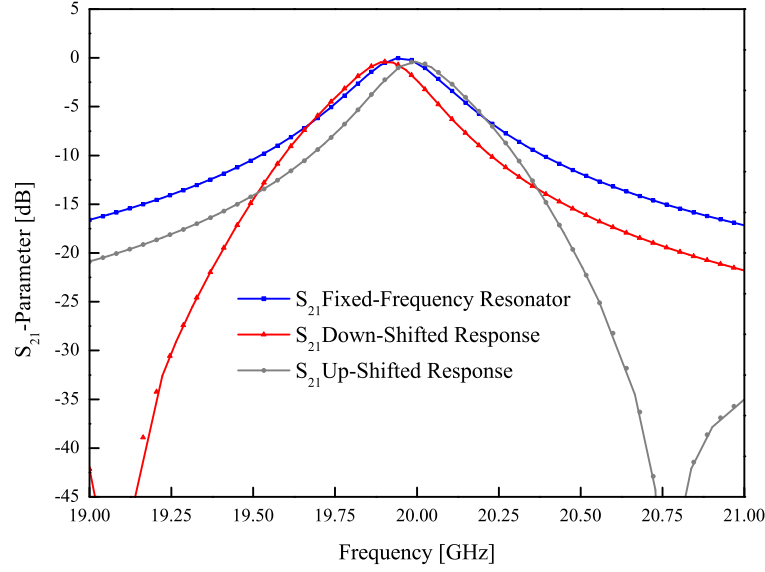


Fig. 2.26: Calculated response of a 2-port cavity resonator with and without tuning device.

S_{21} has been calculated for R , L , and C chosen such that the fixed-frequency resonator exhibits a resonance at 19.95 GHz and an unloaded Q-factor of 1000. The response shifted downwards is obtained for an adjustable stub shorter than a quarter-wavelength corresponding to an inductive behaviour of the reactance X_{var} . The response showing a resonance peak above 19.95 GHz corresponds to an adjustable stub longer than a quarter-wavelength providing a capacitance in parallel to the series resonator.

In this plot also, on the left-hand side for the down-shifted resonance, and on the right-hand side for the up-shifted resonance, transmission zeros are observed. They appear for frequencies, at which the adjustable line creates a short circuit in parallel with the series resonator. Also, depending on K and K_{Z1} parasitic resonances might appear on the outside of these transmission zeros. For this reason, in order to preserve the shape of the response, these frequencies of zero transmission shall be far enough away from the resonance peak. Nevertheless, according to (2.5.8), the influence of the adjustable stub is inversely proportional to Z_{var} , and the terms $\frac{1}{Z_{\text{var}}}$ and $\frac{K^2}{Z_{\text{var}}Z_0}$ vanish for large values of the variable impedance. Hence, the smaller the reactance X_{var} , the better is the tunability of the resonance frequency. From that, to ensure both, a good tunability and a well-shaped resonance peak, the ideal value of X_{var} is a small tunable reactance, which does not cancel itself around the resonance frequency. From (2.5.7), this is achieved by choosing the characteristic impedance $Z_{0,\text{as}}$, and more importantly the impedance inverter K_{Z1} , as large as possible. Beyond these parameters, the length of the adjustable stub for both states of the switch plays also a major role. The choice of this length determines both the position of the zeros and the tunability of the filter. These on/off lengths have to be chosen as a trade-off between a satisfactory shape of the resonance peak and the best possible tuning range for the filter.

Concept for the Hybrid Integration of the RF-MEMS Switches

The RF-MEMS switches may be integrated in two different ways onto the micro-machined filters, monolithically or in a hybrid fashion. Nevertheless, because of the 1.6 mm-thickness of the complete filter, it is a challenging task to process MEMS circuits directly on top of the bonded silicon wafers. For this reason, a preferred approach is to integrate the RF-MEMS devices in a hybrid fashion, with the micro-machined cavities and the RF-MEMS processed separately and in parallel. In this case, the adjustable stub is composed of two parts: the microstrip line section directly processed on the top silicon wafer of the filter, and the RF-MEMS tunable stub (Fig. 2.27). The adjustable stubs with the RF-MEMS switches are processed on 300 μm -thick high-resistivity silicon. The silicon chips are placed in cavities diced out of the top silicon wafer, approximately 250 μm away from the micro-machined cavities. They are fixed directly on top of the metal plane processed on the bottom silicon wafer by means of conductive epoxy. The use of conductive glue is necessary to ensure a continuity of the ground plane between the two parts of the microstrip line stub. The microstrip line on the top silicon wafer and the one on the chip are connected using bond-wires. Thanks to the cavity diced out of the top silicon wafer, the length of the bond-wires is kept as small as possible. This allows for a reduction of the parasitic inductance added in series with the microstrip lines. Also, the influence of this unwanted inductance can be further reduced by placing several bond-wires in parallel.

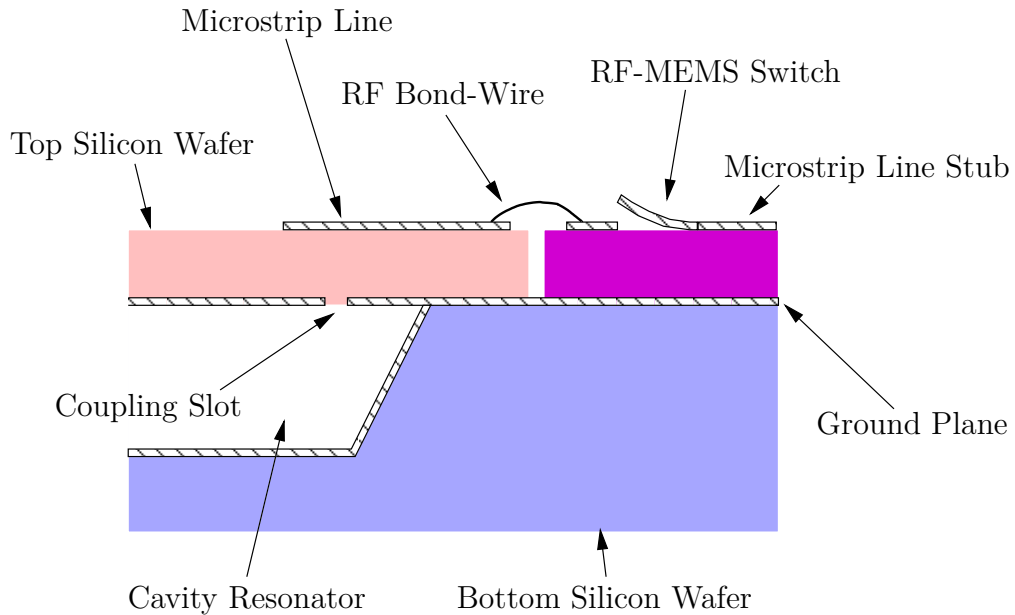


Fig. 2.27: Hybrid integration concept of the RF-MEMS tunable stub on the micro-machined cavity resonator silicon substrate.

The major advantage of this tuning concept is its low complexity. According to the proposed architecture, the RF-MEMS circuits are placed outside the cavity resonators, where they are integrated after the silicon wafers are bonded. This enables a fabrication with independent processes for the micro-machined cavities and the RF-MEMS. Also, the assembly does not require the bonding of silicon dielectrics equipped with MEMS structures, as it would be the case if the RF-MEMS circuits were processed inside the cavities [109]. Between others, it overcomes the issue of the high

bonding temperature for the RF-MEMS circuits. The temperature of about 300°C required for the Au-Au thermo-compression bonding is beyond the temperature sustainable by a large majority of RF-MEMS technologies. This makes the integration of RF-MEMS circuits inside micro-machined cavities a challenging task. In return, the proposed method shows also some limitations, especially in terms of tunability. Due to the distortion of the resonance peak observed when the response is steered, the frequency shift reasonably achievable is limited to 4-5%. It is below the tunability reached by some alternative concepts [103], [54], which are however only suitable for planar structures. Also, the method is based on the coupling of cavity resonators to planar transmission lines. These transmission lines contain switches, bond-wires, and they are fabricated on silicon dielectric. Hence, despite the use of low-loss RF-MEMS switches and high resistivity silicon, they suffer from ohmic, dielectric, and radiation losses, which decrease the Q-factor of tunable cavity resonators.

Design of the Frequency-Agile Filter

One frequency-agile cavity resonator and one 3-pole tunable filter have been designed according to the technique presented above. However, in order to maximise their tunability, these structures have not been designed with one but with two adjustable stubs coupled to each cavity resonator. In this case, for each cavity, the two tunable lines are placed on opposite sides of the cavity resonator as depicted in Fig. 2.28. The use of an additional adjustable stub for each cavity resonator provides a second variable reactance in parallel with the series resonance of the cavity. For this reason, it allows for a larger on/off reactance ratio and results in an increased tuning of the resonance frequency. In return, this increased tunability is at the price of a lower Q-factor for the tunable resonators because of the higher loss dissipated in the two adjustable stubs.

In a first development step, the frequency-agile cavity resonator shown in Fig. 2.28 has been designed.

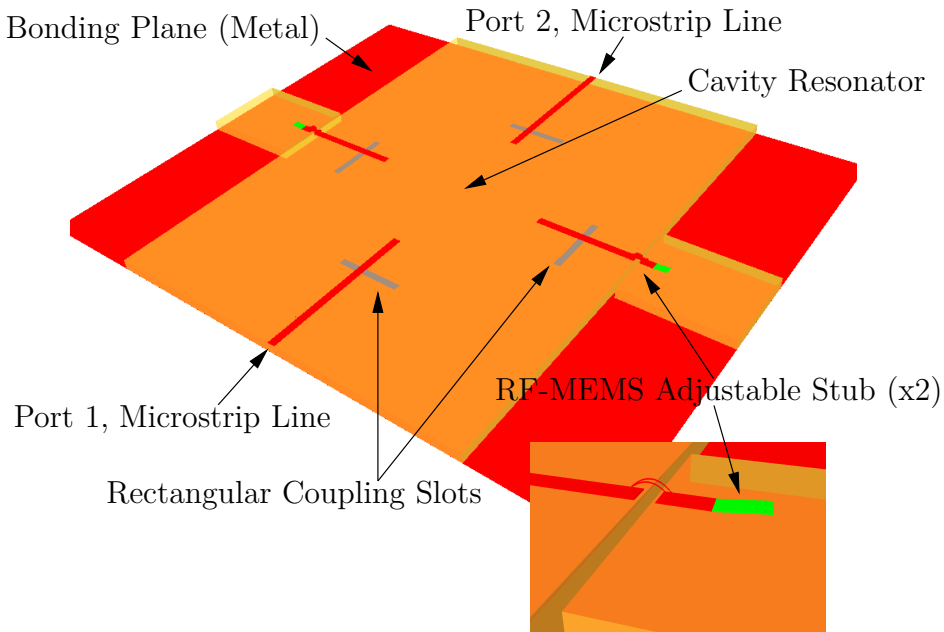


Fig. 2.28: 3D view of the 2-port frequency-agile micro-machined cavity resonator.

The resonator is made tunable by two adjustable stubs coupled to the cavity through rectangular coupling slots. For the design of this cavity resonator however, RF-MEMS cantilevers were used instead of the previously mentioned switches. The RF-MEMS cantilevers are $400\mu\text{m}$ -long, and in the upstate they are bent $40\mu\text{m}$ above the substrate. They are actuated electrically in the same way as the RF-MEMS switches. In this case, the variation of the electrical length is only achieved by changing the effective dielectric constant of the microstrip cantilever. RF-MEMS cantilevers have the advantage of being easier to process than RF-MEMS switches. In return, they have only a limited influence on the electrical length of the stub and are for this reason more appropriate for trimming than for wide range tuning. In the presented design, the reconfigurable microstrip lines as well as the input/output transmission lines are coupled by $2000\mu\text{m}$ -long and $200\mu\text{m}$ -wide rectangular coupling slots. These slots are all placed $1218\mu\text{m}$ away from their respective adjacent side-wall.

The second tunable structure based on the same principle is a 3-pole Tchebycheff band-pass filter (Fig. 2.29). Contrary to the single cavity resonator, the 3-pole filter is made steerable with RF-MEMS switches. It is designed with H-shaped coupling slots for both, the input/output couplings and the couplings of the adjustable microstrip stubs. The coupling slots for the input/output microstrip lines are $3300\mu\text{m}$ -long and $500\mu\text{m}$ -wide. They are patterned $1004\mu\text{m}$ away from their respective side-wall. The other coupling slots for the adjustable microstrip lines are all identical.

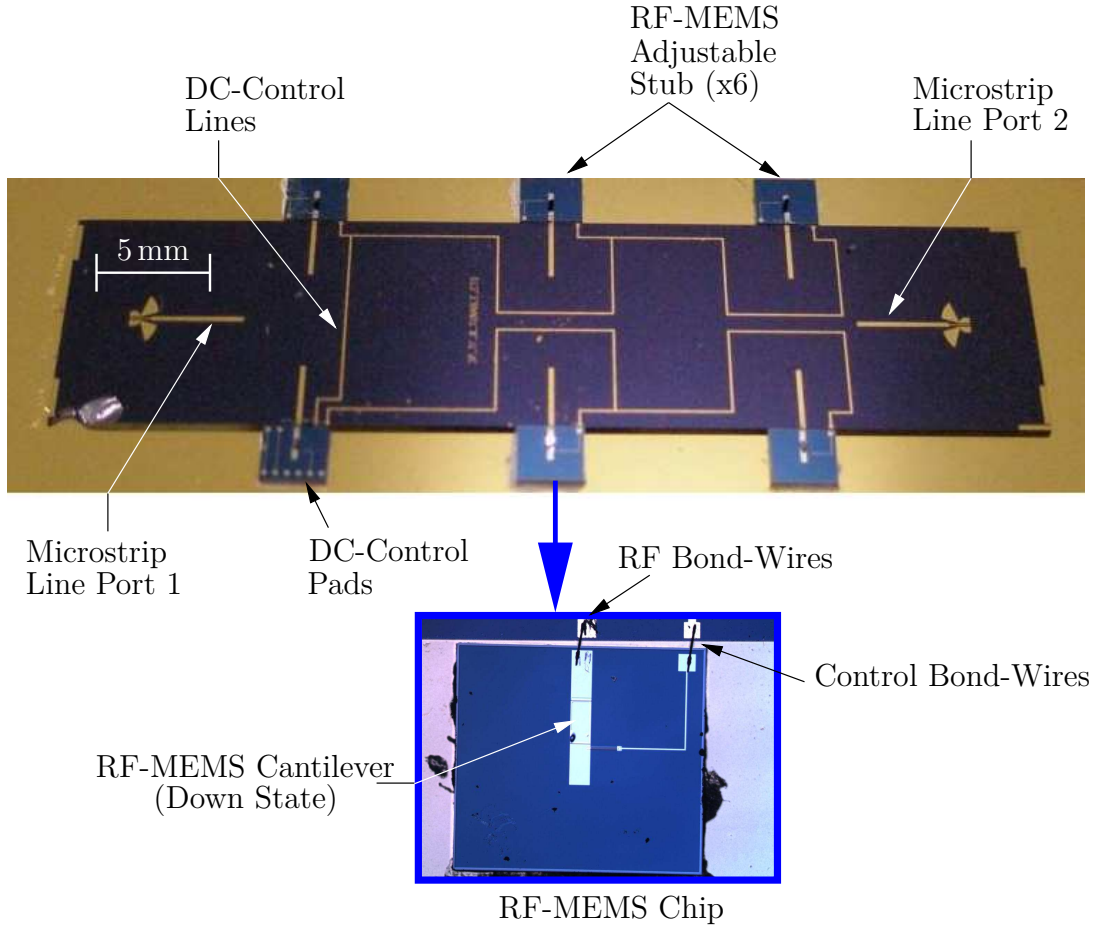


Fig. 2.29: Photograph of the 3-pole frequency-agile filter micro-machined in silicon.

They are 2000 μm -long and 200 μm -wide, and they are placed 1222 μm away from their respective adjacent side-wall. In this design, H-shaped coupling slots have been chosen because they allow for stronger couplings between the microstrip lines and the cavity resonators. Also, according to (2.5.7) and (2.5.8), strong couplings favour the tuning range of the filter and preserve the shape of the response around the pass-band. Further, for a given coupling coefficient, the area that has to be left free from metal is smaller for H-shaped slots than for rectangular slots. Hence, H-shaped slots optimise the loss in the coupling structures, and lead to better Q-factors of coupled cavity resonators.

The two inter-resonator coupling cavities are 2000 μm -long and 4492 μm -wide. Also, the first and last cavity resonators are identical and are 10470 μm -long and 10000 μm -wide. The middle cavity resonator is slightly smaller. It is only 10000 μm -long to compensate for the electrical lengths of the two coupling cavities. Finally, the fixed part of the adjustable stubs is 1261 μm -long (approximately $\lambda_g/4$ at the design frequency), and their length can be adjusted in one step between 2566 μm and 3566 μm on the adaptive side.

Measurement and Simulation Results

Both, the tunable cavity resonator and the 3-pole frequency-agile filter have been simulated with the commercial electromagnetic simulator EMPIRE. Nevertheless, within the limited time frame of this work, it was impossible to fabricate both structures, and the choice has been made to manufacture only the 3-pole filter. For this reason, by the time this thesis was written, only simulated responses were available for the tunable cavity resonator. The response of that cavity resonator simulated for both, the up- and the downstate of the RF-MEMS switches, is plotted in Fig. 2.30. On the other hand, because of the large size of the tunable filter and the numerous geometrically small details in the structure, the full-wave simulations of the 3-pole structure have been found to be somewhat inaccurate and laborious. Thus, for this filter most of the design has been performed analytically and no acceptable simulated response could be presented here. In return, the filter was successfully measured on-wafer and the measured steered responses are shown in Fig. 2.31 and 2.32.

The response simulated for the tunable cavity resonator and plotted in Fig. 2.30 exhibits a resonance peak at 19.65 GHz when the cantilevers are left in the upstate, and 19.93 GHz when they are actuated down. This shift of the resonance frequency corresponds to a tuning range of 280 MHz (1.4%). It is relatively modest in regards to what is expected for the tunable filter. As already mentioned, this limited tunability is justified by the use of RF-MEMS cantilevers for adjusting the microstrip stubs, and by the implementation of rectangular slots for their coupling to the cavity. Further, as one can see on the left-hand part of the graph in Fig. 2.30, the transmission zeros and parasitic resonances observed and discussed with the schematic (Fig. 2.25 and 2.26) are also visible in the full-wave simulation. For the cavity resonator presented here, the parasitic resonances appear at 17.99 GHz in the "downstate" response, and 22.42 GHz in the "upstate" response. The amplitude of these resonances are -14.6 dB and -26.4 dB in the two configurations, respectively.

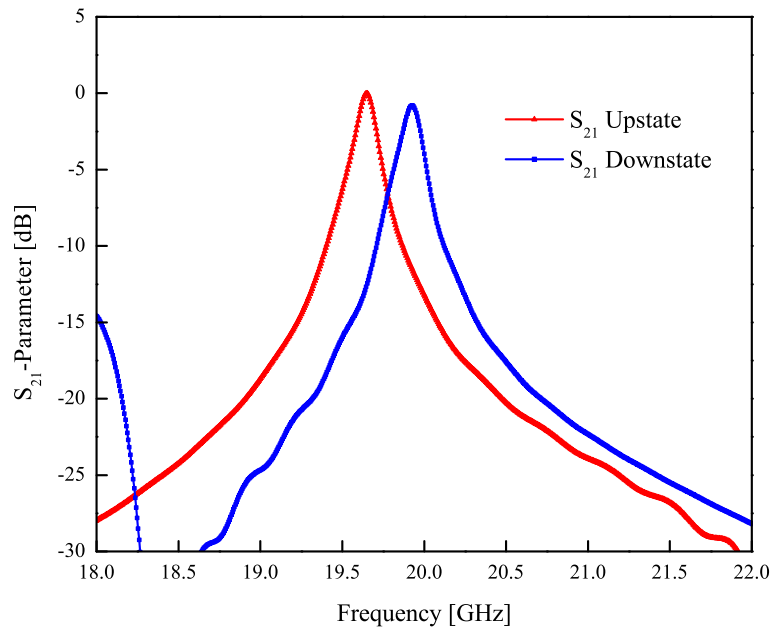


Fig. 2.30: Response of the tunable cavity resonator simulated for open/closed RF-MEMS switches.

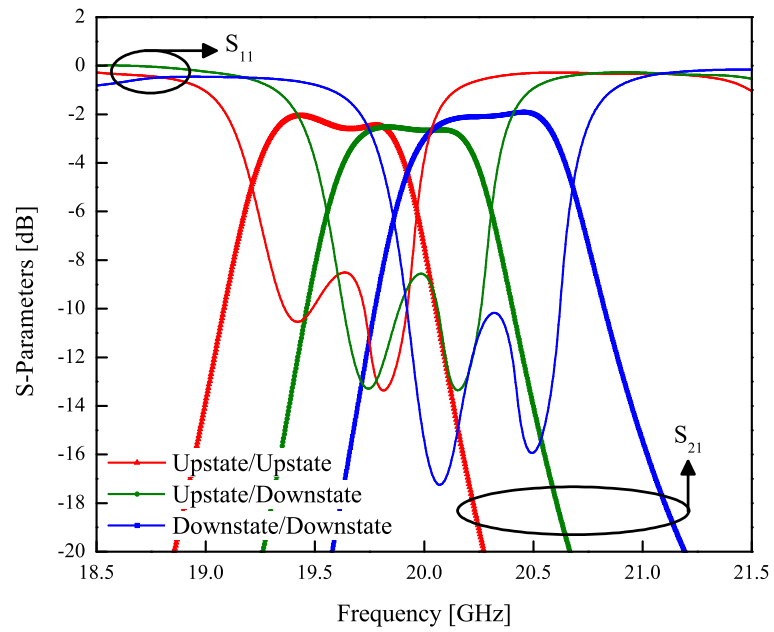


Fig. 2.31: Measured response of the 3-pole frequency-agile band-pass filter.

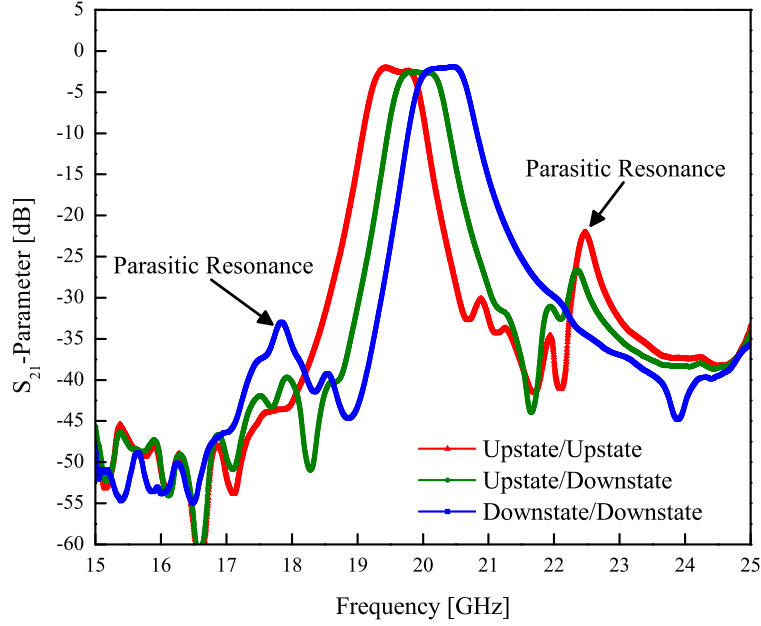


Fig. 2.32: Measured response of the 3-pole frequency-agile band-pass filter - wideband plot.

The graphs in Fig. 2.31 and 2.32 show the filter responses corresponding to the three possible switching states of the 3-pole filter. The three plots referred to as "upstate/upstate", "upstate/downstate", and "downstate/downstate", indicate the position of the RF-MEMS switches on the two sides of the filter. The curve named "upstate/upstate" corresponds to the response of the filter when all the six switches are left open. The curve designated "upstate/downstate" is the filter response achieved when three switches, all on the same side of the filter, are actuated down. Finally, the plot named "downstate/downstate" is the response of the filter measured when all the switches are closed. Among the six switches mounted in the filter, all the switches placed on a same side of the filter, top or bottom, have to be actuated together and at the same time. This grouped actuation of the switches is mandatory to ensure that all cavity resonators exhibit their resonance at the same frequency. This is necessary to achieve a satisfactory shape for the filter response in the pass-band.

In Fig. 2.31, the plots show well-formed pass-band filter responses steered around 20 GHz. For a configuration of the filter with all the switches open, i.e. the adjustable stubs are shorter than $\lambda/4$, the filter response shows a pass-band centred at 19.57 GHz. In this case also, it has an in-band ripple of 0.6 dB, slightly above the 0.3 dB of ripple allowed by the requirements in Table 2.2. The bandwidth of the response measured at that same level is 500 MHz (2.55%). It corresponds exactly to the expected bandwidth specified however at -0.3 dB. In the second switching configuration when three switches are actuated down, the filter response is steered up to 19.94 GHz. This centre frequency measured for the middle state is close to the targeted frequency specified at 19.95 GHz. Finally, for the third switching state when all switches are closed, the filter shows a response with a pass-band centred at 20.31 GHz. These three frequencies measured for the three states of the filter correspond to a satisfactory tuning range of 0.74 GHz (3.71%). It is nevertheless sensibly below the

challenging tuning range of 1 GHz (5%) targeted for the filter. In the three switching configurations, the filter exhibits an almost constant bandwidth close to the goal bandwidth of 500 MHz. When all the switches of the filter are closed, the bandwidth is 520 MHz (2.56%). In the "upstate/downstate" configuration, it is exactly 500 MHz (2.51%) as well as in the "upstate/upstate" configuration. Further, the in-band insertion loss of the filter is 2 dB/2.5 dB/1.9 dB, in the "upstate/upstate", "upstate/downstate", and "downstate/downstate" configurations, respectively. These levels of in-band insertion loss are approximately 0.5 to 1 dB above what was allowed for the filter. However, they correspond to satisfactory unloaded Q-factors of 332/271/348 for each tunable cavity resonator and for the three states of the filter. For any switching state, the return loss in the pass-band is better than 8 dB. Finally, as previously mentioned and as shown in Fig. 2.32, the steered filter responses have transmission zeros and parasitic resonances in the neighbourhood of the pass-band. However, for the demonstrated filter they are relatively far from the pass-band, 12% below and 10% above the resonance peaks. Also, the amplitude of these parasitic resonances is rather small and below -22 dB for the highest resonance.

2.6 Fixed and Tunable Substrate-Integrated Cavity Resonator Filters at 15 GHz in LTCC

2.6.1 Motivations and Targeted Application for LTCC Filters in Ku-Band

The fixed-frequency and tunable filters presented in the next sections have been developed for Unmanned Air Vehicle (UAV) military data-link at Ku-band. They are foreseen for integration on both sides of the communication link: on-board of UAV and in the control station on ground. They aim at replacing interdigital filters, which have been successfully implemented up to now as Local Oscillator (LO) filters of UAV transceivers. Nevertheless, these filters are the largest components of the front-end, and they represent now a bottleneck for a further size reduction of the complete system. As the next generation of products will require improved performance and reduced size, the newly developed filters have been chosen to be realised in LTCC. The LTCC technology allows for 3D-integration of different components in the same ceramic board, and it offers the advantage of being low-cost for large fabrication scale. Further, thanks to recently developed low-loss ceramic tapes like DuPont 943, satisfactory RF-performance is expected for the filters.

The electrical specifications of the fixed-frequency filter are defined by the communication channel used for the data-link. These specifications are listed in Table 2.6.

Parameter	Value
Centre Frequency F_0	15 GHz
3 dB Bandwidth ΔF	800 MHz
Insertion Loss IL in 200 MHz	<0.5 dB
In-Band Return Loss	16 dB
Out-of-Band Rejection at 12.6 GHz	>24 dB

Table 2.6: Electrical specifications of the fixed-frequency LTCC filter.

The out-of-band rejection given in this table aims at filtering the second harmonic of the LO of the transceiver working at 6.3 GHz. Also, in order to assess the opportunity of a frequency-agile filter integrated in LTCC, the specifications of a 2-state tunable filter have been derived from those of the fixed-frequency filter. These specifications are given in Table 2.7 for the two states of the filter.

Parameter	Value State 1	Value State 2
Centre Frequency F_0	15.6 GHz	16.0 GHz
3 dB Bandwidth ΔF	800 MHz	800 MHz
Insertion Loss IL in 200 MHz	<0.5 dB	<0.5 dB
In-Band Return Loss	16 dB	16 dB
Out-of-Band Rejection:		
13.2 GHz	>24 dB	–
13.6 GHz	–	>24 dB

Table 2.7: Electrical specifications of the frequency-agile LTCC filter.

2.6.2 Fixed-Frequency Filter

Design of the Fixed-Frequency Filter

The fixed-frequency band-pass filter is designed with two inductively coupled cavity resonators. The cavity resonators are realised in LTCC according to the Substrate-Integrated Waveguide (SIW) technique [110], [36]. Each cavity resonator is closed on its top and bottom sides by fully metallised planes. The side-walls of the cavities are designed with rows of vias manufactured in LTCC. The vias connect the top and bottom metal planes of the cavities. They are separated by a pitch of $513\mu\text{m}$ (approx. $1/14\lambda_d$ at 15 GHz). Also, these vias are connected together using metal stripes patterned between the LTCC layers, which the vias traverse. The stripes connecting the vias are separated by one $110\mu\text{m}$ -thick layer of LTCC. These stripes and the vias form a 2-dimensional grid. This design of the side-walls aims at the realisation of electrical boundaries, which are as dense as possible to prevent the electromagnetic field from propagating outside the cavity. The cavity resonators are five $110\mu\text{m}$ -thick LTCC layers deep ($550\mu\text{m}$).

The filter was designed using the low-pass to band-pass transformation technique already used for the previously presented micro-machined filters [34]. The filter is a 2-pole Tchebycheff filter with 0.5 dB of in-band ripple. The coefficients of the low-pass prototype filter as well as the electrical parameters of the band-pass filter are given in Table 2.8. The electrical parameters, external Q-factors and coupling inductance, have been calculated using successively (2.4.14), (2.4.15), (2.4.16), and (2.4.19), in the same way as for the micro-machined filters presented in section 2.5.

In a first step, the behaviour of a single 2-port cavity resonator was investigated. The cavity resonator is inductively coupled to input and output 50Ω lines. These input/output transmission lines are microstrip lines buried in LTCC, one layer below the metal plane closing the cavity on its top side. Also, the ground plane of the buried microstrip lines is formed by an extension of that same top metal plane.

Parameter	Value
Low-Pass Prototype Filter	
$(g_0; g_1; g_2; g_3)$	(1; 1.4029; 0.7071; 1.9841)
Band-Pass Filter	
$(Q_e)_A$	42.512
$(Q_e)_B$	(made symmetric) 42.512
$\frac{X_{1,2}}{Z_0}$	0.1063

Table 2.8: Coefficients of the low-pass prototype filter and electrical parameters of the 2-pole substrate-integrated band-pass filter.

The lines are led into the cavity resonator through openings realised in the rows of vias forming the side-walls of the cavity. The coupling itself is achieved using vias processed inside the cavity resonator. These so-called "coupling vias" are parallel to the adjacent side-wall of the cavity resonator. They are realised between the end of the input/output lines, and the bottom of the cavity. A 3D view of the described coupling structure is shown in Fig. 2.33.

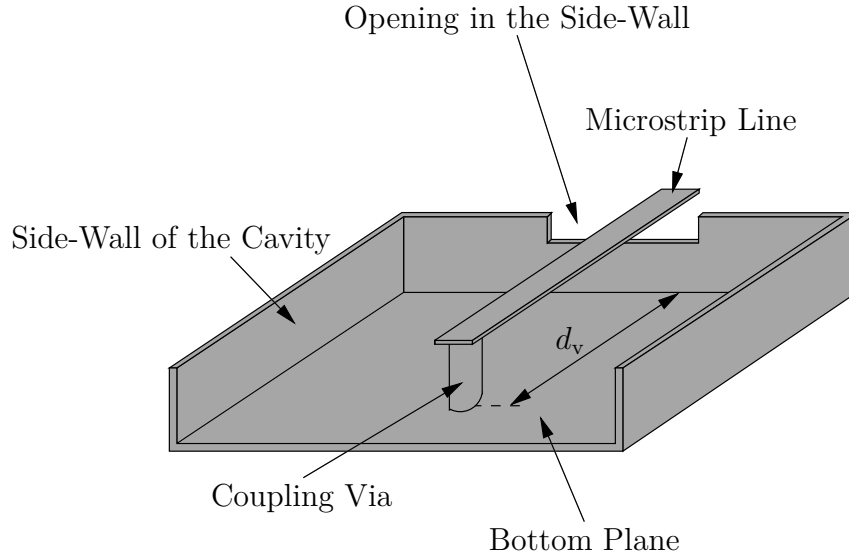


Fig. 2.33: 3D view of the input/output coupling structure of the substrate-integrated cavity resonator (top plane removed and side-walls idealised).

There are different configurations possible for the design of the coupling via. Depending on the desired coupling, the via can be long (up to 440 μm) or short (no via), and it can be placed at various distances from the side-wall of the cavity. In order to reduce the number of possibilities to study, the maximum length of 440 μm has been chosen for the coupling via. This configuration has been selected because it allows for a very wide range of achievable coupling coefficients. Also, since the length of the coupling via is fixed, the coupling coefficient is controlled by the position of the via inside the cavity. For design purposes, the 2-port cavity resonator has been simulated for different positions of the input/output coupling vias. The 1-port external Q-factor has been calculated from the simulated S_{21} -parameter using successively (2.4.12), (2.4.13), (2.4.11), and (2.4.10).

It is plotted versus the position of the coupling via in the cavity resonator in Fig. 2.34.

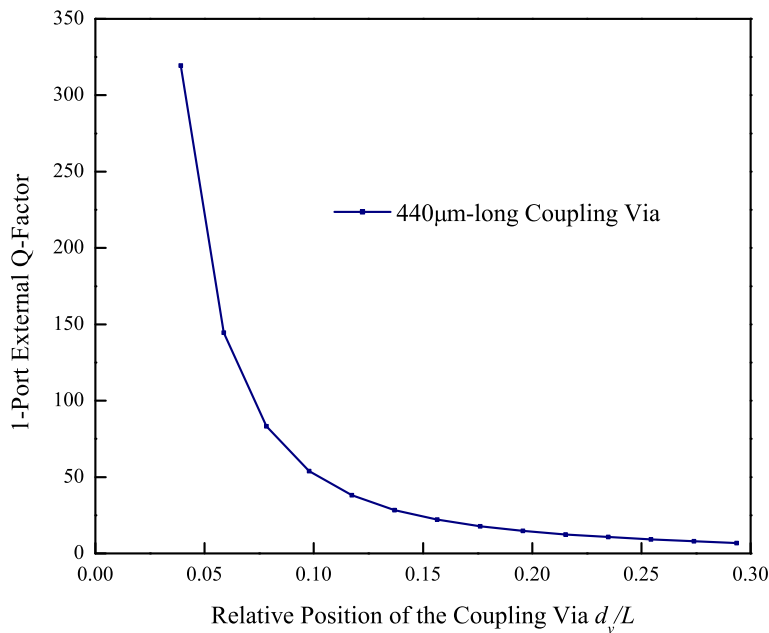


Fig. 2.34: Value of the 1-port external Q-factor versus via position.

These values calculated for the external Q-factor are valid for coupling vias placed on the axis of symmetry of the cavity resonator. The position of the coupling via is referenced by the distance d_v between the centre of the coupling via and the side-wall of the cavity (Fig. 2.33). In the plot, this distance is normalised to the length L of the cavity resonator. The calculations have been performed for a diameter of $120\mu\text{m}$ for the coupling via. However, further simulations have highlighted the relatively low influence of that diameter on the coupling coefficient. Further, in order to be able to calculate the position of the coupling via $\frac{d_v}{L}$ corresponding to a targeted external Q-factor, the simulated values have been interpolated with a 4th order polynomial. It is given by

$$\begin{aligned} \frac{d_v}{L} = & 0.44791312 - 0.28613651 \cdot 10^{-1} \cdot (Q_{e,1/2}) + 0.92755911 \cdot 10^{-3} (Q_{e,1/2})^2 \\ & - 0.11009298 \cdot 10^{-4} (Q_{e,1/2})^3 + 0.26210014 \cdot 10^{-7} (Q_{e,1/2})^4. \end{aligned} \quad (2.6.1)$$

The 2-pole filter is designed with two cavity resonators juxtaposed such that they have exactly one entire side-wall in common. The two cavities are coupled through an inductive iris opened in the row of vias forming the inter-cavity wall. This inductive iris is similar to apertures commonly implemented to couple resonators in waveguide filters. However, due to the diameter of the vias, and more importantly due to the width of the metal stripes connecting them (approx. $200\mu\text{m}$), the iris is thick. For this reason, the achieved coupling is weaker than that obtained for a thin iris having the same width. The S_{21} -parameter of the iris has been calculated for various openings using full-wave simulations. The inductance $\frac{X}{Z_0}$ calculated from the simulated S_{21} using (2.5.4) is plotted against the relative width of the iris $\frac{W_1}{A}$ in Fig. 2.35.

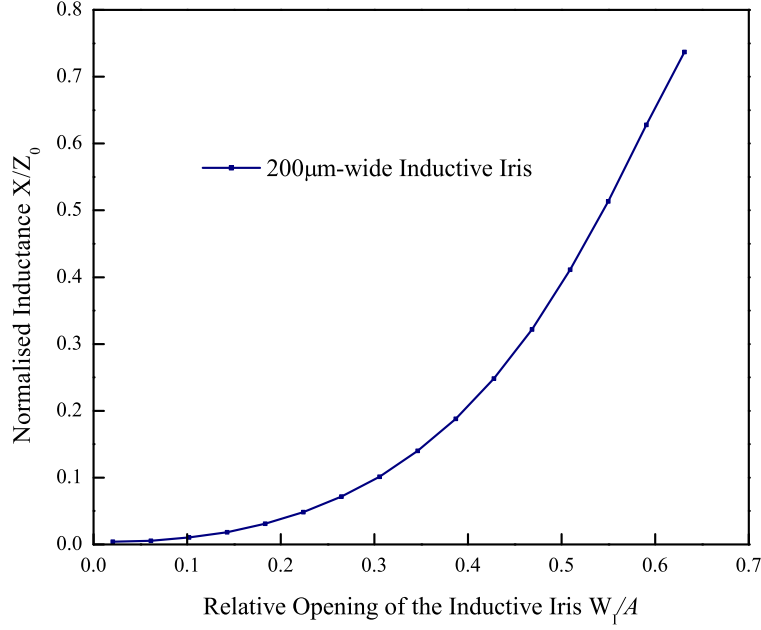


Fig. 2.35: Value of the normalised inductance achieved by the thick inductive iris.

In this plot, the discrete values obtained by simulations have been interpolated with a 4th order polynomial given by

$$\begin{aligned} \frac{W_I}{A} = & -0.20802512 \cdot 10^{-1} + 10.62321824 \cdot \left(\frac{X}{Z_0}\right) - 102.18347231 \left(\frac{X}{Z_0}\right)^2 \\ & + 314.17192547 \left(\frac{X}{Z_0}\right)^3 - 262.51797656 \left(\frac{X}{Z_0}\right)^4. \end{aligned} \quad (2.6.2)$$

(2.6.1) and (2.6.2) are the design equations of the substrate-integrated filter presented here. They are used together with the electrical parameters given in Table 2.8 to determine the dimensions of the coupling structures of the band-pass filter. From this, the position of the input and output coupling vias is $\frac{d_v}{L}=0.122$, and the relative width of the inductive iris is $\frac{W_I}{A}=0.297$. A 3D view of the 2-pole substrate-integrated filter showing the E_y -component of the electromagnetic field at the design frequency of 15 GHz is given in Fig. 2.36.

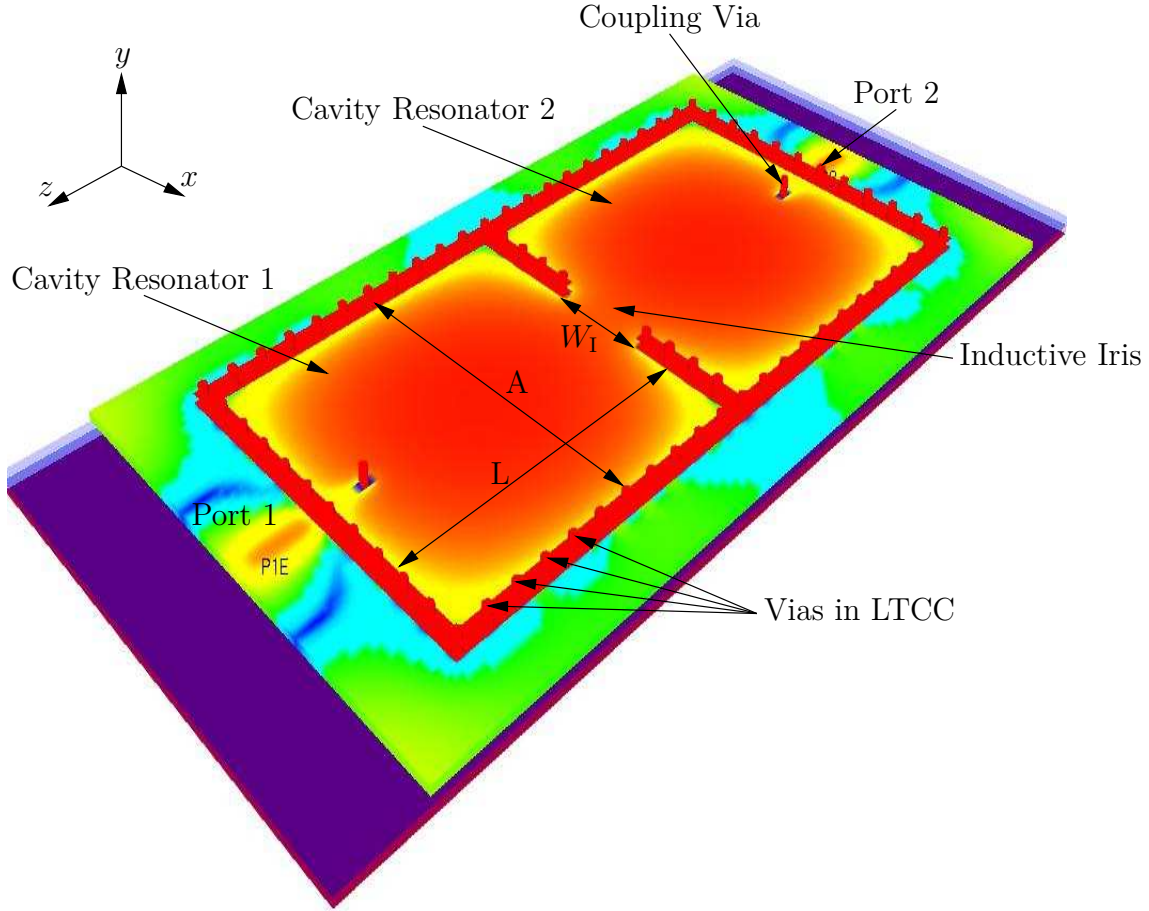


Fig. 2.36: 3D view of the 2-pole substrate-integrated filter with the E_y -field component at 15 GHz (top metal plane removed).

Characterisation and Measurements

In order to measure the structures using 250 μm -pitch coplanar measurement probes, a buried microstrip line to coplanar transition has been designed. The transition is realised with one via processed in the uppermost LTCC layer, between the buried microstrip line and the centre conductor of the coplanar line. The transition can be de-embedded using TRL calibration standards. However, the subsequent measurements were performed using SOLT calibration at the probes tips, and the transitions are included in the measured S-parameters. Firstly, a square cavity resonator of length $A=L=5431 \mu\text{m}$ has been realised and measured. Also, in order to calculate its unloaded Q-factor with a good accuracy, the cavity is weakly coupled in input and output, and the coupling vias are only 110 μm -long. The S_{21} -parameter measured around the resonance peak is shown in Fig. 2.37.

The measured resonance peak of the cavity resonator is at 15.25 GHz. It is 890 MHz (5.8%) above the theoretical resonance frequency of 14.36 GHz calculated for an ideal cavity resonator having the same dimensions. This frequency shift can be explained by the influence of different phenomena. The first source of inaccuracy are the fabrication tolerances of the structures. Nevertheless, the shrinkage of LTCC, 9.4%-10% for DuPont 943, is a well-controlled mechanism. It is compensated

by up-scaling the layout before patterning the metal structures on LTCC. In most cases, this compensation, calculated here at 9.6% by the manufacturer, allows for a limited residual shrinkage. The resulting shrinkage is generally about $100\mu\text{m}$ - $150\mu\text{m}$ measured along the diagonal of the entire 4" LTCC wafer. Another possibility could be an inaccuracy in the value used for the dielectric constant of the ceramic material. However, the dielectric constant of DuPont 943 has been intensively investigated in the literature [68], [67], and it is not expected to be responsible for such a frequency shift. The last effect is due to the via-based input/output coupling structures. The coupling vias are designed inside the cavity resonator at a certain distance (here $442\mu\text{m}$) from the side-walls of the cavity. The vias are parallel to the electric field of the TE_{101} -mode, and they reduce the effective electrical length of the cavity resonator. Nevertheless, this phenomenon does not constitute a limitation of the proposed coupling technique, as long as it is taken into account when designing the structures. The unloaded Q-factor calculated from the measured S_{21} -parameter is $Q_u=290$. This value is in good agreement with the theoretical Q-factor of 284.6, calculated from $\tan\delta=0.0015$ for the ceramic dielectric and $\sigma=4.09\text{e}7\text{ S/m}$ for the Au-metallisation.

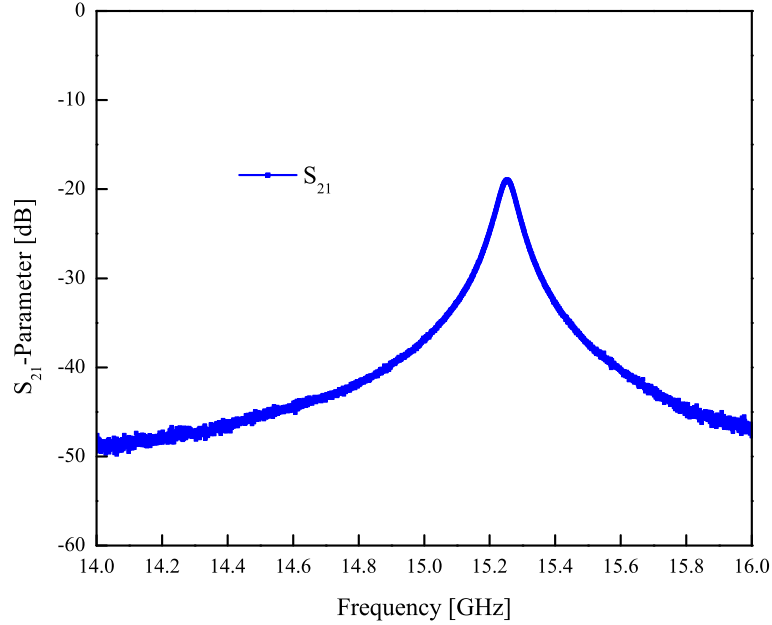


Fig. 2.37: Resonance peak of the weakly coupled substrate-integrated cavity resonator.

The response of the 2-pole band-pass filter has been measured in the same way as the 2-port cavity resonator. The measured S_{11} and S_{21} -parameters of the filter response are plotted in Fig. 2.38. The measured filter response has a pass-band centred at 15.09 GHz, 0.6% above the targeted centre frequency of 15 GHz. The bandwidth of the filter response 3 dB below the transmission maximum is 813 MHz (5.39%). It is only 13 MHz wider than the bandwidth required in Table 2.6, at that same attenuation level. Finally, the return loss is better than 13.8 dB and the minimum in-band insertion loss is about 1 dB. From (2.5.6), this in-band insertion loss corresponds to an unloaded Q-factor of $Q_u=160$ for the two substrate-integrated resonators. This unloaded Q-factor is too low

to meet the requirement of 0.5 dB of insertion loss for the filter. This situation can be overcome by implementing resonators with higher Q-factors like air-filled cavity resonators. This solution would however result in a larger filter.

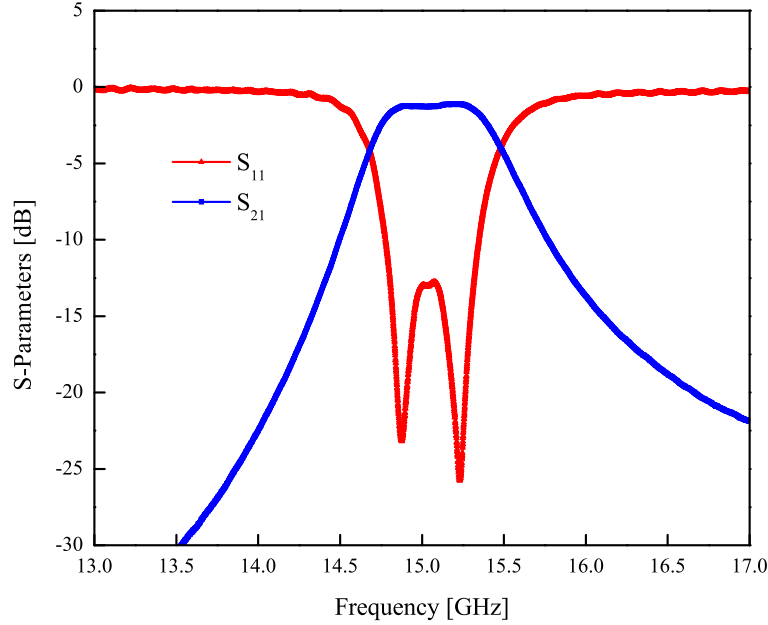


Fig. 2.38: Measured response of the 2-pole substrate-integrated cavity resonator filter.

2.6.3 Frequency-Agile Filters

The fixed-frequency substrate-integrated filter is used as starting-point for the development of the frequency-agile filter. The specifications of the tunable filter were presented previously in Table 2.7. The tunable filter is a 2-pole filter. It aims at the same response as the fixed-frequency filter but steerable in one 400 MHz-step between 15.6 GHz and 16.0 GHz. Nevertheless, in order to assess the performance achievable with the proposed tuning technique, two frequency-agile filters are presented in the coming sections. They are based on a tuning concept similar to the technique introduced for the frequency-agile micro-machined filters.

Tuning Concept and Hybrid Integration of the RF-MEMS Devices

For both filters, the response is tuned by means of adjustable stubs coupled inductively to the cavity resonators. The adjustable stubs are coplanar lines. They are realised in two parts processed separately on the LTCC substrate and on silicon chips. The electrical length of the stubs is controlled electrically by actuating RF-MEMS cantilevers processed on silicon. The RF-MEMS cantilevers are 400 μm -long and the silicon chips are made out of 300 μm -thick high resistivity silicon dielectric. The silicon chips are integrated in a hybrid fashion in cavities processed in LTCC. These cavities are approximately 200 μm away from the cavity resonators. The metal structures patterned on the silicon chips are connected to the metal lines on LTCC by means of Al bond-wires. These

bond-wires are kept as short as possible by manufacturing the cavities with a three LTCC layer depth ($330\mu\text{m}$). This compensates well the thickness of the silicon chips once they are fixed on about $100\mu\text{m}$ of conductive epoxy glue. The DC-control lines necessary to actuate the RF-MEMS circuits are designed in free layers of the LTCC substrate. They connect bond-pads placed near the RF-MEMS chips to a foot-print, on which the actuation signals are applied. The DC-control pads on LTCC and the bias pads on silicon are connected using Al bond-wires as for the RF signal. A cross-sectional drawing of the LTCC board with the RF-MEMS chips is depicted in Fig. 2.39.

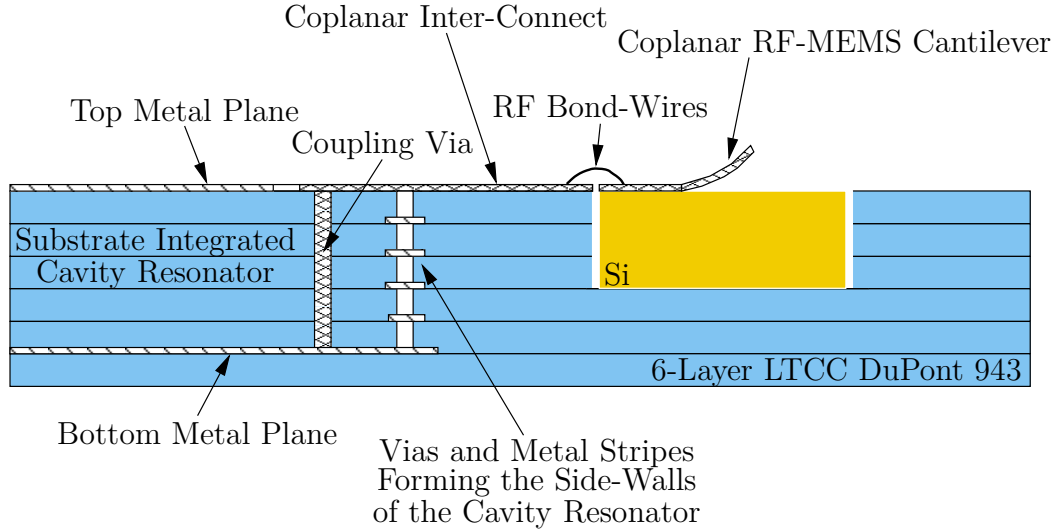


Fig. 2.39: Hybrid integration concept of the coplanar RF-MEMS cantilevers on the LTCC substrate.

Design of the Frequency-Agile Filters

One 2-port cavity resonator and two tunable filters have been realised according to the tuning technique described here. The single cavity resonator and the first filter are designed with one adjustable stub per cavity resonator. The second filter aiming at an increased tuning range is designed with two adjustable coplanar stubs for each cavity resonator. For these filters, RF-MEMS cantilevers have been preferred to switches because they are easier to produce, and they offer a satisfactory tuning range sufficient for the required specifications. Depending on the state of the RF-MEMS cantilevers, the impedance seen by the cavity resonator is capacitive or inductive, and the resonance frequency is shifted upwards or downwards, respectively. The length of the adjustable stubs in both the up- and the down-state has been optimised using full-wave simulations to take the influence of the bond-wires into account. The dimensions are summarised in Table 2.9.

The structure used to couple the adjustable stubs is similar to the coupling vias implemented in input/output of the filters. Nevertheless, since the adjustable stubs are on top of the LTCC substrate (Fig. 2.39), these vias are $110\mu\text{m}$ (one LTCC layer) longer than the input/output vias. Also, in order to achieve a large tuning range, the vias of the adjustable stubs are designed to achieve a strong coupling with the cavity resonators (2.5.7), (2.5.8). This is implemented by placing them $890\mu\text{m}$ away from the side-walls of the cavities for the first filter, and $690\mu\text{m}$ for the second filter. From the graph in Fig. 2.34, these distances correspond to external Q-factors of about 15, for a

via that is nevertheless $110\text{ }\mu\text{m}$ shorter. This strong coupling between the cavity resonators and the tuning stubs is chosen to favour the tunability of the filters, which is however at the price of larger insertion loss.

Parameter	Coplanar line on LTCC	Coplanar line on Si (Downstate)
Line Gap G	$100\text{ }\mu\text{m}$	$224\text{ }\mu\text{m}$
Line Width W	$90\text{ }\mu\text{m}$	$208\text{ }\mu\text{m}$
Line Length	$1160\text{ }\mu\text{m}$ (1 st filter), $960\text{ }\mu\text{m}$ (2 nd filter)	$620\text{ }\mu\text{m}$ (both filters)

Table 2.9: Dimensions of the coplanar adjustable stubs of the LTCC tunable filters.

A photograph of the two frequency-agile filters is shown in Fig. 2.40. The filter with one adjustable stub per cavity resonator is shown on the left-hand side of the photograph. The filter with enhanced tunability and with two adjustable stubs per cavity resonator is shown on the right-hand side. A micrograph of the RF bond-wire connection between the lines patterned on LTCC, and the RF-MEMS structures processed on silicon is depicted on the lower part of the picture.

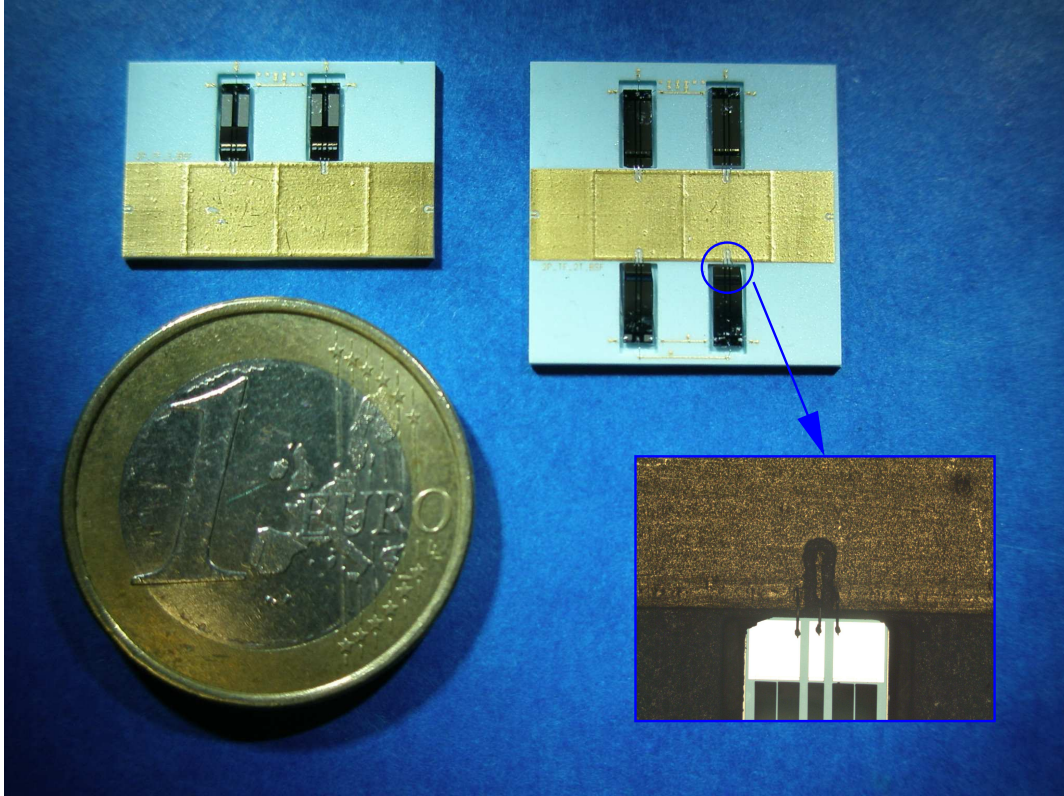


Fig. 2.40: Photograph of the RF-MEMS frequency-agile filters on LTCC DuPont 943.

Characterisation and Measurements

The frequency-agile cavity resonator and 2-pole filters have been measured using a setup similar to the one used for the fixed-frequency LTCC filter. In the present case however, the on-wafer probing station was equipped with a DC-wedge enabling the control of the RF-MEMS circuits. The S_{21}

parameter measured for the cavity resonator and for the two states of the RF-MEMS cantilever is shown in Fig. 2.41. The measured responses of the tunable filters are plotted in Fig. 2.42 and 2.43 for the filter with one adjustable stub per cavity resonator, and in Fig. 2.44 for the filter with two adjustable stubs per cavity resonator.

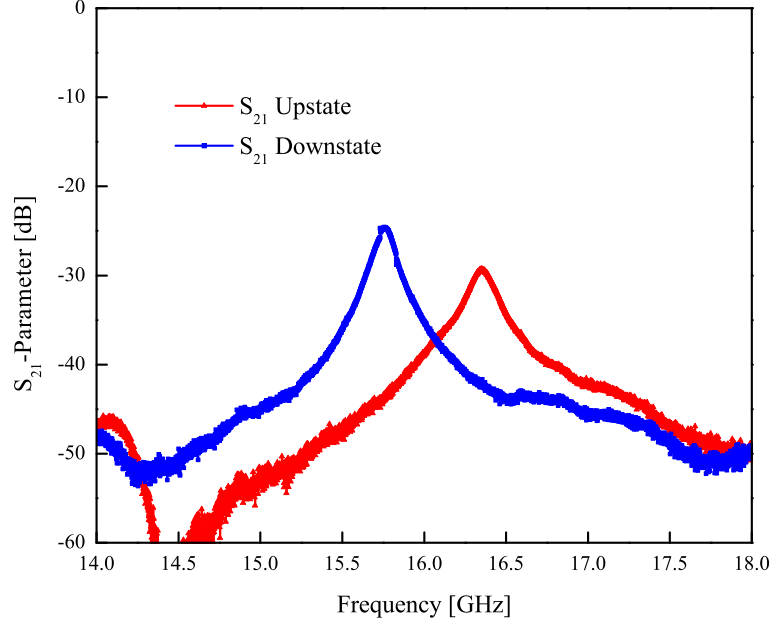


Fig. 2.41: Response of the tunable substrate-integrated cavity resonator with one adjustable stub.

The resonance peak of the cavity resonator is shifted from 15.77 GHz for the cantilever in the down-state to 16.37 GHz, when it is in the up-state. The unloaded Q -factor of the resonator calculated from the measured S_{21} parameter is 115.4 in the down-state, and 81.0 in the up-state (2.4.12), (2.4.13). These values of the unloaded Q -factor are considerably below the Q -factor measured for the fixed-frequency resonator. This increased loss in the resonator is justified by the power dissipated in the planar transmission lines, but also most probably by a sub-optimal realisation of the RF bond-wire connection.

The graphs plotted in Fig. 2.42 and 2.44 show well-formed filter transfer functions. For the filter realised with one adjustable stub per cavity resonator, the filter response is tuned over 3% (446 MHz). The filter designed for enhanced tunability has a tuning range that is greater than twice the tuning range of the first filter: 7.2% (1077 MHz). The 3 dB bandwidth of the filters is about 4.8% for the first filter and 4.3% for the enhanced filter. For both filters, these bandwidths are rather constant when the responses are tuned over frequency. Finally, the measured insertion loss are 3.1/4.0 dB and 5.7/5.0/4.7 dB for the first and second filter, respectively. This level of in-band insertion loss is above the 0.5 dB of loss allowed for the filter. It is also nearly 3 to 4 dB above the insertion loss measured for the fixed-frequency filter. As previously mentioned, this increased loss level for the tunable filters was expected, and it is due to the loss dissipated in the tuning structures. Further, as presented in section 2.5.3, the filters made steerable according to the proposed tuning

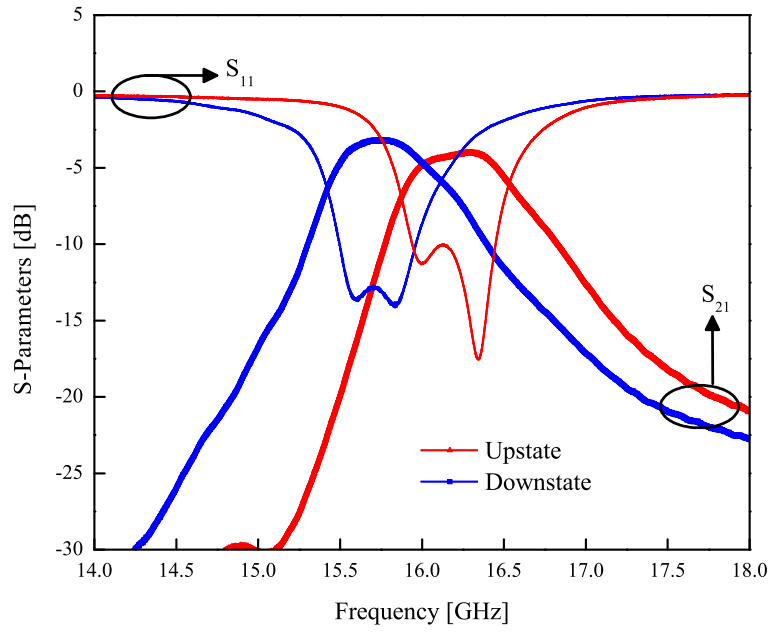


Fig. 2.42: Response of the tunable LTCC filter with one adjustable stub per cavity resonator.

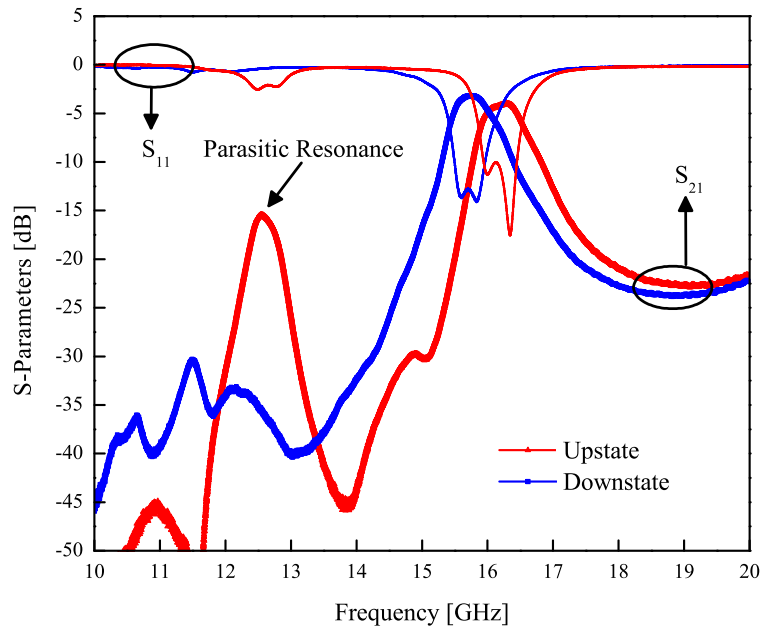


Fig. 2.43: Response of the tunable LTCC filter with one adjustable stub per cavity resonator - wideband plot.

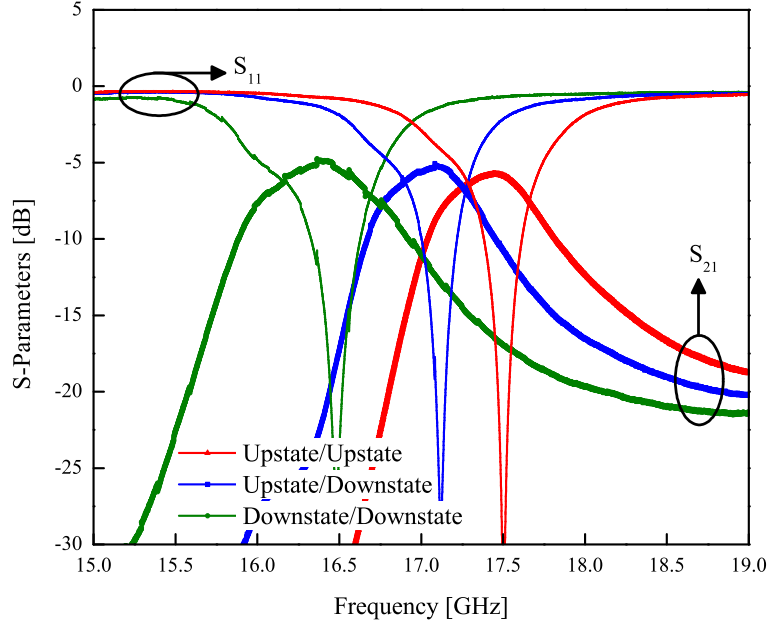


Fig. 2.44: Response of the tunable LTCC filter with two adjustable stubs per cavity resonator.

technique have transmission zeros and parasitic resonances in the vicinity of the pass-band. For the tunable filters demonstrated here, these appear approximately 20% below and above the pass-band. Depending on the coupling between the adjustable stubs and the cavity resonators, the parasitic resonances may be relatively high up to -15 dB (Fig. 2.43). These parasitic resonances depend on the tuning range of the filter, and they move closer to the pass-band as the tuning range increases. If they are cumbersome for the performance of the entire system, band-stop filters may be designed to filter them out.

2.7 Ferro-Electric Varactor based Temperature-Compensated Substrate-Integrated Cavity Resonator

As the integration density of RF front-ends increases, the dissipation of thermal power becomes a major challenge. There exist basically two ways of facing that thermal power management issue. A first approach aims at keeping the temperature of the whole module at a level acceptable for the components. In most cases, this is implemented by means of structures like thermal vias or other heat dissipating structures. These structures allow for a better heat extraction out of the system, and compensate the reduced surface available for the thermal exchange. Nevertheless, in complex systems an accurate control of the temperature is a challenging task, and the components might be exposed to temperature variations. For this reason, components of highly integrated front-ends have to be rather insensitive to operating temperature, and the electrical properties of devices like filters and amplifiers shall remain almost stable over the temperature range specified for the system. This is addressed in the next sections for the previously presented LTCC-integrated resonator.

2.7.1 Influence of Temperature on the DuPont 943 Ceramic Substrate

In order to investigate the temperature behaviour of the DuPont 943 LTCC dielectric, two resonators have been measured over temperature. The resonators are a substrate-integrated cavity resonator and a stripline resonator, both realised on a same 6-layer DuPont 943 wafer. They are weakly coupled in input and output to ensure an accurate measurement of their resonance frequency. The cavity resonator used to perform the measurements is the substrate-integrated cavity resonator presented in section 2.6. This cavity is square and its length and width is $A=L=5431\text{ }\mu\text{m}$. The stripline resonator is a side-coupled resonator realised with one half-wavelength transmission line section. It is open-circuited at both ends, and it is capacitively coupled to input/output striplines as shown in Fig. 2.45.

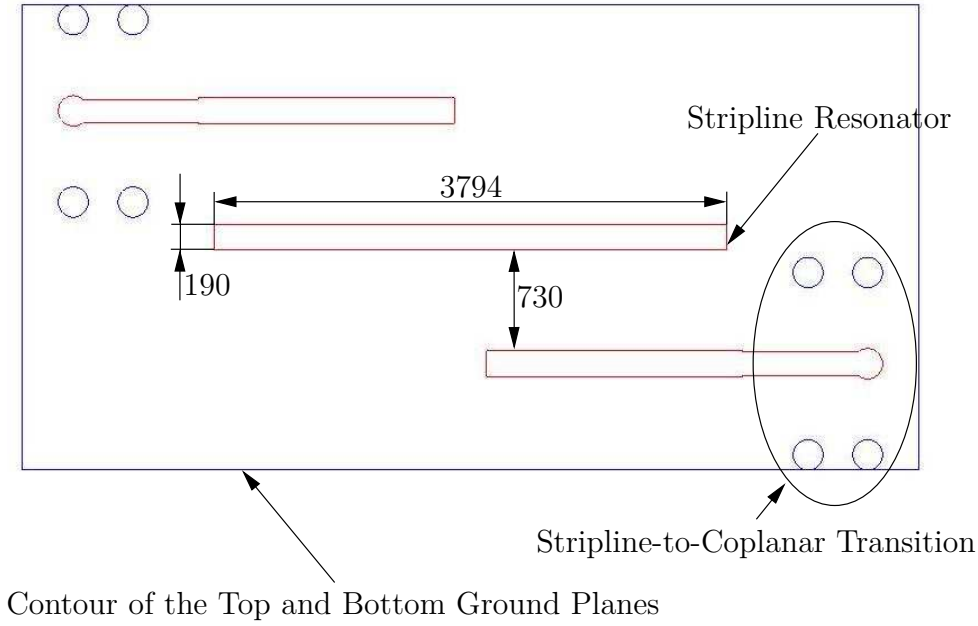


Fig. 2.45: Layout of the weakly coupled stripline resonator in LTCC DuPont 943 (dimensions in μm).

The fundamental resonance frequency of the resonators is calculated by

$$\text{Rectangular Cavity Resonator: } F_{0,\text{RC}} = \frac{c}{2\pi\sqrt{\mu_r\epsilon_r}} \cdot \sqrt{\left(\frac{\pi}{A}\right)^2 + \left(\frac{\pi}{L}\right)^2}, \quad (2.7.1)$$

$$\text{Stripline Resonator: } F_{0,\text{Strip}} = \frac{c}{2\pi\sqrt{\mu_r\epsilon_r}} \cdot \left(\frac{\pi}{D}\right), \quad (2.7.2)$$

where A and L are the length and the width of the rectangular cavity resonator, and D is the length of the stripline resonator. In order to achieve the same resonance frequency with both resonators, A , L , and D shall verify

$$A = L = \sqrt{2}D. \quad (2.7.3)$$

The stripline resonator is patterned in the middle metal layer, three LTCC layers below and above the top and bottom ground planes, respectively. In order to measure the S-parameters with coplanar measurement probes, the input and output striplines are terminated by stripline-to-coplanar transitions. These transitions are designed with vias punched in LTCC. The resonance peak of the resonators has been measured between room temperature (30°C) and 120°C. This temperature range of the experiment was limited by the maximum temperature sustainable by the on-wafer measurement probes. The variation of the resonance frequency of the two resonators versus temperature is plotted in Fig. 2.46.

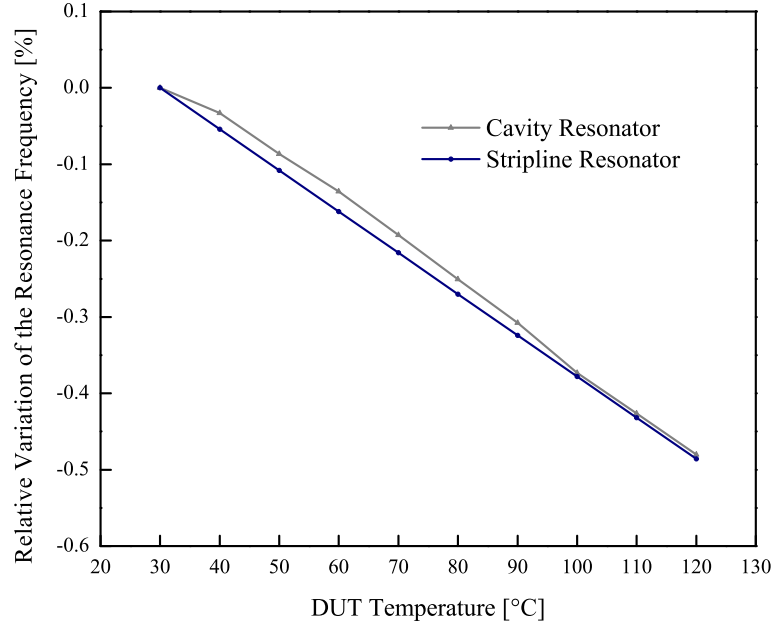


Fig. 2.46: Variation in % of the resonance frequency of the cavity and stripline resonators against temperature.

For both resonators, the measured resonance frequency is shifted by about -0.48% over the 90°C-temperature range. This variation occurs with a nearly constant slope of -53.3 ppm/°C, at any point within 30°C - 120°C. This down-shift of the resonance frequency is explained by two mechanisms: the geometrical dilatation of the structures when the temperature increases, and the variation of the dielectric constant of the substrate with the temperature. From this and according to (2.7.1) and (2.7.2), the variation of the resonance frequency of the resonators versus temperature is calculated by

$$\text{Rectangular Cavity Resonator: } \frac{\partial F_{0,RC}}{\partial T} = \frac{\partial F_{0,RC}}{\partial \epsilon_r} \cdot \frac{\partial \epsilon_r}{\partial T} + \frac{\partial F_{0,RC}}{\partial A} \cdot \frac{\partial A}{\partial T} + \frac{\partial F_{0,RC}}{\partial L} \cdot \frac{\partial L}{\partial T}, \quad (2.7.4)$$

$$\text{Stripline Resonator: } \frac{\partial F_{0,Strip}}{\partial T} = \frac{\partial F_{0,Strip}}{\partial \epsilon_r} \cdot \frac{\partial \epsilon_r}{\partial T} + \frac{\partial F_{0,Strip}}{\partial D} \cdot \frac{\partial D}{\partial T}. \quad (2.7.5)$$

Further, in the special case of a square cavity resonator with $A=L$ as described above, the resonance frequency of the cavity is reduced to

$$\text{Square Cavity Resonator: } F_{0,SC} = \frac{c}{\pi\sqrt{2 \cdot \mu_r \epsilon_r}} \cdot \left(\frac{\pi}{A}\right), \quad (2.7.6)$$

and the variation of the resonance frequency of this cavity versus temperature is calculated by

$$\text{Square Cavity Resonator: } \frac{\partial F_{0,SC}}{\partial T} = \frac{\partial F_{0,SC}}{\partial \epsilon_r} \cdot \frac{\partial \epsilon_r}{\partial T} + \frac{\partial F_{0,SC}}{\partial A} \cdot \frac{\partial A}{\partial T}. \quad (2.7.7)$$

The geometrical response of a material to temperature changes is given by its so-called linear Thermal Coefficient of Extension (TCE). This coefficient describes the way solids typically expand in response to heating and contract on cooling. The variation of the resonance frequency due to the temperature-dependent dilatation of the dielectric material is calculated by

$$\text{Square Cavity Resonator: } \frac{\partial F_{0,SC}}{\partial A} \cdot \frac{\partial A}{\partial T} = \frac{c}{\sqrt{2 \cdot \mu_r \epsilon_r}} \left(\frac{-1}{A^2}\right) \cdot TCE_{\text{DuPont943}} \cdot A, \quad (2.7.8)$$

$$\text{Stripline Resonator: } \frac{\partial F_{0,Strip}}{\partial D} \cdot \frac{\partial D}{\partial T} = \frac{c}{2\sqrt{\mu_r \epsilon_r}} \left(\frac{-1}{D^2}\right) \cdot TCE_{\text{DuPont943}} \cdot D. \quad (2.7.9)$$

For the LTCC DuPont 943 material, the value of that TCE is given in the literature at 6 ppm/°C [66]. Thus, from (2.7.8) and (2.7.9), the variation of the resonance frequency due to thermal expansion is -86151.3 Hz/°C and -87203 Hz/°C for the LTCC-filled cavity and the stripline resonator, respectively. Hence, for the 90°C-temperature span considered here, the geometrical dilatation is responsible for a frequency shift of -7.75 MHz for the cavity resonator, and -7.85 MHz for the stripline resonator.

These values calculated for the two resonators are extremely close to each other. They correspond approximately to 10% of the overall measured frequency shift. The remaining frequency shift is attributed to a change of the dielectric constant of the LTCC material when the temperature increases. This is determined from the resonance frequency measured for the resonators at a given temperature and from their actual dimensions at that same temperature. The value of ϵ_r at a temperature $T = T_0$ is calculated using

$$\text{Square Cavity Resonator: } \epsilon_{r,T_0} = \frac{c^2}{2F_{0,T_0}^2 A_{T_0}^2}, \quad (2.7.10)$$

$$\text{Stripline Resonator: } \epsilon_{r,T_0} = \frac{c^2}{4F_{0,T_0}^2 D_{T_0}^2}, \quad (2.7.11)$$

where A_{T_0} is the length of the square cavity resonator, and D_{T_0} is the length of the stripline resonator, both at T_0 . The relative variation of ϵ_r is plotted versus temperature in Fig. 2.47. For both resonators, the relative variation of the dielectric constant is about 0.87% between 30°C and 120°C. From this, the temperature coefficients of the dielectric constant (TCK) calculated for the cavity and the stripline resonator are very close. They are almost constant and about 96 ppm/°C over the entire 90°C temperature-range. This value obtained for the TCK of DuPont 943

is remarkable. It indicates that the dielectric constant of DuPont 943 increases with temperature, whilst it decreases for some other microwave substrates. An example of that is the Teflon based Rogers RT/Duroid 5880 material, which has a TCK of $-125 \text{ ppm}/^\circ\text{C}$ [111].

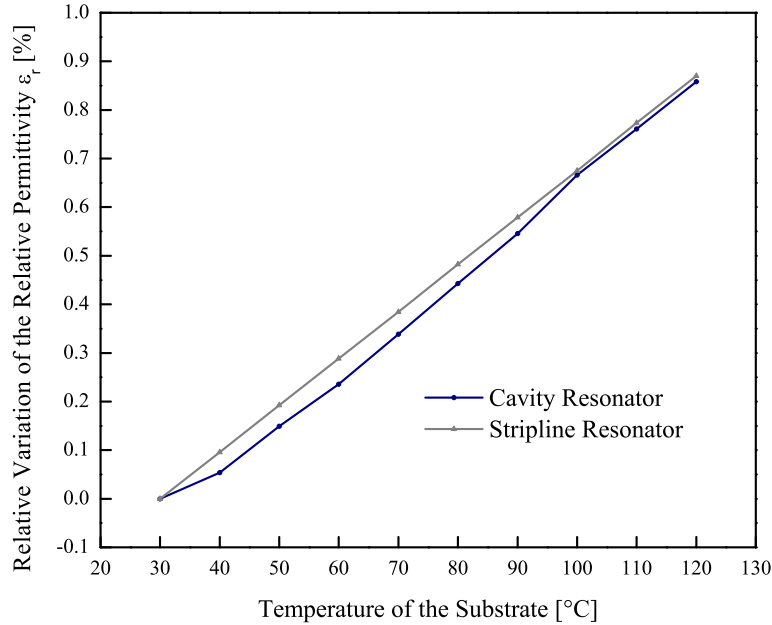


Fig. 2.47: Variation in % of the relative permittivity of the DuPont 943 material over temperature.

2.7.2 Previous Work on Temperature-Compensated Resonators and Filters

There exist several ways of reducing the influence of temperature on the resonance frequency of resonators. A first technique consists in optimising the composition of the dielectric materials. Advanced chemical engineering makes possible the realisation of materials with low TCE and TCK, which offer almost constant performance over temperature. In [112], a microwave dielectric with enhanced temperature stability for the dielectric constant is demonstrated. The paper presents a way to reduce the TCK of a ceramic dielectric from $500 \text{ ppm}/^\circ\text{C}$ down to $50 \text{ ppm}/^\circ\text{C}$ by adding bismuth to the original material. According to a similar principle but with different materials, [113] and [114] present dielectrics with nearly constant permittivity. They demonstrate high-permittivity ceramic dielectrics with outstanding TCK of $2 \text{ ppm}/^\circ\text{C}$ and beyond. Besides a compensation of the substrate itself, the influence of the temperature can be overcome by designing compensating structures. In most cases, these structures are coupled directly to the temperature-sensitive resonators. They are either implemented with active components controlled by an explicit actuation [115], [116], or using passive devices. Among these techniques, passive structures constitute the most promising approach. Due to the influence of the temperature on their electrical or mechanical properties, they compensate the shift observed in the performance of the uncompensated resonators. In the literature, passive mechanical compensation techniques have been extensively investigated. Often, they are used to reduce the frequency shift of waveguide filters versus temperature [117], [118], [119].

These structures are based on the use of different materials or metals having different TCE. They are designed in such a way that the influences of the temperature on the different parts cancel each other. Nevertheless, these techniques rely on bulky mechanical connections between the resonators and the compensation structures, and they are not appropriate for miniature filters. To remedy this situation, some other solutions with resonators loaded electrically by compensating structures have been proposed. In [120], a technique using a temperature-dependent capacitance is patented. The capacitance is coupled thermally and electrically to a transmission line resonator processed in a dielectric block. The dielectric used for the capacitance has a temperature-dependence of opposite sign to that of the resonator to compensate. For this reason, it does not require any actuation signal for the temperature compensation.

2.7.3 Principle and Design of the Temperature-Compensated Cavity Resonator

The technique used to compensate the temperature-dependence of the LTCC-integrated resonator utilises Barium Strontium Titanate ferro-electric materials ($\text{Ba}_x\text{Sr}_y\text{TiO}_3$ or BST). BST ferro-electrics are dielectrics with high dielectric constants from hundreds up to several thousands. They exhibit a remarkable temperature behaviour because their dielectric constant varies strongly with the temperature. Also, when they are used in thin films, they allow for the realisation of capacitances, which can be controlled by an electrostatic field or thermally. However, in the frame of the described application, it is for their temperature behaviour that ferro-electric varactors have been introduced.

The ferro-electric varactors implemented for the temperature compensation are presented in section 1.4.3. According to the proposed technique, the temperature-sensitive capacitance is inductively coupled to the cavity resonator. Also, the coupling coefficient between them is determined in order to compensate the frequency shift measured for the original resonator with the variable capacitance. Two kinds of BST capacitor were available to design the compensating structures. A first family of capacitances was processed using BST 70-30 ($\text{Ba}_{0.7}\text{Sr}_{0.3}\text{TiO}_3$) thin films. The other capacitors were fabricated with BST 55-45 ($\text{Ba}_{0.55}\text{Sr}_{0.45}\text{TiO}_3$) thin films. The properties of these two ferro-electric materials are similar. Nevertheless, BST 55-45 varactors allow for a higher tunability and are more temperature-sensitive than BST 70-30 varactors. In return, BST 70-30 films enable the realisation of capacitors with better Q-factors.

The ferro-electric capacitor is integrated in a hybrid fashion on the LTCC substrate of the cavity resonator (Fig. 2.48). It is placed in a 2-LTCC-layer deep cavity processed in the substrate, and it is fixed using epoxy glue. As for the LTCC tunable filters, the cavity is manufactured 200 μm away from the side-wall of the cavity resonator. The ferro-electric varactor is inductively coupled to the cavity resonator by means of a coplanar line terminated with a coupling via. This coupling structure is similar to that presented for the coupling of the RF-MEMS of the frequency-agile filters. Nevertheless, in the present case the capacitor is mounted in series, and its second port is connected to a quarter-wavelength open-circuited stub. Both interfaces, between the capacitor on LAO and the centre conductor of the coplanar line on LTCC are realised with Al bond-wires.

As already mentioned, the position of the coupling via in the cavity determines the strength of the coupling between the varactor and the resonator. This position of the via has been optimised for the BST 70-30 varactor. It has been calculated for the best compensation at the limits of the considered temperature range: 30°C and 120°C. At these temperatures, the values of the BST 70-30 varactor are 290 fF and 120 fF, respectively. The simulations have been performed using the

full-wave simulator to take the influence of the bond-wires into account. From these simulations, an optimum distance of $764\mu\text{m}$ has been chosen between the centre of the coupling via and the side-wall of the cavity.

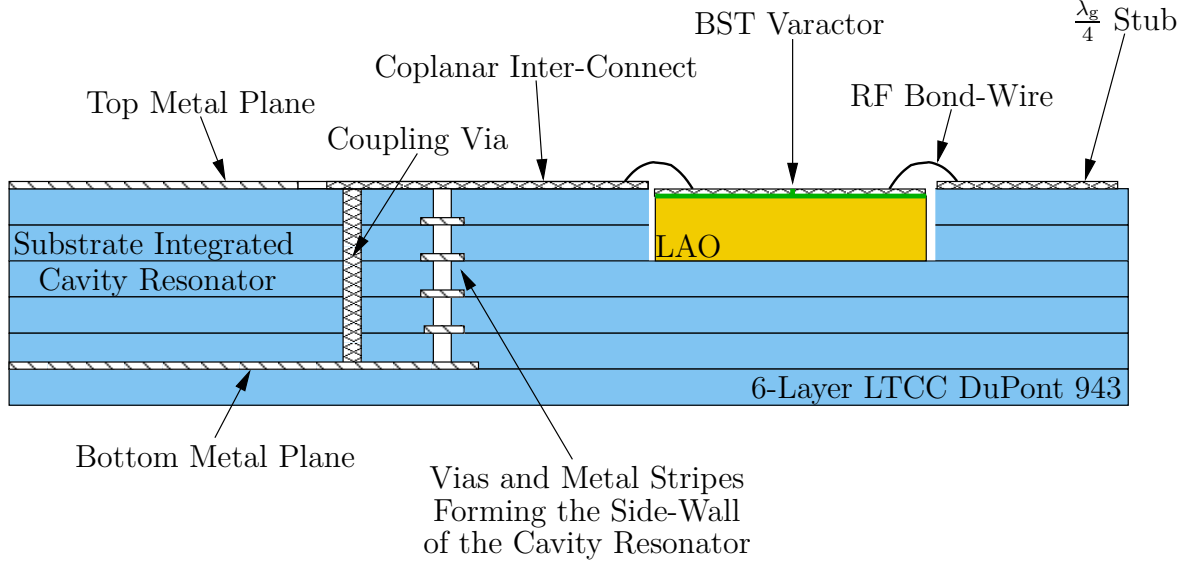


Fig. 2.48: Hybrid integration concept for the ferro-electric varactor on LTCC.

Characterisation and Measurements

Two temperature-compensated resonators have been realised according to this principle (Fig. 2.49). For both resonators, the structures in LTCC are identical. However, a first resonator was assembled with a BST 70-30 varactor and the second one was mounted with a BST 55-45 varactor. The two compensated resonators have been measured using the same setup and over the same temperature range as the original resonator. Also, the frequency shift measured for the two compensated resonators has been compared to that of the uncompensated resonator. The variation of the resonance frequency of all three resonators is plotted against temperature in Fig. 2.50.

As it was expected, the two ferro-electric capacitors offer different compensations of the frequency shift. At 120°C , the resonance frequency of the cavity with the BST 70-30 varactor (for which the design has been optimised) is only 0.03% below the resonance frequency, which it shows at room temperature. In return, the other resonator equipped with a BST 55-45 varactor is slightly overcompensated: $+0.27\%$. This is due to the higher sensitivity of the BST 55-45 material against temperature. Nevertheless, this demonstrates the capability of the proposed technique to compensate for even larger frequency shifts, up to 0.75% . The plot in Fig. 2.50 shows however that the compensation is not constant over the entire temperature range. The slope of the compensated resonance frequency changes abruptly between 70°C and 90°C . This can be explained by the difference between the slope of the capacitances and that of the resonance frequency at these temperatures. More precisely, the variation of the capacitance of the varactors over temperature is not as linear as the temperature-dependence of the resonance frequency of the resonator. For this reason, the maximum deviation of the resonance frequency of the BST 70-30 resonator is -0.12% at about 100°C . Also, the maximum slope of the resonance frequency is $-161.2\text{ ppm}/^\circ\text{C}$ between 80°C and 90°C . The unloaded Q-factor of the compensated resonators has been extracted from the measured

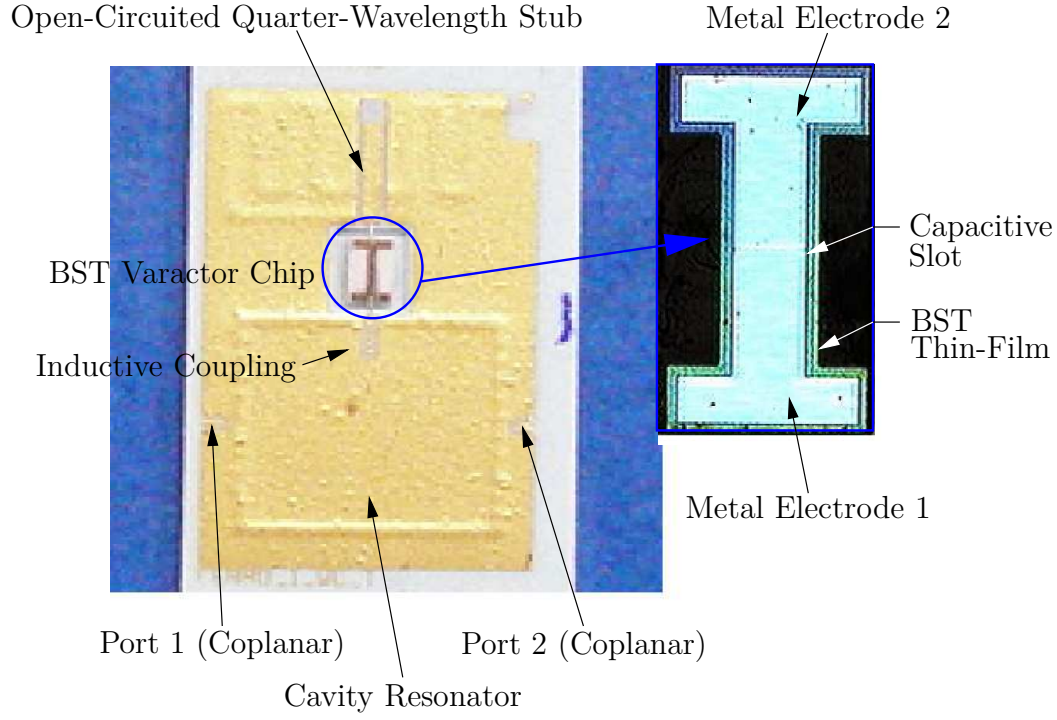


Fig. 2.49: Photograph of the BST varactor based temperature-compensated cavity resonator in LTCC.

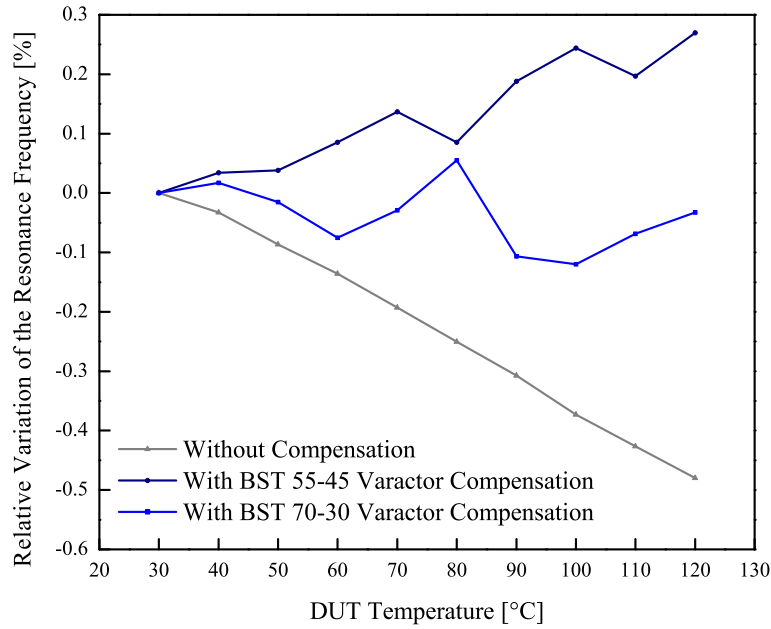


Fig. 2.50: Relative variation of the resonance frequency of the LTCC resonators over temperature, with and without BST varactor compensation.

S_{21} -parameters. It is 62.3 for the resonator equipped with the BST 70-30 varactor and 59.2 for the resonator with the BST 55-45 varactor. These values are considerably lower than the unloaded Q-factor of 290 measured for the original resonator. This increase of loss in the resonators is partly due to the limited Q-factor of the ferro-electric capacitors at 15 GHz. Nevertheless, it may be also justified by the discontinuities in the coplanar line on LTCC (Fig. 2.49). Around the ferro-electric varactor and because of the large width of the chip, the coplanar line is designed with a large ground-to-ground spacing. This design of the coplanar line is sub-optimal and may increase the loss in the compensating stub.

2.8 Conclusion

In this chapter, various fixed-frequency, tunable, and temperature-compensated cavity resonators and filters have been demonstrated. The filters are designed in two different technologies, on silicon and on LTCC, and they are foreseen for two major spaceborne and airborne applications.

In a first section, band-pass filters micro-machined out of silicon have been presented. These filters are designed for operation at K-band, and they are intended for the replacement of waveguide filters in data-link satellite transceivers. In this technology, a single micro-machined cavity resonator has been demonstrated with an outstanding Q-factor of 1410. Also, the design of 2-, 3-, and 4-pole fixed-frequency filters has been described, and the presented filters have been characterised by measurement. The filters implement a novel concept based on a KOH-etched coupling cavity for the coupling of the micro-machined resonators. The novel coupling cavity was introduced to improve on the fabrication costs and complexity of the filters, which all have been demonstrated with well-shaped pass-band response and little insertion loss. Later in the section, an RF-MEMS based technique was presented to tune micro-machined cavity resonator filters. The technique was implemented to tune a 3-pole filter demonstrated firstly as fixed-frequency filter. For this tunable filter, 3.71% of tunability and 2 dB of insertion loss have been measured.

In another section of the chapter, the design of band-pass filters integrated in DuPont 943 dielectric has been addressed. The filters are 2-pole filters designed for UAV data-link at Ku-band. They have been realised according to the substrate-integrated cavity technique, and they are formed by two resonators filled with LTCC material. A Q-factor of 290 has been measured for a single 2-port cavity resonator, and 1 dB of insertion loss has been demonstrated for the fixed-frequency 2-pole filter. Further in the section, two 2-pole tunable filters have been also presented. The filters are made tunable over frequency by means of RF-MEMS cantilevers. These frequency-agile filters are tuned according to a technique similar to that introduced for the micro-machined filters, and they have been demonstrated with 3% and 7.2% of tunability. Nevertheless, the measurement of the filters highlighted also some limitations that concern mainly the insertion loss about 5 dB.

Finally, the last section of the chapter discussed the influence of temperature on the resonance of LTCC-integrated cavity resonators. Also, it proposed an actuation-free compensation technique, which reduces the drift of the resonance frequency from -0.48% to -0.03% between 30°C and 120°C. Through these developments, the aim of this chapter was to assess the opportunities that the next generation of millimetre-wave front-end could benefit from modern materials and processes. Further, as reconfigurable front-ends are becoming a trend, these platforms have been associated to RF-MEMS circuits with the ambition to develop tuning techniques for cavity resonators and filters.

3 RF-MEMS based Phased Array Antennas for Millimetre-Wave Front-Ends

3.1 Introduction

Phased Array Antennas (PAA), also known as Electrically Steerable Antennas (ESA), are directive antennas realised with several elementary radiating elements. The radiation characteristic of ESA is electrically steerable in one or two dimension(s) of the space. This beam steering functionality can be implemented according to two different concepts: with hardware working on analog HF signals or by means of Digital Beam Forming units (DBF) (Fig. 3.1). In both cases, the beam steering is achieved by weighting the signal of the different radiators with a relative phase shift gradient. For DBF antennas, the phase shift gradient is achieved by means of delay and sum beamformers processing digital signals. In this case, the beam forming is implemented in software, and it processes signals coming from Analog/Digital converters (A/D) placed behind the radiators. On the other hand, for antennas based on analog beam forming, the direction of the main beam is steered by means of HF phase shifters placed between the radiating elements and an RF distribution network. In both cases, the relative delay between the signals of the radiating elements can be reconfigured at any time to achieve the required direction for the main beam of the antenna.

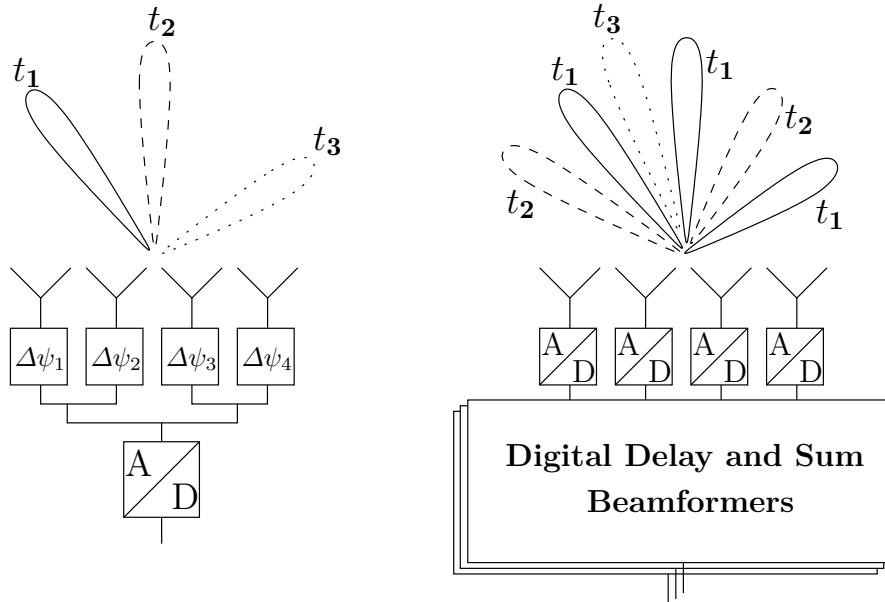


Fig. 3.1: Analog beam forming (left)/digital beam forming (right).

Both, analog and digital beam steering techniques have advantages and disadvantages depending on the targeted application. A major advantage of DBF antennas is their multi-beam capability. Digital processing techniques offer the opportunity to implement several beam forming routines running in parallel, and processing a same set of data (Fig. 3.1). The method enables several simultaneous main beams pointing in different directions, and it allows for Spatial Domain Multiple Access (SDMA) or simultaneous tracking of multiple targets. In return, DBF techniques require an important processing effort, that is up to now difficult to implement in miniaturised on-board systems. For this reason, the following of this third chapter on phased array antennas focuses on electrically steerable antennas based on analog beam forming techniques.

The unique beam steering capability of ESA presents major benefits over conventional antenna array techniques, and especially over Mechanically Steerable Antennas (MSA). First, electrically steerable antennas make better use of the radiated power than fixed-beam antennas. The radiation characteristic of ESA is adjustable in real time and, beyond the beam steering, often the width of the main beam, the side lobe level, and the directions of zero radiation can be adapted. Thanks to that, the power radiated by an ESA can be focused in a direction interesting a specific communication or tracking task. This is further emphasised by the fast beam switching capability of ESA. The antenna remaining fixed, ESA are able to shift rapidly the radiated beam from one pointing direction to another, without being handicapped by the displacement of mechanical parts. This fast beam switching aptitude enables multiple radar or communication functions interlaced in time or even simultaneously for multi-beam antennas. On top of this, the use of electrical components in place of moveable mechanical parts makes ESA lighter, more compact, and thus easier to integrate than MSA. Finally, ESA are more reliable than their mechanically steerable counterparts. They are easier to maintain, have lower life cycle costs, and longer life expectancy because they tolerate a certain amount of failures and defaults. This property of ESA is called "graceful degradation".

However, while ESA offer interesting opportunities, they exhibit also some limitations. The first and probably the most troublesome drawback of ESA is the power dissipated in the additional electrical components. In ESA, the phase shifters increase the electrical loss in the feed network and reduce the antenna efficiency. In order to compensate for this supplementary loss, high and low-noise power amplifiers as well as circulators and limiters are sometimes implemented between the phase shifters and the radiators. For these antennas called Active ESA (AESAs), a cooling network may be also necessary to evacuate the heat dissipated by the active circuitries. These extra features required in some ESA make them more complex and more challenging to manufacture than fixed or mechanically steerable antennas. On the other hand, since the antenna array of ESA is physically fixed, their projected aperture does not remain constant for all steering directions, and it decreases drastically for large scan angles. This results in a limited field of view generally below $\pm 60^\circ$, but also in a wider half-power beamwidth (3.1.1) and a reduced antenna gain (3.1.2) at large scan angles [121].

$$\theta_{-3\text{dB}}(\theta_0) \approx \frac{\theta_{-3\text{dB}}(0^\circ)}{\cos(\theta_0)} \quad (3.1.1)$$

$$G(\theta_0) \approx G(0^\circ) \cdot \cos(\theta_0) \quad (3.1.2)$$

In (3.1.1) and (3.1.2), $\theta_{-3\text{dB}}(0^\circ)$ and $G(0^\circ)$ are the half-power beamwidth and the antenna gain of the radiation characteristic pointing in the broadside direction. Also, θ_0 is the pointing direction of the steered main beam measured from broadside.

Finally, another important factor limiting a wider use of ESA is their fabrication costs. The manufacturing of ESA implies the fabrication of a large number of precision phase shifters, which can, depending on the technology, be rather costly. This aspect is of course an important matter of choice playing unfavourably for ESA in consumer-oriented applications and large antenna arrays.

Nevertheless, these limitations of phased array antennas are constantly being improved and do not compromise the opportunities of ESA. Fast, reconfigurable in real time, allowing multi-tasking, convenient to integrate, and reliable; ESA appear today as major components of modern millimetre-wave front-ends for communication and sensing.

3.2 Theory of Fixed-Beam and Phased Array Antennas

3.2.1 Various Types of Phased Array Antennas

ESA can be classified according to different criteria. Each class of antennas has its advantages and disadvantages depending on the application, the space available to integrate the antenna, and the technology affordable for the targeted market. The first distinction between ESA concerns the way the radiating elements are arranged. For an array having its radiators distributed along a straight line, the array is said to be linear. If the radiators are spread over a plane, the array is planar. Finally, if the elements are distributed on a non-planar surface, generally a plane curved in one or two dimension(s), the array is said to be conformal [122]. The choice between the possible arrangements is usually driven by the radiation characteristic to achieve and by the system, in which the antenna has to be mounted. The design and development of conformal array antennas are more complex than those of linear and planar arrays. Nevertheless, conformal antennas have the advantage of being convenient to integrate on curved surfaces, which can be the fuselage of an aircraft, for example.

Further, as already mentioned ESA can be classified between active and passive antennas. Active phased array antennas, also called AESA, implement active modules with power amplifiers close to the radiating elements. AESA are in general more complicated and more costly than passive ESA. In return, they exhibit a better Equivalent Isotropic Radiated Power (EIRP), and hence also improved performance in terms of antenna coverage for communication systems or detection and tracking for AESA based radars.

Finally, phased array antennas can be categorised according to the way the RF power is distributed to the radiating elements. Beside Direct Radiating Array (DRA) configurations, where the radiating elements are fed using transmission lines or waveguides directly connected to them, alternative feeding techniques may be implemented. Among these, the "reflect array" and "transmit array" techniques are noteworthy solutions. In these configurations, the electrically steerable antenna plays the role of a reflector or acts as a "microwave lens", respectively. It receives and re-radiates the RF signal sent by a primary antenna placed several wavelengths away from the beam forming array. These techniques present the advantage of being simple to design: there are no power

dividers/combiners to implement, and the phased array benefits naturally from the illumination taper of the primary source. Further, these feeding techniques are low-loss because the RF signal is transmitted from the primary source to the antenna array using free-space radiation. Nevertheless, this advantage is balanced by spill-over losses because the antenna array cannot capture all the power emitted by the primary source.

3.2.2 Antenna Basics and Array Factor Theory

Definitions and Useful Formulas

A fundamental specification of microwave front-ends is the width of the beam radiated by the antenna 3 dB below its maximum. This beamwidth is noted $\theta_{\text{-3dB}}$. For the ideal case of a uniformly illuminated continuous line source, this half-power beamwidth depends only on the wavelength and on the size of the aperture. From [123], it is given by

$$\theta_{\text{-3dB}} = \frac{k \cdot \lambda}{l}, \quad (3.2.1)$$

where k is a constant, λ is the free-space wavelength, and l is the length of the aperture. The constant k is 50 for a beamwidth expressed in degrees and 0.87 for $\theta_{\text{-3dB}}$ in radians. The beamwidth calculated with (3.2.1) is the narrowest beamwidth of any illumination of length l . Also, if no signal processing is applied, the width of the beam radiated by the antenna is directly related to its cross-range resolution δ . In this case, it is defined by the product of the beamwidth $\theta_{\text{-3dB}}$ in radians by the range R in meters between the antenna and the plane in which δ is given:

$$\delta = \theta_{\text{-3dB}} \cdot R. \quad (3.2.2)$$

The formulas (3.2.1) and (3.2.2) are valid for both, 1D and 2D continuous apertures. For uniformly illuminated continuous line sources, l is the physical length of the antenna. For uniformly illuminated continuous planar apertures, the beamwidth is defined in all planes perpendicular to the aperture and passing through the geometrical centre of the aperture. In these planes where the beamwidth is defined and where the projected illumination is uniform (for example, the cardinal planes of a uniformly illuminated rectangular aperture), $\theta_{\text{-3dB}}$ is calculated using (3.2.1), where l is the length of the projected planar aperture in the plane in which the beamwidth is calculated. Another measure for the ability of an antenna to radiate or receive signals in a given direction is its so-called directivity D . For a transmit antenna, the directivity is defined as the ratio of the power intensity per radiant radiated by the actual antenna in a given direction (θ, ϕ) to the power intensity that would be radiated in that same direction (θ, ϕ) by an isotropic radiator radiating the same total amount of power. From this and according to [124], the directivity of a transmit antenna is calculated by

$$D(\theta, \phi) = 4\pi \cdot \frac{\text{Radiation Intensity in}(\theta, \phi)}{\text{Totally Radiated Power}}. \quad (3.2.3)$$

Nevertheless, the directivity D does not take the loss in the antenna into account. This is overcome by introducing the gain of the antenna noted G . The gain of an antenna includes all losses dissipated

in the antenna, but not its mismatch [125],[124]. The gain function resembles the directivity function, except for the totally radiated power that has to be replaced by the totally accepted power at the feeding port of the transmit antenna. This can be explained by the fact that the difference between the accepted power and the radiated power are the losses dissipated in the antenna. From [124], the gain of a transmit antenna is calculated by

$$G(\theta, \phi) = 4\pi \cdot \frac{\text{Radiation Intensity in}(\theta, \phi)}{\text{Totally Accepted Power}}. \quad (3.2.4)$$

From (3.2.3) and (3.2.4) and for the transmit case, a factor k_{eff} called radiation efficiency is defined as the ratio of the overall radiated power to the net input power accepted by the antenna [125]. This leads to the following relation between the gain of an antenna and its directivity:

$$G(\theta, \phi) = k_{eff} \cdot D(\theta, \phi). \quad (3.2.5)$$

All formulas (3.2.3), (3.2.4), and (3.2.5) apply also to receive antennas. In this last case however, the *radiated* power shall be replaced by the *received* power.

The maximum value of the directivity is called peak directivity, and it is noted D_0 . From [126], for uniformly illuminated continuous planar apertures with an area A , this maximum is reached in the broadside direction, and it is given by

$$D_0 = \frac{4\pi \cdot A}{\lambda^2}. \quad (3.2.6)$$

For any antenna or antenna array of aperture area A with or without tapered excitation, the peak directivity is inevitably less than that calculated by (3.2.6). The gain and directivity of an antenna are ratios and are usually expressed in dBi: dB with respect to an isotropic radiator.

Experimental Determination of the Gain, Directivity, and Efficiency of Antenna Arrays

The gain, peak directivity, and efficiency of antennas and antenna arrays can be determined experimentally from their measured radiation characteristic. In the particular case of rectangular antenna arrays, an approximate of the peak directivity can be calculated from the widths θ_{-3dB} and ϕ_{-3dB} , measured for the main beam in the two main planes of the aperture. From [127], it is given by (3.2.7) for uniformly fed rectangular arrays and by (3.2.8) for rectangular arrays fed with tapered distributions.

$$D_{a,u}(\theta_0, \phi_0) \approx \frac{32400}{\theta_{-3dB} \cdot \phi_{-3dB}} \quad (3.2.7)$$

$$D_{a,t}(\theta_0, \phi_0) \approx \frac{27000}{\theta_{-3dB} \cdot \phi_{-3dB}} \quad (3.2.8)$$

These expressions calculate the directivity in linear scale and are valid for both, fixed-beam and phased array antennas with rectangular aperture. Further, since the gain of an antenna array can be measured, the expressions (3.2.7) or (3.2.8) can be used with (3.2.5) to calculate the experimental value of the efficiency k_{eff} of an antenna array.

Principle of Pattern Multiplication

The radiation characteristic of an antenna array depends on numerous parameters: the overall dimensions of the array, the number and distribution of the radiating elements in the array, the radiation characteristic of the individual elements, and their excitations. Nevertheless, according to the principle of pattern multiplication, the radiation characteristic of an array supposed without coupling and having all its radiators identical and oriented in a same direction can be expressed as

$$D_a(\theta, \phi) = D_e(\theta, \phi) \cdot AF(\theta, \phi), \quad (3.2.9)$$

where D_e is the radiation characteristic of a single radiator and AF is the so-called array factor AF [128]. Thanks to (3.2.9), the influence of the various parameters on the radiation characteristic of the array D_a can be investigated independently. In a separated development step, the design of a single radiating element is performed, so that it achieves an aimed radiation characteristic D_e . In parallel to this, the antenna array supposed ideal and with isotropic radiators is designed to realise an expected array factor AF . This last point is exclusively concerned with the geometry of the array, the disposition of the radiators inside it, and the excitation coefficients of the radiating elements. All this is addressed in the so-called Array Factor Theory, whose main lines are described in the coming section.

Array Factor Function of Fixed-Beam Linear and Planar Arrays

In order to derive expressions for the array factor of linear and planar antenna arrays, the systems of coordinates depicted in Fig. 3.2 and 3.3 are defined. The notations and systems of coordinates defined in the figures are identical to those used to describe the antennas demonstrated in the following sections of this chapter.

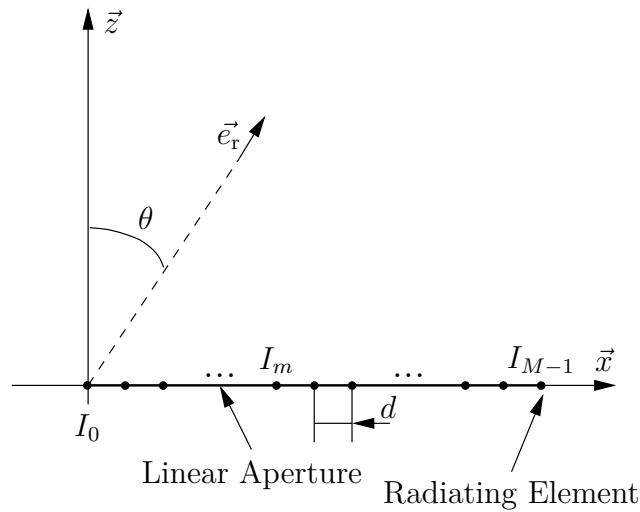


Fig. 3.2: Equally spaced linear array of isotropic point sources.

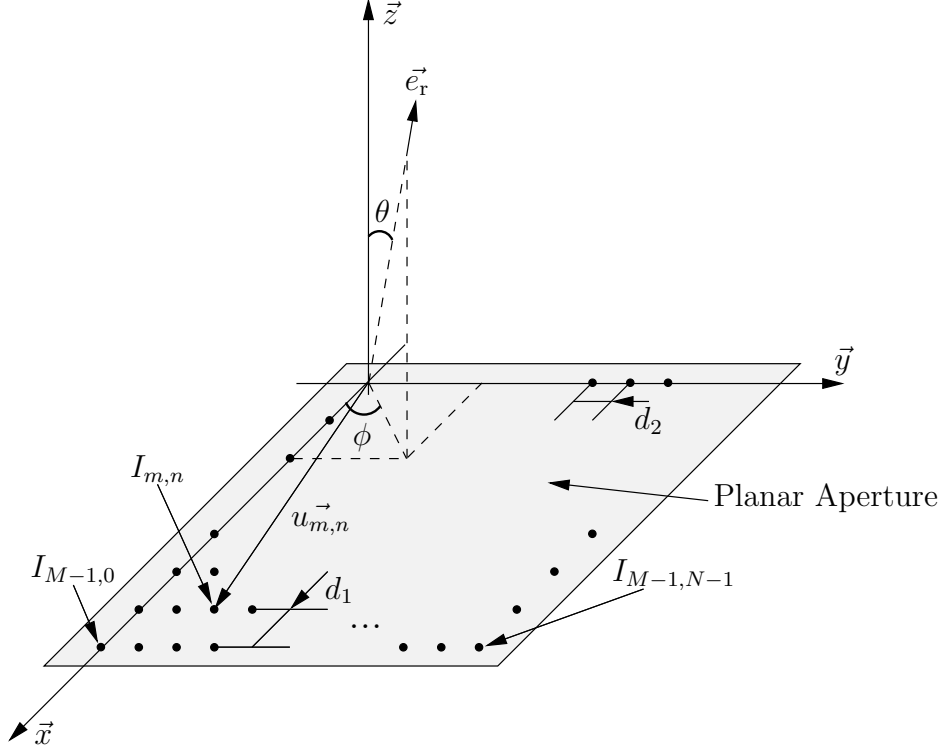


Fig. 3.3: Rectangular array of isotropic point sources with a regular rectangular grid.

The array factor of an antenna array corresponds to the radiation characteristic of the array if it were implemented with perfect isotropic radiators and without coupling between them. In this way, it indicates how an antenna array receives or radiates electromagnetic signals independently of the type of radiator used. According to [128], the array factor of the equally spaced linear array in Fig. 3.2 is given by (3.2.10). That of the regular rectangular array in Fig. 3.3 is given by (3.2.11).

$$AF(\theta) = \sum_{m=0}^{M-1} I_m \cdot e^{jk(\vec{e}_r \cdot \vec{u}_m)} \quad (3.2.10)$$

$$AF(\theta, \phi) = \sum_{n=0}^{N-1} \sum_{m=0}^{M-1} I_{m,n} \cdot e^{jk(\vec{e}_r \cdot \vec{u}_{m,n})} \quad (3.2.11)$$

In (3.2.10), I_m is the complex excitation coefficient of the m^{th} radiating element in Fig. 3.2. Also, $\vec{u}_m = m d \vec{x}$ is the vector describing its position with respect to the point source I_0 . In the same way, in (3.2.11), $I_{m,n}$ is the complex excitation coefficient of the radiating element with the indexes m and n along the X- and Y- axes, respectively (Fig. 3.3). Also, $\vec{u}_{m,n} = m d_1 \vec{x} + n d_2 \vec{y}$ is the vector running over the array lattice and indicating the position of the element with the same indexes. From (3.2.10) and (3.2.11) and replacing \vec{e}_r by its coordinates in the Cartesian system, the array factors of the linear and rectangular arrays are written as [129], [130]

$$AF(\theta) = \sum_{m=0}^{M-1} I_m \cdot e^{j m k d \sin(\theta)}, \quad (3.2.12)$$

$$AF(\theta, \phi) = \sum_{n=0}^{N-1} \sum_{m=0}^{M-1} I_{m,n} \cdot e^{j(mkd_1 \sin(\theta) \cos(\phi) + nkd_2 \sin(\theta) \sin(\phi))}. \quad (3.2.13)$$

Further, the additional assumption is made that the excitation coefficients of the rectangular array are separable. $I_{m,n}$ can be written as a product of two functions with the discrete values I_m and I_n at the respective element positions:

$$I_{m,n} = I_m \cdot I_n, \quad (3.2.14)$$

According to [123], the array factor of that rectangular array can be written as the product of two linear array factors. This new expression of the array factor is given by

$$AF(\theta, \phi) = AF_x(\theta, \phi) \cdot AF_y(\theta, \phi), \quad (3.2.15)$$

where AF_x and AF_y are the linear array factors generated by the linear excitation functions $I_m(x)$ and $I_n(y)$, respectively. From this and replacing AF_x and AF_y by the expression in (3.2.12), the array factor of a rectangular antenna array with a regular rectangular grid and fed with a separable aperture distribution is calculated by

$$AF(\theta, \phi) = \sum_{n=0}^{N-1} I_n e^{jnk d_2 \sin(\theta) \sin(\phi)} \cdot \sum_{m=0}^{M-1} I_m e^{jmk d_1 \sin(\theta) \cos(\phi)}, \quad (3.2.16)$$

where M and N are the number of radiating elements along the X- and Y-axes, respectively, and d_1 and d_2 are the inter-element spacings in these two planes.

According to (3.2.12) and (3.2.16), the array factor of fixed-beam antenna arrays fed with in-phase excitation coefficients exhibits an absolute maximum called main lobe in the broadside direction at $\theta = 0^\circ$. The other *absolute* maxima of the array factor are called grating lobes. For equally spaced linear arrays, they appear at the θ angles defined by

$$\sin(\theta) = \pm \frac{p\lambda}{d}, \quad (3.2.17)$$

where p is a positive integer different from zero. Thus, for fixed-beam antenna arrays the directions of the grating lobes depend only on the array lattice. If the distance between two neighbouring radiators is $d \leq \lambda/2$, the grating lobes do not appear in the real space, and they are invisible in the array factor. In return, if $d \geq \lambda/2$, (3.2.17) is verified for real values of θ and grating lobes may be visible in the radiation pattern depending on the radiating elements. A special case is when the radiators are separated by exactly one free-space wavelength $d = \lambda$. In this case, the array factor exhibits grating lobes in the $\theta = \pm 90^\circ$ directions. However, because most elements, especially planar, do not radiate in the end-fire directions, the grating lobes present in the array factor are cancelled by the radiation characteristic of the individual elements.

3.2.3 Theory of Phased Array Antennas

Equally Spaced Linear Arrays

The pointing direction of phased array antennas is driven by a phase shift gradient applied between the different elementary radiators. This phase taper is chosen so that the contributions of all radiating elements produce constructive interferences in the pointing direction targeted for the main beam. To do so, the phase gradient is calculated in order to have the signals of the various radiators in-phase in any plane perpendicular to the aimed pointing direction. Such planes are called equiphase fronts, or equiphase planes.

An equally spaced linear array of isotropic sources steered in XZ-plane is depicted in Fig. 3.4. The elements of the array are separated by a distance d , and they are fed with a linear phase gradient $n\psi_0$. In this sketch also, the element indexed with "0" is taken as the reference with zero phase.

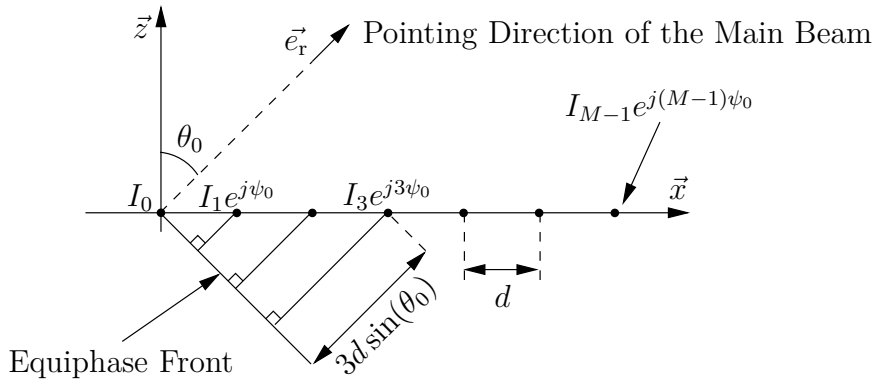


Fig. 3.4: Equally spaced linear array of isotropic sources fed with a linear phase gradient.

From (3.2.10), the array factor of this linear phased array is calculated by

$$AF(\theta) = \sum_{m=0}^{M-1} I_m e^{j(m\psi_0)} \cdot e^{jk(\vec{e}_r \cdot \vec{u}_m)}. \quad (3.2.18)$$

According to [121], the phase shift ψ_0 necessary to achieve a beam steering in the direction θ_0 is determined using

$$\psi_0 = -\frac{2\pi d}{\lambda} \cdot \sin(\theta_0). \quad (3.2.19)$$

Replacing this for ψ_0 in (3.2.18) gives a more convenient expression for the array factor of equally spaced phased linear arrays. Again from [121], it is given by

$$AF(\theta) = \sum_{m=0}^{M-1} I_m e^{jmkd(\sin(\theta) - \sin(\theta_0))}. \quad (3.2.20)$$

For such a linear array having a main beam steered in the θ_0 direction, the angles at which the grating lobes occur are given by [121]. They are the θ_g verifying

$$\frac{\pi d}{\lambda} \cdot (\sin(\theta_g) - \sin(\theta_0)) = \pm p\pi, \quad (3.2.21)$$

with p an integer not equal to zero. From this, an equally spaced linear array which shall be capable of steering up to θ_0 without grating lobe has to be designed with an inter-element spacing d satisfying

$$\frac{d}{\lambda} \leq \frac{1}{1 + |\sin(\theta_0)|}. \quad (3.2.22)$$

According to (3.2.22), a grating lobe-free array factor steerable up to end-fire requires an inter-element spacing $d \leq 0.5\lambda$. However, in practice a large majority of radiating elements is not capable of radiating up to $\theta = \pm 90^\circ$, and the beam cannot be steered beyond approximately $\pm 60^\circ$. In this more realistic case, an inter-element spacing $d = 0.54\lambda$ is small enough to prevent the onset of grating lobes in $[-90^\circ; 90^\circ]$.

Rectangular Arrays with Regular Rectangular Grid

It is assumed now that the rectangular array of Fig. 3.3 is fed with a 2-dimensional linear phase gradient: ψ_x for the elements along the X-axis, and ψ_y for the elements along the Y-axis. From (3.2.11), the array factor of the rectangular array excited in this way is calculated with

$$AF(\theta, \phi) = \sum_{n=0}^{N-1} \sum_{m=0}^{M-1} I_{m,n} e^{j(m\psi_x + n\psi_y)} \cdot e^{jk(\vec{e}_r \cdot \vec{u}_{m,n})}. \quad (3.2.23)$$

Also, as for the fixed-beam rectangular array, the assumption is made that the aperture distribution of the array is separable and can be written under the form

$$I_{m,n} e^{j(m\psi_x + n\psi_y)} = I_m e^{j(m\psi_x)} \cdot I_n e^{j(n\psi_y)}, \quad (3.2.24)$$

with $I_m e^{j(m\psi_x)}$ and $I_n e^{j(n\psi_y)}$, the excitation coefficients in the two main planes of the rectangular aperture, along the X- and the Y-axis, respectively. Thus, according to [123], the array factor of this rectangular array can be calculated as the product of two array factors AF_x and AF_y so that

$$AF_x(\theta, \phi) = \sum_{m=0}^{M-1} I_m e^{j(m\psi_x)} \cdot e^{jk(\vec{e}_r \cdot \vec{u}_m)}, \quad (3.2.25)$$

$$AF_y(\theta, \phi) = \sum_{n=0}^{N-1} I_n e^{j(n\psi_y)} \cdot e^{jk(\vec{e}_r \cdot \vec{u}_n)}, \quad (3.2.26)$$

$$\vec{u}_{m,n} = \vec{u}_m + \vec{u}_n = md_1 \vec{x} + nd_2 \vec{y}. \quad (3.2.27)$$

Finally, from [131], in order to steer the main beam of the array in a given direction (θ_0, ϕ_0) , the phase shifts ψ_x and ψ_y shall be calculated using

$$\psi_x = -\frac{2\pi d_1}{\lambda} \cdot \sin(\theta_0) \cos(\phi_0), \quad (3.2.28)$$

$$\psi_y = -\frac{2\pi d_2}{\lambda} \cdot \sin(\theta_0) \sin(\phi_0). \quad (3.2.29)$$

From this, the array factor of a rectangular phased array with a regular rectangular grid and fed with a separable aperture distribution can be calculated as the product of two linear array factors. Thanks to this property of such rectangular arrays, their analysis and synthesis can be reduced to two 1-dimensional problems. Therefore, the discussions and formulas presented previously for linear phased arrays can be used to study also rectangular arrays of the kind described above.

3.2.4 Errors in Fixed-Beam and Phased Array Antennas

The array factor theory presented above is an idealised explanation of what happens in antenna arrays. Also, the formulas introduced in the previous sections do not take various mechanisms into account. Among these, a first phenomenon to consider on top of the array theory is the so-called mutual coupling. Mutual coupling is the mechanism by which each radiating element in an array receives back a certain amount of power from the other radiators in its vicinity. For this reason, the performance of a radiating element inside an array is different from that when it is alone. Mutual coupling affects both, the radiation characteristic and the input impedance of radiators. Nevertheless, it is a challenging task to solve this analytically, and in most cases it is determined experimentally by measuring or simulating the entire or a part of the array. This is what has been done in the work presented below, where antenna arrays have been full-wave simulated to take mutual coupling into account in the design.

Another source of error which may appear in the practical realisation of antenna arrays is an inaccuracy in the excitation coefficients of the radiating elements. There are several factors, which can influence the excitation coefficients of an antenna array. One distinguishes the errors due to the design and fabrication of the feed network, those caused by the environment of the antenna like the presence of a radome, and the errors depending on the conditions of use of the antenna such as temperature, ageing, and vibrations. These various sources of inaccuracy are classified between "systematic errors" and "random errors".

Systematic errors, like the influence of an antenna carrier, are usually simple to overcome because they can be trimmed out by correcting the beam forming network. Also, for electrically steerable antennas, small errors in the various paths of the feed network can be balanced by in-factory calibration of the antennas, after the final assembly. For example, a path of the feed network with higher loss is compensated by a lower attenuation of the corresponding amplitude setter. Nevertheless, not all systematic errors can be corrected. It is the case of quantisation errors of digital phase shifters and amplitude setters, which can only achieve discrete attenuation and phase shift values [132]. From this, a residual error limited by the value of the smallest bit (amplitude and/or phase) will always remain and cannot be reduced but by increasing the number of bits in the components.

On the other hand, random errors like those due to fabrication tolerances are not always correlated from element to element. These errors cannot be compensated with a simple adjustment of the

design, but in ESA, they are also most often reduced by calibration. The influence of random errors on the radiation characteristic of an array is often assessed using a statistical approach. In this case, the root mean square errors (rms) of the excitation coefficients are taken as random variables for the statistical equations. Assuming σ_a and σ_p the rms amplitude and phase (in radians) errors of the excitation coefficients, respectively; the overall rms error σ is defined by

$$\sigma^2 = \sigma_a^2 + \sigma_p^2. \quad (3.2.30)$$

This excitation error σ increases the side lobe level of the radiation characteristic of the antenna array. According to [133], this increased side lobe level is calculated by

$$|SLL| = |SLL_0| + \frac{2\sigma}{\sqrt{\eta \cdot N}}, \quad (3.2.31)$$

where $|SLL_0|$ is the side lobe level of the ideal radiation characteristic, η is the aperture efficiency, and N is the total number of elements in the array. Further, errors in the aperture distribution also result in a lowering of the antenna gain G . Again from [133], this is estimated using

$$\frac{G}{G_0} = \frac{1}{1 + \frac{3\pi}{4} \cdot \left(\frac{d}{\lambda}\right)^2 \cdot \sigma^2}, \quad (3.2.32)$$

in which d/λ is the inter-element spacing in wavelengths and G_0 is the gain of the antenna array fed without error.

Finally, the pointing accuracy of the main beam may be also reduced by inaccurate excitation coefficients. This pointing error is noted δ_φ and it is calculated by

$$\delta_\varphi = \theta_{-3\text{dB}} \sqrt{\frac{3}{N}} \frac{\sigma}{0.88\pi}, \quad (3.2.33)$$

with $\theta_{-3\text{dB}}$, the half-power beamwidth in radians [133].

Active Reflection Coefficient

In phased array antennas, the excitation coefficients of the elements are constantly adjusted to steer the main beam in real time. Also, the mutual coupling between the radiators varies with the pointing direction of the main beam, and the return loss of the array depends on the scan angle. In order to take this variation of the return loss into account, a so-called "active reflection coefficient" is defined [133]. This coefficient gives the return loss of a phased array antenna versus the pointing direction of its main beam. It is especially useful to detect the directions, in which the cumulative effects of internal and external couplings result in a reflection coefficient close to 1. For these scan angles, the antenna cannot interact with its environment and it is said to be blind.

3.2.5 Conclusion

This section has presented a summary of the theory of fixed-beam and phased array antennas. It aims at providing the reader with the techniques on which wide-aperture antennas are based, and it gives an insight into their working principle. The various concepts and formulas introduced in this section 3.2 constitute the theoretical background of the work reported in the rest of the chapter.

3.3 W-Band Antenna Arrays for On-Board Wake Vortex FMCW-Radar

3.3.1 Description of the Targeted Application

The fast growth of air traffic observed in the last decade has highlighted the importance of increasing the number of landing and take-off sequences in a majority of the airports worldwide. Also, in order to increase the aircraft throughput without compromising the security, a better understanding of the aircrafts' environment is necessary. Among the different risky phenomena to identify are wake vortices, which are generated by airplanes during landing and take-off. These turbulences present a risk for following airplanes and limit the maximum throughput of arriving and departing airplanes. If it were possible to detect the wake vortices from an airplane, the starting and landing time sequence could be reduced, and air traffic could be relaxed [134].

Several sensors are under development for on-board detection of wake vortices. Nevertheless, most of these systems like LIDAR equipments are based on an optical detection of air turbulences and are mainly limited to the clean air case [135], [136]. In return, they are less efficient in presence of rain or dusty air. These conditions however, represent the ideal situation for a microwave sensor because of the presence of snow, dust, or water drops as scatterers of electromagnetic radiation. Therefore, the development of dual sensor systems, optical and radar, is the most promising approach for all-weather operability [137], [138]. The basic specifications required for the on-board detection of wake vortices such as a high angular resolution, a compact size, and a sufficient scattering echo, lead naturally to the implementation of a millimetre-wave sensor. Furthermore, thanks to the relatively high attenuation of the signal at these frequencies, the millimetre-wave band allows for a limited operational range, which prevents interferences with other systems. Finally, due to the similarity of the system specifications, the considered wake vortex detection sensor is foreseen to be based on the same architecture as the next generation of automotive cruise control radar [139], [140]. The main differences between the two applications are limited to the lower detection threshold of the wake vortex radar, and the different radiation characteristic of the antennas.

The antennas presented in this section are the transmit and receive antennas developed for an on-board wake vortex detection sensor at W-Band. The front-end is a bi-static FMCW (Frequency Modulated Continuous Wave) radar with Doppler processing. Thanks to the reflection of the signal by small scatterers present in front of the aircraft, the rotating movement of the particles displaced by the wake vortices can be detected, and the turbulences become visible to the system. To implement this, a fixed-beam receive antenna and a steerable transmit antenna are designed for operation at 76.5 GHz. The transmit antenna is an RF-MEMS based phased array antenna radiating a narrow pencil beam fixed in the vertical plane, and electrically steerable in the horizontal plane. In the horizontal plane, it is intended to be steerable in twenty-one discrete positions between $\pm 30^\circ$. In the horizontal plane also, the main beam of the receive antenna is wide enough to cover the entire area scanned by the transmit antenna: $\pm 30^\circ$. Vertically, both antennas have identical broadside patterns with 5° half-power beamwidth. The horizontal specifications of the receive and transmit antennas are summarised in Fig. 3.5.

From the system point of view, in order to determine accurately the distance between the wake vortices and the nose of the aircraft, a minimum range resolution of 1 m is required for the sensor.

This specification determines the minimum bandwidth of the entire front-end, and thus also of the antennas. The minimum bandwidth of the front-end is determined from the required range resolution using

$$\Delta R = \frac{c}{2B}, \quad (3.3.1)$$

where ΔR is the range resolution of the sensor, c is the speed of light, and B is the bandwidth of the sensor. Hence, a range resolution of 1 m is achieved with a bandwidth of 150 MHz (0.2% at 76.5 GHz). Finally, in order to achieve a satisfactory Signal-to-Noise Ratio (SNR) for the echo, an antenna gain of 32 dBi for the transmit antenna, and 19 dBi for the receive antenna shall be achieved.

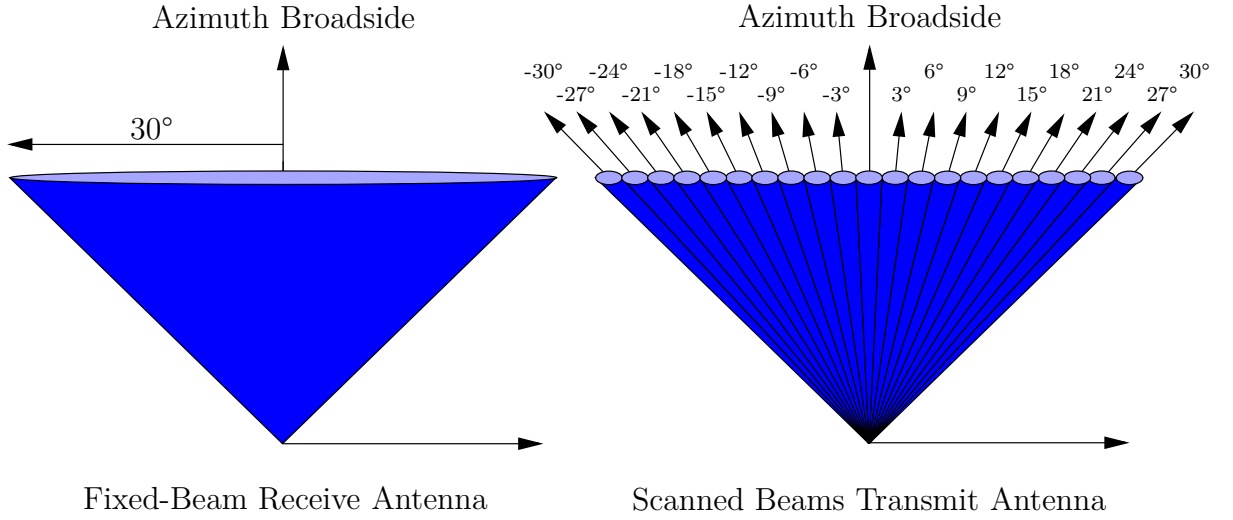


Fig. 3.5: Specifications of the transmit and receive antennas in the horizontal plane.

3.3.2 Fixed-Beam Patch Antenna Arrays on Rogers RT/Duroid 5880 Substrate

Design of the Antennas: Serially Fed Patch Antenna Array

The antennas are planar microstrip antenna arrays printed on low-loss Rogers RT/Duroid 5880 substrate ($\epsilon_r=2.2$, $\tan \delta=0.0009$ at 10 GHz [111]). The two arrays are realised with several serially fed patch antenna sub-arrays connected in parallel by a corporate feed network. The vertical (E-Plane) radiation characteristic of the antennas is determined by the length of the microstrip antenna sub-arrays and by the relative excitations of the patches. Thus, the sub-arrays are identical for both, the transmit and the receive antenna. They are realised with sixteen patches connected in series by narrow microstrip lines. On the other hand, the horizontal (H-plane) radiation characteristic is defined by the juxtaposition of several sub-arrays in that same plane. Also, since the radiation characteristics are different for the transmit and receive antennas in that plane, the number of sub-arrays in the two antennas is not the same. The transmit antenna radiates a narrow pencil-beam and is realised with twenty-eight sub-arrays. The receive antenna designed to achieve a 60°-wide main beam is realised with only three sub-arrays.

The design of the serially fed patch antenna array is achieved using the Extended Transmission Line Model (ETLM) presented in [37] and depicted in Fig. 3.6. The model takes the effect of the additional current density at the microstrip line/patch discontinuity into account. It is therefore more accurate than the model proposed in [141].

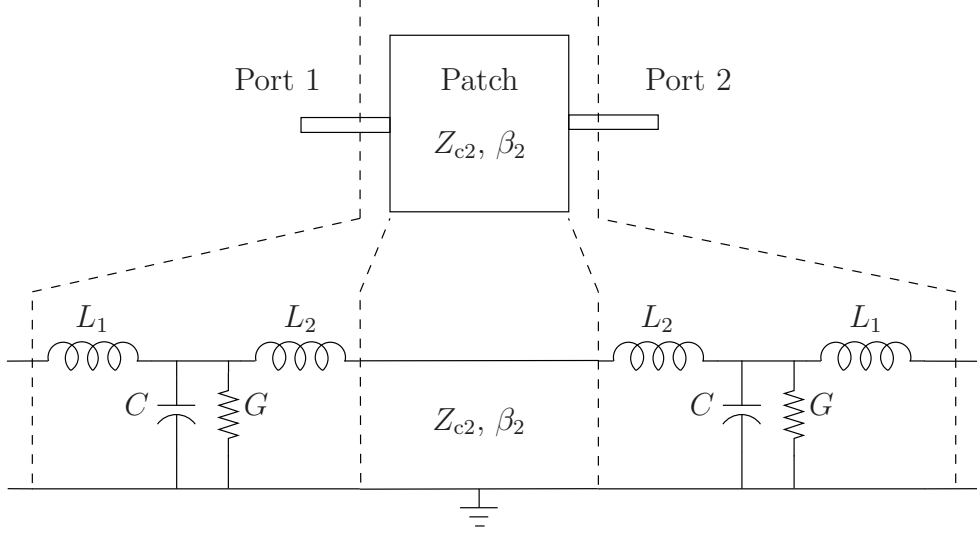


Fig. 3.6: Extended Transmission Line Model of a 2-port microstrip antenna.

According to the ETLM model, a single radiating slot is modelled by four lumped elements:

- L_1, L_2 : Inductances modelling the additional current density due to the step in width between the narrow feeding microstrip line and the patch.
- C : Capacitance modelling the additional electrical length of the patch due to the fringing fields.
- G : Conductance modelling the power radiated by the slot.

The patch itself is modelled by a simple transmission line having a low characteristic impedance Z_{c2} and a given propagation constant β_2 . The values of the lumped elements are calculated either from the formulas given by (3.3.2), (3.3.3), (3.3.4), and (3.3.5), or from the S-parameters simulated for the 2-port discontinuity. The formulas below are from [141] and [142].

$$L_1 = \frac{L_{w1}}{L_{w1} + L_{w2}} L_s \quad (3.3.2)$$

$$L_2 = \frac{L_{w2}}{L_{w1} + L_{w2}} L_s \quad (3.3.3)$$

$$C = \frac{\Delta l}{v Z_{c2}} \quad (3.3.4)$$

$$G = \frac{1}{\pi} \sqrt{\frac{\epsilon}{\mu}} \int_0^\pi \frac{\sin^2 \left(\frac{\pi w \cos \theta}{\lambda_0} \right)}{\cos^2 \theta} \sin^3 \theta \, d\theta \quad (3.3.5)$$

with

$$L_{w1} = \frac{Z_{c1} \sqrt{\epsilon_{r,eff1}}}{c} \quad (3.3.6)$$

$$L_{w2} = \frac{Z_{c2} \sqrt{\epsilon_{r,eff2}}}{c} \quad (3.3.7)$$

$$L_s(\text{nH}) = 0.000987 \cdot 10^6 h \left(1 - \frac{Z_{c2}}{Z_{c1}} \sqrt{\frac{\epsilon_{r,eff2}}{\epsilon_{r,eff1}}} \right)^2 \quad (3.3.8)$$

$$\frac{\Delta l}{h} = 0.412 \frac{\epsilon_{r,eff2} + 0.300 \frac{w}{h} + 0.262}{\epsilon_{r,eff2} - 0.258 \frac{w}{h} + 0.813} \quad (3.3.9)$$

In these formulas, h is the substrate thickness, w is the width of the patch, λ_0 is the free-space wavelength, and v is the phase velocity on the transmission line modelling the patch. Also, Z_{c1} (Z_{c2}) and $\epsilon_{r,eff1}$ ($\epsilon_{r,eff2}$) are the characteristic impedance and relative effective dielectric constant of the feeding microstrip line (of the transmission line modelling the patch), respectively.

The broadside pattern in the E-plane is achieved by choosing the appropriate length for the microstrip lines connecting the patches. It is calculated using the ETLM model in order to have one half of a guided wavelength between two consecutive radiating slots at 76.5 GHz. Such an antenna array is said to be resonant because of the 180°-electrical length between two neighbouring radiating slots at the design frequency. Further, if the transmission lines between the patches are supposed lossless, this 180°-electrical length can be removed, and the equivalent circuit shown in Fig. 3.7 is valid.

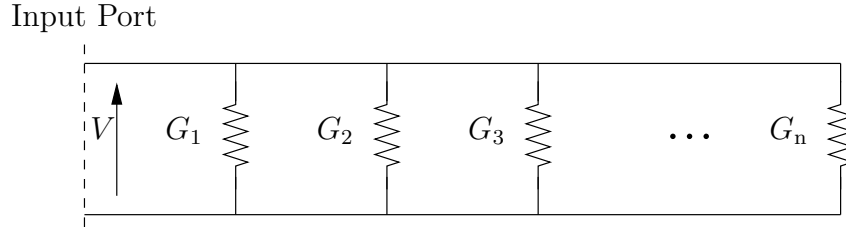


Fig. 3.7: Equivalent circuit of a resonant serially fed patch antenna array.

At the design frequency, the conductances G_i modelling the different slots of the array are all excited, in magnitude, by a same voltage V . This voltage is that applied at the input of the first patch. Hence, according to the power radiated by a slot given by

$$P_i = \frac{1}{2} \cdot \Re(V^2 \cdot G_i), \quad (3.3.10)$$

the ratio of the power levels radiated by two slots is equal to the ratio of their respective radiating conductances G_i/G_j . This property of serially fed antenna arrays is used to implement an excitation taper in the E-plane [143]. From (3.3.5), the radiating conductance of a slot depends on the width w of the patch. Thus, in an array, the relative power radiated by the different slots is determined by the relative widths of the patches. According to this, the equations (3.3.10) and (3.3.5) are used to determine the ratios between the widths of the patches to achieve the aimed excitation taper.

Further, the width of the microstrip lines connecting the patches is chosen as small as possible to prevent the fringing fields from being disturbed. For the antennas described here and in order to keep this width compatible with the technology, the microstrip lines are 100 μm -wide. Finally, the serially fed antenna sub-array has been optimised using full-wave simulations. The dimensions of the antenna sub-array obtained from these simulations are summarised in Table 3.1. A photograph of the sub-array realised on Teflon substrate is depicted in Fig. 3.8.

Patch and MSL N°	Patch Width [μm]	Patch Length [μm]	MSL Length [μm]
1	1100	1225	1381
2	1100	1225	1381
3	1100	1225	1381
4	1100	1225	1381
5	1200	1238	1381
6	1300	1231	1361
7	1400	1227	1331
8	1600	1227	1331
9	1600	1227	1331
10	1400	1227	1361
11	1300	1231	1381
12	1200	1238	1381
13	1100	1225	1381
14	1100	1225	1381
15	1100	1225	1381
16	1100	1225	—

Table 3.1: Dimensions of the serially fed microstrip antenna array with sixteen patches.

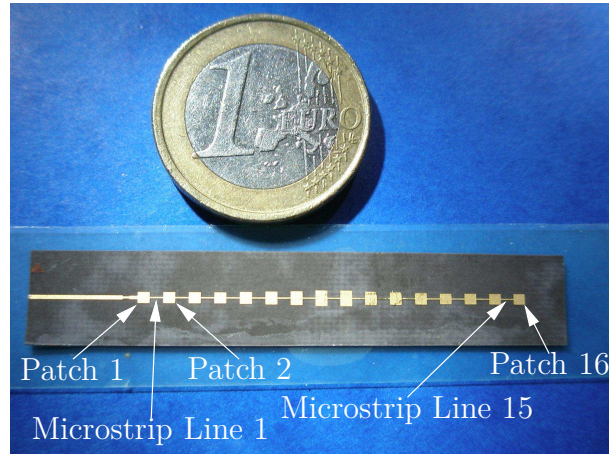


Fig. 3.8: Photograph of the serially fed patch antenna sub-array with sixteen patches.

In Table 3.1, the patch with the index "1" is the patch directly connected to the input port of the sub-array. Also, the microstrip line with the index "1" is the line between the patch "1" and the

patch "2". This numbering chosen for the elements of the sub-array is illustrated in Fig. 3.8. The widths of the patches are tapered from 1100 μm for the radiators placed at the extremities of the sub-array up to 1600 μm for those close to its centre. This allows for a stronger radiation of the elements in the middle of the array and reduces the side lobe level in the E-plane characteristic. The lengths of the patches do not vary much along the sub-array and are only a couple of microns shorter for the wider elements. In return, the lengths of the various microstrip lines differ to a larger extend. About the centre of the array, they are 50 μm shorter than at its ends.

Design of the Antennas: Fixed-Beam Transmit and Receive Antennas

The 3° of beamwidth required for the transmit antenna in the H-plane is achieved with twenty-eight microstrip antenna sub-arrays placed side by side. They are connected in parallel by a 1 to 28 corporate feed network. The feed network is realised using asymmetrical 1 to 2 T-junction power dividers designed to achieve an excitation taper for the twenty-eight sub-arrays. The excitation coefficients were computed by a so-called "Remez"-type algorithm [42]. The algorithm calculates excitation coefficients providing an array factor that is the best approximation in the Tchebycheff sense of a targeted ideal radiation pattern [43], [44]. The coefficients computed with the method allow for the realisation of an aimed beamwidth, here 3°, as well as for a minimum uniform side-lobe level. A layout of the corporate feed network is depicted in Fig. 3.9. The theoretical coefficients aimed for the twenty-eight sub-arrays and the full-wave simulated coefficients of the designed feed network are shown in Fig. 3.10.

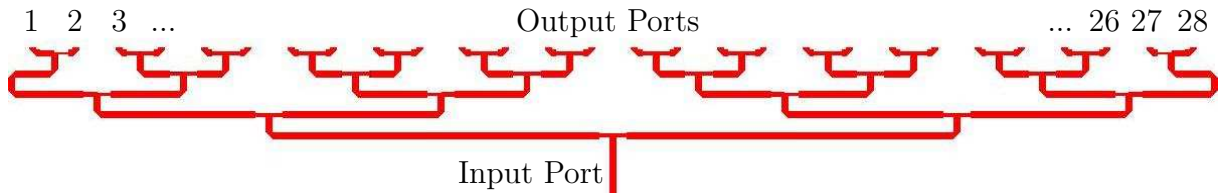


Fig. 3.9: Layout of the 1 to 28 corporate feed network.

The histogram shows a slight discrepancy between the theoretical coefficients and those calculated by full-wave simulations. This is mainly explained by the finite width achievable for the microstrip lines in the power dividers. In order to ensure a good repeatability of the structures, the minimal width allowed by the technology for the microstrip lines is 100 μm . This limits the values of the ratios available to distribute the power to the two output ports of the power dividers, and implies an approximation of the theoretical excitation coefficients. For this reason, it is challenging to design a network feeding the first and last sub-arrays (1 and 28) with a strong coefficient (13.5% of the overall power each), whilst the neighbouring elements have to be fed with only 1% of the total power. The approximated feeding coefficients modify the pattern radiated by the antenna in the H-plane. The influence on the array factor can be estimated using the statistical approach presented in section 3.2.4. The rms amplitude and phase errors calculated from the simulated coefficients are $\sigma_a = 0.04167$ and $\sigma_p = 0.08489$, respectively. They correspond to an overall rms error of $\sigma = 0.09457$ for the coefficients of the feed network. From (3.2.31) and assuming an aperture efficiency of $\eta = 0.4$, this error increases the side lobe level from -17.8 dB (theoretical value) up to -13.5 dB. Nevertheless, the decrease in gain caused by that same error is not significant. Calculated

using (3.2.32), the actual antenna gain is expected to be only 0.035 dB below the gain that would be achieved with the ideal excitation taper.

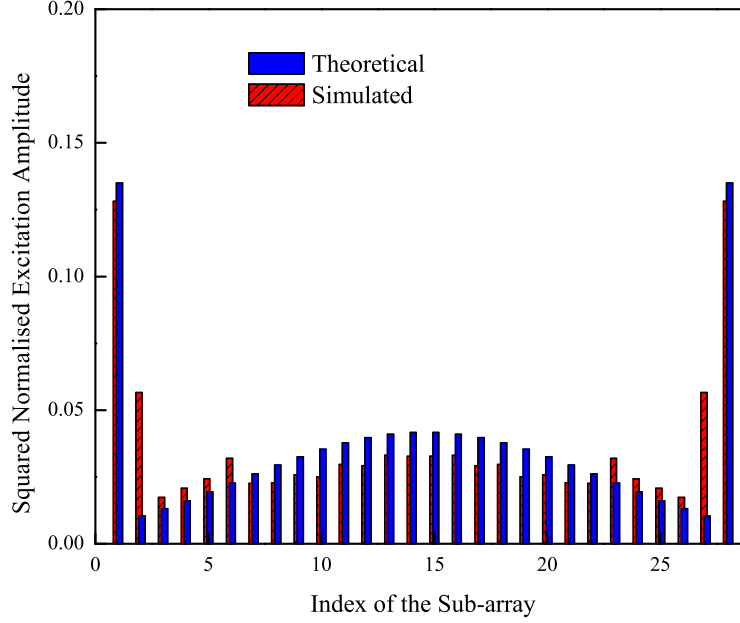


Fig. 3.10: Theoretical and simulated excitation coefficients of the 1 to 28 corporate feed network.

Finally, in order to steer electrically the main beam of the antenna in $\pm 30^\circ$ without grating lobes, the antenna array is designed with an inter-element spacing of $2400\text{ }\mu\text{m}$ (0.612λ). It is more than the conventional $\lambda/2$ spacing, but it is sufficient to achieve a grating lobe-free pattern and limits the coupling between neighbouring sub-arrays. A photograph of the fixed-beam transmit antenna is shown in Fig. 3.11.

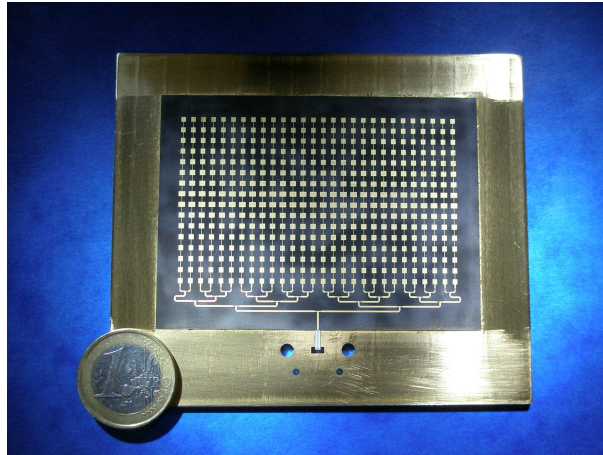


Fig. 3.11: Photograph of the fixed-beam transmit antenna.

The feed network of the receive antenna is realised with a 3 to 1 coupled transmission line directional coupler. The structure allows for a weak excitation of the two side sub-arrays, which is necessary to achieve the 60°-wide main beam required for that antenna. The theoretical and simulated excitation coefficients of the 3 to 1 power combiner are plotted in Fig. 3.12. The graph shows a very good agreement between the theoretical values and the full-wave simulated excitation coefficients. A photograph of the receive antenna on Rogers substrate is depicted in Fig. 3.13.

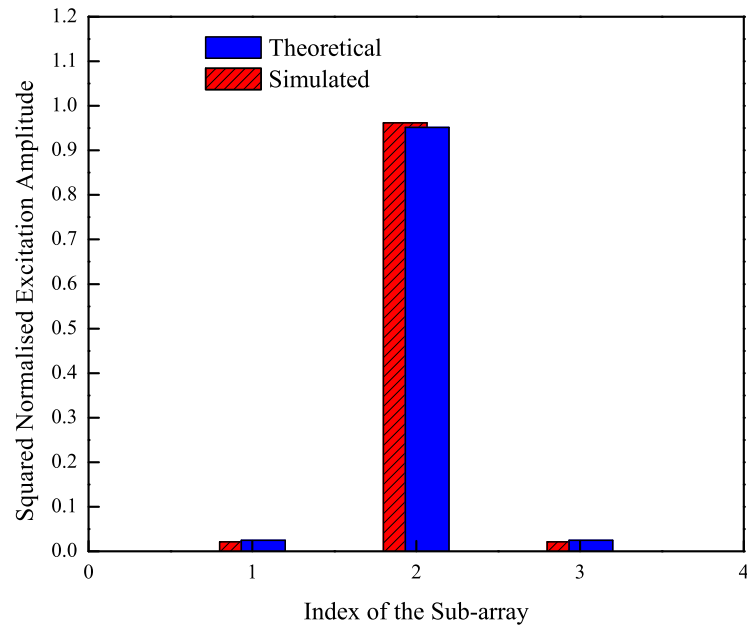


Fig. 3.12: Theoretical and simulated excitation coefficients of the 3 to 1 power combiner.

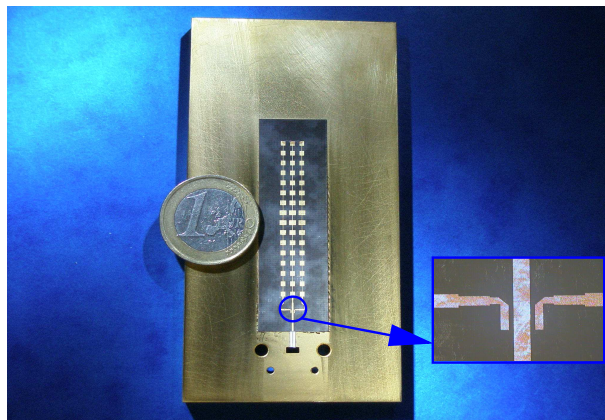


Fig. 3.13: Photograph of the receive antenna.

Technology and Fabrication Tolerances

The transmit and receive antennas have been fabricated on 5 mil-thick ($127\text{ }\mu\text{m}$) Rogers RT/Duroid 5880 substrate. The substrate was fully metallised on both sides with $8\text{ }\mu\text{m}$ -thick electroplated copper. The antennas were etched out of the top copper foil by lithography, and the back side metallisation has been left un-patterned. Due to the high operating frequency of the antennas at 76.5 GHz, their electrical properties are highly sensitive to fabrication tolerances. This is especially true for the matching frequency of the antennas, which might be shifted upwards if the under-etching of the structures is too pronounced. Also, in order to determine the fabrication accuracy required for the structures designed at 76.5 GHz, a single patch has been simulated for $8\text{ }\mu\text{m}$, $5\text{ }\mu\text{m}$, and $3\text{ }\mu\text{m}$ of under-etching. For these values, the simulated frequency shifts were found to be 1.3%, 0.8%, and 0.5%, respectively. From this, it was decided to keep the under-etching of the structures below at least $3\text{ }\mu\text{m}$ to ensure satisfactory matching properties for the antennas.

Characterisation and Measurements

First, the microstrip antenna sub-array shown in Fig. 3.8 has been manufactured and measured in an anechoic chamber. The E-plane radiation characteristic measured for the sub-array is plotted together with the simulated far field pattern in Fig. 3.14. This radiation characteristic is identical to the E-plane pattern of the complete transmit and receive antennas, providing that their feed networks are shielded as it is intended in the demonstrator.

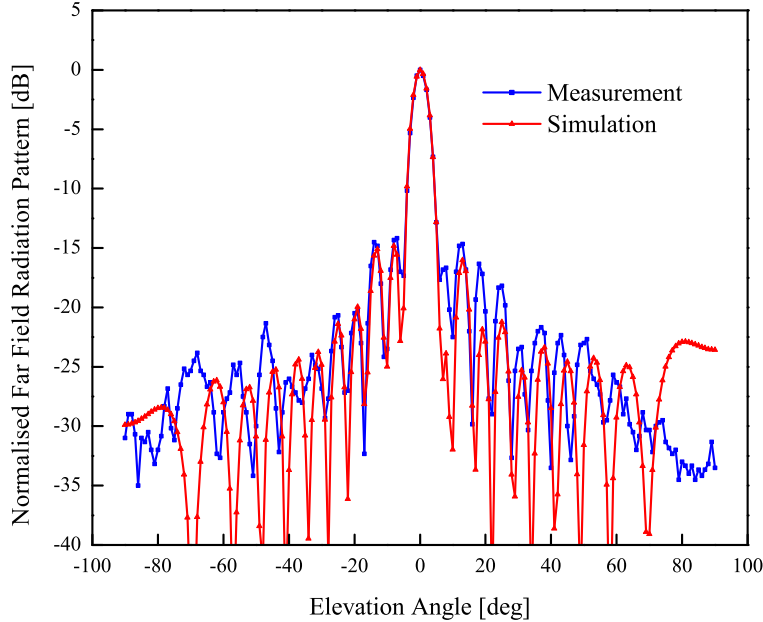


Fig. 3.14: Measured and simulated E-plane far field pattern of the antenna sub-array at 76.5 GHz.

According to the measurement, the side lobe level of the antenna array is below -14 dB and the 3 dB beamwidth is 5° , as specified for the antennas in the E-plane. The gain measured for the array is 15 dBi and the radiation pattern is exactly broadside at 76.5 GHz. Away from the design frequency, a slight off-axis angle is observed for the direction of the main lobe. This beam squint is about 1° per GHz and is due to the intrinsic principle of the antenna. Above or below the design frequency, the microstrip lines between the patches have an electrical length different from the one they have at the design frequency, and the radiating slots are fed with a phase gradient. Nevertheless, for bandwidths below 2-3% this off-axis pointing remains small and below 1° . In the present case also, thanks to the small 150 MHz bandwidth required for the sensor, it does not represent a limitation for the overall performance of the system. The return loss of the serially fed array measured around the design frequency is shown in Fig. 3.15. The input matching is better than -10 dB from below 75 GHz up to above 77.1 GHz (2.7%).

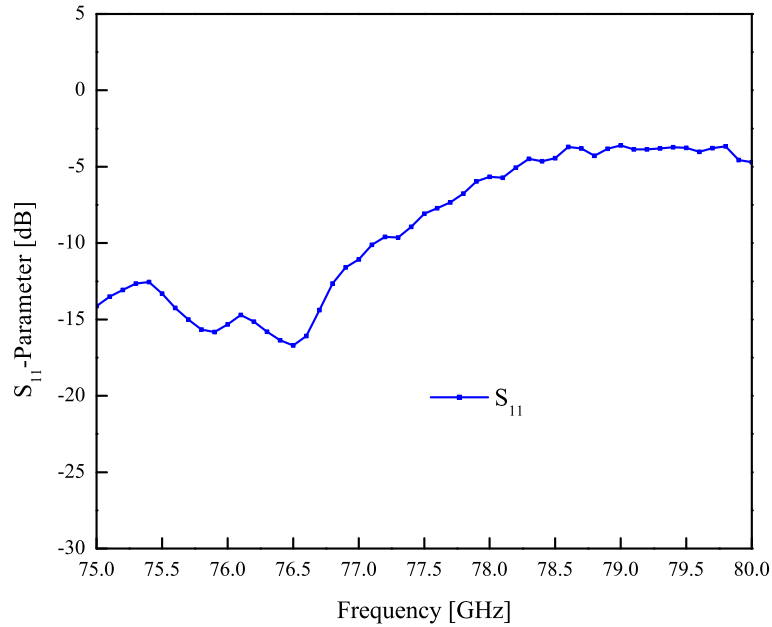


Fig. 3.15: Measured return loss of the serially fed patch antenna sub-array.

The complete transmit and receive antennas shown in Fig. 3.11 and 3.13, respectively, have been also measured in an anechoic chamber. As already mentioned, for these antennas the measurements of the far field characteristic and return loss have been performed with an absorber covering the feed network. This was necessary to prevent an increase of the side lobes due to the radiation of the feed networks fabricated on low permittivity substrate. The simulated and measured H-plane far field pattern of the fixed-beam transmit antenna is given in Fig. 3.16. The H-plane far field pattern of the receive antenna is plotted in Fig. 3.17.

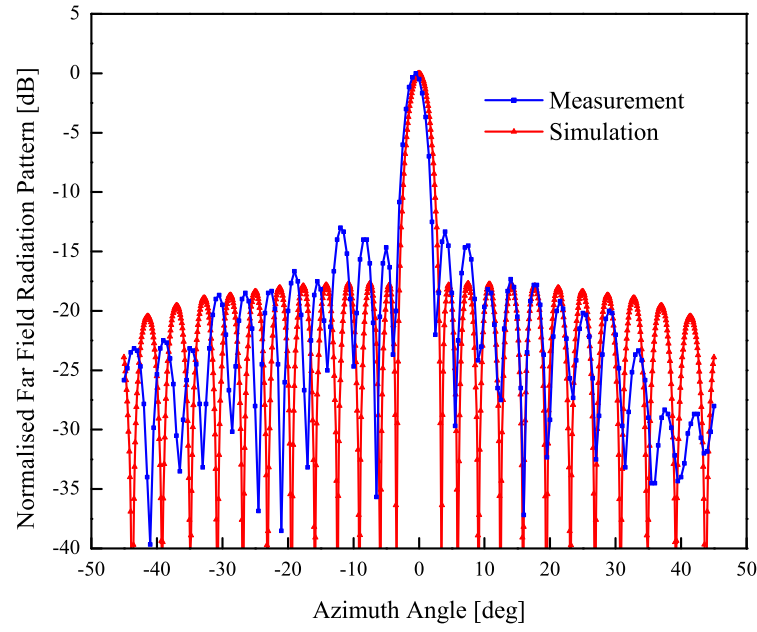


Fig. 3.16: Measured and simulated H-plane far field pattern of the transmit antenna at 76.5 GHz.

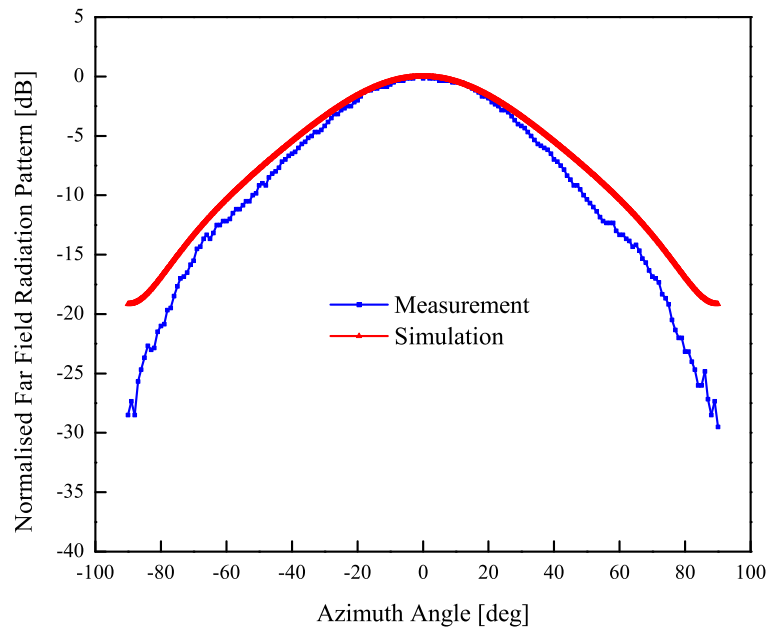


Fig. 3.17: Measured and simulated H-plane far field pattern of the receive antenna at 76.5 GHz.

In Fig. 3.16, the measured radiation characteristic exhibits a side lobe level of about -13 dB and a 3 dB beamwidth of 3°, as required in the specifications. The gain of the transmit antenna measured at 76.5 GHz is 25.5 dBi, which corresponds to a radiation efficiency of 19.7%. This radiation efficiency is limited by the dielectric, ohmic, and radiation losses in the entire array, and more importantly in the corporate feed network. The total level of loss in the antenna is estimated at about 7.8 dB. The deviations observed for the measured far field pattern are explained, among others, by the previously discussed inaccuracies in the excitation coefficients of the feed network (Fig. 3.10). The radiation pattern measured for the receive antenna is in good agreement with the simulation (Fig. 3.17). However, the measured 3 dB beamwidth is 51.5° and is slightly narrower than the specified one (60°). The gain measured for the receive antenna is 14.2 dBi. From (3.2.5) and (3.2.8), this corresponds to a radiation efficiency of 25.1% for that antenna with 3 sub-arrays. In this case however, because of the short length of the transmission lines in the feed network, this limited radiation efficiency cannot be justified by the same lossy mechanisms as for the transmit antenna. The receive antenna has been fabricated in a separated process run, and it has been measured with a different feeding structure. Contrary to the previous antennas, this antenna was fed through a coplanar to microstrip transition different from the E-field probe presented in the first chapter. For this reason, the gain and efficiency of this receive antenna cannot be directly compared to those demonstrated for the two firstly presented antennas. This explains also why the gain measured for this receive antenna is lower than the gain of 15 dBi measured for a single antenna sub-array. The return loss measured for the transmit and receive antennas is plotted in Fig. 3.18 and 3.19, respectively.

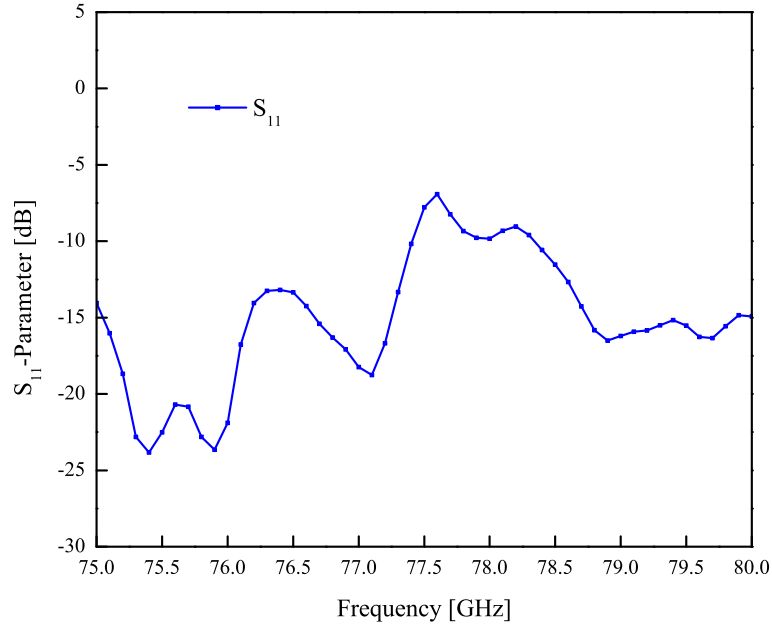


Fig. 3.18: Measured return loss of the transmit antenna.

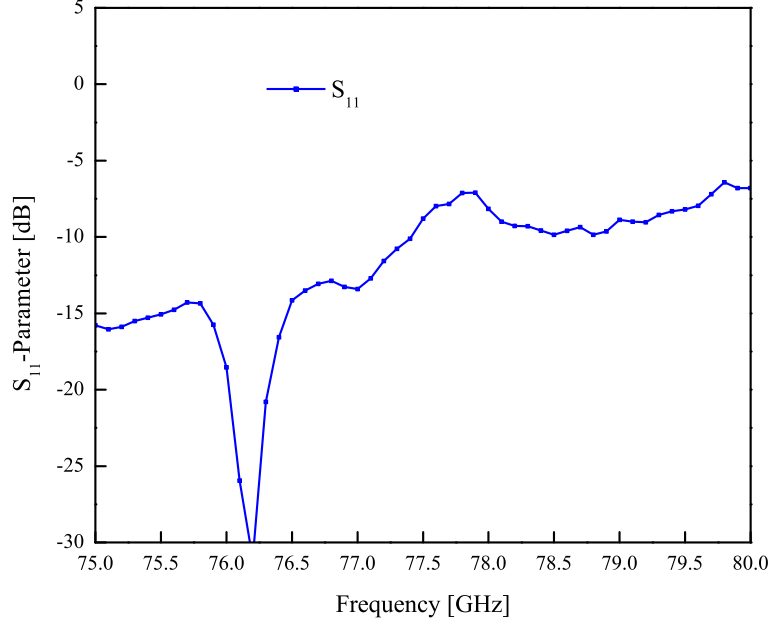


Fig. 3.19: Measured return loss of the receive antenna.

For the transmit antenna, the return loss is better than 10 dB from 75 GHz up to 77.3 GHz. This bandwidth is almost identical to that measured for the receive antenna: better than 10 dB from below 75 GHz up to 77.4 GHz. Both antennas have a bandwidth larger than 3%, which is also wider than the 0.2% of bandwidth required for the sensor.

Optimisation of the 1 to 28 Corporate Feed Network

The realisation of the previously presented 1 to 28 corporate feed network has highlighted some drawbacks, which might be cumbersome for the overall performance of the antenna. On one hand, the low permittivity Rogers RT/Duroid 5880 substrate favours radiation from the feed network. Also, if the feed network is not shielded, this radiation increases the side lobe level of the antenna characteristic and augments the insertion loss in the feed network. For this reason, high permittivity substrates are often preferred for the realisation of feed networks. On the other hand, the T-junction power dividers implemented in the feed network are simple to design and to manufacture, but they offer limited performance. They are not matched at the output ports ($S_{22} \neq 0$ and $S_{33} \neq 0$), and these two output ports are not isolated ($S_{23} \neq 0$ and $S_{32} \neq 0$). This can be overcome by using other kinds of power dividers such as Wilkinson or branch line coupler power dividers. In these structures, the addition of a lumped resistance enables a satisfactory matching at all ports as well as a theoretically infinite decoupling of the output ports ($S_{23} = 0$ and $S_{32} = 0$).

For these reasons, the 1 to 28 feed network was intended to be redesigned on LTCC DuPont 943 substrate ($\epsilon_r = 7.4$, $\tan \delta = 0.0015$), and using branch line coupler power dividers. A layout of the foreseen feed network is shown in Fig. 3.20.

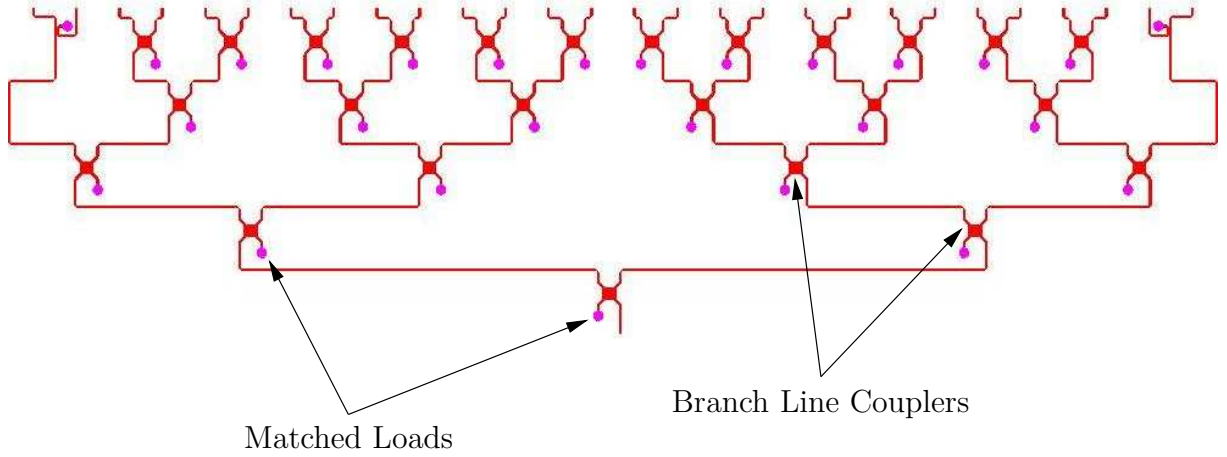


Fig. 3.20: Layout of the foreseen 1 to 28 corporate feed network with branch line couplers and on LTCC.

Nevertheless, despite the higher dielectric constant of the LTCC material and the lower radiation from the feed network on ceramic, the loss in the microstrip lines on LTCC (1.4 dB/cm at 76.5 GHz) is higher than that on Rogers RT/Duroid 5880 (0.5 dB/cm at 76.5 GHz). This is justified by the better performance of Teflon based substrates in terms of loss tangent, roughness, and conductivity of the metallisation. This appears as the price to pay for a substrate that limits radiation.

3.3.3 Conclusion

The work presented in this section 3.3 constitutes the first step towards an RF-MEMS based phased array antenna at W-band. The RF-MEMS phase shifters intended for integration in the transmit antenna are 4-bit phase shifters processed in the EADS Innovation Works RF-MEMS technology [38], [144]. In a later integration, they will be mounted between the feed network on LTCC and the antenna sub-arrays on soft substrate [139]. In the section, the performance measured for the transmit and receive antennas is satisfactory and meets the specifications, except in terms of antenna gain. The gain of the transmit antenna was demonstrated to 25.5 dBi at 76.5 GHz. This is 6.5 dB below the peak gain targeted for that antenna.

3.4 Ka-Band Phased Array Antenna for Satellite Communication

3.4.1 Description of the Targeted Application

Since the advent of satellite communication in the late 60's, two kinds of antennas have been widely implemented in satellite transceivers: parabolic dishes on-board of large satellites and Omni-Directional Antennas (ODA) in small satellites. Thanks to their directional pattern, parabolic dishes enable high transmission data rates and allow for a reduced transmit/receive power. However, because of their large size and bulkiness, parabolic dishes cannot be mounted on small satellites having limited payloads. Also, small satellites, commonly known as micro- or nano-satellites, are in most cases constrained to operate ODA with limited performance. Furthermore, small satellites are sensitive to inertia and they cannot sustain mechanically steerable antennas for beam scanning. To overcome this situation, electrically steerable antennas have been recently considered

for implementation in small satellites [145], [146]. Also, besides the advantages that they provide for communication links, phased antennas offer un-precedent opportunities for micro-satellites in the field of imaging and earth observation [147], [148].

The antenna demonstrated in the coming sections is a phased array antenna designed for up-link satellite communication at 35 GHz. The antenna is electrically steerable in the H-plane and shows a fixed broadside pattern in the E-plane. In order to facilitate the integration of the antenna in the complete front-end, a ceramic dielectric was favoured over an organic soft substrate for its fabrication. The antenna is made out of a 6-layer LTCC DuPont 943 substrate ($\epsilon_r=7.4$, $\tan \delta=0.0015$). Later on, in a complete front-end, these ceramic layers could be the top layers of a 3D integrated LTCC module that contains the different components of the transceiver. The beam radiated by the antenna is steered by means of RF-MEMS phase shifters processed on silicon. As it is described in the coming sections, these phase shifters are integrated in a hybrid fashion onto the ceramic substrate of the antenna.

3.4.2 Fixed-Beam Aperture Coupled Patch Antenna Array on LTCC

Architecture of the Fixed-Beam Antenna

The fixed-beam antenna is a four by four microstrip antenna array. The antenna is designed with four sub-arrays connected in parallel by a 1 to 4 corporate feed network. The corporate feed network distributes the RF-power to four feeding microstrip lines, where each microstrip line is used to feed one of the four sub-arrays. The radiating patches are patterned on the top LTCC layer. The feed network, corporate feed network plus feeding microstrip lines, is processed five layers below the patches, i.e. one LTCC layer above the back side of the 6-layer LTCC substrate. Three LTCC layers below the patches, a metal plane is realised. It serves as ground plane for both, the patches and the buried microstrip feed network. Each one of the four sub-arrays is designed with four patches connected in series by a buried feeding microstrip line. The patches are connected to the feeding line according to the aperture coupling principle, with coupling slots patterned in the common ground plane [39]. A cross-section of the multilayer ceramic substrate showing the various metal layers is depicted in Fig. 3.21.

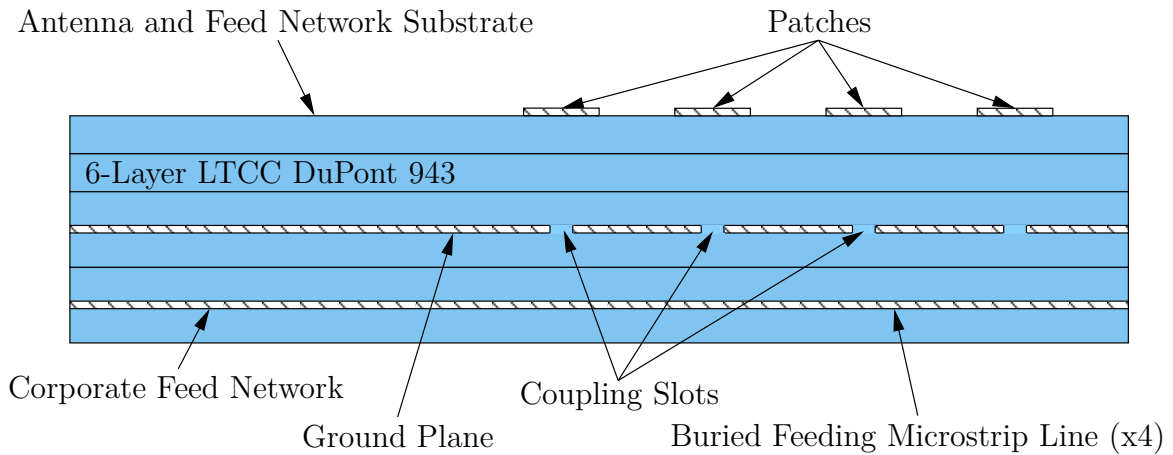


Fig. 3.21: Cross-section of the Ka-band antenna array on 6-layer LTCC DuPont 943 substrate.

The aperture coupling technique offers major advantages over standard probe-fed structures. Firstly, the feed network is separated from the antenna by a fully metallised plane acting as a shield. Thanks to this, the far field pattern of the antenna is not disturbed by the radiation of the feed network, as discussed in section 3.3. Further, microstrip antennas radiate because of the presence of fringing fields at the edges of the patch. For probe-fed patches, these fringing fields are influenced by the feeding line, and the far field characteristic is disturbed especially in terms of symmetry and cross-polarisation. Another advantage of aperture coupled feedings is that the thickness of the substrate can be chosen independently for the radiators and for the feed network. Typically, a large thickness is chosen for the substrate of the antenna in order to maximise its radiation and bandwidth, whilst a thinner dielectric is often preferred for the feeding lines. Nevertheless, in the present case, the position of the ground plane could not be chosen arbitrarily, and it had to be placed in the middle metal layer of the 6-layer LTCC setup. This was imposed by technological reasons specific to the LTCC process.

In each sub-array, the four patches are inductively coupled to the H-field of the microstrip line mode. The feeding structures are designed with H-like slots coupling with the microstrip line processed $220\text{ }\mu\text{m}$ below the ground plane. The last patch of the sub-array is placed one quarter of guided wavelength away from the open-circuited end of the buried microstrip line, at a maximum of the magnetic field. Further, since the radiation pattern to achieve in the E-plane is broadside, all four patches of a sub-array have to be fed in phase. This is done by placing them one guided wavelength away from each other. All coupling slots, feeding lines, and microstrip patches have their symmetry axes that coincide, and there is no offset between them.

Model and Design of the Fixed-Beam Antenna

A metal-free aperture patterned in the ground plane of a microstrip line and coupling with its H-field is seen as an impedance in series. Also, for an aperture coupled patch at resonance, the value of that impedance is real and corresponds to the radiating resistance of the patch. Thus, at the design frequency, the patch antenna sub-array with four patches can be represented with four resistances in series and spaced by a guided wavelength. This 360° -electrical length between the patches may be removed to simplify the model, and the sub-array is modelled only by four series resistances. A schematic of the aperture coupled sub-array with four microstrip antennas is shown in Fig. 3.22.

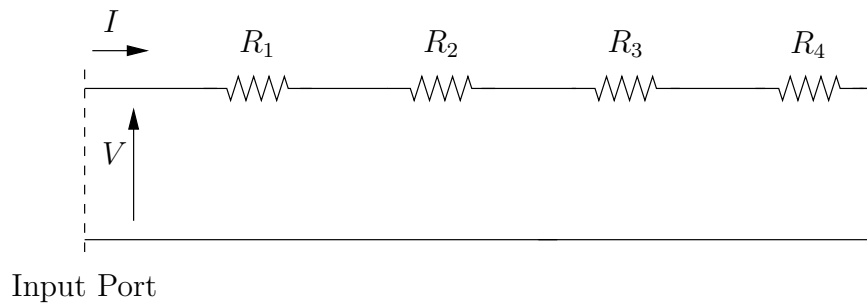


Fig. 3.22: Schematic of the aperture coupled sub-array realised with four patches at the design frequency.

In order to optimise the side lobe level of the antenna characteristic in the E-plane, an excitation taper is implemented among the four patches of the sub-array. Since all four patches are in series, they are all fed by the same current, or H-field. Thus, the ratio of the power radiated by two patches is equal to the ratio of their respective radiating resistances. From this, an excitation taper can be implemented by choosing suitable radiating resistances for the elements of the sub-array. There exist principally two techniques to design aperture coupled microstrip antennas with prescribed resistances. This may be done by adjusting the width of the patch itself as demonstrated in section 3.3, or by choosing the appropriate size for the coupling slot. Nevertheless, in the particular case of aperture coupled patches, antennas with a width twice as long as their length are convenient in order to prevent higher modes. Thus, all patches are designed according to this technique and the excitation taper is achieved by adjusting the length of the coupling slots. Large coupling slots provide strong couplings between the feeding line and the radiator, and they achieve large radiating resistances. In return, small coupling slots achieve weak couplings between them and the effective radiating resistance is small. For this reason, the four sub-arrays are designed with $600\mu\text{m}$ -long coupling slots for the two patches close to the array centre, and with $525\mu\text{m}$ -long coupling slots for the first and last patches. All coupling slots are H-shaped and are $100\mu\text{m}$ -wide.

The feed network is designed with three power dividers. They are asymmetrical T-junction power dividers, and they are designed to implement an excitation taper in the H-plane of the aperture. The excitation coefficients used to feed the four sub-arrays have been calculated using the method already presented in section 3.3 and described in [42]. The theoretical excitation coefficients as well as those calculated by full-wave simulation of the designed feed network are given in Fig. 3.23.

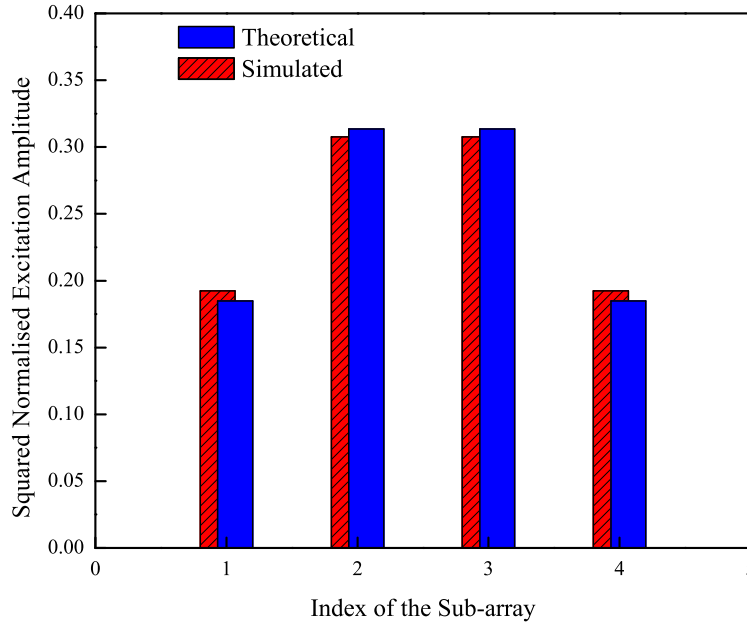


Fig. 3.23: Theoretical and simulated excitation coefficients of the feed network in LTCC DuPont 943.

A transparent drawing of the complete fixed-beam antenna array displaying the features described above is given in Fig. 3.24. A photograph of the realised antenna is shown in Fig. 3.25. As indicated on the illustration 3.24, metal-free areas are patterned in the ground plane of the antenna. These metal-free areas allow for ceramic-to-ceramic contact regions and aim at preventing a delamination of the ceramic substrate. They are placed $800\mu\text{m}$ (approximately $\lambda_d/4$) away from the microstrip antennas, where they do not influence the RF-behaviour of the structures.

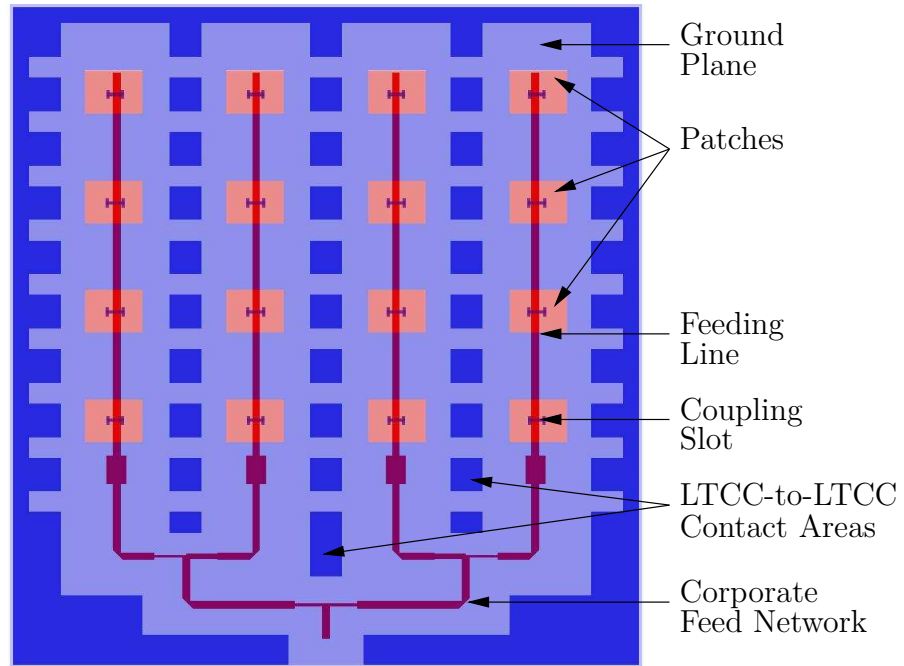


Fig. 3.24: Transparent drawing of the fixed-beam patch antenna array on LTCC DuPont 943.

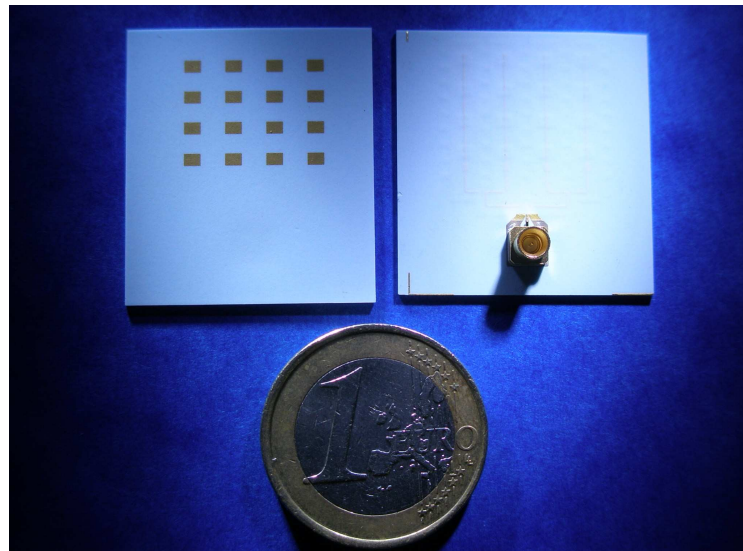


Fig. 3.25: Photograph of the Ka-band fixed-beam antenna array on LTCC: front view(left) and back view(right).

The antenna has been fabricated by Via Electronic GmbH, whose design rules for both, the DuPont 951 and 943 LTCC green tapes, are summarised in [70]. The RF-interface is achieved with a mini-SMP connector manufactured by Rosenberger Hochfrequenztechnik GmbH & Co. KG. The connector itself is designed for operation up to 40 GHz [149], and it is soldered on a footprint patterned on the back side of the antenna. The footprint is connected to the buried microstrip feed network by means of LTCC vias. The mini-SMP to microstrip line transition has not been de-embedded in the measurement results presented below.

Characterisation and Measurements

The antenna has been measured in an anechoic chamber at the University of Ulm. The radiation characteristic measured in the H- and E-planes is plotted in Fig. 3.26 and 3.27, respectively. Also, the measured and full-wave simulated return loss of the antenna is given in Fig. 3.28.

The measurement results presented in these three graphs show good agreement between measurement and simulation. The 3 dB beamwidth is 26° in the H-plane and 37° in the E-plane. In these two planes also, the side lobe level is -13 dB and -16.8 dB, respectively. In the H-plane, the antenna is strictly symmetric, and the slight 3° off-axis angle observed between simulation and measurement is attributed to an inaccuracy in the positioning of the antenna during the measurement. This beam squint is close to that observed in the E-plane: 4.5° . The gain measured for the antenna is 13.4 dBi, and its directivity, determined experimentally using (3.2.8), is 14.5 dBi. From this, the radiation efficiency of the antenna calculated using (3.2.5) is 78%.

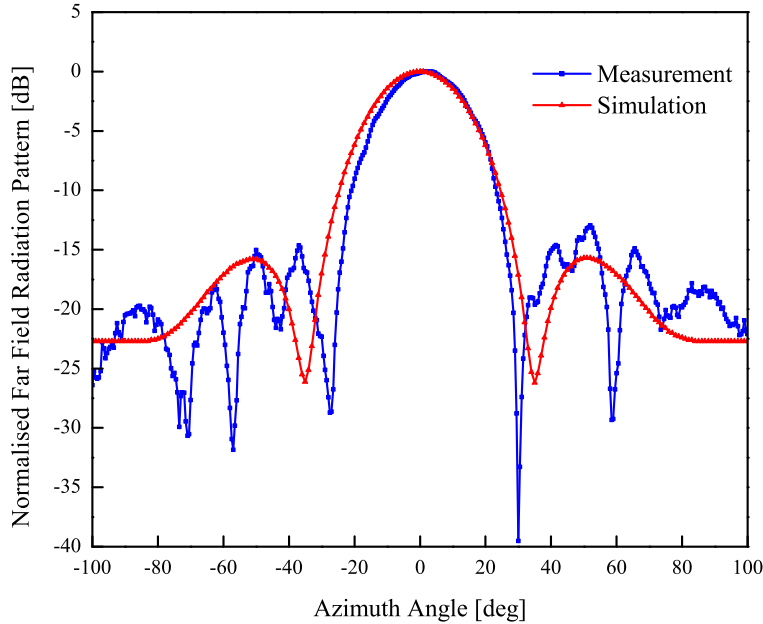


Fig. 3.26: H-plane far field pattern of the fixed-beam antenna on DuPont 943 at 35 GHz.

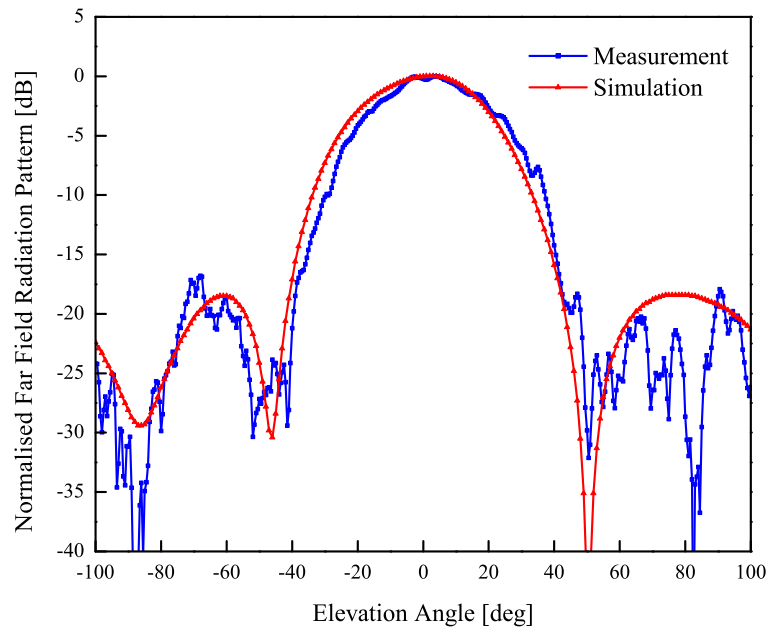


Fig. 3.27: E-plane far field pattern of the fixed-beam antenna on DuPont 943 at 35 GHz.

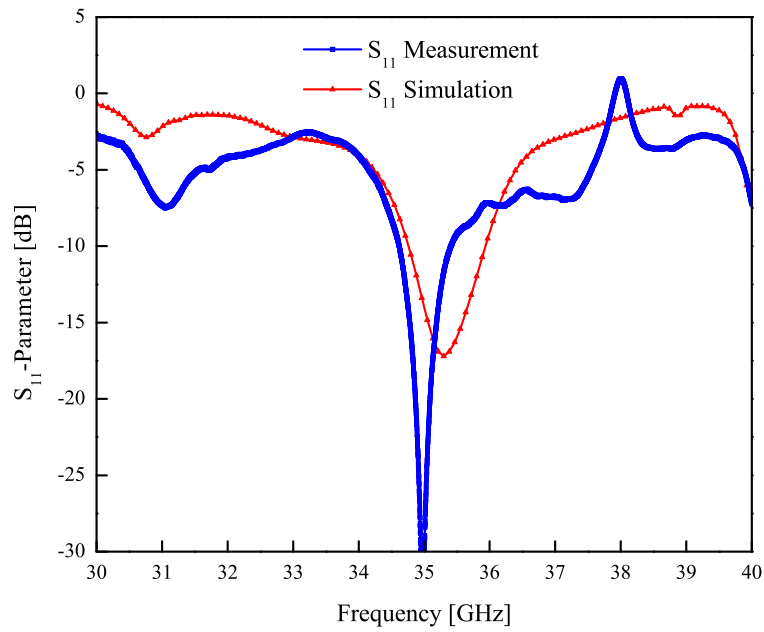


Fig. 3.28: Return loss of the fixed-beam antenna on LTCC DuPont 943.

Further, since the antenna is intended for integration on top of a 3D integrated module, its operational performance shall remain satisfactory even at high temperatures. This has been tested by measuring its return loss over temperature. The temperature range of the experiment, limited by the setup, was between room temperature and approximately 130°C. The matching properties of the antenna, resonance frequency and return loss at 35 GHz, have been extracted from the measurements and are summarised in Fig. 3.29.

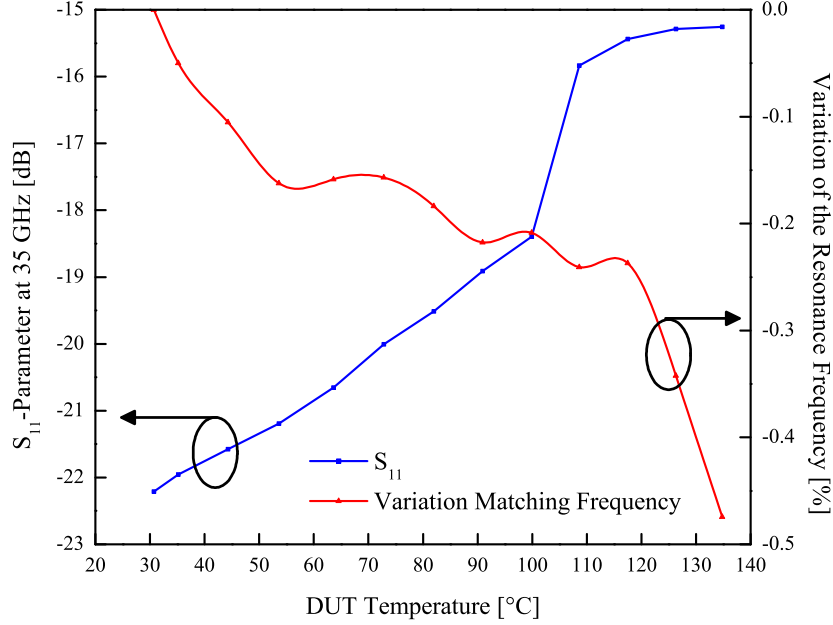


Fig. 3.29: Resonance frequency and return loss at 35 GHz of the fixed-beam antenna over temperature.

A direct conclusion that can be drawn from the experiment concerns the matching frequency. It decreases of about 0.47% as the temperature of the substrate increases between 30°C and 130°C. This down shift of the resonance frequency was expected, and it can be explained by two different phenomena. On one hand, it is explained by the geometrical extension of the structures, when the antenna substrate is warmed up. This geometrical dilatation is quantified by the TCE of the material, given at 6 ppm/°C for the DuPont 943 substrate.

The second phenomenon, which contributes to this shift is the temperature-dependence of the dielectric constant of the material. The variation of ϵ_r over temperature for that same ceramic material has been investigated in the second chapter of the thesis. In section 2.7, it was shown that the dielectric constant increases of about 96 ppm/°C, as the temperature increases within a similar range. Logically, this higher dielectric constant at high temperature leads to a down shift of the matching frequency of the antenna. On the other hand, the plot in Fig. 3.29 shows also the return loss of the antenna at 35 GHz and over temperature. S_{11} increases as the temperature of the DUT goes up, from -22.2 dB at 30.7° up to -15.25 dB at 134.8°. This degradation of the return

loss is justified by the same mechanisms, geometrical extension and temperature-dependence of the dielectric constant, as those explaining the down shift of the resonance frequency. The return loss remains nevertheless acceptable and better than 15 dB over the entire temperature range up to 130°C.

3.4.3 Phased Array Antenna

The fixed-beam antenna demonstrated in the previous section has been used for the development of a 1-dimensional electrically steerable antenna. To do so, it has been equipped with four digital RF-MEMS phase shifters, which are placed between the corporate feed network and the four antenna sub-arrays. They enable the feeding of the sub-arrays with a controlled relative phase gradient and allow for a beam steering in the H-plane of the aperture.

Three RF-MEMS technologies were originally intended for integration into the antenna. These technologies, all based on silicon, are provided by EADS Innovation Works (EADS-IW), Thales Research and Technology (Thales-RT), and by the Fraunhofer Institute for Silicon Technology (Fraunhofer-ISIT). The three technologies are realised in different topologies, microstrip or coplanar, and they are processed on silicon dielectrics of different thickness. For this reason, three integration and packaging concepts were developed to fit each kind of phase shifter onto the ceramic substrate of the antenna.

In the frame of this work, a 3-bit phase shifter has been designed in the technology provided by Thales-RT, and integration techniques have been developed for all three technologies. Also, the different components of the antenna have been processed and integrated together to realise a stand-alone electrically steerable antenna demonstrator. The performance of the antenna demonstrator is validated by measurement results presented at the end of the section.

Ka-Band Phase Shifters in Silicon Technology

The phase shifters processed in the Thales-RT technology are realised in coplanar topology. They are fabricated on 500µm-thick high-resistivity silicon dielectric. The switching device implemented in the phase shifter is a coplanar RF-MEMS shunt switch, developed within the frame of the European funded project "AHRMS". A top and a cross-sectional view of the switch are depicted in Fig. 3.30.

The switch is realised with a MEMS membrane processed with two metal layers made out of TiW and Al, respectively. In the up state, it is suspended 3.30µm above the centre conductor of the coplanar line by means of two anchors processed on the coplanar ground planes. The centre conductor of the coplanar line is thinned under the membrane, and it is covered by a 0.20µm-thick layer of Si₃N₄ dielectric ($\epsilon_r = 7.5$).

As a large majority of RF-MEMS, the membrane of the switch is actuated down by an electrostatic field. This field is generated by a bias voltage applied between the centre conductor, or a DC-control pad connected to it, and the ground planes of the coplanar line. Also, the Si₃N₄ dielectric layer processed on top of the centre conductor prevents from an ohmic contact between the centre conductor and the MEMS membrane in the down-state, and the switch is therefore capacitive.

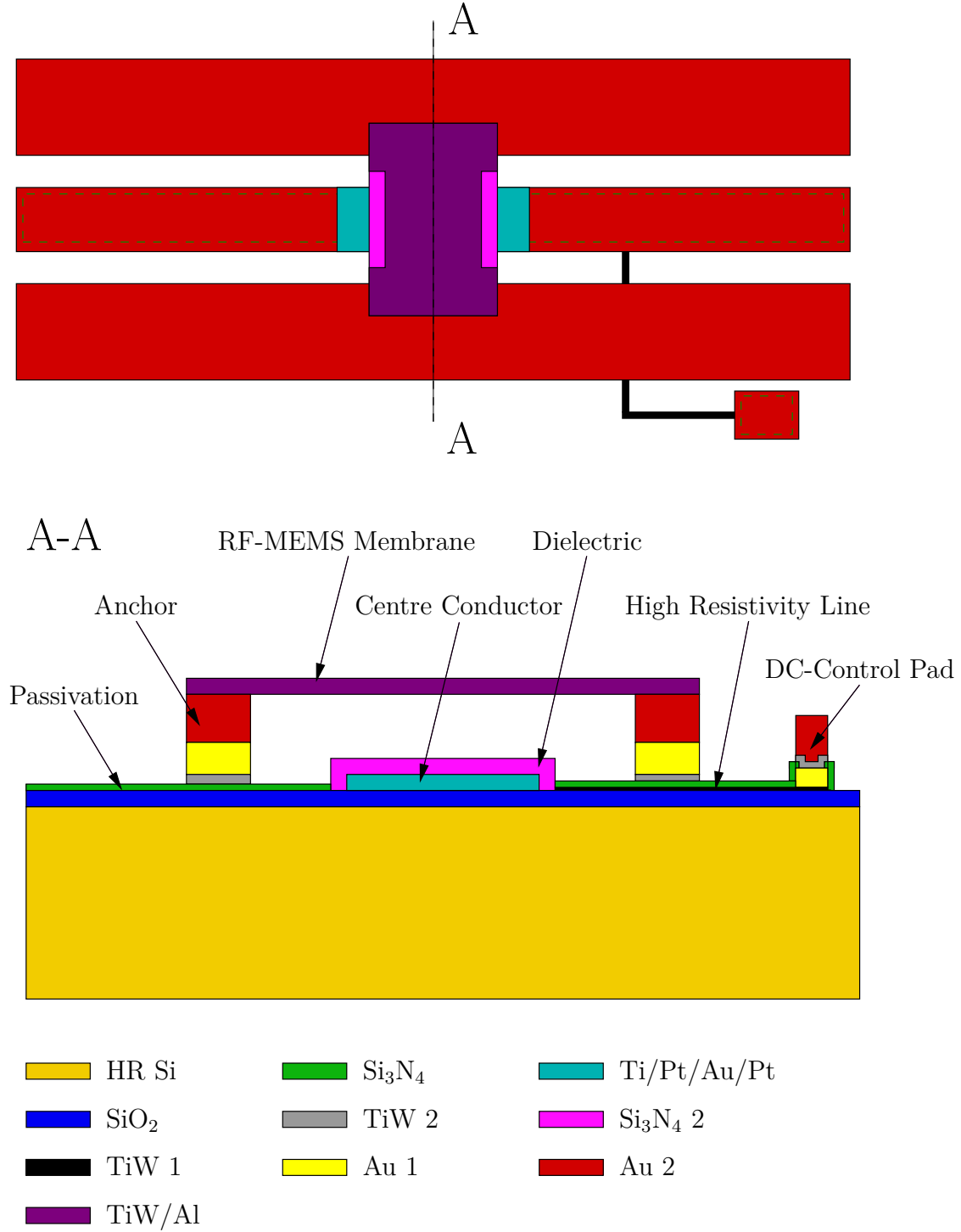


Fig. 3.30: Drawing of the Ka-band RF-MEMS coplanar shunt switch in Thales-RT technology: top view(top) and A-A cross-sectional view(bottom).

The switch has been characterised using full-wave simulations, and an equivalent circuit has been established from the simulated S-parameters. This equivalent circuit is given in Fig. 3.31. In the schematic, the capacitance and inductance modelling the switch are $C_{\text{up}} = 0.0278 \text{ pF}$ and $L_{\text{up}} = 0.0010 \text{ nH}$ for a membrane in the up state, and $C_{\text{down}} = 3.6500 \text{ pF}$ and $L_{\text{down}} = 0.0056 \text{ nH}$

when the membrane is actuated down. A comparison between the S-parameters calculated using the schematic in Fig. 3.31 and those obtained by lossless full-wave simulations is given in Fig. 3.32.

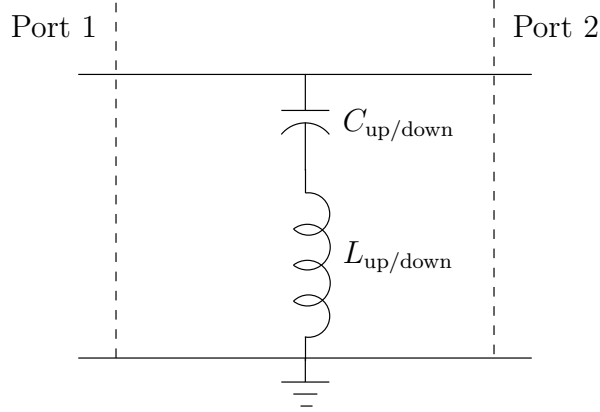


Fig. 3.31: Schematic of the Ka-band RF-MEMS coplanar shunt switch in Thales-RT technology.

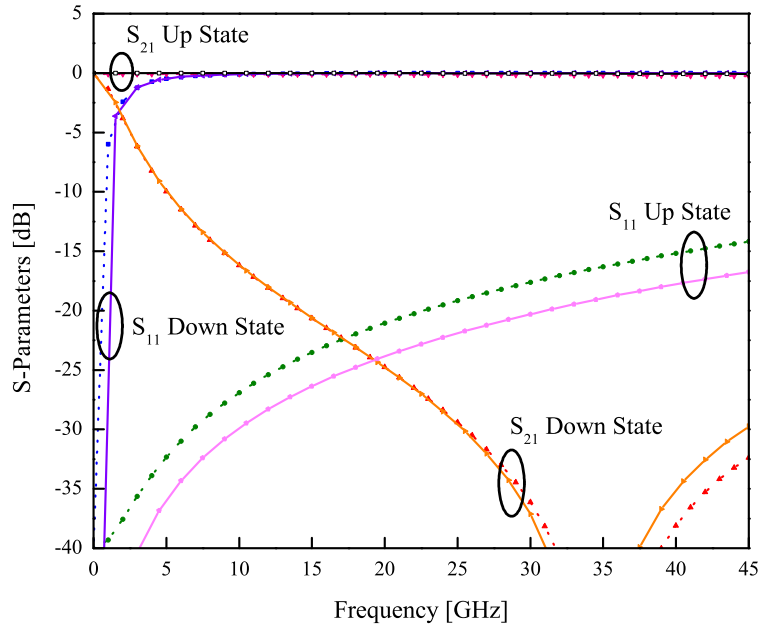


Fig. 3.32: Schematic(dashed) and full-wave simulated(solid) S-parameters of the Ka-band RF-MEMS coplanar shunt switch in Thales-RT technology.

The graph shows very good agreement between the full-wave simulated S-parameters and those of the equivalent circuit. In the up state, the switch has a satisfactory broadband transmission, and it exhibits a return loss better than 20 dB from 15 GHz up to the Ka-band. When the membrane is actuated down, it shows a good isolation between the input and output ports. The simulated isolation is better than -40 dB at the design frequency of 35 GHz.

The switch has been used to design a Ka-band 3-bit phase shifter. It is realised with three bits providing phase shifts of 45° , 90° , and 180° , all connected in series. A layout of the RF-MEMS phase shifter is depicted in Fig. 3.33.

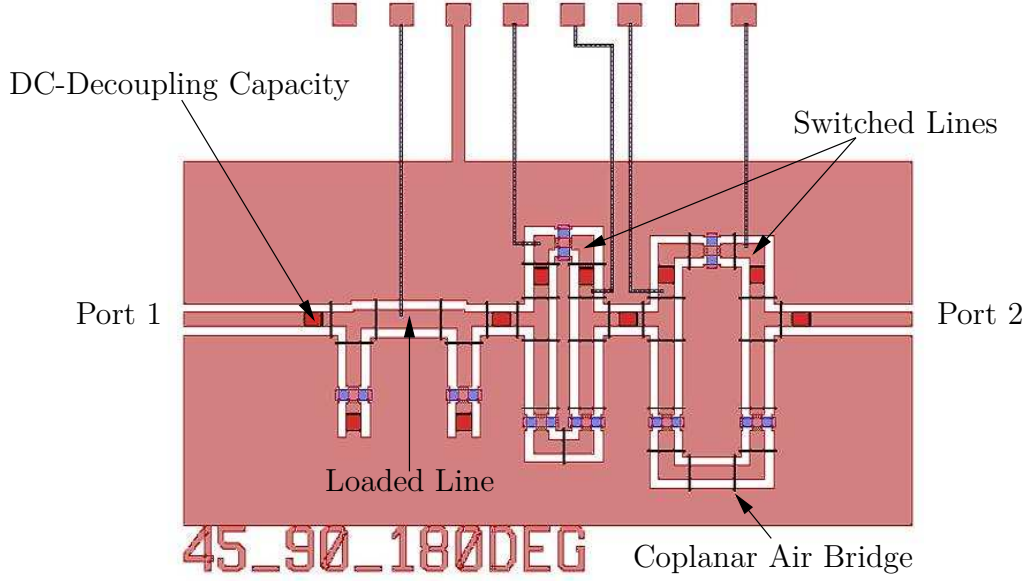


Fig. 3.33: Layout of the Ka-band RF-MEMS phase shifter in Thales-RT technology.

The 45° bit is designed in a loaded line topology [150]. According to this technique, the main coplanar line is loaded with two short-circuited stubs made adjustable by means of RF-MEMS switches. Depending on the up- or down-state of the switches, the adjustable stubs achieve two different susceptances, B_1 and B_2 , that change the phase of the signal on the main coplanar line. The values of the susceptances B_1 and B_2 to achieve are calculated from the phase shift $\Delta\psi$ to realise with the bit. They are calculated using

$$B_{1,2} = \frac{1}{Z_0} \left(\frac{\cos \theta}{\cos(\Delta\psi/2)} \pm \tan(\Delta\psi/2) \right). \quad (3.4.1)$$

There exist principally three kinds of loaded line structures. They are called "class I", "class II", and "class III" loaded line structures [150]. Among these, class III structures are often preferred over the two others, because they exhibit a constant insertion loss for the two states of the switches. Also, they have a relatively broadband constant-phase response, sensibly better than that offered by the other structures.

Class III loaded line bits are designed using two identical stubs separated by a $\lambda/4$ -long transmission line. The characteristic impedance of this mid-section is chosen such that the structure is matched for both, the up- and down-states of the RF-MEMS switches (3.4.2). The length of the stubs as well as the location of the switches along them are determined after the values of the susceptances B_1 and B_2 to achieve. These dimensions are calculated so that the impedances realised by the stubs in the up-state are complex conjugate with those achieved in the down state.

The remaining design equations of class III loaded line structures are given by

$$Z_c = Z_0 \frac{\cos(\Delta\psi/2)}{\sin \theta}, \quad (3.4.2)$$

$$B_1 = \frac{1}{Z_s} \tan(\theta_1 + \theta_2), \quad (3.4.3)$$

$$B_2 = \frac{1}{Z_s} \tan(\theta_1). \quad (3.4.4)$$

In (3.4.1), (3.4.2), (3.4.3), and (3.4.4), Z_0 and Z_s are the characteristic impedances of the mid-section coplanar line and adjustable stubs, respectively. $\Delta\psi$ is the phase shift to achieve with the bit expressed in degrees. θ is the electrical length of the coplanar mid-section, equal to 90° for class III loaded line bits. Finally, θ_1 and θ_2 are the electrical lengths of the first and second sections of the adjustable stubs, before and after the switch, respectively.

Phase shifters based on loaded line structures have very low insertion loss. Nevertheless, for large phase shifts above 45° , the low loss is at the price of a limited bandwidth and some alternative designs are often preferred. For this reason, the 90° - and 180° -bits of the phase shifter have been designed according to a technique known as "switched line". Here, the bits are realised with two transmission lines of different lengths and addressed by means of switches. The switches are identical to those used for the 45° -bit, and they are used to short-circuit one or the other transmission line. Also, since the switches are shunt switches, they are placed one-quarter of wavelength away from the ends of the transmission lines to address. In this way, they enable the selection of a given path, and thus of a given phase for the RF-signal. Finally, the difference between the lengths of the two transmission lines is chosen so that their phase difference corresponds to the phase shift to achieve. This means 90° and 180° for the bits considered here.

As already mentioned, the electrodes of the switches are the centre conductors and ground planes of the coplanar lines. In order to be easily accessible, the centre conductors of the switches in the phase shifter are connected to DC-control pads. This is done by means of narrow high-resistivity lines patterned under the metal structures and made out of TiW. They allow for an actuation of the switches with the appropriate DC-control voltage without changing the RF-behaviour of the coplanar lines. Further, in order to actuate separately the different bits of the phase shifter, DC-decoupling capacitances are implemented between the different switches. They are Metal Insulator Metal (MIM) capacitors realised with $0.2\mu\text{m}$ of Si_3N_4 as dielectric between the electrodes. The capacitors are $145\mu\text{m}$ -long and $130\mu\text{m}$ -wide. This corresponds to a capacitance of about 6.25 pF and ensures a satisfactory transmission of the RF-signal from approximately 2 GHz . Finally, in order to prevent the excitation of parasitic modes in the coplanar lines, the ground planes are connected with so-called "air bridges". The different features of the phase shifter described here are shown in Fig. 3.33.

The three bits of the phase shifter have been optimised separately and together using full-wave simulations. The simulated return loss of the complete 3-bit phase shifter is presented with its insertion loss in Fig. 3.34. The phase shifts achieved for the different switching states of the phase shifter are given in Fig. 3.35. Also, the standard phase deviation and mean insertion loss of the

phase shifter have been calculated using (3.4.5) and (3.4.6), respectively [151]. They are plotted against frequency in Fig. 3.36.

$$\sigma_{\psi}(f) = \sqrt{\frac{1}{12 \cdot 360} \cdot \sum_{i=1}^N (\psi_{i+1}(f) - \psi_i(f))^2} \quad (3.4.5)$$

$$\bar{IL}(f) = 20 \log \left(\frac{1}{N} \cdot \sum_{i=1}^N |S_{21,i}(f)| \right) \quad (3.4.6)$$

In these formulas, N is the total number of switching states of the phase shifter, eight for a 3-bit phase shifter, and i is the index of the various states. Also, $\psi_i(f)$ and $|S_{21,i}(f)|$ are the phase shift and insertion loss of the phase shifter in the i^{th} switching state, respectively.

At 35 GHz, the simulated insertion loss is below 2.5 dB, and the return loss is better than 14 dB for any switching state. Further, from 31.5 GHz up to above 38 GHz, the phase shifter exhibits very good performance. Over this frequency range of 18.6% (6.5 GHz), it has a standard phase deviation better than 14.4° and a mean insertion loss below 3.4 dB.

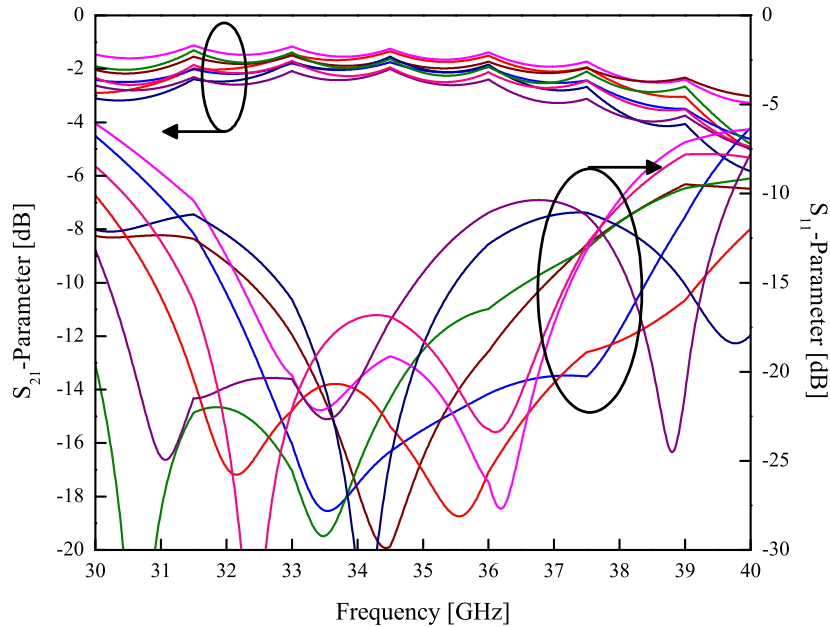


Fig. 3.34: Simulated return loss and insertion loss of the Ka-band RF-MEMS phase shifter for the different switching states.

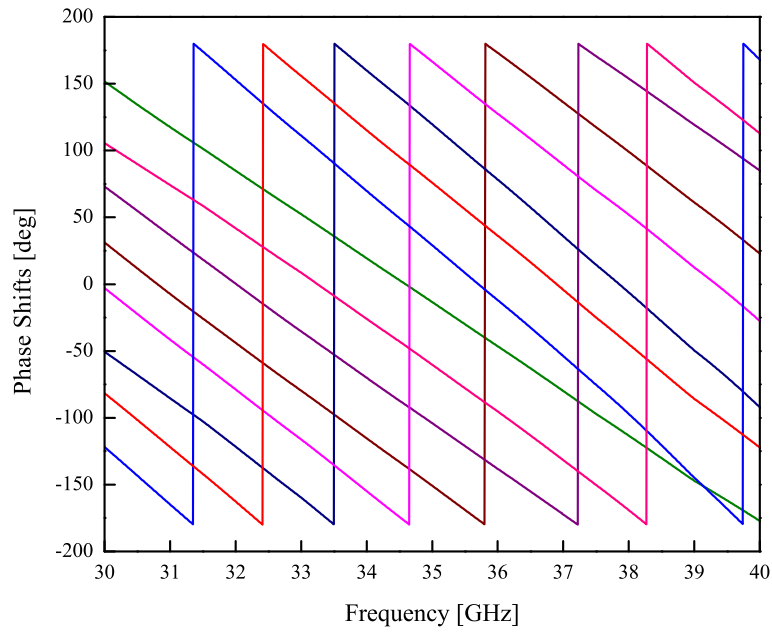


Fig. 3.35: Phase shifts simulated for the eight switching states of the Ka-band RF-MEMS phase shifter.

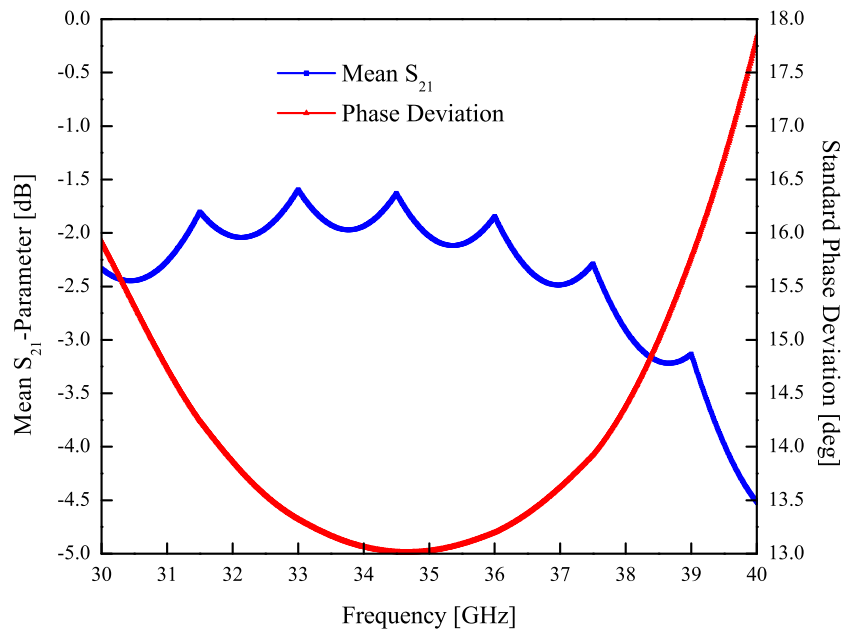


Fig. 3.36: Simulated mean insertion loss and standard phase deviation of the Ka-band phase shifter.

This deviation of the achievable phase shifts from the ideal linear phase gradient will influence the radiation pattern of the antenna, especially when it is steered away from broadside. This concerns mainly the pointing direction of the main beam, the side lobe level of the radiation pattern, and the gain of the antenna. Also, the standard phase deviation is used to calculate an equivalent number of bits for the phase shifter. This is equal to 2.85 bits for 14.4° of standard phase deviation. For the antenna in which the phase shifter will be integrated, this means a beam pointing error of 0.1 (in beamwidths) and a gain 0.28 dB lower. According to the continuous array approximation [152], an equivalent number of bits of 2.85 corresponds also to a peak side lobe level of -17.2 dB. These characteristics of phase shifters are calculated by (3.4.7) for the equivalent number of bits, (3.4.8) for the decrease in gain, (3.4.9) for the beam pointing accuracy, and by (3.4.10) for the peak side lobe level due to quantisation errors [132].

$$N_B = \frac{\log\left(\frac{180^\circ}{\sigma_\psi \cdot \sqrt{3}}\right)}{\log(2)} \quad (3.4.7)$$

$$\Delta G \approx 10 \log\left(1 - \left(\sigma_\psi \cdot \frac{\pi}{180}\right)^2\right) \quad (3.4.8)$$

$$\delta_\varphi = \frac{\pi}{4 \cdot 2^{N_B}} \quad (3.4.9)$$

$$SLL_{pk,Q} = 20 \log\left(\frac{1}{2^{N_B}}\right) \quad (3.4.10)$$

Hybrid Integration Concepts for the Phase Shifters onto the LTCC Antenna Board

Three integration concepts were developed for the three previously mentioned RF-MEMS phase shifters. All phase shifters were intended to be integrated in a hybrid fashion onto the ceramic substrate of the antenna presented in section 3.4.2. The technique developed for the integration of the phase shifters fabricated by EADS-IW is presented in Fig. 3.37.

The phase shifters manufactured by EADS-IW implement a microstrip topology, and they are processed on 200 µm-thick silicon dielectric. According to the proposed technique, all four phase shifters are placed in a single large cavity realised in the LTCC substrate. The bottom of the cavity is fully metallised by an extension of the ground plane of the buried antenna feed network. Also, in order to connect this ground plane on LTCC to the ground plane processed on the back side of the silicon chips, the phase shifters are placed in the cavity by means of conductive glue. The input and output microstrip lines of the phase shifters are connected to the antenna feed network, corporate network on one side and feeding lines on the other side, with Al RF bond-wires. Nevertheless, since the feed network of the antenna is realised with microstrip lines buried in LTCC, a transition bringing them to the bottom of the substrate was designed (Fig. 3.38). It is realised with a 110 µm-long LTCC via that connects the buried line to a bond-pad processed on the back side of the ceramic dielectric. Further, in order to keep the bond-wires as short as possible, the cavity in LTCC is processed with a depth of 330 µm, which corresponds to three layers of LTCC. The DC-control lines (not represented in Fig. 3.37) are realised in free layers of the LTCC substrate. They are patterned one and two ceramic layer(s) above the ground plane, where no RF structures are realised. The control lines are connected to the phase shifters with LTCC vias, themselves

connected to bond-pads on the back side of the substrate. The bond-pads on LTCC and those on the silicon chips are connected using Al DC bond-wires. Finally, the phase shifters were intended to be packaged with a glass lid placed on top of a 100 μm -high SU-8 frame. This packaging concept foreseen for the phase shifters is not hermetic but protects MEMS structures against dust. Also, it allows a sawing of the silicon chips.

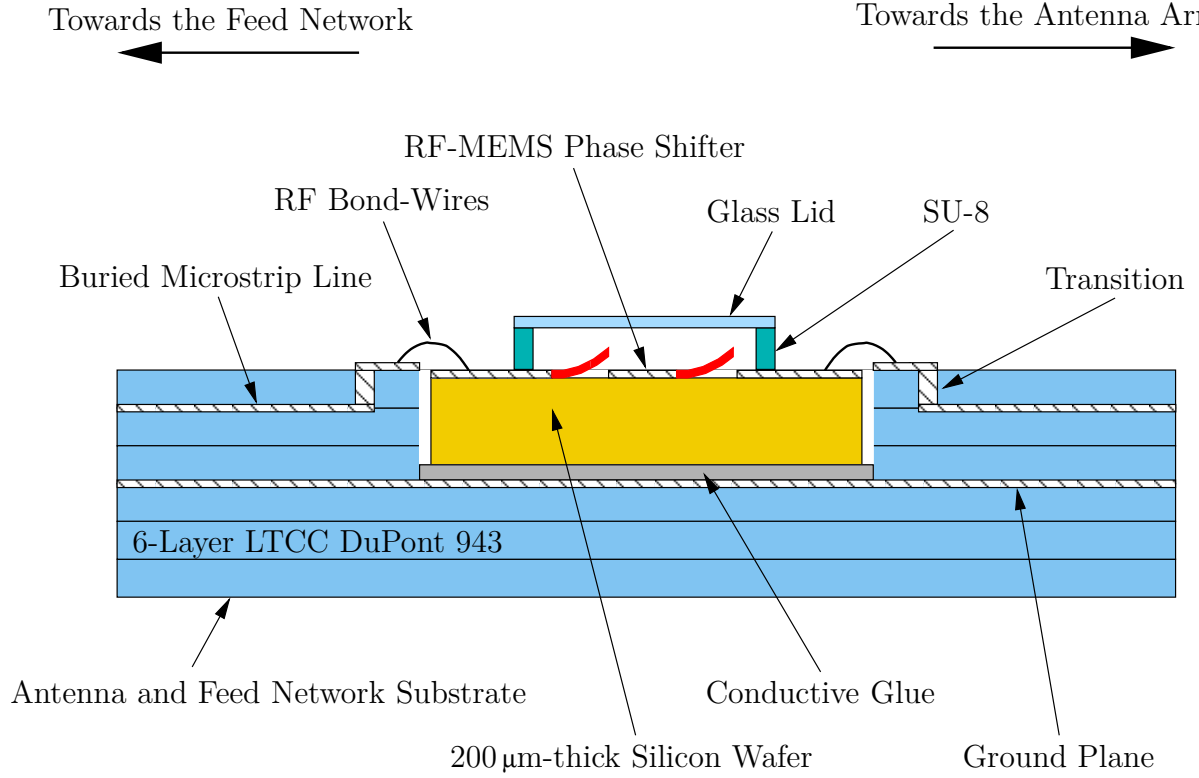


Fig. 3.37: Hybrid integration concept for the EADS-IW RF-MEMS phase shifters.

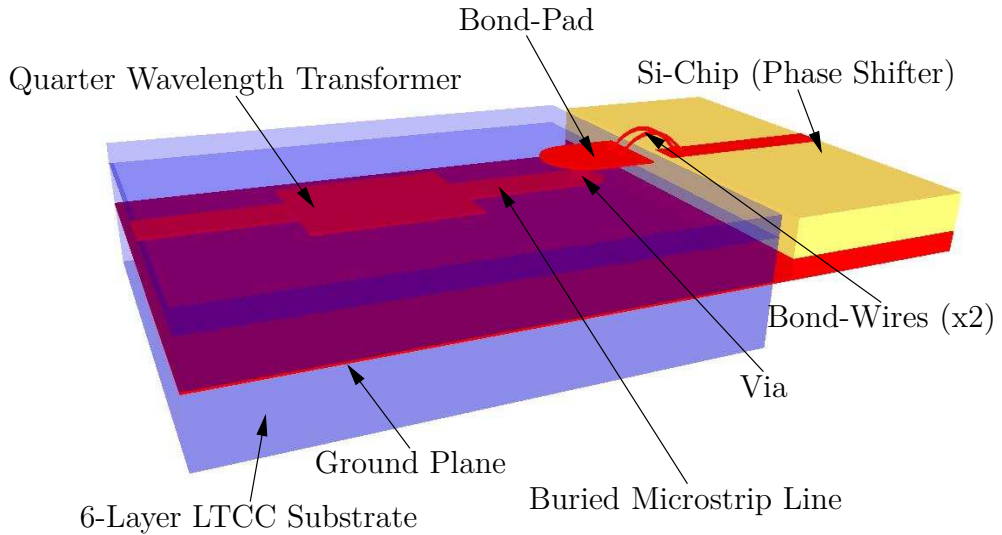


Fig. 3.38: 3D view of the buried microstrip line to microstrip line transition in LTCC DuPont 943.

The RF-MEMS phase shifters manufactured by Thales-RT have been described in detail in a previous paragraph of this section. They are coplanar phase shifters processed on 500 μm -thick silicon dielectric. The hybrid integration concept developed for these phase shifters is depicted in Fig. 3.39 and 3.40.

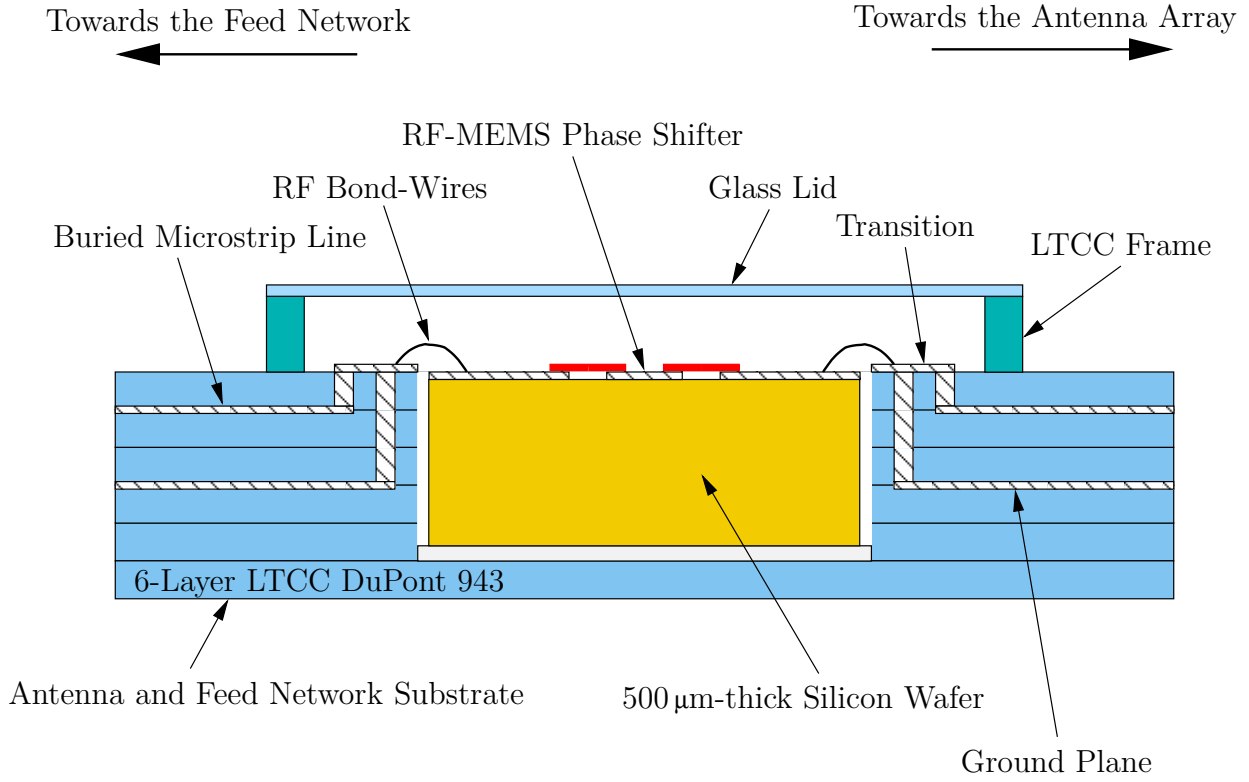


Fig. 3.39: Hybrid integration concept for the Thales-RT RF-MEMS phase shifters.

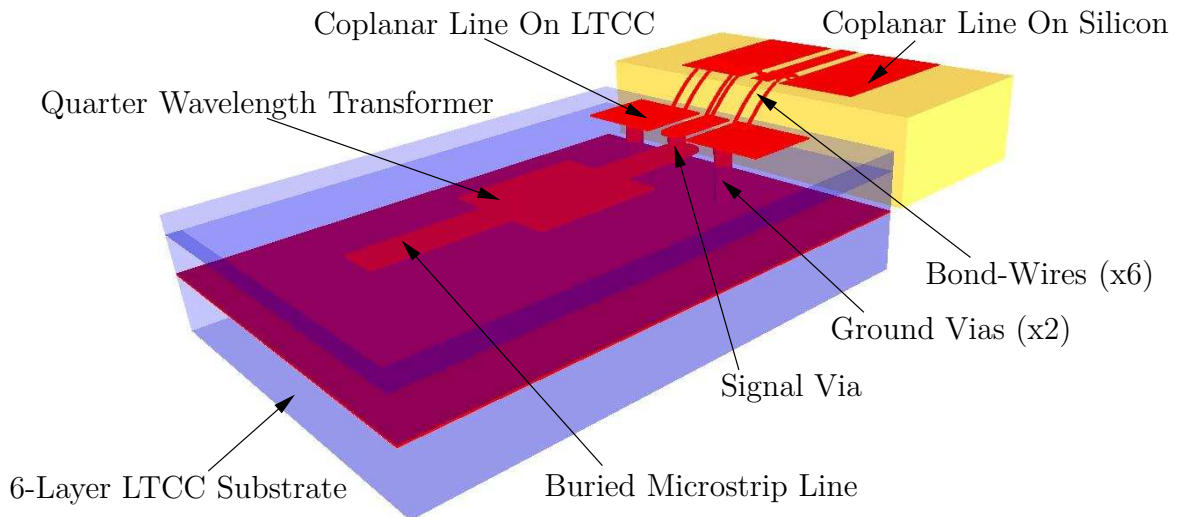


Fig. 3.40: 3D view of the buried microstrip line to coplanar line transition in LTCC DuPont 943.

Here, each chip is placed in an individual cavity processed in the LTCC antenna board. Since the phase shifters are made out of 500 μm -thick dielectric, the cavities are manufactured with a 550 μm depth. Thus, according to the proposed architecture, only one 110 μm -thick LTCC layer is left for the bottom of the cavity. The chips are placed in the cavities using non-conductive glue. The phase shifters are connected to the feed network of the antenna using Al RF bond-wires. As for the EADS-IW phase shifters, a transition has been designed for the buried microstrip lines. Nevertheless, in the present case, both the buried line and its ground plane are led to the back side of the substrate with vias in LTCC. A 3D view of this transition is shown in Fig. 3.40. At 35 GHz, the transition calculated using full-wave simulations exhibits a return loss better than 10 dB and an insertion loss of about 1 dB.

On top of this, the phase shifters are intended to be packaged using a glass lid mounted on top of a LTCC frame. The ceramic frame is 800 μm -high. It is placed on the back side of the antenna substrate, around the cavities processed for the phase shifters. Further, due to the sensitiveness of MEMS structures against temperature, a glue curable at high temperature cannot be used for the assembly. Thus, a UV-curable glue shall be utilised to fix the ceramic frame and the glass lid. The proposed packaging prevents the RF-MEMS from being damaged by dust but it is not hermetic. A major difference with the firstly proposed SU-8 packaging is that the present technique does not enable a separation of the chips by sawing. In return, it covers all the four phase shifters with only one frame and one lid, and it cares for the bond-wires between the silicon chips and the LTCC board.

The third and last phase shifters intended for integration onto the ceramic substrate of the antenna are developed and processed by Fraunhofer-ISIT. Like the phase shifters manufactured by Thales-RT, they are realised in coplanar topology and are fabricated on 500 μm -thick silicon dielectric. In the integration concept presented in Fig. 3.41, the phase shifters are flip-chipped onto the LTCC substrate of the antenna.

According to the integration technique foreseen for these phase shifters, bond-wires are no longer used for the RF- and DC-connections. They are replaced by stud bumps made out of Au and approximately 25-30 μm high. Stud bumps present some advantages over RF bond-wires for millimetre-wave applications. At high frequencies, even a short length of RF bond-wire is inductive and increases the return loss of the transition. This can be overcome by implementing several bond-wires in parallel, or by designing matching networks close to the bond-wires. In most cases however, the design of broadband matching networks is a challenging task, and such networks often reduce the bandwidth of the transition. In return, from the mechanical point of view, bond-wires allow for a better geometrical flexibility, especially convenient when the thermal extension of the materials is different: TCE of silicon=3 ppm/ $^{\circ}\text{C}$, and TCE of LTCC DuPont 943=6 ppm/ $^{\circ}\text{C}$. Bond-wires accept variations in the relative dimensions of the devices, contrary to stub-bumps which are loaded with stress when the components do not extend by the same amount. This tension may lead stud bumps to crack after a number of warming-up and cooling-down cycles, which is of course critical for the reliability of the connections. For this reason, the material used for the stud bumps shall be chosen elastic enough to follow the geometrical changes of the connected devices. Another constraint to observe when choosing stud bumps material is the melting temperature. The material chosen to solder the MEMS chips shall have a low-enough melting temperature, and the flip-chip process must be executed within a maximum duration. These two parameters, melting temperature and process duration, are driven by the thermal requirements of the considered RF-MEMS technology.

In order to prevent the MEMS bridges from touching the ceramic substrate, four 110 μm -deep cavities are manufactured in LTCC and below the phase shifters. The packaging concept foreseen for the Fraunhofer-ISIT phase shifters is basically the same as the one described for the Thales-RT phase shifters. Nevertheless, for these phase shifters, it does not represent an issue for separating the chips because they are intended to be cleaved by laser (stealth dicing). For this reason, they do not need to be packaged before dicing. Finally, a buried microstrip line to coplanar transition has been designed. The transition is similar to that presented for the Thales-RT phase shifters, but with a different pitch of the coplanar line. Also, it implements a different design for the matching network, since RF bond-wires are no longer used.

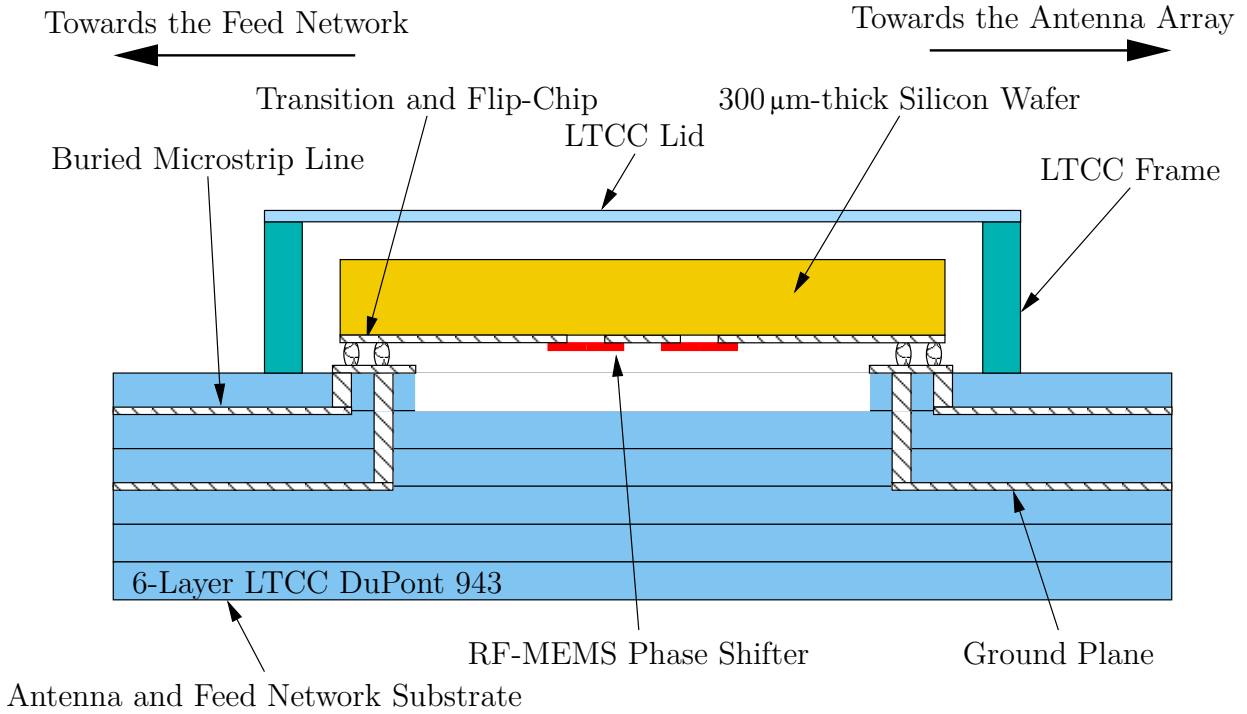


Fig. 3.41: Hybrid integration concept for the Fraunhofer-ISIT RF-MEMS phase shifters.

Ka-Band Electrically Steerable Antenna Demonstrator

The previously presented Ka-band antenna array has been equipped with EADS-IW RF-MEMS phase shifters, which were the only phase shifters available within the limited time frame of this work. Nevertheless, the design, the realisation, and the measurement of these phase shifters were not parts of the work reported here, and are therefore presented in appendix of the thesis. A photograph of the fully integrated electrically steerable antenna is shown in Fig. 3.42. This antenna was assembled according to the concept described in Fig. 3.37.

The photograph shows a front view and a rear view of the steerable antenna. The radiating patches patterned on top of the ceramic substrate are visible on the front view of the antenna. The four phase shifters mounted in a cavity on the back side of the substrate are shown on the rear view of the antenna. As already mentioned, the phase shifters are between the corporate feed network and the feeding microstrip lines. These are however not visible on the photograph because they are in a buried layer of the substrate. Finally, on the left-hand side of the illustration, a micrograph of

the bond-wire interface is shown. It displays the bond-wire connections implemented for both, the RF- and DC-control signals. As shown on the micrograph, two bond-wires are used in parallel to connect the RF microstrip lines on silicon to the bond-pads on ceramic. This aims at reducing by half the inductance added by the bond-wires in order to preserve the return loss of the antenna.

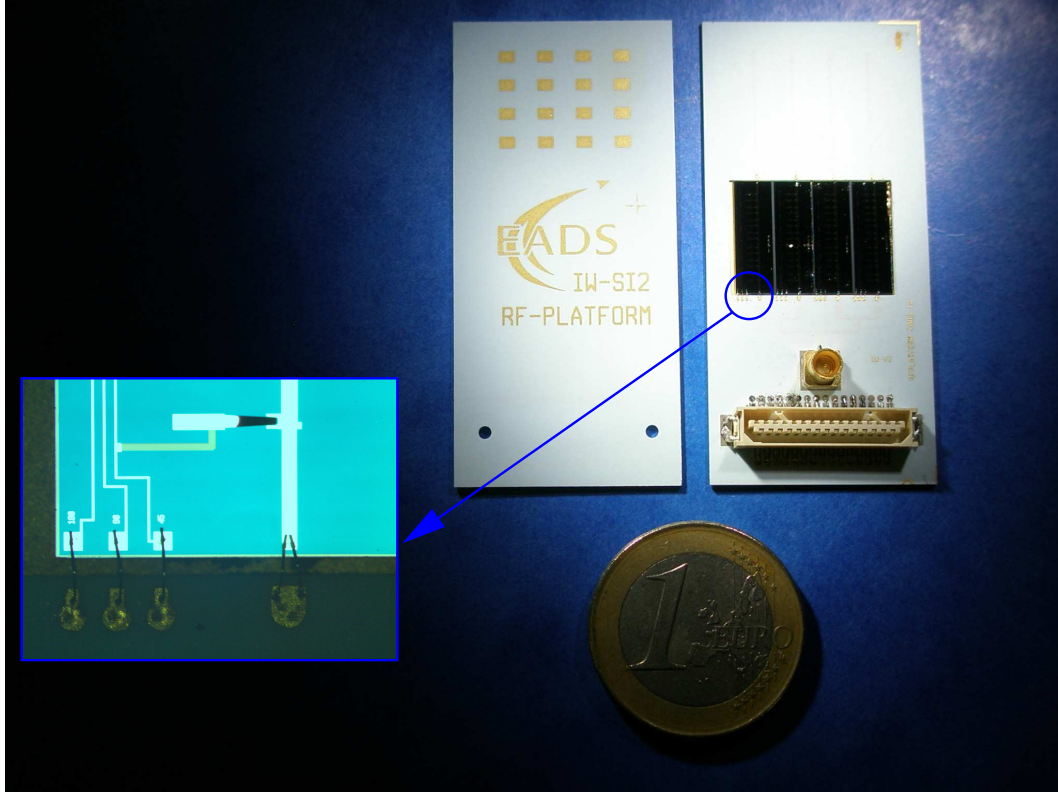


Fig. 3.42: Photograph of the Ka-band RF-MEMS electrically steerable antenna on LTCC: front view (middle), back view (right), and bond-wire connections (left).

Characterisation and Measurements

The far field radiation characteristic of the antenna has been measured in an anechoic chamber at the University of Ulm. It has been measured at 35 GHz, and for three switching states of the phase shifters: for a main beam pointing the broadside direction and the $\pm 15^\circ$ steered directions. For this measurement, the phase shifters have been actuated using the antenna control setup described in the first chapter of this thesis. The H-plane far field patterns measured for the antenna are plotted in Fig. 3.43.

In this graph, the radiation characteristics point the -11° , 4.5° , and 22° directions, and they exhibit 24° , 21.5° , and 20.2° of half-power beamwidth, respectively. The side lobe level of the three H-plane patterns is -11.8 dB, -8.4 dB, and -5 dB, respectively. The asymmetry observed in the radiation characteristics cannot be attributed to the antenna itself, because it is strictly symmetric in the H-plane. Thus, the relatively high side lobe level and the pointing error of about 4° can be only justified by inaccuracies in the integration of the phase shifters. These inaccuracies are believed to be mainly differences between the lengths of the various bond-wires, as well as a perfectible positioning of the silicon chips in the cavity. The return loss of the complete RF-MEMS antenna

has been measured for both, the broadside and the 15° steered beam states. The S_{11} -parameter measured for both configurations is plotted in Fig. 3.44.

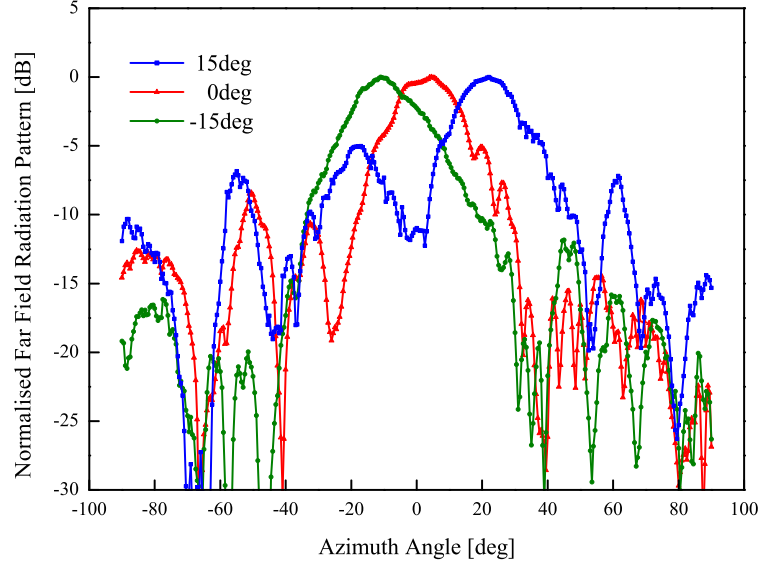


Fig. 3.43: Radiation characteristics measured in the H-plane for the RF-MEMS electrically steerable antenna at 35 GHz.

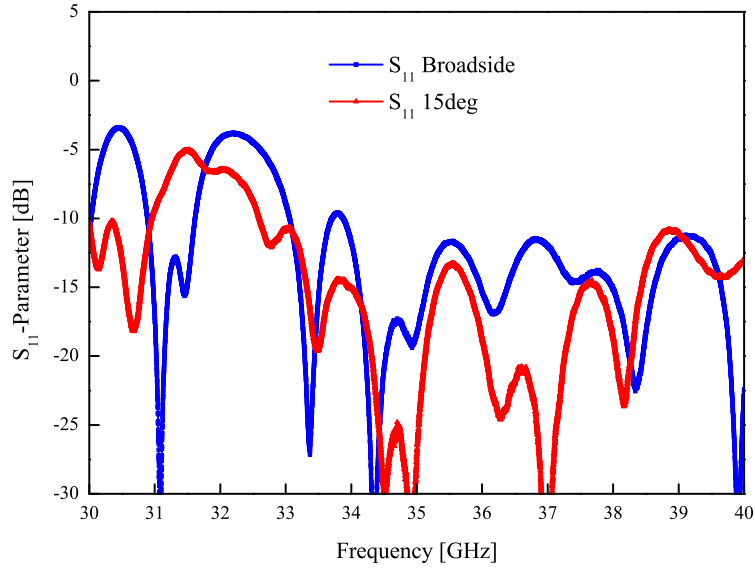


Fig. 3.44: Measured return loss of the RF-MEMS electrically steerable antenna on LTCC.

For the main beam pointing the broadside direction, the return loss is better than 10 dB from 33.88 GHz up to above 40 GHz. Also, when the main beam is steered in the 15° direction, the return loss of the antenna remains very good and better than 10 dB from 32.60 GHz up to 40 GHz and beyond.

The gain of the antenna has been measured for all three pointing directions of the main beam. It exhibits a satisfactory value of about 8 dBi in both, the broadside and the $\pm 15^\circ$ steered directions. According to (3.2.5) and (3.2.8), this corresponds to a radiation efficiency of 18.6% for the broadside characteristic. This gain measured for the electrically steerable antenna is 5.4 dB below the gain of the fixed-beam antenna. This decrease in gain is explained partly by the insertion loss of the RF-MEMS phase shifters of about 2.5 dB (see Appendix A) but also by the loss in the two additional transitions. The two buried microstrip line to microstrip line transitions plus bond-wires implemented on both sides of the phase shifters are accounted for 2.9 dB of loss.

3.4.4 Conclusion

In the different paragraphs of this section, a fixed-beam and a phased array antenna for operation at Ka-band have been demonstrated. The antennas are made out of low-loss ceramics, and the electrically steerable antenna is equipped with RF-MEMS phase shifters. These antennas were developed with the ambition to investigate what emerging technologies will enable in terms of cost, integration, and performance, for the next generation of millimetre-wave front-ends. Also, beyond these two antennas, three hybrid integration concepts have been proposed for three different technologies of RF-MEMS phase shifters. Each one of the integration and packaging techniques was described with its pros and cons, depending on the configuration of the front-end. Finally, as it was highlighted by the measurement results presented for the electrically steerable antenna, the hybrid integration of millimetre-wave phase shifters is a challenging task. On top of the tight fabrication tolerances mandatory for the components, the performance of millimetre-wave phased antennas depends also largely on the quality of the assembly of these components, which has to be executed with a very high accuracy.

3.5 X-Band Phased Array Antenna

3.5.1 Architecture and Hybrid Integration Concept

The X-band electrically steerable antenna presented in the coming sections is similar to the W-band antenna presented in section 3.3. The antenna is steerable in the H-plane, and it shows a fixed broadside pattern in the E-plane. It is realised with four microstrip antenna sub-arrays connected in parallel by a corporate feed network. A 3D model of the antenna array with two simulated steered beams is shown in Fig. 3.45.

The electrically steerable antenna is realised with a microstrip antenna array, a microstrip feed network, and four RF-MEMS phase shifters. The antenna array as well as the feed network are manufactured on 31 mil-thick (787 μm) Rogers RT/Duroid 5880 substrate. The RF-MEMS phase shifters are processed on 300 μm -thick high-resistivity silicon dielectric. They are placed between the feed network and the antenna array, and they are connected on both sides by means of Al RF bond-wires. Further, a DC-control board made out of multilayer FR4 is mounted under the

antenna and feed network. In its middle metal layer, the control board contains the DC-control lines necessary for the actuation of the phase shifters. The DC-control pads patterned on the silicon chips are connected to the DC-control lines in the FR4 board by means of bond-wires and vias. Two cross-sectional views showing the hybrid integration of the different elements are shown in Fig. 3.46.

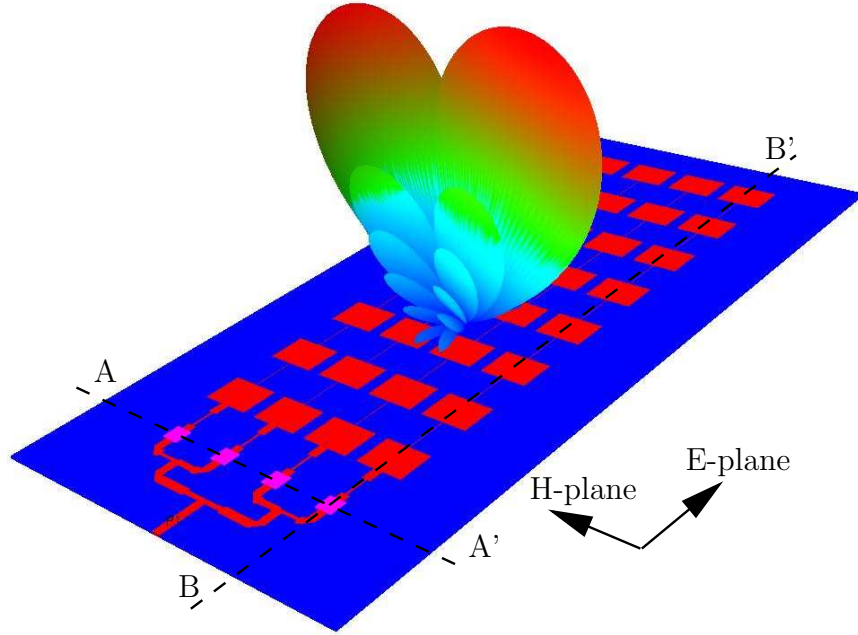


Fig. 3.45: Model of the X-band RF-MEMS phased array antenna with two simulated radiation patterns steered in the H-plane.

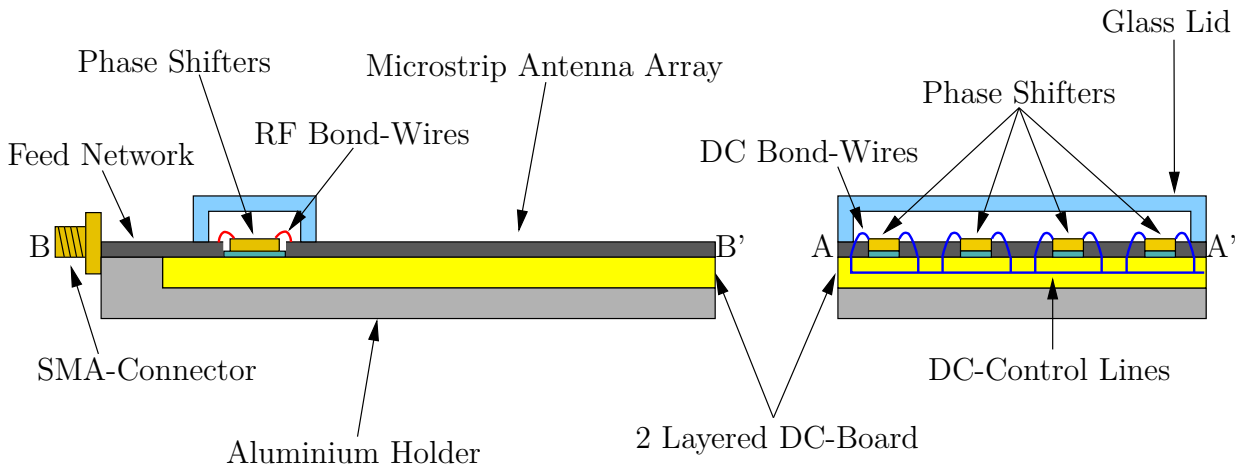


Fig. 3.46: Architecture of the X-band electrically steerable antenna.

The components of the antenna are mounted onto an aluminium holder providing a good rigidity to the entire demonstrator. All components of the antenna: feed network, antenna array, and phase shifters are realised in microstrip topology. Thus, in order to achieve a common ground plane for all of them, the top of the DC-control board is almost fully metallised, and the components are placed on it with conductive epoxy. The difference in thickness between the silicon chips and the soft Teflon substrate is about 500 μm . This implies the use of 700 μm -long RF bond-wires, which, thanks to the relatively low operating frequency, do not increase much the return loss of the antenna. In return, the lengths of these bond-wires have to be similar in order to keep the unsteered radiation characteristic of the antenna pointing towards the broadside. The RF-interface is realised using an SMA connector manufactured by Rosenberger GmbH. It is fixed on the aluminium holder and soldered to the microstrip line of the feed network. The DC-control lines in the FR4 substrate are connected to a 24-pin connector provided by Darwin. The connector is placed in a window realised in the Rogers substrate, and it is soldered on a footprint patterned on top of the FR4 board. Finally, the RF-MEMS chips are packaged using a glass lid placed on top of the Rogers substrate. It is fixed on the bottom part of the antenna substrate and on the top part of the feed network substrate. The lid covers all the four phase shifters and covers also the bond-wires. In order to prevent the RF bond-wires from touching the glass lid, a cavity is also realised on its back side.

3.5.2 Fixed-Beam Patch Antenna Array

Design of the Antenna Array

The E-plane radiation pattern of the antenna is determined by the length of the serially fed patch antenna sub-arrays, as well as by the excitations chosen for the radiators along it. On the other hand, the H-plane pattern depends on the position of the four sub-arrays, and on their respective feeding coefficients. All four serially fed patch antenna sub-arrays are identical, and they have been designed using the ETLM model presented in section 3.3. They are realised with eight patches connected in series by 200 μm -wide microstrip lines. They are connected in parallel by a corporate feed network. This feed network is achieved in two stages with 1-to-2 T-junction power dividers. The power dividers are asymmetrical and their distribution ratios are designed to feed the four antenna sub-arrays with an excitation taper. As for the antennas demonstrated in the other sections of the chapter, the excitations of the sub-arrays are computed by the technique presented in [42]. The theoretical excitation coefficients and those full-wave simulated for the 1-to-4 corporate feed network are given in Fig. 3.47.

In the histogram, each sub-array is represented by its index on the X-axis. The indexes 1 and 4 represent the outermost sub-arrays, and the indexes 2 and 3 represent the sub-arrays close to the centre of the antenna. The excitations are normalised in order to have the overall power (sum of the squared amplitudes) equal to unity. In the E-plane, no excitation taper is implemented and all eight patches of the sub-array radiate the same amount of power.

The antenna has been designed with an inter-element spacing of 15800 μm , i.e. 0.5λ at 9.5 GHz, in the H-plane. This spacing ensures a grating lobe-free radiation characteristic for a beam steering up to end-fire, which is more than the scan angle effectively achievable with the antenna. A photograph of the fixed-beam antenna is depicted in Fig. 3.48.

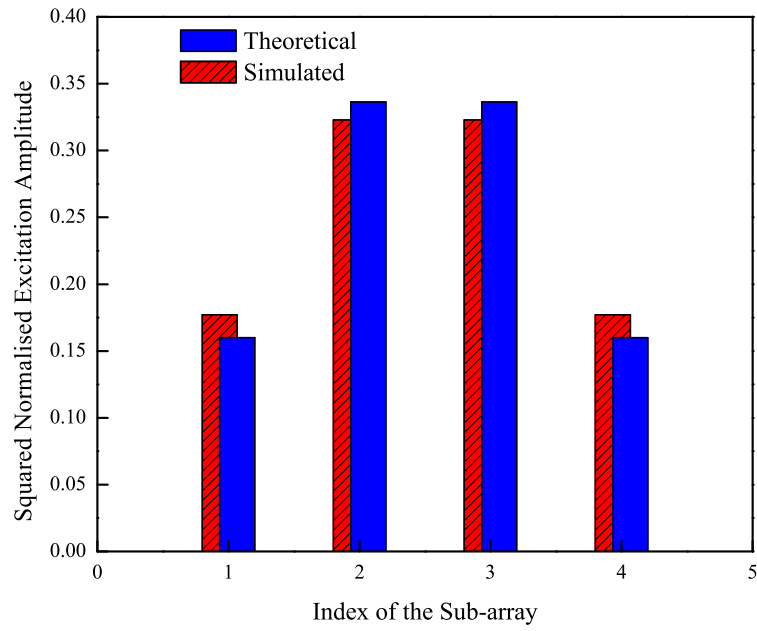


Fig. 3.47: Theoretical and simulated excitation coefficients of the 1-to-4 corporate feed network.

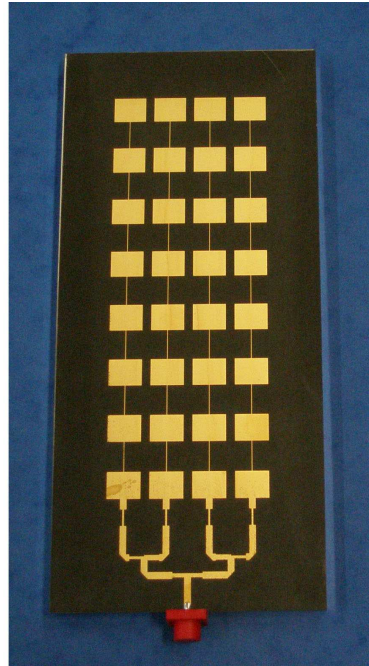


Fig. 3.48: Photograph of the fixed-beam X-band antenna array.

Characterisation and Measurements

The E- and H-plane radiation characteristics of the antenna have been measured in an anechoic chamber at the University of Ulm. Also, its return loss as well as the SMA to microstrip line transition have been measured at EADS Innovation Works using an Agilent E8363B PNA network analyser. The insertion loss measured for the transition alone is 0.17 dB at 10 GHz. Beyond the X-band, the measured S-parameters have shown that the transition exhibits good performance up to at least 15 GHz with a return loss better than 20 dB.

The E- and H-plane far field radiation characteristics of the antenna are shown in Fig. 3.49 and 3.50, respectively. The measured 3 dB beamwidth is 10° in the E-plane, and 22° in the H-plane. The side lobe level is better than -11 dB and -17 dB in these two planes, respectively. Also, the gain measured for the antenna is 17 dBi at the design frequency of 9.5 GHz. A measurement of the antenna pattern over a larger frequency range has also highlighted a satisfactory behaviour of the antenna between 9.3 GHz and 9.7 GHz. This corresponds to a bandwidth of 4.2%, which is limited by the principle of the serially fed antenna array technique. As already mentioned in section 3.3, serially fed antenna arrays exhibit off-broadside squinted beams when the operating frequency moves away from the design frequency. The measured and simulated return loss of the antenna is depicted in Fig. 3.51. It is better than 10 dB between approximately 9.45 GHz and 9.72 GHz (2.8%). Over this frequency range, the off-axis angle measured for the main beam is smaller than 4° , which is 0.4 times the E-plane beamwidth.

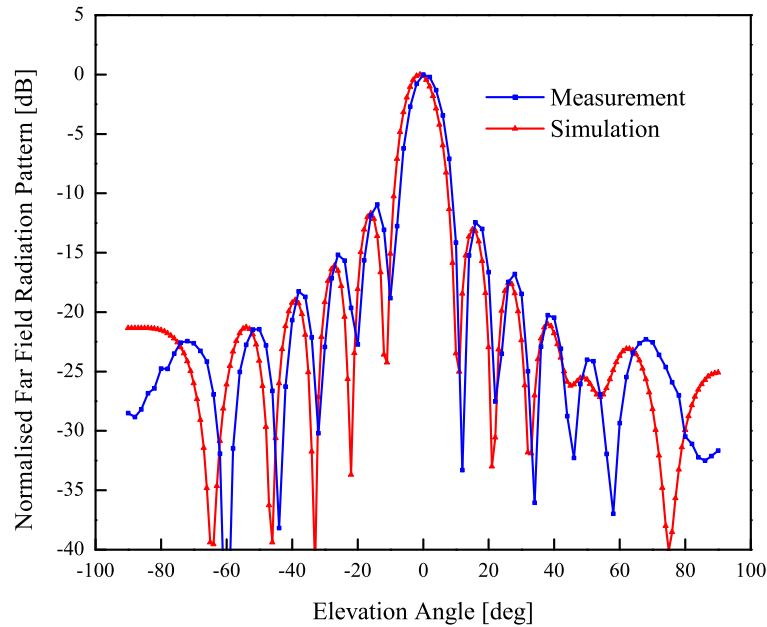


Fig. 3.49: Measured and simulated E-plane far field pattern of the fixed-beam antenna at 9.5 GHz.

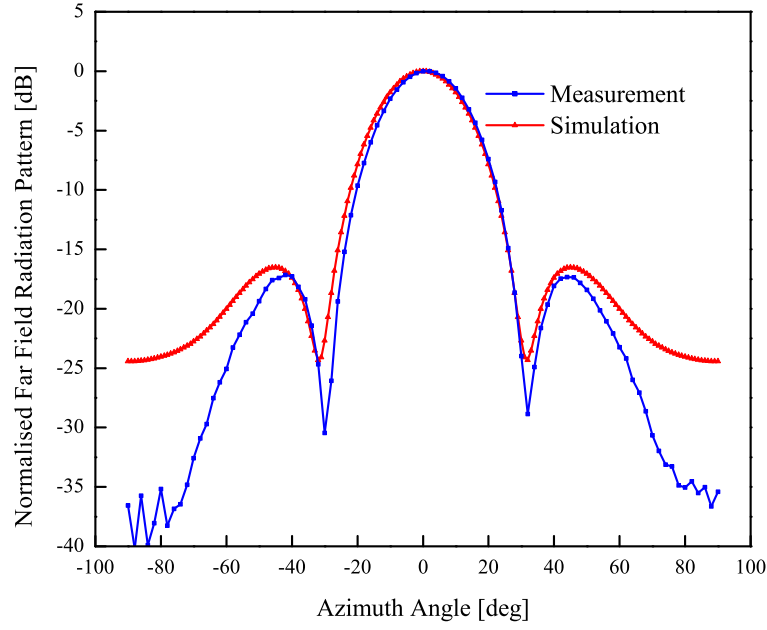


Fig. 3.50: Measured and simulated H-plane far field pattern of the fixed-beam antenna at 9.5 GHz.

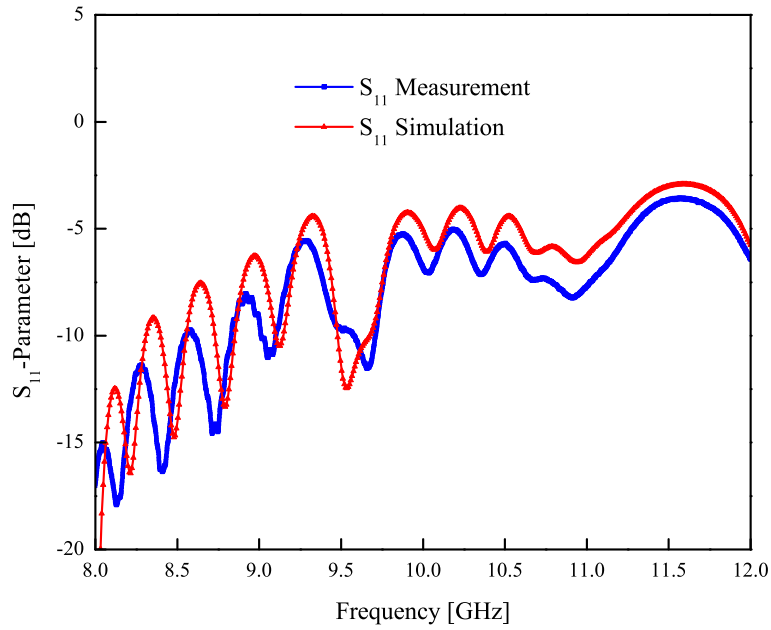


Fig. 3.51: Measured and simulated return loss of the fixed-beam antenna.

3.5.3 Phased Array Antenna

X-Band RF-MEMS Phase Shifters on Silicon

The RF-MEMS phase shifters integrated in the X-band phased array antenna were not designed in the frame of this thesis [153]. Nevertheless, in order to serve the consistency of the work presented here, some key design features and measurement results are presented in the following paragraphs. The RF-MEMS phase shifters are realised in microstrip topology on 300 μm -thick high-resistivity silicon dielectric. The phase shifting is achieved with three bits of 45°, 90°, and 180°, all designed according to the switched line technique. The transmission lines are addressed by two SP2T (Single Pole Double Throw) RF-MEMS serial switches for the 90° bit, and two SP4T (Single Pole Four Throw) switches for the 45° and 180° bits. Also, in the proposed design, the 45° and 180° bits are designed in parallel. Thus, an additional switched line of 225° had to be also designed to overcome that these two bits cannot be added as in a full serial arrangement of the phase shifter [154]. The overall size of the chip is about 7.5 mm x 8.5 mm, which is not yet pushed to the limit of the miniaturisation of the phase shifter. A photograph of the phase shifter is shown in Fig. 3.52.

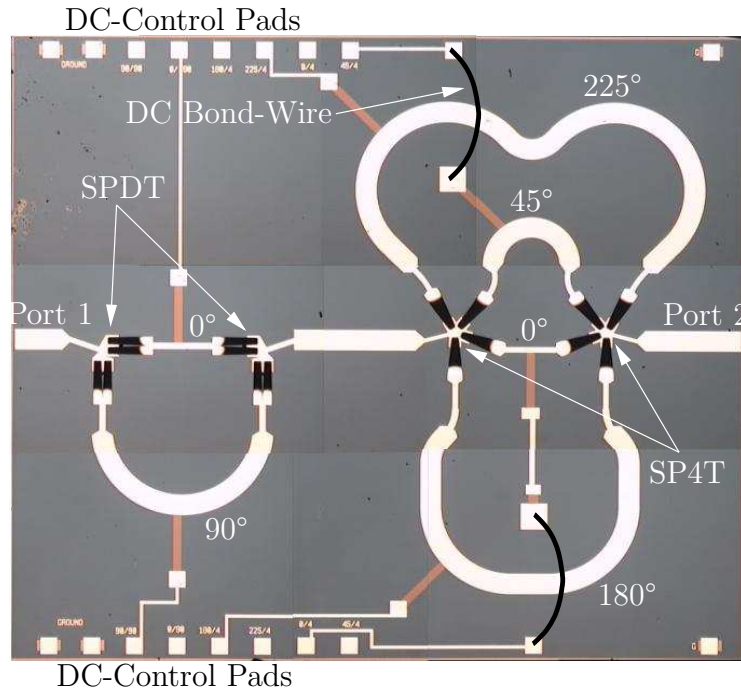


Fig. 3.52: Photograph of the X-band 3-bit RF-MEMS phase shifter.

The switches are processed in the low-complexity EADS Innovation Works RF-MEMS technology [52]. In order to assess the performance of the switches alone, they have been fabricated and characterised separately, before the phase shifter was designed. The SPDT switch is realised using two SPST serial switches connected at 90°, and both switches have the same performance. In return, the SP4T switch has been completely redesigned to allow for a higher space efficiency necessary to gather the four switches as close as possible to the line which they have in common. The performance of the switches measured at 9.5 GHz is summarised in Table 3.2.

	SPDT	SP4T
Insertion Loss	0.2 dB	0.4 dB
Isolation	19 dB	25 dB
Return Loss	25 dB	27 dB

Table 3.2: Measured performance of the SPDT and SP4T RF-MEMS switches.

The phase shifts measured for the eight switching states of the phase shifter are plotted in Fig. 3.53. The return loss and insertion loss measured for the same switching states are plotted in Fig. 3.54.

At the design frequency of 9.5 GHz, the insertion loss of the phase shifter is below 2 dB and its return loss is better than 13 dB, for any switching state. Also, according to the measurements in Fig. 3.54, the phase shifter shows a satisfactory broadband behaviour from below 8 GHz up to 12 GHz and beyond. Nevertheless, due to the digital nature of the phase shifter, only discrete phase shifts multiple of 45° are achievable, and the ideal phase gradient required to steer the main beam cannot be exactly realised [132]. This is assessed by calculating the standard phase deviation of the phase shifter. The rms phase error and the mean insertion loss of the phase shifter are plotted versus frequency in Fig. 3.55.

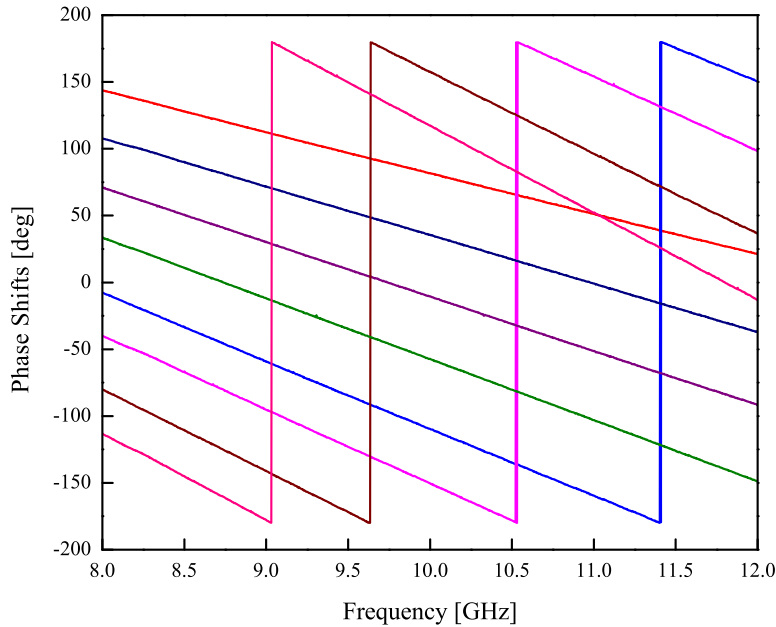


Fig. 3.53: Phase shifts measured for the eight switching states of the X-band phase shifter.

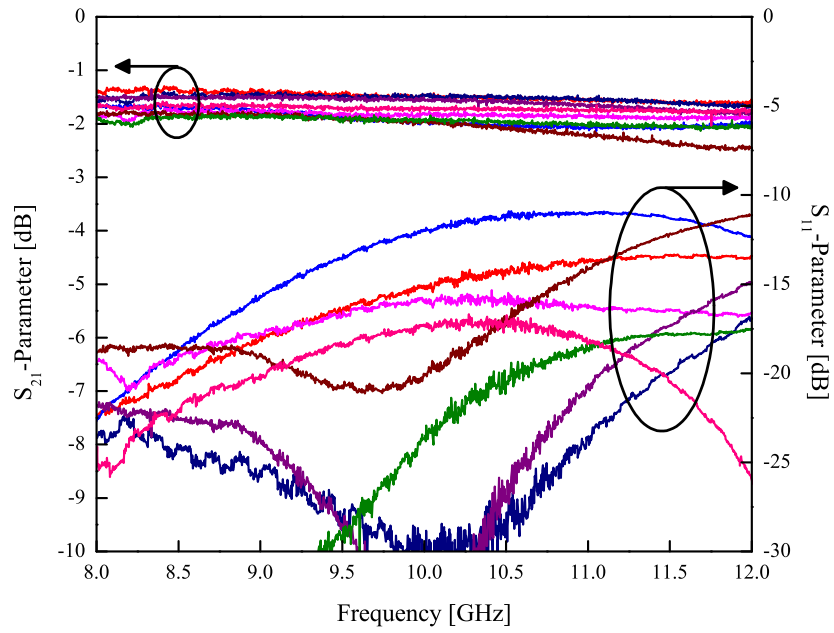


Fig. 3.54: Insertion loss and return loss measured for the X-band phase shifter.

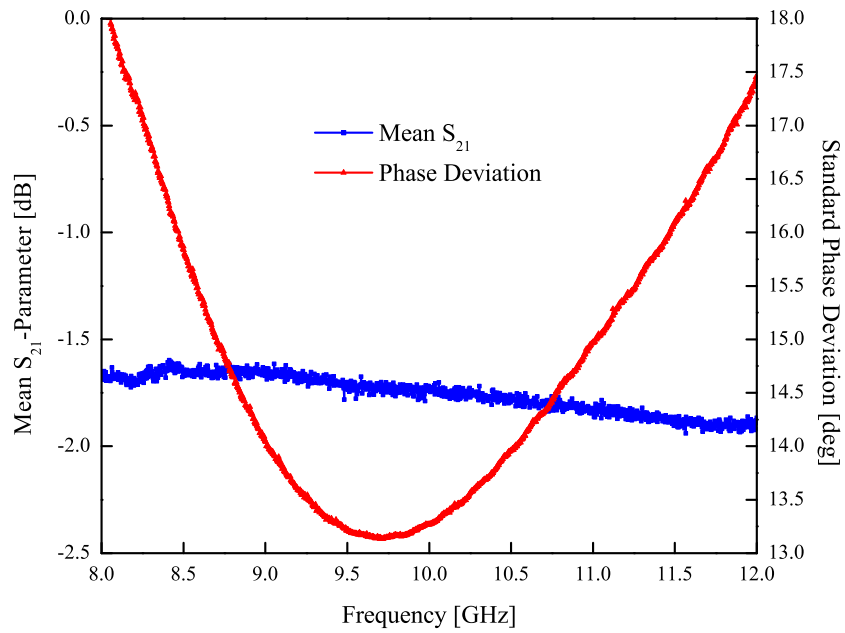


Fig. 3.55: Standard phase deviation and mean insertion loss of the X-band phase shifter.

The phase shifter exhibits a rms phase deviation better than 14° from 9 GHz up to 10.5 GHz, with a minimum of 13.1° at 9.66 GHz. From (3.4.7), 14° of standard phase deviation corresponds to an equivalent number of bits of 2.89. This corresponds also to a rms pointing accuracy of 0.14 (in beamwidths) for the antenna characteristic (3.4.9). Further, according to (3.4.10) and (3.4.8), 2.89 bits provide a peak side lobe level of -17.40 dB for a continuous aperture, and a quantisation loss of 0.26 dB. These performances are close to those of an ideal 3-bit phase shifter which are, a pointing accuracy of 0.1 beamwidths, a peak side lobe level of -18.06 dB, and a quantisation loss of 0.26 dB.

Phased Array Antenna Demonstrator

The complete phased array antenna has been assembled according to the architecture described in section 3.5.1. A photograph of the fully integrated antenna connected to its RF-coaxial and DC-control cables is depicted in Fig. 3.56.

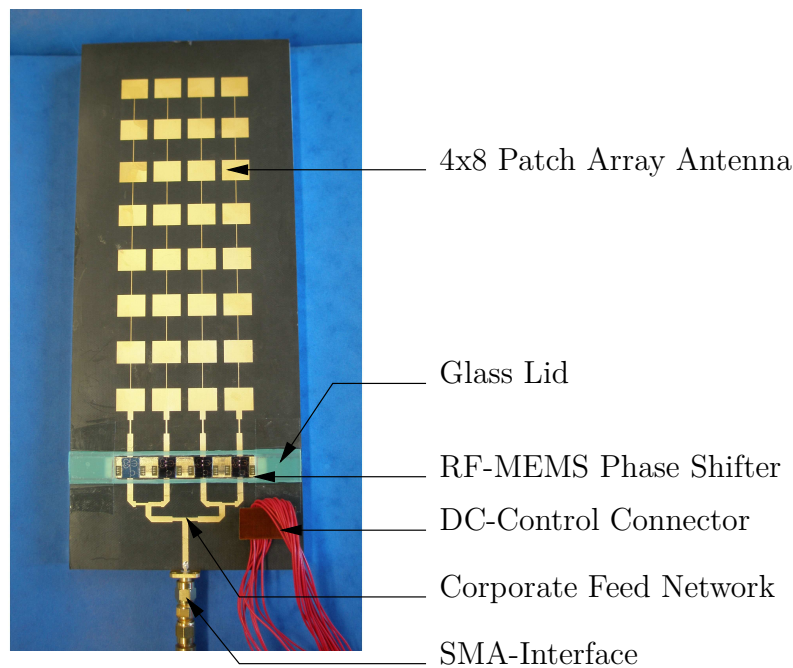


Fig. 3.56: Photograph of the X-band phased array antenna demonstrator.

The photograph shows the different elements of the antenna mounted on a rigid aluminium holder. The 4-by-8 microstrip antenna array and the corporate feed network are depicted on the top and bottom parts of the picture, respectively. Between them and under the glass lid, the four RF-MEMS phase shifters are the dark silicon chips. The DC-control board made out of metallised FR4 is visible between these silicon chips, in the gold-coloured areas. In these gold regions also, the DC bond-pads and bond-wires for the control lines are apparent. The 24-pin connector on the right-hand side of the feed network is the DC-control connector. It is connected to a switch matrix and allows for a control of the phase shifters according to the technique described in the first chapter. Finally, as previously mentioned, the RF-interface is implemented with an SMA connector mounted on the holder and soldered to the microstrip line on Rogers substrate. This SMA interface is shown on the lowermost part of the photograph.

Characterisation and Measurements

The far field radiation characteristic of the antenna has been measured at 9.5 GHz in the facilities of EADS Astrium in Ottobrunn. The E-plane pattern, which is fixed and does not depend on the switching state of the phase shifters is plotted in Fig. 3.57.

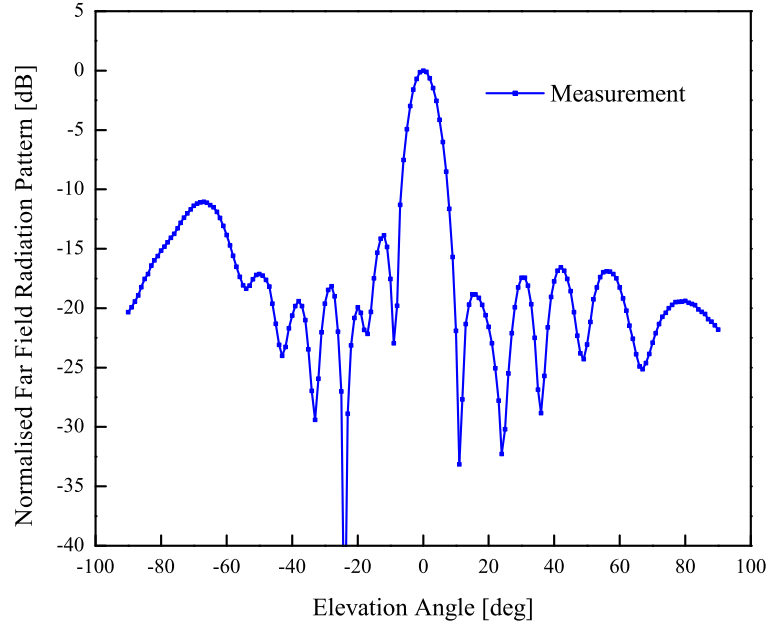


Fig. 3.57: Measured E-plane far field characteristic of the electrically steerable antenna at 9.5 GHz.

In the E-plane, the electrically steerable antenna exhibits a broadside radiation pattern very similar to that measured for the original fixed-beam array. The half-power beamwidth of this characteristic is 8.3° . It is slightly narrower than the 10° of beamwidth measured at the same level for the fixed-beam antenna. Also, the measured side lobe level is -11 dB and is identical to that measured for the fixed-beam antenna. However, it occurs for different side lobes in the two radiation characteristics. The highest side lobe appears at 16° for the fixed-beam antenna, and at 70° for the electrically steerable antenna. This difference is believed to be caused by parasitic radiations of the RF bondwires used to connect the silicon chips. The H-plane radiation characteristic of the electrically steerable antenna has been measured for three pointing directions of the main beam. The three radiation characteristics are plotted in Fig. 3.58.

The plot shows well-formed main beams scanned in the -17° , -2° , and $+12^\circ$ directions. The 3 dB beamwidth is 24.7° for the broadside beam, and about 26.5° for the two beams steered in the -17° and $+12^\circ$ directions. The side lobe level is -8.8 dB, -9.2 dB, and -6.7 dB, for the characteristics scanned in the -17° , -2° , and $+12^\circ$ directions, respectively. Thus, for the broadside pattern, it is 7.8 dB above the side lobe level measured for the fixed-beam antenna. The return loss of the electrically steerable antenna was measured for a main beam pointing in the broadside direction. It is plotted in Fig. 3.59.

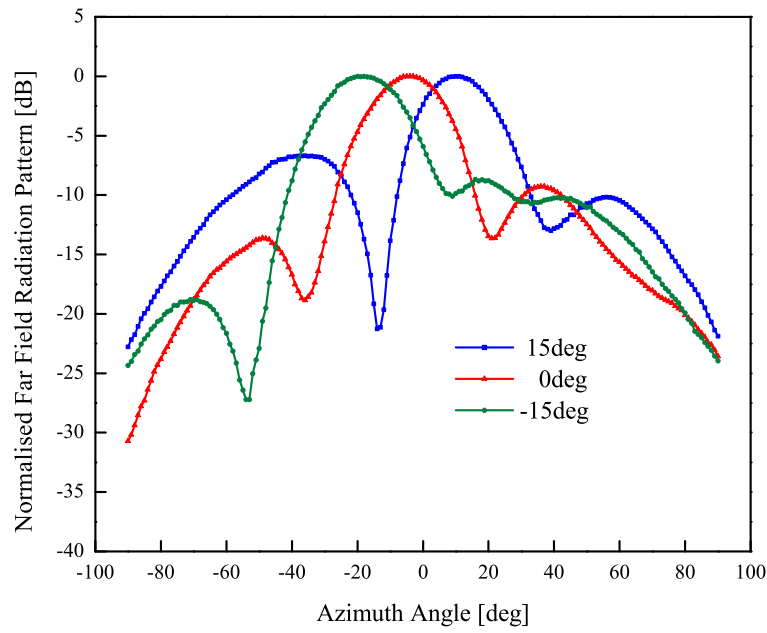


Fig. 3.58: Measured H-plane far field characteristics of the electrically steerable antenna at 9.5 GHz.

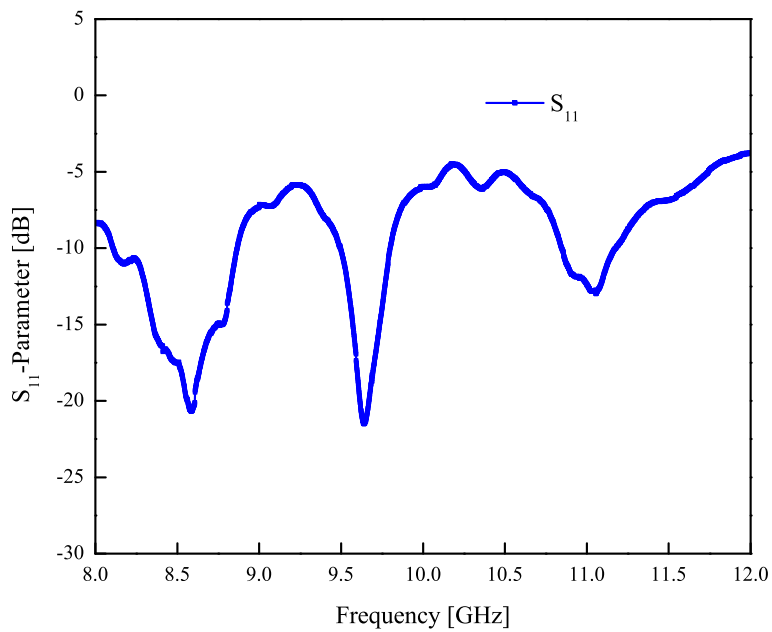


Fig. 3.59: Measured return loss of the X-band electrically steerable antenna.

The return loss is better than 10 dB between 9.49 GHz and 9.80 GHz. This corresponds to a relative bandwidth of 3.3%, slightly larger than the bandwidth measured for the fixed-beam antenna (2.8%). The high side lobe level and the asymmetry observed in the H-plane radiation characteristics might be explained by different factors. Firstly, a known source of inaccuracy is the quantisation error due to the digital phase shifters. As already noticed, 3-bit phase shifters are limited to 45° -stepped phase shifts, and they cannot achieve the linear phase gradient ideally required for the excitations. For this reason, the four sub-arrays are fed with phase errors, which may increase the side lobes in the H-plane pattern. Also, this is emphasised by the design of the phase shifters that is not perfect, and the actual quantisation error of the real phase shifters is even further pronounced. Another source of error is due to parasitic radiations from the feed network. Contrary to the signals radiated from the phased array, those of the feed network are fixed and do not depend on the switching state of the phase shifters. This leads to an increased side lobe level, generally in the broadside direction. However, the quantisation of the phase shifters and the radiation of the feed network cannot be responsible for an asymmetrical broadside characteristic. For this, a justification is more likely in the use of bond-wires with unequal lengths for the connection of the silicon chips. If they are of different lengths, bond-wires create phase and amplitude errors in the feeding signals. Such errors affect both steered and broadside radiation patterns.

In order to assess the influence of the different sources of inaccuracy discussed here, additional electromagnetic simulations corresponding to these different cases have been performed. The re-simulated far field patterns and the measured H-plane radiation characteristic are compared in Fig. 3.60 for a -15° steered beam.

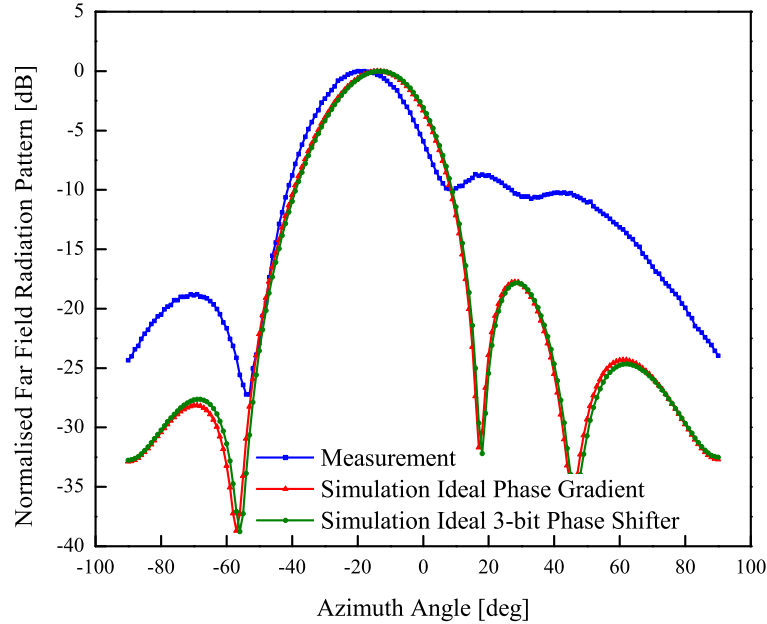


Fig. 3.60: Measured and simulated H-plane far field pattern of the X-band electrically steerable antenna.

To perform these simulations, the four sub-arrays of the antenna have been excited with four individually-controlled discrete ports. This enables the calculation of the radiation characteristic of the antenna for any complex excitation of the sub-arrays. The graph shows three H-plane radiation characteristics. The characteristic in red is calculated when the sub-arrays are fed with the ideal linear phase gradient, that in green is obtained when the phase distribution is achieved by ideal 3-bit phase shifters, and the radiation pattern measured for the antenna in the H-plane is plotted in blue for comparison purposes. Another simulation performed with the phase shifts actually measured for the phase shifters implemented in the demonstrator was also performed. Nevertheless, this radiation characteristic being extremely close to that obtained for ideal 3-bit phase shifters, it is not plotted in the graph for better visibility.

The first conclusion which can be drawn from the comparison concerns the side lobe level of the patterns. In both simulated characteristics, it is very similar and about -18 dB. It is 9 dB below the side lobe level actually measured for the antenna. Also, for the chosen scan angle, the simulated radiation characteristics exhibit an excellent pointing accuracy. The calculated pointing directions are very close to -15° , and are approximately 2° away from the measured main beam direction. From this, the distorted shape of the characteristics measured for the steerable antenna is not imputable to the quantisation of the digital phase shifters. The differences between simulated and measured characteristics in Fig. 3.60 show that the deviations of the measured characteristics are caused by a perfectible physical integration of the phase shifters. These inaccuracies are most probably to find in the irregular lengths of the bond-wires, a sub-optimal positioning of the silicon chips, or in the use of the conductive glue employed to fix them.

3.5.4 Conclusion

In this section 3.5, a X-band phased array antenna was demonstrated. The antenna is made steerable in the H-plane by means of RF-MEMS phase shifters integrated in a hybrid fashion. The design of the different components, phase shifters, antenna array, and feed network, is validated by measurement results in good agreement with simulations. Also, the radiation characteristic of the fully integrated phased array antenna was presented for three switching states of the phase shifters, for a main beam in the $\pm 15^\circ$ and broadside directions. The radiation characteristics were measured with a satisfactory pointing accuracy, approximately 2° away from the aimed scan angle, but suffer from relatively high side lobes. This increased side lobe level is attributed to the use of RF bond-wires with slightly different lengths for the connection of the silicon chips. To overcome this, a further development would be to implement shorter, and more importantly, more uniform bond-wires. In parallel to this, alternative assembly techniques like flip-chip could be also investigated.

3.6 Conclusion

The third chapter of this thesis has presented the development of three fixed-beam and RF-MEMS electrically steerable antennas. The antennas are designed for operation at W-band, Ka-band, and X-band, and are realised in different technologies. The antenna intended for W-band airborne sensing as well as that designed for X-band are fabricated on low-loss soft substrate. The antenna developed for Ka-band satellite communication is processed out of low-loss ceramic dielectric. Also, for the antennas at X- and Ka-band, the hybrid integration concept of the phase shifters was

described in detail, and the design of the phase shifters was presented. In the chapter also, the design of all three antennas was validated by good measurement results, and two electrically steerable antennas at X- and Ka-band have been demonstrated. Both phased antennas have been measured for a main beam steered in three directions of the H-plane, and a radiation efficiency of 18.6% was demonstrated for the Ka-band phased array on LTCC.

The work presented throughout this chapter demonstrates techniques to accommodate emerging technologies into compact, low-loss, and cost effective millimetre-wave phased antennas. In this quest however, hybrid integration presents both, opportunities for combining the advantages of different technologies, and limitations in terms of integration density and repeatability. Also, from the work presented in this chapter, compact, broadband, and low-loss transitions, as well as reliable hermetic packaging arise as major developments remaining towards efficient and low-cost hybrid front-ends.

4 Future Work

Along the work described in this thesis, possible optimisations came up, which could improve on the performance, the size, the complexity, and the costs, of the presented components. They constitute a bench of ideas for later developments of the demonstrated structures, and might be also applicable to other devices. Beyond the adjustments always necessary after a first design iteration, potential enhancements at technological level and for the integration arose. Among these, a first topic in which one sees room for improvement is the hybrid integration of the RF-MEMS silicon chips. In the thesis, most of the techniques presented to answer this challenge utilise transitions implemented with RF bond-wires. Nevertheless, since RF bond-wires are inductive at high frequencies, they often reduce the bandwidth of the transitions, and alternative techniques are sometimes preferred. Furthermore, as it is highlighted in the third chapter on phased antennas, it is sometimes difficult to control accurately the length of bond-wires, and the repeatability is not always as good as expected. To overcome this, other kinds of transitions using stud bumps or electromagnetically coupled lines can be designed. In the particular case of RF-MEMS circuits however, the stud bumping process is a rather challenging task because of the limited temperature that MEMS devices can sustain. Therefore, transitions simply based on capacitive or inductive coupling of transmission lines appear as a promising solution. Further, these transitions might be designed to have a broadband behaviour, which is of course of particular interest for the overall performance of the device [155]. An example of what can be done in the field of hybrid integration using electromagnetically coupled transitions is shown in Fig. 4.1.

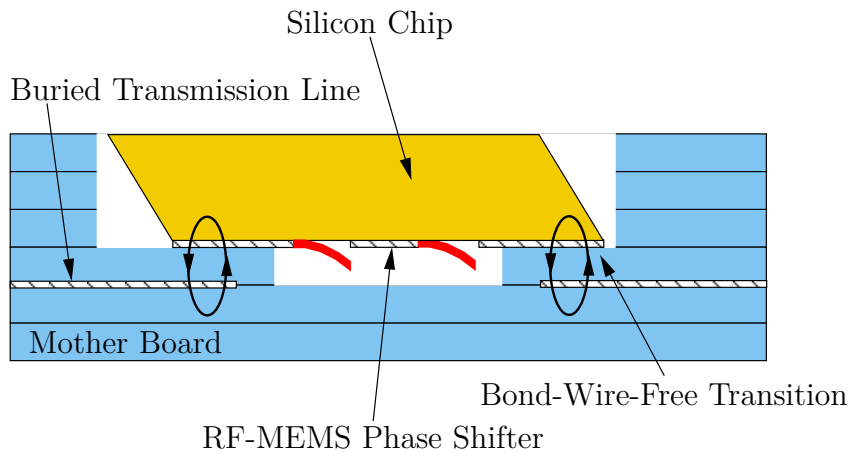


Fig. 4.1: Example of RF bond-wire-free hybrid integration concept for sawn or hand-broken silicon chips.

Another matter, which might deserve further attentions concerns the integration of the RF-MEMS onto the silicon substrate of micro-machined filters (Fig. 2.27). Here, since both, the RF-MEMS chips and the top wafer of the filters are made out of silicon material, a monolithic integration

of the RF-MEMS circuits directly on top of the wafer is possible. As depicted in Fig. 4.2, this would allow for a larger flexibility in the positioning of the adjustable stubs, and the RF-MEMS switch could be placed closer to the coupling structure. Furthermore, a monolithic integration of the RF-MEMS circuits would not require laborious adjustments of the chips, and it would avoid the use of bond-wires. In return, the technique needs RF-MEMS processes capable of handling two wafers bonded together, which is thinkable, but not standard.

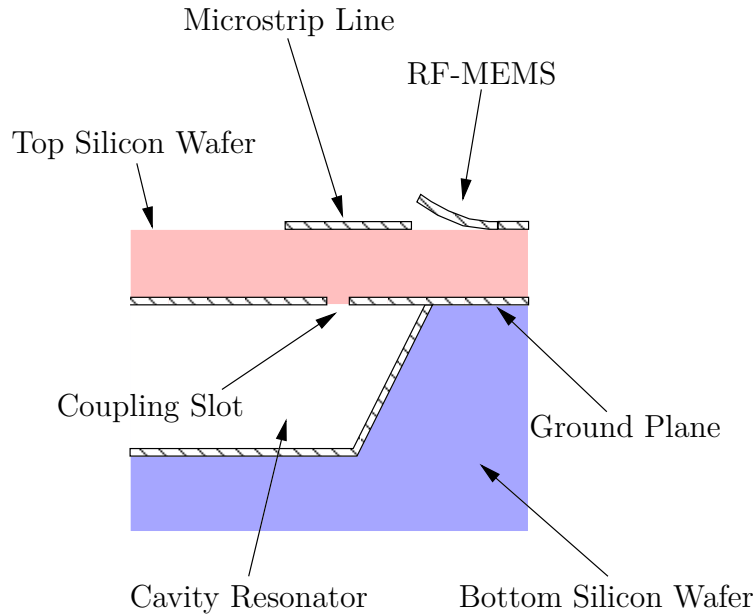


Fig. 4.2: Monolithic integration of the RF-MEMS tunable stub on the micro-machined cavity filter.

Besides these advantages, monolithic integration overcomes another recurrent challenge of hybrid integration of RF-MEMS. Due to their sensitiveness, and especially in regards to the temperature RF-MEMS can sustain, only few reliable RF-MEMS packaging techniques have been demonstrated up to now [58], [156], [157]. Without safe packaging, the dicing of RF-MEMS chips remains a delicate operation, because they cannot be separated using standard sawing processes, which would expose them to dust and water. For this reason, RF-MEMS chips are at present mostly broken per hand. Beyond the fact that the technique is inappropriate for large production scales, it produces chips with slanted edges (Fig. 4.3 and 4.1). Thus, the hybrid integration of "hand-broken" silicon chips implies the use of long and often asymmetrical RF bond-wires, which are cumbersome for the performance of the transitions. Nevertheless, integration is only one aspect of a more general concern pushing the development of reliable packaging technologies for RF-MEMS [158]. Indeed, even if some RF-MEMS technologies have been demonstrated with outstanding performance and endurance under lab conditions [159], [160], their implementation in real systems is limited by this lack of robust packagings, and their long-term reliability under operational conditions is still to prove.

The development of automatised methods for reliable and hermetic packaging of RF-MEMS arises as a major challenge remaining in the field. It constitutes one of the last but decisive developments necessary to provide RF-MEMS technology with reliable, high yield, and low-cost processes, mandatory to ensure its break through on the competitive but prosper commercial and military markets.

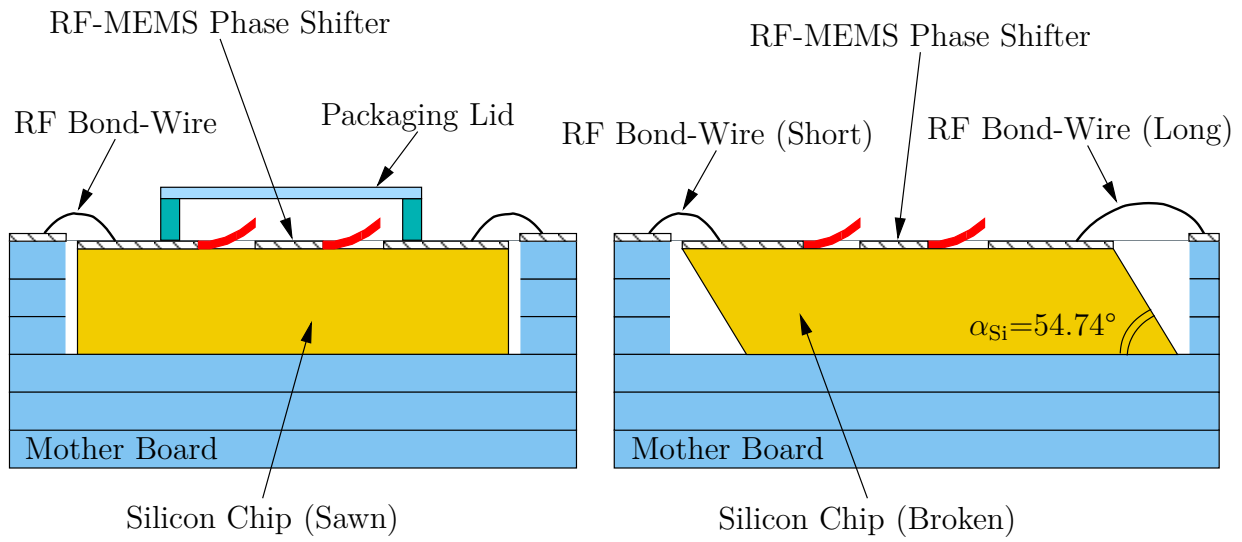


Fig. 4.3: Importance of RF-MEMS packaging for integration: packaged and sawn silicon chip (left), and chip separated per hand (right).

Summary

This thesis is dedicated to the development of RF-MEMS based components for passive millimetre-wave front-ends. It presents the design and the realisation of fixed and reconfigurable filters and antennas, in various technologies, and for operation between the X- and the W-band.

First, cavity resonator band-pass filters are presented. The filters are realised using micro-machining of silicon and on low-loss multilayer ceramic substrate. The micro-machined filters are designed at 20 GHz, and they are intended for implementation on-board of satellite transceivers. The filters implement a 2-wafer architecture, in which the cavity resonators are processed in a thick bottom silicon wafer, and the coupling structures are realised in the top wafer. The novelty of the design, as proposed in the thesis, is in the realisation of the inter-resonator couplings. They are manufactured using the same KOH-wet etching of silicon, as that used for the cavity resonators. Using this KOH micro-machining technology, an outstanding unloaded Q-factor of 1410 is demonstrated for a 2-port cavity resonator. Also, 2-, 3-, and 4-pole fixed-frequency filters are measured with both, well-shaped pass-band responses and little insertion loss. This insertion loss is about 0.3 dB for the 2-pole filter, and 1 dB for the 4-pole filter. Further, a solution based on RF-MEMS is proposed for the tuning of micro-machined cavity resonator filters. According to the tuning concept, adjustable stubs are coupled to the micro-machined cavity resonators of the filter. The tuning technique is described and a method is proposed for the hybrid integration of the RF-MEMS circuits. The technique is implemented to tune the 3-pole band-pass filter firstly demonstrated as fixed-frequency filter. The frequency-agile filter is designed with six RF-MEMS adjustable stubs, which are coupled to the three micro-machined cavity resonators of the filter. It is measured with a good tunability of 3.71% and an insertion loss of about 2 dB. The micro-machined filters realised according to the technique are low-loss, and they can be easily integrated in a hybrid fashion or monolithically onto a large variety of substrates. Also, their compactness makes them particularly suitable for on-board applications, where low-loss is mandatory but in which the space and weight are too limited for high-Q and bulky waveguide filters.

The second family of filters is manufactured on 6-layer DuPont 943 ceramic substrate. These filters are designed for operation at 15 GHz. They are cavity resonator filters integrated in ceramics according to the substrate-integrated waveguide technique. The cavity resonators are formed by rows of vias processed in LTCC, and connected with metal stripes. For these filters, a novel input/output coupling structure is also introduced. It is implemented with one via processed inside the cavity resonator, and connecting the I/O transmission lines to the bottom of the cavity. The technique is implemented to design and realise a 2-port cavity resonator and a 2-pole band-pass filter. The method is validated by satisfactory measurement results in good agreement with full-wave simulations. For the single cavity resonator, an unloaded Q-factor of 290 is measured, and the 2-pole filter is demonstrated with about 1 dB of insertion loss. The presented architecture integrated in low-loss ceramics offers a good compromise between insertion loss and size of the resonators, smaller than air-filled cavities for example. Beyond fixed-frequency filters, two frequency-agile filters are also demonstrated. The tunable filters are implemented again with the method introduced to

tune micro-machined filters, but fitted to these filters in ceramics. The hybrid integration of the RF-MEMS adjustable stubs is described, and the way they are coupled to the cavity resonators is presented. The two tunable filters exhibit 3% and 7.2% of tuning range, respectively.

On top of this work on fixed and tunable filters, a method is also introduced to compensate the temperature-dependence of cavity resonators. The technique presented in the thesis for substrate-integrated cavity resonators is based on ferro-electric varactors. According to the proposed concept, BST-varactors are inductively coupled to the cavity resonators. Also, the coupling is designed in order to compensate the temperature-dependence of the cavity resonator with the natural variation of the capacitance of the varactor over temperature. The actuation-free compensation technique is validated by measurement of a compensated resonator. For the demonstrated structure, the frequency shift of -0.48% observed without compensation and over a 90°C temperature range is reduced down to below -0.12% with compensation.

The second concern of this thesis is the development of RF-MEMS based electrically steerable antennas. This includes the design, the realisation, and the measurement of all components of passive phased array antennas such as, the antenna, the phase shifters, and the distribution network. On top of this, the integration of these components in stand-alone phased antenna demonstrators is also described.

Three antennas for operation at X-, Ka-, and W-band are presented. First, a transmit and a receive antenna developed for airborne wake-vortex detection at 76.5 GHz are described. The transmit antenna, demonstrated here as fixed-beam antenna, is intended to be steered by means of W-band 4-bit RF-MEMS phase shifters. It is designed with twenty eight serially fed microstrip antenna sub-arrays manufactured on Teflon substrate. The sub-arrays of the antenna are connected in parallel by a corporate feed network realised on the same substrate. The antenna is demonstrated with a pencil main beam having 5° and 3° of beamwidth, in the E- and H-planes, respectively. Also, a radiation efficiency of 19.7% was obtained for that antenna.

The second antenna is realised on 6-layer DuPont 943 ceramic substrate. It is foreseen for satellite communication link, and it is designed for operation at Ka-band. The antenna itself is designed with a four by four patch antenna array. It is fed by a distribution network buried in LTCC, and connected to the microstrip antennas according to the aperture coupled principle. Based on this fixed beam antenna also, an electrically steerable antenna is demonstrated. It is realised with four RF-MEMS phase shifters, which are integrated between the feed network and the microstrip antenna array. The design and integration concept implemented for the antenna are validated by good measurement results obtained for the phased array demonstrator. The antenna was measured for three switching states of the phase shifters providing a main beam steered in the -11°, 4.5°, and 22° directions. In the broadside direction, the gain of the antenna is 8 dBi and corresponds to a radiation efficiency of 18.6%.

Finally, the last presented antenna is a X-band electrically steerable antenna. It is designed with four serially fed patch antenna sub-arrays, containing eight microstrip antennas each. The beam steering of the antenna is achieved with four 3-bit RF-MEMS phase shifters placed between the corporate feed network and the microstrip antenna sub-arrays. For this phased array demonstrator also, the hybrid integration of the phase shifters with the other components of the antenna is described. As for the electrically steerable antenna on ceramics, measurement results are provided for this antenna, for three pointing directions steered in the H-plane. The antenna is demonstrated with three well-formed main beams pointing the -17°, -2°, and +12° directions.

Appendix A: A 3-bit RF-MEMS Phase Shifter for Ka-Band Electrically Steerable Antennas

The appendix describes the design, the realisation, and the measurement of a Ka-band RF-MEMS phase shifter [161]. The phase shifter has been implemented in the electrically steerable antenna presented in section 3.4. The phase shifter is a digital RF-MEMS phase shifter designed with three bits of 45° , 90° , and 180° . It is processed in the EADS Innovation Works RF-MEMS technology, and it is fabricated on $200\mu\text{m}$ -thick high resistivity silicon [52]. The three bits of the phase shifter are all designed according to the loaded line technique, implemented here in microstrip topology [150]. The 45° -bit is realised with two adjustable stubs, which load the main microstrip line passing through the entire phase shifter. The two other bits of 90° and 180° are designed in the same way, but with four and eight RF-MEMS adjustable stubs, respectively. These bits are realised by duplication of the first designed 45° -bit, twice for the 90° -bit, and four times for the 180° -bit. The design results in a rather long but narrow phase shifter, especially suitable for millimetre-wave antennas with limited inter-element spacings. A major advantage of loaded line technique is that it requires only simple Single Pole Single Throw switches (SPST). These switches are easier to design than switches with multiple throws (SPMT), often necessary when other design techniques are used. A photograph of the Ka-band phase shifter is depicted in Fig. A.1.

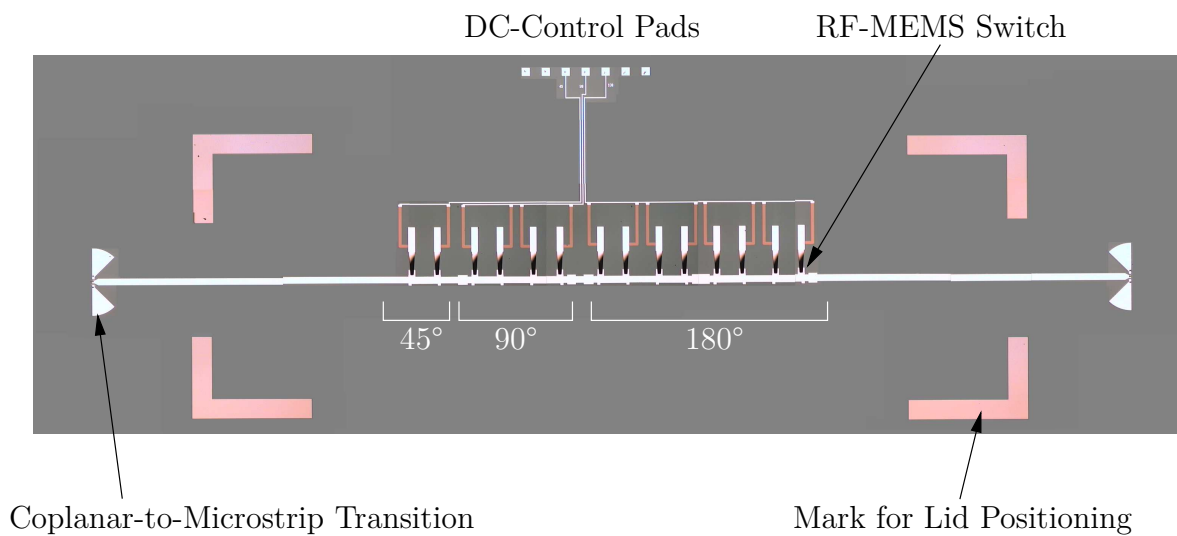


Fig. A.1: Photograph of the EADS Innovation Works Ka-band RF-MEMS phase shifter.

The phase shifter has been processed in the clean room of EADS Innovation Works in Ottobrunn. It has been characterised on-wafer using the RF measurement setup described in the first chapter of the thesis. Also, in order to connect the microstrip phase shifter to coplanar measurement probes, coplanar-to-microstrip line transitions have been designed at its input and output. For the characterisation of the phase shifter, these transitions have been de-embedded out of the measurement using TRL calibration. The insertion loss and return loss of the phase shifter measured for the eight switching states are given in Fig. A.2. The phase shifts measured between the input and output of the phase shifter for these same switching states are given in Fig. A.3.

At the design frequency of 35 GHz, the measured return loss of the phase shifter is better than 12.5 dB for any switching state. Also, it exhibits a very low insertion loss below 4 dB over a large frequency range, from about 32.9 GHz up to above 40 GHz. The phase shifts achieved by the phase shifter are very close to what can be reached with an ideal 3-bit phase shifter. Around the design frequency, the measured phase shifts are distributed every 45° with a very good accuracy, and they cover the complete 2π angular range. In order to further assess the performance of the phase shifter, its standard phase deviation and mean insertion loss have been calculated using (3.4.5) and (3.4.6), respectively. They are plotted together in Fig. A.4.

Between 33.2 GHz and 36.3 GHz, the phase shifter has a standard phase deviation better than 14.5° and a mean insertion loss below 2.7 dB. Such a phase deviation of 14.5° corresponds to an equivalent number of bits of 2.84. For the antenna in which the phase shifter is implemented, this means a drop of the antenna gain by 0.28 dB, and a rms beam pointing accuracy of 0.11, expressed in fraction of beamwidth.

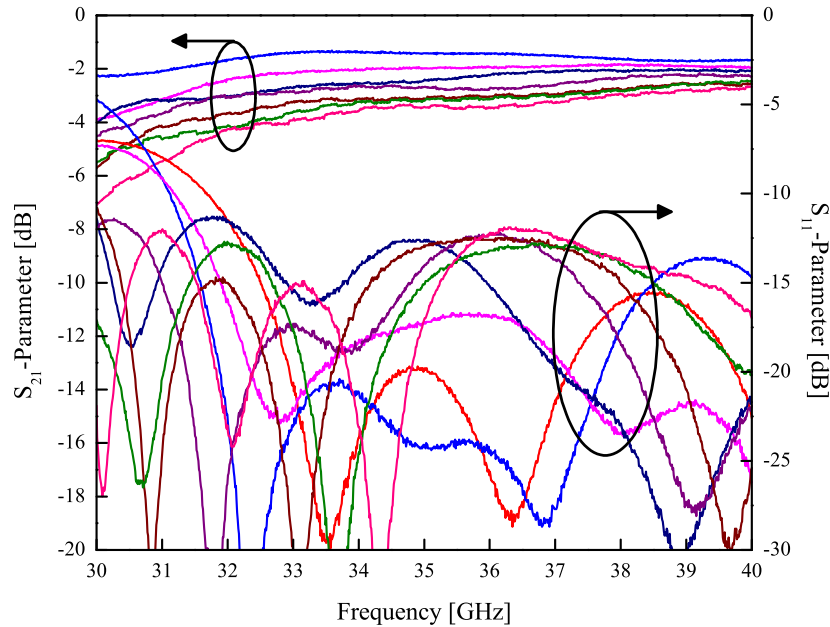


Fig. A.2: Measured return loss and insertion loss of the EADS Innovation Works Ka-band RF-MEMS phase shifter for the eight switching states.

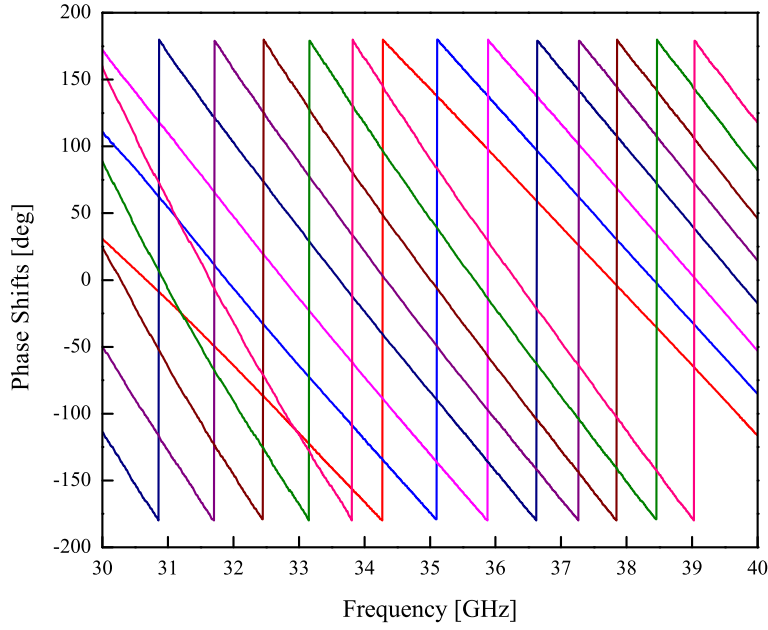


Fig. A.3: Phase shifts measured for the EADS Innovation Works Ka-band RF-MEMS phase shifter for the eight switching states.

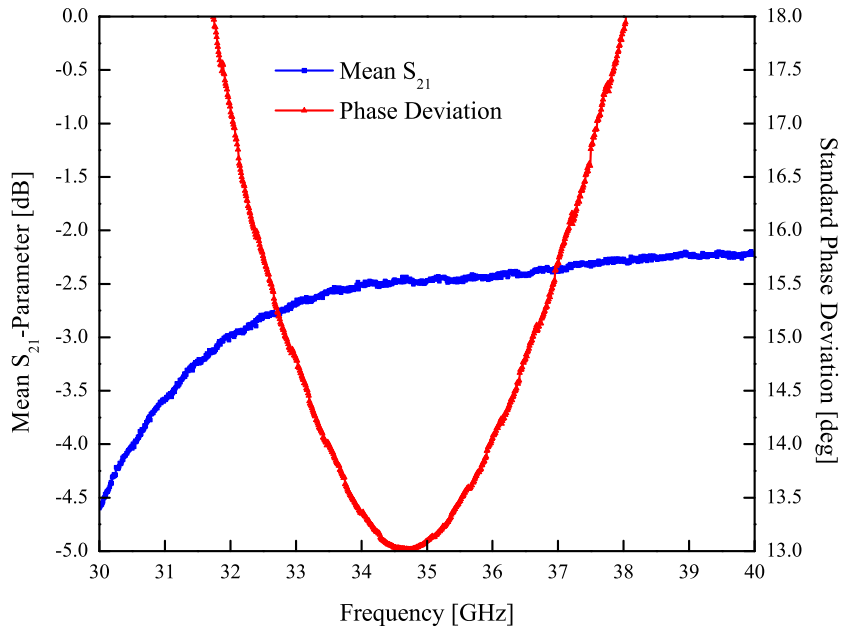


Fig. A.4: Mean insertion loss and standard phase deviation of the EADS Innovation Works Ka-band RF-MEMS phase shifter.

Bibliography

- [1] M. Camiade, D. Domnesque, Z. Ouarch, and A. Sion. Fully MMIC based front end for FMCW automotive radar at 77GHz. In *Proceedings of the 30th European Microwave Conference*, pages 1–4, 2000. DOI: 10.1109/EUMA.2000.338612.
- [2] J. Grubert, J. Heyen, C. Metz, L. C. Stange, and A. F. Jacob. Planar millimeter wave radar front end for automotive applications. *Advances in Radio Science*, 1:125–129, 2003.
- [3] K. Takahashi, S. Fujita, U. Sangawa, A. Ono, T. Urabe, S. Takeyama, H. Ogura, and H. Yabuki. K-band receiver front-end IC integrating micromachined filter and flip-chip assembled active devices. In *IEEE MTT-S International Microwave Symposium Digest*, volume 1, pages 229–232, 1999. DOI: 10.1109/MWSYM.1999.779464.
- [4] The european table of frequency allocations and utilisations covering the frequency range 9KHz to 275GHz.
- [5] C. H. Doan, S. Emami, D. Sobel, A. M. Niknejad, and R. W. Brodersen. 60GHz CMOS radio for Gb/s wireless LAN. In *IEEE Radio Frequency Integrated Circuits Symposium*, pages 225–228, 2004.
- [6] C. Karnfelt, P. Hallbjorner, H. Zirath, and A. Alping. High gain active microstrip antenna for 60GHz WLAN/WPAN applications. *IEEE Trans. on Micro. Theory and Techniques*, 54(6):2593–2603, 2006. DOI: 10.1109/TMTT.2006.872923.
- [7] S. Sarkar. *Silicon-based millimeter-wave front-end development for multi-gigabit wireless applications*. PhD thesis, Georgia Institute of Technology, 2007.
- [8] S. Reynolds, B. Floyd, U. Pfeiffer, and T. Zwick. 60GHz transceiver circuits in SiGe bipolar technology. In *IEEE International Solid-State Circuits Conference*, volume 1, pages 442–538, 2004. DOI: 10.1109/ISSCC.2004.1332784.
- [9] G. E. Brehm. Trends in microwave/millimeter-wave front-end technology. In *Proceedings of the 1st European Microwave Integrated Circuits Conference*, pages 1–4, 2006. DOI: 10.1109/EMICC.2006.282734.
- [10] M. M. Tentzeris, J. Laskar, J. Papapolymerou, S. Pinel, V. Palazzari, R. Li, G. Dejean, N. Papageorgiou, D. Thompson, R. Bairavasubramanian, S. Sarkar, and J. H. Lee. 3D integrated RF and millimeter wave functions and modules using liquid crystal polymer (LCP) system-on-package technology. *IEEE Trans. on Advanced Packaging*, 27:332–340, 2004. DOI: 10.1109/TADVPP.2004.828814.

- [11] J. Laskar, A. Sutono, C. H. Lee, M. F. Davis, M. Maeng, N. Lal, K. Lim, S. Pinel, M. Tentzeris, and A. Obatoyinbo. Development of integrated 3D radio front-end system-on-package (SOP). In *23rd Annual Technical Digest, Symposium on Gallium Arsenide Integrated Circuit*, pages 215–218, 2001. DOI: 10.1109/GAAS.2001.964381.
- [12] L. Xia, R. Xu, and B. Yan. LTCC-based highly integrated millimeter-wave receiver front-end module. *International Journal of Infrared and Millimeter Waves*, 27(7):975–983, 2006.
- [13] E. M. Biebl. Millimeter wave systems based on SIMMWICs. *Topical Meeting on Silicon Monolithic Integrated Circuits in RF Systems*, pages 1–4, 2000. DOI: 10.1109/SMIC.2000.844284.
- [14] P. Russer and R. Lachner. Silicon-monolithic integrated millimeterwave circuits for vehicular technology. In *XXVIIIth URSI General Assembly*, 2005.
- [15] P. Russer. Si and SiGe millimeter-wave integrated circuits. *IEEE Trans. on Micro. Theory and Techniques*, 46(5):590–603, 1998. DOI: 10.1109/22.668668.
- [16] C. L. Goldsmith, Y. Zhimin, S. Eshelman, and D. Denniston. Performance of low-loss RF-MEMS capacitive switches. *IEEE Microwave and Guided Wave Letters*, 8(8):269–271, 1998. DOI: 10.1109/75.704410.
- [17] A. Stehle, D. Noetel, C. Siegel, V. Ziegler, B. Schoenlinner, U. Prechtel, H. Seidel, and U. Schmid. High isolation Ka-band SPST RF-MEMS switch for radiometer. In *Proceedings of the German Microwave Conference*, 2008.
- [18] C. L. Goldsmith, A. Malczewski, Z. J. Yao, S. Chen, J. Ehmke, and D. H. Hinzl. RF-MEMS variable capacitors for tunable filters. *International Journal of RF and Microwave Computer-Aided Engineering*, 9(4):362–374, 1999.
- [19] D. Peroulis and L. P. B. Katehi. Electrostatically-tunable analog RF-MEMS varactors with measured capacitance range of 300%. *IEEE MTT-S International Microwave Symposium Digest*, 3:1793–1796, 2003.
- [20] A. Stehle, C. Siegel, V. Ziegler, B. Schoenlinner, U. Prechtel, H. Seidel, and U. Schmid. High-power handling capability of low complexity RF-MEMS switch in Ku-band. *Electronics Letters*, 43(24), November 2007. DOI: 10.1049/el:20072827.
- [21] T. Vaehae-Heikkilae, J. Varis, and J. Tuovinen. MEMS based tunable circuits for millimetre wave systems. In *XXVIIIth URSI General Assembly*, 2005.
- [22] K. Entesari and G. M. Rebeiz. A 12-18GHz three-pole RF MEMS tunable filter. *IEEE Trans. on Microwave Theory and Techniques*, 53(8):2566–2571, 2005.
- [23] S. J. Park. *High performance RF-MEMS tunable filters*. PhD thesis, University of Michigan, 2008.
- [24] C. Siegel, V. Ziegler, U. Prechtel, B. Schoenlinner, and H. Schumacher. A Ka-band RF-MEMS phase shifter approach based on a novel dual-state microstrip line. In *Proceedings of the 37th European Microwave Conference*, October 2007.

-
- [25] J. B. Rizk and G. A. Rebeiz. W-band microstrip RF-MEMS switches and phase shifters. In *IEEE MTT-S International Microwave Symposium Digest*, volume 3, pages 1485–1488, 2003.
- [26] G. Subramanyam, F. Ahamed, and R. Biggers. A Si MMIC compatible ferroelectric varactor shunt switch for microwave applications. *IEEE Microwave and Wireless Components Letters*, 15(11):739–741, 2005.
- [27] A. Vorobiev, P. Rundqvist, K. Khamchane, and S. Gevorgian. Silicon substrate integrated high Q-factor parallel-plate ferroelectric varactors for microwave/millimeterwave applications. *Applied Physics Letters*, 83(15):3144–+, 2003. DOI: 10.1063/1.1619213.
- [28] S. Abadei, A. Deleniv, and S. Gevorgian. Filter-phase shifters based on thin film ferroelectric varactors. In *Proceedings of the 34th European Microwave Conference*, pages 1493–1496, 2004.
- [29] S. Mueller, C. Felber, P. Scheele, M. Wittek, C. Hock, and R. Jakoby. Passive tunable liquid crystal finline phase shifter for millimeter waves. In *Proceedings of the 35th European Microwave Conference*, volume 1, 2005. DOI: 10.1109/EUMC.2005.1608852.
- [30] N. Martin, P. Laurent, G. Prigent, P. Gelin, and F. Huret. Technological evolution and performances improvements of a tunable phase-shifter using liquid crystal. *Microwave and Optical Technology Letters*, 43(4):338–341, 2004.
- [31] H. Moritake, S. Morita, R. Ozaki, T. Kamei, and Y. Utsumi. Microwave variable phase shifter of coplanar waveguide using ferroelectric liquid crystal. *Japanese Journal of Applied Physics*, 47:1367–1370, 2008. DOI: 10.1143/JJAP.47.1367.
- [32] S. Mueller, F. Goelden, P. Scheele, M. Wittek, C. Hock, and R. Jakoby. Passive phase shifter for W-band applications using liquid crystals. In *Proceedings of the 36th European Microwave Conference*, 2006.
- [33] J. Papapolymerou, J. C. Cheng, J. East, and L. P. B. Katehi. A micromachined high-Q X-band resonator. *IEEE Microwave and Guided Wave Letters*, 7:168–170, 1997.
- [34] G. L. Matthaei, L. Young, and E. M. T. Jones. *Microwave filters, impedance-matching networks, and coupling structures*. Number ISBN: 0-89006-099-1. Artech House, Inc., 1980.
- [35] D. Mercier, M. Chatras, J. C. Orlianges, C. Champeaux, A. Catherinot, P. Blondy, D. Cros, and J. Papapolymerou. A micromachined tunable cavity resonator. In *Proceedings of the 33th European Microwave Conference*, 2003.
- [36] Y. Cassivi, L. Perregrini, K. Wu, and G. Conciauro. Low-cost and high-Q millimeter-wave resonator using substrate integrated waveguide technique. In *Proceedings of the 32nd European Microwave Conference*, pages 1–4, 2002. Digital Object Identifier: 10.1109/EUMA.2002.339390.
- [37] J. Freese, R. Jakoby, H. L. Blocher, and J. Wenger. Synthesis of microstrip series-fed patch arrays for 77GHz-sensor applications. In *Asia-Pacific Microwave Conference*, 2000.
- [38] A. Stehle, G. Georgiev, V. Ziegler, B. Schoenlinner, U. Prechtel, H. Seidel, and U. Schmid. RF-MEMS switch and phase shifter optimized for W-band. In *Proceedings of the 38th European Microwave Conference*, pages 104–107, 2008. DOI: 10.1109/EUMC.2008.4751398.
-

- [39] J. F. Zuercher and F. E. Gardiol. *Broadband patch antennas*. Number ISBN: 0-89006-777-5. Artech House, Inc., 1995. ISBN-10: 0890067775.
- [40] IMST. www.empire.de.
- [41] AppliedWaveResearch. web.awrcorp.com/Usa/Products/Microwave-Office.
- [42] W. Gautier. Array antenna pattern synthesis. Master's thesis, Ecole Nationale d'Ingénieurs de Brest, September 2005.
- [43] D. J. Shpak. A method for the optimal pattern synthesis of linear arrays with prescribed nulls. *IEEE Trans. on Antennas and Propagation*, 44(3):286–294, 1996. DOI: 10.1109/8.486295.
- [44] G. D. Taylor and M. J. Winter. Calculation of best restricted approximations. *SIAM Journal on Numerical Analysis*, 7(2), 1970.
- [45] P. N. Boon, H. E. Meng, and K. Chichung. A flexible array synthesis method using quadratic programming. *IEEE Trans. on Antennas and Propagation*, 41:1541–1550, 1993. DOI: 10.1109/8.267354.
- [46] SussMicroTec. IZI probe technology. www.suss.com/products/test_systems.
- [47] GGBIndustries. Calibration substrates. www.ggb.com/calsel.html.
- [48] Charakterisierung von Millimeterwellenschaltern. Master's thesis, Universitaet Dortmund.
- [49] Measurement Computing corporation: USB-ERB24, data sheet and full specifications. www.measurementcomputing.com/usb-erb24specs.html, July 2006.
- [50] A. Stehle, C. Siegel, V. Ziegler, B. Schoenlinner, and U. Prechtel. Low complexity RF-MEMS switch optimized for operation up to 120°C. In *Proceedings of the 37th European Microwave Conference*, pages 1229–1232, October 2007. DOI: 10.1109/EUMC.2007.4405422.
- [51] V. Ziegler, C. Siegel, B. Schoenlinner, A. Stehle, W. Gautier, and U. Prechtel. Switchable microwave circuits using the EADS low-complexity RF-MEMS process. *Frequenz*, 61:199–202, September-October 2007. ISSN: 0016-1136.
- [52] C. Siegel, V. Ziegler, B. Schoenlinner, U. Prechtel, and H. Schumacher. Simplified RF-MEMS switches using implanted conductors and thermal oxide. In *Proceedings of the 36th European Microwave Conference*, September 2006.
- [53] C. Siegel, V. Ziegler, U. Prechtel, and H. Schumacher. Low-complexity RF-MEMS technology for microwave phase shifting applications. In *Proceedings of the German Microwave Conference*, 2005.
- [54] C. Siegel, V. Ziegler, U. Prechtel, B. Schoenlinner, and H. Schumacher. Very low complexity RF-MEMS technology for wide range tunable microwave filters. In *Proceedings of the 35th European Microwave Conference*, volume 1, October 2005. Digital Object Identifier: 10.1109/EUMC.2005.1608937.

-
- [55] C. M. Siegel, W. Gautier, V. Ziegler, U. Prechtel, and H. Schumacher. Reconfigurable patch antenna based on a very low complexity RF-MEMS technology on silicon. In *Memswave*, 2006.
 - [56] A. Stehle, G. Georgiev, V. Ziegler, B. Schoenlinner, U. Prechtel, H. Seidel, and U. Schmid. Broadband single pole multi throw RF-MEMS switches for Ka-band. In *Proceedings of the German Microwave Conference*, 2009.
 - [57] C. M. Siegel, V. Ziegler, B. Schoenlinner, U. Prechtel, and H. Schumacher. RF-MEMS based 2-bit reflective phase shifter at X-band for reconfigurable reflect-array antennas. In *Memswave*, 2007.
 - [58] A. Stehle, G. Georgiev, V. Ziegler, B. Schoenlinner, U. Prechtel, H. Seidel, and U. Schmid. Glass cap packaged high isolating Ka-band RF-MEMS switch. In *Memswave*, 2008.
 - [59] A. Stehle, V. Ziegler, B. Schoenlinner, U. Prechtel, H. Seidel, and U. Schmid. RF-MEMS switches for W-band applications. In *Memswave*, 2007.
 - [60] A. Stehle, V. Ziegler, B. Schoenlinner, U. Prechtel, H. Seidel, and U. Schmid. Coplanar RF-MEMS switch for W-band applications. In *Transducers*, 2007.
 - [61] C. Siegel, V. Ziegler, C. Waechter, B. Schoenlinner, U. Prechtel, and H. Schumacher. Switching speed analysis of low complexity RF-MEMS switches. In *Proceedings of the German Microwave Conference*, 2006.
 - [62] C. H. Lee, S. Chakraborty, A. Sutono, S. Yoo, D. Heo, and J. Laskar. Broadband highly integrated LTCC front-end module for IEEE 802.11a WLAN applications. In *IEEE MTT-S International Microwave Symposium Digest*, volume 2, pages 1045–1048, 2002. Digital Object Identifier: 10.1109/MWSYM.2002.1011816.
 - [63] Y. S. Lin, C. C. Liu, K. M. Li, and C. H. Chen. Design of an LTCC tri-band transceiver module for GPRS mobile applications. In *IEEE MTT-S International Microwave Symposium Digest*, volume 2, pages 633–636, 2004. Digital Object Identifier: 10.1109/MWSYM.2004.1336065.
 - [64] J. Mueller, R. Perrone, H. Thust, K. H. Drue, C. Kutscher, R. Stephan, J. Trabert, M. Hein, D. Schwanke, J. Pohlner, G. Reppe, R. Kulke, P. Uhlig, A. F. Jacob, T. Baras, and A. Molke. Technology benchmarking of high resolution structures on LTCC for microwave circuits. In *Electronics Systemintegration Technology Conference*, volume 1, pages 111–117, September 2006. Digital Object Identifier: 10.1109/ESTC.2006.279987.
 - [65] D. Schwanke, T. Haas, M. Harnack, A. Bittner, U. Schmid, E. Feurer, S. Hoyler, and B. Holl. LTCC-Duennfilm-Polymer Kombination fuer 77-81GHz Radarsysteme. In *VDE Kongress, Innovations for Europe*. VDE-VDI, 2006.
 - [66] T. P. Mobley, M. Smith, D. Zimmerman, M. Miller, D. Nair, and M. Walsh. 20 to 90GHz broadband characterization of LTCC materials for transceiver modules and integrated antennas. In *IMAPS/ACerS International Conference and Exhibition on Ceramic Interconnect and Ceramic Microsystems Technologies*, 2006.

- [67] R. Kulke, W. Simon, C. Günner, G. Moellenbeck, D. Koether, and M. Rittweger. RF-benchmark up to 40GHz for various LTCC low loss tapes. In *IMAPS-Nordic*, 2002. www.ltcc.de/downloads/rd/pub/12-doc-imaps-benchm-2002.pdf.
- [68] D. I. Amey and S. J. Horowitz. Characterization of low loss LTCC materials at 40GHz. *International Symposium on Microelectronics*, pages 89–94, 1999. DuPont Microcircuits Materials.
- [69] Micro Systems Engineering GmbH. *Thickfilm and LTCC design guide*, December 2006.
- [70] Via Electronic GmbH. *Design rules for LTCC, DuPont system 951*, 2004.
- [71] R. Levy and S. B. Cohn. A history of microwave filter research, design, and development. *IEEE Trans. on Micro. Theory and Techniques*, 32:1055–1067, 1984.
- [72] K. M. Lakin, C. Andrus, J. R. Belsick, K. T. McCarron, and W. Thornhill. Wide bandwidth thin film BAW filters. In *IEEE Ultrasonics Symposium*, volume 1, pages 407–410, 2004. DOI: 10.1109/ULTSYM.2004.1417749.
- [73] H. P. Loeb, C. Metzmacher, R. F. Milsom, R. Mauczok, W. Brand, P. Lok, A. Tuinhout, and F. Vanhelmont. Narrow band bulk acoustic wave filters. In *IEEE Ultrasonics Symposium*, volume 1, pages 411–415, 2004. DOI: 10.1109/ULTSYM.2004.1417750.
- [74] M3TR multiband multimode multirole tactical radio - Rhode&Schwarz publication.
- [75] E. Lopelli, J. VanDerTang, and A. H. M. VanRoermund. Ultra-low power frequency-hopping spread spectrum transmitters and receivers. *Analog Circuit Design*, 3:377–441, December 2006.
- [76] N. Cho, J. Lee, L. Yan, J. Bae, S. Kim, and H. J. Yoo. A 60Kb/s-to-10Mb/s 0.37 nJ/b adaptive frequency-hopping transceiver for body-area network. In *IEEE International Solid State Circuits Conference*, 2008.
- [77] W. R. McGrath, C. Walker, M. Yap, and Y. C. Tai. Silicon micromachined waveguides for millimeter-wave and submillimeter-wave frequencies. *IEEE Microwave and Guided Wave Letters*, 3(3):61–63, March 1993.
- [78] S. V. Robertson, L. P. B. Katehi, and G. M. Rebeiz. Micromachined W-band filters. *IEEE Trans. on Micro. Theory and Techniques*, 44:598–606, 1996.
- [79] P. Blondy, A. R. Brown, D. Cros, and G. B. Rebeiz. Low-loss micromachined filters for millimeter wave communication systems. *IEEE Trans. on Micro. Theory and Techniques*, 46:2283–2288, 1998.
- [80] C. Y. Chi and G. M. Rebeiz. Conductor-loss limited stripline resonator and filters. *IEEE Trans. on Micro. Theory and Techniques*, 44(4):626–630, April 1996.
- [81] A. R. Brown, P. Blondy, and G. M. Rebeiz. Microwave and millimeter-wave high-Q micromachined resonators. *International Journal of RF and Microwave Computer-Aided Engineering*, 9:326–337, 1999. Issue: 4.

-
- [82] L. Harle and L. P. B. Katehi. A vertically integrated micromachined filter. *IEEE Trans. on Micro. Theory and Techniques*, 50:2063–2068, September 2002. Digital Object Identifier: 10.1109/TMTT.2002.802317.
- [83] L. Harle. *Microwave micromachined cavity filters*. PhD thesis, The University Of Michigan, 2003.
- [84] Z. Yong, Z. Jian, Y. Yuanwei, C. Chen, and J. S. Xing. A Ku-band novel micromachined band pass filter with two transmission zeros. In *Symposium on Design, Test, Integration and Packaging of MEMS/MOEMS*, 2006.
- [85] L. Bergstedt, S. Gevorgian, and M. Gustafsson. Component for electromagnetic waves and a method for manufacturing the same, 2007.
- [86] P. J. Koh and D. T. Nemeth. Coupled resonator filters formed by micromachining, 2004.
- [87] C. Song, C. Kim, I. Song, Y. Kwon, and C. Cheon. Cavity resonator for reducing phase noise of voltage controlled oscillator, 2002.
- [88] J. Uher and W. J. R. Hoefer. Tunable microwave and millimeter-wave band-pass filters. *IEEE Trans. on Micro. Theory and Techniques*, 39:643–653, 1991.
- [89] R. W. deGrasse. Low-loss gyromagnetic coupling through single crystal garnets. *Journal of Applied Physics*, 30:1555–1559, 1958.
- [90] C. S. Tsai, G. Qiu, H. Gao, L. W. Yang, G. P. Li, S. A. Nikitov, and Y. Gulyaev. Tunable wideband microwave band-stop and band-pass filters using YIG/GGG-GaAs layer structures. *IEEE Trans. on Magnetics*, 41(10):3568–3570, October 2005. Digital Object Identifier: 10.1109/TMAG.2005.855191.
- [91] M. Yoshikazu, O. Takahiro, and O. Tsutomu. A 0.5-4.0GHz tunable bandpass filter using YIG film grown by LPE. *IEEE Trans. on Micro. Theory and Techniques*, 35:1192–1198, 1987.
- [92] A. R. Brown and G. M. Rebeiz. Micromachined micropackaged filter banks and tunable bandpass filters. In *Proceedings of the Wireless Communications Conference*, pages 193–197, August 1997. Digital Object Identifier: 10.1109/WCC.1997.622276.
- [93] K. Kageyama, K. Saito, H. Murase, H. Utaki, and T. Yamamoto. Tunable active filters having multilayer structure using LTCC. *IEEE Trans. on Micro. Theory and Techniques*, 49:2421–2424, 2001.
- [94] O. Y. Buslov, C. Y. Kang, V. N. Keis, I. V. Kotelnikov, A. Y. Shimko, M. F. Ivanova, A. V. Tumarkin, S. F. Karmanenko, and A. B. Kozyrev. Dielectric resonators loaded by ferroelectric varactors for tunable Ka-band filter. *Integrated Ferroelectrics*, 86:171–179, 2006.
- [95] S. Courrèges, Y. Li, Z. Zhao, K. Choi, A. Hunt, and J. Papapolymerou. Ferroelectric tunable bandpass filters for Ka-band applications. In *Proceedings of the 38th European Microwave Conference*, 2008.
-

- [96] A. Tombak, F. T. Ayguavives, J. P. Maria, G. T. Stauf, A. I. Kingon, and A. Mortazawi. Tunable RF-filters using thin film barium strontium titanate based capacitors. In *IEEE MTT-S Digest*, 2001.
- [97] J. Papapolymerou, C. Lugo, Z. Zhiyong, W. Xiaoyan, and A. Hunt. A miniature low-loss slow-wave tunable ferroelectric band pass filter from 11-14GHz. In *IEEE MTT-S International Microwave Symposium Digest*, pages 556–559, 2006. Digital Object Identifier: 10.1109/MWSYM.2006.249653.
- [98] J. B. Muldavin. *Design and analysis of series and shunt MEMS switches*. PhD thesis, The University Of Michigan, 2001.
- [99] D. Peroulis, S. Pacheco, K. Sarabandi, and P. B. Katehi. MEMS devices for high isolation switching and tunable filtering. In *IEEE MTT-S International Microwave Symposium Digest*, volume 2, pages 1217–1220, 2000. Digital Object Identifier: 10.1109/MWSYM.2000.863578.
- [100] H. T. Kim, J. H. Park, Y. K. Kim, and Y. Kwon. Millimeter-wave micromachined tunable filters. In *IEEE MTT-S Digest*, 1999.
- [101] Y. Liu, A. Borgioli, A. S. Nagra, and R. A. York. Distributed MEMS transmission lines for tunable filter applications. *International Journal of RF and Microwave*, 2:254–260, 2001.
- [102] B. Lakshminarayanan and T. Weller. Tunable bandpass filter using distributed MEMS transmission lines. In *IEEE MTT-S Digest*, 2003.
- [103] A. Abbaspour-Tamijani. *Novel components for integrated millimeter-wave front-ends*. PhD thesis, The University Of Michigan, 2004.
- [104] G. Boudouris. *Cavités électromagnétiques*. Dunod, 1971.
- [105] D. Kajfez. Q-factor measurement techniques. *RF Design*, pages 56–73, 1999.
- [106] G. Strauss, P. Ehret, and W. Menzel. On-wafer measurements of microstrip based MIMICs without via holes. In *IEEE MTT-S International Microwave Symposium Digest*, pages 1399–1402, 1996.
- [107] J. D. Rhodes. The theory of generalized interdigital networks. *IEEE Trans. on Circuit Theory*, 16(8):280–288, August 1969.
- [108] M. Viertel. *Nichtminimalphasige Mikrowellenfilter und Eingangsmultiplexer fuer die Satellitenkommunikation*. PhD thesis, Universität Wuppertal, 2003.
- [109] RF-MEMS and RF-MEMS packaging. Technical report, IMEC, 2007. <http://www.imec.be/ScientificReport/SR2007/html/1384105.html>.
- [110] D. Deslandes and K. Wu. Design consideration and performance analysis of substrate integrated waveguide components. In *Proceedings of the 32nd European Microwave Conference*, 2002.
- [111] Rogers corporation, data sheet: RT/Duroid 5870/5880 high frequency laminates. www.rogerscorporation.com/mwu/pdf/5000data.pdf, 2008.

- [112] H. C. Ling, M. F. Yan, and W. W. Rhodes. High dielectric constant and small temperature coefficient bismuth-based dielectric compositions. *Journal of Materials Research*, 5(8):1752–1762, 1990. DOI: 10.1557/JMR.1990.1752.
- [113] M. Onoda, J. Kuwata, K. Kaneta, K. Toyama, and S. Nomura. Ba-Sr solid solution ceramics with temperature-stable high dielectric constant and low microwave loss. *Japanese Journal of Applied Physics*, 21:1707–1710, 1982. DOI: 10.1143/JJAP.21.1707.
- [114] R. J. Cava and J. J. Krajewski. Low temperature coefficient dielectric material comprising binary calcium niobate and calcium tantalate oxides, 1999.
- [115] M. Hopcroft, R. Melamud, R. N. Candler, W. T. Park, B. Kim, G. Yama, A. Patridge, M. Lutz, and T. W. Kenny. Active temperature compensation for micromachined resonator. In *IEEE Solid-State Sensor and Actuator Workshop*, 2004.
- [116] S. S. Toncich and T. Forrestier. Tunable voltage-controlled temperature-compensated crystal oscillator, 2002.
- [117] D. P. Kaegebein. Temperature compensating cavity bandpass filter, 2001.
- [118] Y. Wang and Q. Sui. A new temperature compensation method of rectangular waveguide resonant cavities. In *Proceedings of the Asia-Pacific Microwave Conference*, volume 5, 2005. DOI: 10.1109/APMC.2005.1607117.
- [119] D. J. Small and J. A. Lunn. Temperature compensated high power bandpass filter, 2003.
- [120] H. Jantunen and A. Turunen. Temperature compensated dielectric filter, 1991-1994.
- [121] H. J. Visser. *Array and phased array antenna basics*. Wiley, 2005. pp. 201-219, ISBN: 978-0-470-87117-1.
- [122] R. J. Mailloux. *Phased array antenna handbook*. Artech House, Inc., 2005. pp. 185-221, ISBN: 1580536891.
- [123] R. J. Mailloux. *Phased array antenna handbook*. Artech House, Inc., 2005. pp. 17-19, ISBN: 1580536891.
- [124] IEEE Standard definitions of terms for antennas, std 145-1993.
- [125] H. J. Visser. *Array and phased array antenna basics*. Wiley, 2005. pp. 83-120, ISBN: 978-0-470-87117-1.
- [126] R. J. Mailloux. *Phased array antenna handbook*. Artech House, Inc., 2005. pp. 3-4, ISBN: 1580536891.
- [127] R. J. Mailloux. *Phased array antenna handbook*. Artech House, Inc., 2005. p. 24, ISBN: 1580536891.
- [128] W. L. Stutzman and G. A. Thiele. *Antenna theory and design*. Wiley, 1997. pp. 108-168, ISBN: 0471025909.

- [129] H. J. Visser. *Array and phased array antenna basics*. Wiley, 2005. p. 127, ISBN: 978-0-470-87117-1.
- [130] H. J. Visser. *Array and phased array antenna basics*. Wiley, 2005. p. 245, ISBN: 978-0-470-87117-1.
- [131] H. J. Visser. *Array and phased array antenna basics*. Wiley, 2005. p. 258, ISBN: 978-0-470-87117-1.
- [132] B. Schoenlinner and V. Ziegler. RF-MEMS phase shifters. In *Amicom Sommer School*, September 2005.
- [133] C. Renard. Phased array antennas in airborne applications: effect of errors in a PAA. In *Antenna Centre of Excellence Workshop, The Hague*, page 10, 2005.
- [134] T. Gerz. Wirbelschleppen bremsen den Luftverkehr. *Mitteilungen des Deutschen Zentrums fuer Luft- und Raumfahrt*, G 12625:60–63, 2000.
- [135] T. Halldorsson, A. Langmeier, A. Pruecklmeier, V. Banakh, and A. Falits. Particle and speckle imaging velocimetry applied to a monostatic lidar. *SPIE Newsroom*, 2007. DOI: 10.1117/2.1200706.0615.
- [136] M. Keane, D. Buckton, M. Redfern, C. Bollig, C. Wedekind, F. Koepp, and F. Berni. Axial detection of aircraft wake vortices using doppler lidar. *Journal of Aircraft*, 39, 2002.
- [137] T. Halldorsson, V. Ziegler, and R. Schneider. Bordgestuetztes Wirbelschleppen Erkennungssystem (BoWES). In *DGLR Symposium*, 2005.
- [138] U. Schmid, H. Seidel, R. Koerber, V. Ziegler, A. Wuertz, D. Schwanke, S. Hoyler, and H. L. Bloecher. RADARAUGE - Phasengesteuertes Radarmodul bei 79GHz auf keramischen und organischen Substraten. In *VDE Kongress, Innovations for Europe*. VDE-VDI, 2006.
- [139] R. Koerber. Phasengesteuertes Radarmodul bei 79GHz auf keramischen und organischen Substraten. In *Mikrosystemtechnik fuer Fahrerassistenzsysteme, FASVision, BMBF Auftaktveranstaltung*. VDE-VDI, 2007.
- [140] H. L. Bloecher and J. Dickmann. Improvement of safety and driver assistance functions using environment sensing. In *Mikrosystemtechnik fuer Fahrerassistenzsysteme, FASVision, BMBF Auftaktveranstaltung*. VDE-VDI, 2007.
- [141] A. G. Derneryd. Linearly polarized microstrip antennas. *IEEE Trans. on Antennas Propag.*, AP-24:846–851, November 1976.
- [142] R. Garg, P. Bhartia, I. Bahl, and A. Ittipiboon. *Microstrip antenna design handbook*. Number ISBN: 0-89006-513-6 in Artech House Antennas and Propagation Library. Artech House, Inc., 2001.
- [143] B. B. Jones, F. Y. M. Chow, and A.W. Seeto. The synthesis of shaped patterns with series-fed microstrip patch arrays. *IEEE Trans. on Antennas Propag.*, AP-30(6):1206–1212, November 1982.

-
- [144] V. Ziegler, A. Stehle, C. Siegel, B. Schoenlinner, U. Prechtel, U. Schmid, S. Klein, and A. Wuertz. Eine einfache und robuste RF-MEMS Technologie für zukünftige Radarsysteme bei 77-81GHz. In *VDE Kongress, Innovations for Europe*, 2006.
 - [145] H. Yisheng and K. Arichandran. Compact phased array for small LEO satellite. In *International Symposium on Antennas, Propagation and EM Theory*, pages 684–687, 2000. ISBN: 0-7803-6377-9.
 - [146] M. Lisi. Phased arrays for satellite communications: a system engineering approach. In *IEEE International Conference on Phased Array Systems and Technology*, pages 193–196, 2000. Digital Object Identifier: 10.1109/PAST.2000.858938.
 - [147] Y. Zheng and Y. Ruliang. Feasibility study of using small satellite synthetic aperture radar for global 3D imaging. In *International Geoscience and Remote Sensing Symposium*, volume 6, pages 3162–3164, June 2002.
 - [148] A. Wicks, A. da Silva-Curiel, J. Ward, and M. Fouquet. Advancing small satellite earth observation: operational spacecraft, planned missions and future concepts. In *14th AIAA/USU Small Satellite Conference*, August 2000.
 - [149] Rosenberger Hochfrequenztechnik GmbH & Co. KG, data sheet: Series SMP, Mini-SMP. www.rosenberger.de, 2008.
 - [150] G. M. Rebeiz. *RF-MEMS: theory, design, and technology*. Wiley-Interscience, June 2002. ISBN-10: 0471201693.
 - [151] C. Siegel. *Entwicklung und Charakterisierung einer zuverlässigen Technologie fuer Mikro-Elektro- Mechanische Systeme als Mikrowellenbauelemente*. PhD thesis, University of Ulm, 2008.
 - [152] R. J. Mailloux. *Phased array antenna handbook*. Artech House, Inc., 2005. pp. 366-367, ISBN: 1580536891.
 - [153] W. Gautier, A. Stehle, C. Siegel, B. Schoenlinner, V. Ziegler, U. Prechtel, and W. Menzel. Hybrid integrated RF-MEMS phased array antenna at 10GHz. In *38th European Microwave Conference*, 2008.
 - [154] G. L. Tan, R. E. Mihailovich, J. B. Hacker, J. F. DeNatale, and G. M. Rebeiz. Low-loss 2- and 4-bit TTD MEMS phase shifters based on SP4T switches. *IEEE Trans. on Micro. Theory and Techniques*, 51(1):297–304, January 2003.
 - [155] N. L. Vandenberg and L. P. B. Katehi. Broadband vertical interconnects using slot-coupled shielded microstrip lines. *IEEE Trans. on Micro. Theory and Techniques*, 40(1):81–88, 1992.
 - [156] S. Majumder, J. Lampen, R. Morrison, and J. Maciel. A packaged, high-lifetime ohmic MEMS RF switch. In *IEEE MTT-S International Microwave Symposium Digest*, 2003.
 - [157] Y. Oya, A. Okubora, M. VanSpengen, P. Soussan, S. Stoukatch, X. Rottenberg, P. Ratchev, H. Tilmans, W. DeRaedt, E. Beyne, P. DeMoor, I. DeWolf, and K. Baert. A reliable and compact polymer-based package for capacitive RF-MEMS switches. In *IEEE International Electron. Devices Meeting*, pages 31–34, 2004. DOI: 10.1109/IEDM.2004.1419056.
-

- [158] I. DeWolf. The reliability of RF-MEMS: failure modes, test procedures and instrumentation. *SPIE proceedings series*, 5343:1–8, 2004.
- [159] B. Lakshminarayanan, D. Mercier, and G. M. Rebeiz. High-reliability miniature RF-MEMS switched capacitors. *IEEE Trans. on Micro. Theory and Techniques*, 56(4):971–981, 2008.
- [160] H. S. Newman, J. L. Ebel, D. Judy, and J. Maciel. Lifetime measurements on a high-reliability RF-MEMS contact switch. *IEEE Microwave and Wireless Components Letters*, 18(2):100–102, 2008. DOI: 10.1109/LMWC.2007.915037.
- [161] V. Ziegler, B. Schoenlinner, W. Gautier, A. Stehle, G. Georgiev, and U. Prechtel. RF-MEMS based solutions for aeronautic communication and radar systems. In *German Microwave Conference*, 2008.